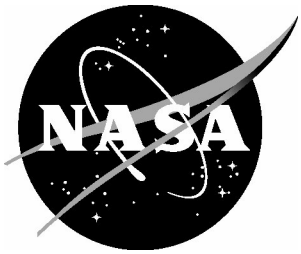
NASA/CR–20220016017 Volume I



Subsonic Ultra Green Aircraft Research: Phase IV Final Report – Volume I Mach 0.80 Transonic Truss-Braced Wing High-Speed Design Report

Neal A. Harrison, Krishna Hoffman, David S. Lazzara
Boeing Research and Technology, Huntington Beach, CA

Eric Y. Reichenbach
Boeing Research and Technology, St. Louis, MO

Anthony J. Sclafani, Christopher K. Droney
Boeing Commercial Airplanes, Long Beach, CA

October 2023

NASA STI Program . . . in Profile

Since its founding, NASA has been dedicated to the advancement of aeronautics and space science. The NASA scientific and technical information (STI) program plays a key part in helping NASA maintain this important role.

The NASA STI program operates under the auspices of the Agency Chief Information Officer. It collects, organizes, provides for archiving, and disseminates NASA's STI. The NASA STI program provides access to the NTRS Registered and its public interface, the NASA Technical Reports Server, thus providing one of the largest collections of aeronautical and space science STI in the world. Results are published in both non-NASA channels and by NASA in the NASA STI Report Series, which includes the following report types:

- TECHNICAL PUBLICATION. Reports of completed research or a major significant phase of research that present the results of NASA Programs and include extensive data or theoretical analysis. Includes compilations of significant scientific and technical data and information deemed to be of continuing reference value. NASA counter-part of peer-reviewed formal professional papers but has less stringent limitations on manuscript length and extent of graphic presentations.

- TECHNICAL MEMORANDUM. Scientific and technical findings that are preliminary or of specialized interest, e.g., quick release reports, working papers, and bibliographies that contain minimal annotation. Does not contain extensive analysis.

- CONTRACTOR REPORT. Scientific and technical findings by NASA-sponsored contractors and grantees.

- CONFERENCE PUBLICATION. Collected papers from scientific and technical conferences, symposia, seminars, or other meetings sponsored or co-sponsored by NASA.

- SPECIAL PUBLICATION. Scientific, technical, or historical information from NASA programs, projects, and missions, often concerned with subjects having substantial public interest.

- TECHNICAL TRANSLATION. English-language translations of foreign scientific and technical material pertinent to NASA's mission.

Specialized services also include organizing and publishing research results, distributing specialized research announcements and feeds, providing information desk and personal search support, and enabling data exchange services.

For more information about the NASA STI program, see the following:

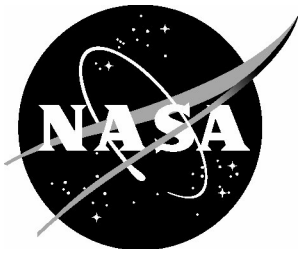
- Access the NASA STI program home page at http://www.sti.nasa.gov

- E-mail your question to help@sti.nasa.gov

- Phone the NASA STI Information Desk at 757-864-9658

- Write to:
  NASA STI Information Desk
  Mail Stop 148
  NASA Langley Research Center
  Hampton, VA 23681-2199

NASA/CR–20220016017 Volume I



Subsonic Ultra Green Aircraft Research: Phase IV Final Report – Volume I Mach 0.80 Transonic Truss-Braced Wing High-Speed Design Report

Neal A. Harrison, Krishna Hoffman, David S. Lazzara
Boeing Research and Technology, Huntington Beach, CA

Eric Y. Reichenbach
Boeing Research and Technology, St. Louis, MO

Anthony J. Sclafani, Christopher K. Droney
Boeing Commercial Airplanes, Long Beach, CA

National Aeronautics and
Space Administration

Langley Research Center
Hampton, Virginia 23681-2199

Prepared for Langley Research Center
under Contract NNL16AA04B

October 2023

BOEING is a trademark of Boeing Management Company.

Abstract

This design report summarizes work performed by the Boeing Subsonic Ultra-Green Aircraft Research (SUGAR) team from December 2016 through June 2018.

In Phase IV of the SUGAR program, Boeing is working to improve the productivity of a TTBW configuration by updating the Mach 0.745 vehicle concept to operate efficiently at Mach 0.80. Due to the aerodynamic and structural design challenges associated with adapting the design to a higher speed, design tasks have been broken into several subtasks. The information in this report (Volume I) documents the development of a Mach 0.80 vehicle outer mold line, maturation of TTBW structural concepts, and presents a preliminary high-lift system assessment. Results from these studies were integrated into an aircraft-level performance code that estimates the benefits of TTBW technology, both on its own and as a part of the SUGAR integrated technology suite.

The aerodynamic performance results presented herein detail the high cruise efficiency of the TTBW concept operating at M=0.80. Results from the RANS code OVERFLOW indicate that the TTBW is aerodynamically well suited for operation at the design M=0.80 transonic cruise Mach number. Aircraft-level performance predictions show that the TTBW offers a 7.2% improvement in fuel burn (per seat) for an economic mission of 900nm, and a 9.0% improvement in fuel burn (per seat) for a 3500nm mission with full passenger payload, relative to an aspect ratio 13 conventional tube and wing configuration of equivalent technology. Integration of the TTBW performance benefits into the SUGAR technology suite shows a 55.9% reduction in fuel burn (for the economic mission) relative to the reference (SUGAR Free) aircraft, which is a consistently sized traditional cantilever wing, single-aisle transport typical of the 2008 fleet. This benefit does not include the performance improvement potential of hybrid-electric systems studied in earlier phases of the SUGAR program

Structural concept development work completed in Phase IV has identified several strut attachment concepts that are worth additional development activity – an inboard strut attachment swivel joint concept (which enables the strut to carry axial loads while avoiding strut bending induced by wing twist during flight) significantly simplifies the construction of the main strut. An outboard offset strut attachment concept holds significant potential for further reductions in wing-strut interference drag.

Based on work performed to date on Phase IV and the previous phases of the SUGAR program, the TTBW concept continues to remain a viable concept for significantly improving the performance of future aircraft. High-fidelity aerodynamic analysis of the Mach 0.80 TTBW aircraft has shown fuel burn improvement that has exceeded initial expectations despite the increase in cruise Mach number. Structural concept maturation has continued to refine the TTBW structure, and has found no obvious ‘show-stoppers’ to date. Therefore, the potential benefit of improved performance through the use of a very high aspect ratio strut-braced wing continues to warrant additional study.

Acknowledgements

This project and report reflect the combined efforts of the Boeing SUGAR team. The coordinated effort of this team has produced this report. Funding for this effort was provided by the NASA Fundamental Aeronautics Program, through the Subsonic Fixed Wing Project followed by the Advanced Air Vehicles Program, through the Advanced Air Transport Technology Project. The contract number is NNL16AA04B task order NNL17AA46T.

The team would like to thank Sally Viken and Greg Gatlin of the NASA Langley Research Center for their guidance as the NASA Contracting Officer Technical Representatives (COTRs).

In particular, credit for this work is due to the Boeing team members noted below.

Boeing Team Members:

Neal Harrison	**Program Manager, Principal Investigator**
Michael Beyar	**Wind Tunnel Test – Lead, High-Lift Aerodynamics**
Eric Dickey	**High-Lift Aerodynamic Design - Lead**
Krishna Hoffman	**Structural Design - Lead**
Tim Allen	Aeroelastic Analysis
Jack Bourbonnais	Aeroelastic Analysis
Dave Bruns	Aerodynamic Performance
Jake Callahan	Aeroelastic Analysis
Pete Camacho	Aerodynamic Performance
Robert Creason	Structural Design
Christopher Droney	Program Manager, 2014 to May 2018
Lie-Mine Gea	Aerodynamic Analysis
Chris Hill	Structural Design
Jeffrey Jonokuchi	Stability and Control
Edward Lawson	Propulsion
David Lazzara	Multidisciplinary Design Optimization
Alexander Lee	Configuration Synthesis
Meghan Luff	Structural Design
Ryan Michel	Structural Analysis
Paul Miller	Weights
Eric Reichenbach	Aeroelastic Design and Analysis
Anthony Sclafani	High-Speed Aerodynamic Design
Hsi-Yung (Tom) Wu	Structural Analysis
Esther Zidovetzki	Structural Design

Table of Contents

Abstract i
Acknowledgements ii
List of Tables v
List of Figures vi
Special Data Rights Assertion xii
Nomenclature xiii
1.0 Introduction 1
2.0 Transonic Truss-Braced Wing Configuration Design 4
2.1 SUGAR TTBW Configuration Evolution 4
2.2 SUGAR Mach 0.80 Configuration Description 5
2.2.1 Integration 5
2.2.2 Wing 9
2.2.3 Main Strut and Jury Strut 11
2.2.4 Vertical Fin 13
2.2.5 Horizontal Stabilizer 14
2.2.6 Fuselage 15
2.2.7 Landing Gear 17
2.2.8 Propulsion 18
3.0 Structural Analysis 20
3.1 Structural Fittings/Joints 20
3.1.1 Inboard – Strut to Sponson 20
3.1.2 Outboard – Strut to Wing 22
3.2 Aeroelastic Analysis 23
3.2.1 Background 23
3.2.2 Phase IV FEM Refinement 24
3.2.3 Configuration Geometry and Data 24
3.2.4 Structural Idealization and Optimization Model 24
3.2.5 Wing, Strut, and Jury Features in the FEM 29
3.2.6 Center Body/Sponson FEM 35
3.2.7 Finite Element Model Integration 36
3.2.8 Nonstructural Mass and Fuel/Payload Cases 39
3.2.9 Aerodynamic Model 40
3.2.10 Maneuver Load Conditions 42
3.2.11 Preliminary Structural Sizing and Optimization 46
3.2.12 Initial Flutter Analysis 49
3.2.13 Gust Loads Analysis 54
3.2.14 Structural Sizing Optimization 58
3.2.15 Aerodynamic Adjustments 60

3.2.16 Flutter Analysis 70
3.2.17 Aeroelastic Analysis Conclusions 74
4.0 Aerodynamic Design 76
4.1 High-Speed Aerodynamic Design 76
4.1.1 Design methodology 76
4.1.2 Wing-Strut Design Overview 85
4.1.3 Regions of Special Consideration 105
4.1.4 1104-001-RG – Final Configuration Aerodynamic Performance 116
5.0 Configuration Analysis 132
5.1 Aerodynamics 132
5.1.1 High Speed 132
5.1.2 Low Speed 135
5.2 Mass Properties 137
5.3 Stability & Control 139
5.3.1 Longitudinal Stability and Control Assessment 139
5.3.2 Lateral Stability and Control Assessment 142
6.0 Performance 148
6.1.1 Sizing Requirements 149
6.1.2 Sizing Results 150
7.0 Summary 157
7.1 Further Considerations 158
7.2 Recommendations 160
References 161

List of Tables

Table 1 - Mach 0.80 Configuration (1104-001-RG) Principal Characteristics. 8
Table 2 – Mach 0.80 Configuration (1104-001-RG) Body Axis Component Origins (units are inches). 8
Table 3 – Wing Reference Geometry. 10
Table 4 – Main strut spar centerline locations (Strut Reference Plane). 12
Table 5 – Jury strut spar locations (Jury Strut Reference Plane) 13
Table 6 – 1104-001-RG Vertical Tail Planform Parameters. 14
Table 7 – 1104-001-RG Horizontal Planform Parameters 15
Table 8 – gFan+ Key Characteristics. 19
Table 9 – Composite Material Properties. 25
Table 10 – Custom Material Properties for Stiffener Layers. 26
Table 11 – Payload and Fuel Combinations. 40
Table 12 – Structural Weights Sized for Strength and Buckling at Critical Maneuver Loads. 47
Table 13 – Modal Analysis Results – Mass Case 4. 50
Table 14 – Initial Flutter Analysis Results. 51
Table 15 – Tuned Discrete Gust Reference Velocity as a Function of Altitude. 55
Table 16 – Structural Weights Sized for Strength and Buckling at Critical Gust and Maneuver Loads. 59
Table 17 – CFD Analysis Conditions. 62
Table 18 – Flutter Summary – Mach 0.59 to 0.85. 71
Table 19 – Flutter Summary – Mach 0.92. 72
Table 20 – SUGAR TTBW Speed Buildup. 133
Table 21 – 1104-001 Group Weight Statement 138
Table 22 – Maximum Steady-State Roll Rate Results Summary. Green cells exceed requirement, orange cells, meet requirement, red cells do not meet requirement. 145
Table 23 – Time-to-bank results summary. Green cells exceed requirement, orange cells meet requirement, red cells do not meet requirement. 146
Table 24 – 765-095-RJ and 1104-001 Mission Performance. 151
Table 25 – 765-095-RJ and 1104-001 Mission Performance Comparison. 152
Table 26 – 765-095-RJ and 1104-001 Sized With and Without Body Fuel Tank. 156

List of Figures

Figure 1 - Phase IV Configuration Evolution. 4
Figure 2 – SUGAR TTBW Mach 0.80 Configuration (1104-001-RG). 6
Figure 3 – SUGAR TTBW Mach 0.80 (1104-001-RG) General Arrangement (3-view). 7
Figure 4 – Planform Change from Phase III to Phase IV. 9
Figure 5 – SUGAR Mach 0.80 (1104-001-RG) Wing Planform (Projected view, units are inches). 10
Figure 6 – SUGAR Mach 0.80 Main Strut Structural Concept. 12
Figure 7 – SUGAR Mach 0.80 (1104-001-RG) Strut Reference Plane Corner Points. 12
Figure 8 – SUGAR Mach 0.80 (1104-001-RG) Jury Strut corner point drawing (jury strut reference plane). 13
Figure 9 – 1104-001-RG Vertical Tail Planform (units are inches). 14
Figure 10 – 1104-001-RG Horizontal Planform (units are inches). 15
Figure 11 – 1104-001-RG Fuselage Cross Section, common for both Mach 0.745 and Mach 0.80 configurations (units are in inches). 15
Figure 12 – 1104-001-RG Layout of Passenger Accommodations, common for both Mach 0.745 and Mach 0.80 configurations. 16
Figure 13 – SUGAR TTBW Landing Gear Layout, common for both Mach 0.745 and Mach 0.80 configurations (765-095 RJ shown). 17
Figure 14 – SUGAR TTBW Landing Gear Arrangement. 18
Figure 15 – gFan+ Concept Layout. 19
Figure 16 – Main Strut Swivel Joint at Sponson. 21
Figure 17 – Main Strut Outboard Attachment Configuration. 23
Figure 18 – Composite Laminate Representation of Stiffened Panels. 25
Figure 19 – Offsets for Nastran PCOMP and PSHELL Entries to Maintain OML during Sizing. 27
Figure 20 – Element Normal Directions in the Wing Box. 27
Figure 21 – Total Laminate Thickness for Balanced Stacking Sequence. 28
Figure 22 – Property Regions of the Wing, Strut, and Jury. 29
Figure 23 – Wing Structural Layout. 30
Figure 24 – Strut Structural Layout. 30
Figure 25 – Jury Structural Layout. 31
Figure 26 – Connection of Strut to Wing (Skins Removed for Clarity). 32
Figure 27 – Connection of Strut to Sponson (Strut Skin Removed for Clarity). 32
Figure 28 – Connections of the Jury to the Strut and Wing (Skins Removed for Clarity). 33
Figure 29 – Control Surface Hinge Connections (Upper Skins Removed for Clarity). 34
Figure 30 – Titanium Splitter (Yellow/Brown) in Strut Leading Edge (Upper Skin Removed for Clarity) 35

Figure 31 – Sponson Structural Model. 36
Figure 32 – Fuselage Barrel Section Structural Model. 37
Figure 33 – Integrated Vehicle Finite Element Model. 37
Figure 34 – Primary Vertical Connection between Wing and Body. 38
Figure 35 – Primary Fore-Aft Connection between Wing and Body. 38
Figure 36 – Primary Lateral Connection between Wing and Body. 39
Figure 37 – Doublet Lattice Aerodynamic Model with Refined Mesh and Updated Panels. 40
Figure 38 – Detail of Aerodynamic Model Showing Carry-through Panels and Updated Tail. 41
Figure 39 – Detail View of Aerodynamic Model of Jury and Strut-to-Wing Connection. 41
Figure 40 – Flight Conditions for Maneuver Loads Survey. 42
Figure 41 – Structural Deflection for a 2.5g Steady Pull-Up at Mach 0.85, Altitude 26,468 feet. 43
Figure 42 – Rigid Pressure Distribution for a 2.5g Steady Pull-Up at Mach 0.85, Altitude 26,468 feet. 44
Figure 43 – Flexible Pressure Distribution for a 2.5g Steady Pull-Up at Mach 0.85, Altitude 26,468 feet. 44
Figure 44 – Wing Critical Design Load Selection. 45
Figure 45 – Strut Critical Design Load Selection. 45
Figure 46 – Structural Sizing Critical Design Load Selection. 46
Figure 47 – Skin Thickness in Initial Optimized Structure. 48
Figure 48 – Airspeed and Altitude Points for Flutter Analysis. 50
Figure 49 – Damping and Frequency Plots for Flutter Analysis at Mach 0.92, 26,000 feet, Mass Case 4. 52
Figure 50 – Critical Flutter Mechanism Eigenvector Analysis at Mach 0.92, 26,000 feet, Mass Case 4. 53
Figure 51 – Critical Flutter Mechanism at Mach 0.92, 26,000 feet, Mass Case 4. 53
Figure 52 – Typical Gust Shapes. 55
Figure 53 – Tuned Discrete Gust Analysis Points in the Sky. 56
Figure 54 – Design Load Case Selection. 57
Figure 55 – Design Flight Loads Comparison. 58
Figure 56 – Skin Thickness in Optimized Structure. 60
Figure 57 – Aerodynamic Pressures from CFD Analysis (M=0.85, C_L=0.264, Re_{mac} = 25.0M). 61
Figure 58 – CFD Results Processing. 62
Figure 59 – Rigid Doublet Lattice Model Pressures at Mach 0.7571, 13,200 ft, Angle of Attack -1.128°. 63
Figure 60 – CFD Solution for Case 15: Mach 0.7571, C_L = 0.158, q = 515.0 psf, Altitude = 13,200 ft, Re_{mac} = 33.9M. 64

Figure 61 – CFD Solution for Case 16: Mach 0.7571, C_L = 0.191, q = 515.0 psf, Altitude = 13,200 ft, Re_{mac} = 33.9M. 64
Figure 62 – CFD Strip Force and Moment Coefficients for Different Angles of Attack at Mach 0.7571, Altitude = 13,200 ft, Re_{mac} = 33.9M. 64
Figure 63 – Aerodynamic Strip Force and Moment Coefficients from DLM and CFD at Mach 0.7571, Altitude 13,200 ft, Re_{mac} = 33.9M. 65
Figure 64 – Rigid Doublet Lattice Model Pressures at Mach 0.92, Altitude = 26,000 ft, α=1°. 66
Figure 65 – CFD Solution for Case 19: Mach 0.92, C_L = 0.182, q = 445.3 psf, Altitude = 26,000 ft, Re_{mac} = 27.5M. 66
Figure 66 – CFD Solution for Case 20: Mach 0.92, C_L = 0.220, q = 445.3 psf, Altitude = 26,000 ft, Re_{mac} = 27.5M. 66
Figure 67 – CFD Strip Force and Moment Coefficients for Different Angles of Attackat Mach 0.92, Re_{mac} = 27.5M. 67
Figure 68 – Aerodynamic Strip Force and Moment Coefficients from DLM and CFD at Mach 0.92 , Re_{mac} = 27.5M. 67
Figure 69 – Section Pressure Distributions (a) Case 16: Mach = 0.757, C_L = 0.191, Re_{mac} = 33.9M (b) Case 20: Mach = 0.92, C_L = 0.2204, Re_{mac} = 27.5M. 68
Figure 70 – Delta Pressure Distributions between α 0.795° and 0.495° at Mach = 0.92, Re_{mac} = 27.5M. 68
Figure 71 – Delta Pressure Distributions between α 0.795° and 0.495° at Station 886 at Mach 0.92, Re_{mac} = 27.5M. 68
Figure 72 – Aerodynamic Box Force Adjustments at Mach = 0.76, Altitude = 13,000 ft, C_L = 0.2204, Re_{mac} =27.5M. 69
Figure 73 – Aerodynamic Box Force Adjustments at Mach 0.92, 26,000 ft, C_L = 0.2204, Re_{mac} = 27.5M. 70
Figure 74 – Flutter Results for Mach 0.76, 13,000 feet, Mass Case 1, Re_{mac} = 33.9M. 73
Figure 75 – Flutter Results for Mach 0.92, 26,000 feet, Mass Case 1, Re_{mac} = 27.5M. 73
Figure 76 – TRANAIR surface and volume discretization. 77
Figure 77 – Typical drag improvement seen in early design iterations for a single-point optimization. 80
Figure 78 – Typical comparisons of seed and optimized results in relation to pressure profiles and deformation modes after single-point optimization at Mach = 0.80, C_L = 0.695, and Re_{mac} = 14M. 80
Figure 79 – Typical comparisons of seed and optimized spanload and lift-distribution after single-point optimization at Mach = 0.80, C_L = 0.695, Re_{mac} = 14M. 81
Figure 80 – Typical multipoint optimization drag history (Mach = 0.80, C_L = 0.695, Re_{mac} = 14M). 82

Figure 81 – Typical comparison between the seed (green) and optimized (orange) geometry after multipoint optimization. 82
Figure 82 – Comparison between seed and optimized result pressure contours and deformation modes after multipoint optimization (Mach = 0.80, C_L = 0.695, Re_{mac} = 14M). 82
Figure 83 – Comparison of seed and optimized spanload and lift-distribution after multipoint optimization (Mach = 0.80, C_L = 0.695, Re_{mac} = 14M). 83
Figure 84 – Spanwise stations where structural box sizing was conducted during optimization. 84
Figure 85 – Typical aero-structural optimization results showing drag improvements and structural feasibility maintained for a single-point case. 84
Figure 86 – The aero-structural optimization tracked the design progress for key design constraints. 85
Figure 87 – Configuration 1104-001-RA, M=0.8, 40kft, C_L=0.695, Re_{mac} = 14M. 86
Figure 88 – Configuration 1104-001-RA Spanload, M=0.8, 40kft, C_L=0.695, and Re_{mac} = 14M. 87
Figure 89 – Configuration 1104-001-RB Wing Twist Modification. 88
Figure 90 – Comparison of the 1104-001-RB wing-alone design wing pressures as compared to 1104-001-RA reference. 89
Figure 91 – OVERFLOW results for 1104-001-RB, M=0.8, 40kft, C_L=0.695, Re_{mac}=14M. 91
Figure 92 – 1104-001-RB Spanload at Mach = 0.80, C_L = 0.695, Re_{mac} = 14M. 91
Figure 93 – Wing twist evolution from 1104-001-RB to 1104-001-RC Configuration. 93
Figure 94 – Strut twist evolution from 1104-001-RB to 1104-001-RC Configuration. 94
Figure 95 – Comparison of surface C_p contours from 1104-001–RB Configuration to 1104-001–RC (Mach = 0.80, C_L = 0.695, Re_{mac} = 14M). 94
Figure 96 – Comparison of Spanload from 1104-001-RB Configuration to 1104-001-RC at Mach = 0.80, C_L = 0.695, Re_{mac} = 14M. 96
Figure 97 – Aerodynamic Efficiency changes as the design has evolved at Mach = 0.80, Re_{mac} = 14M. 97
Figure 98 – Movement in the jury strut-to-strut connection was moved outboard to reduce the load on the outboard strut. 98
Figure 99 – Strut Planform Modification (1104-001-RD_des30). 99
Figure 100 – Modified –RD_des30 strut twist distribution as a function of wing semi-span. 99
Figure 101 – Strut Planform Modification Reduced Peak Cp on Strut in Transition Region (1104-001-RD_des28 vs 1104-001–RD_des30) at Mach = 0.80, C_L = 0.695, Re_{mac} = 14M. 100

Figure 102 – Aerostructural optimization results for a composite-steel strut and composite wing comparing the seed and optimized geometry structural sizing. 101
Figure 103 – Jury-strut location study results with multiple materials and structural box sizing. Weight and stiffness feasibility results are shown for forward/aft spar locations different x/c locations along the local chord. 101
Figure 104 – Strut Concpt a) Baseline Strut and b) Offset Strut (cartoon) 102
Figure 105 – Offset Strut Structural Requirement used in Design. 102
Figure 106 – Alternate and Offset Strut Fairings from Phase III and Phase IV. 103
Figure 107 – OVERFLOW analysis of starting offset strut fairing geometry showed significant flow separation on the inboard and outboard sides at Mach = 0.8, C_L = 0.695, Re_{mac} = 14M. 103
Figure 108 – OVERFLOW analysis of final offset strut fairing geometry at Mach = 0.8, C_L = 0.695, Re_{mac} = 14M. 104
Figure 109 – Comparison of baseline and offset strut performance at Mach = 0.80 Re_{mac} = 14M. 104
Figure 110 – Updated Curved Beam Strut Attachment. 105
Figure 111 – OVERFLOW solutions of the original wing-body fairing design at the start of Phase III. Contours on the left of the symmetry plane are C_p, contours on the right are C_f at Mach = 0.745, C_L = 0.73, Re_{mac} = 12.3M (5). 106
Figure 112 – First Attempt at a re-lofted wing-body fairing (a) CAD geometry (b) Mach = 0.80, C_L = 0.695, Re_{mac} = 14M (c) Mach = 0.20, α = 16°, Re_{mac} = 13M. 107
Figure 113 – Revised fairing increases volume, reduces shock strength, but strengthens the low-speed vortex (a) CAD geometry (b) Mach = 0.80, C_L = 0.695, Re_{mac} = 14M (c) Mach = 0.20, α = 16°, Re_{mac} = 13M. 107
Figure 114 – Reverse planform wing-body strake. 108
Figure 115 – The wing-strut fairing was trimmed back to enable compatibility with a leading edge Krueger. 109
Figure 116 – Revisions to the wing-strut fairing to ensure high-lift system compatibility. 109
Figure 117 - Strut Flap Definition 110
Figure 118 – Flap articulation mechanism schematic (14). 111
Figure 119 – Wing-strut fairing with integrated FHF. 112
Figure 120 – Engine Pylon fairing with integrated FHF. 113
Figure 121 – Configuration with all FHFs installed. 113
Figure 122 – OVERFLOW C_f results of the flow around the middle (unintegrated) FHFs (Mach = 0.80, C_L = 0.695, Re_{mac} = 14M). 114
Figure 123 – Flap Hinge Fairing (FHF) installation on the wing-strut fairing surface C_p (Mach = 0.80, C_L = 0.695, Re_{mac} = 14M). 114
Figure 124 – Design Progression for Jury Strut Location. 115

Figure 125 – OVERFLOW results of the final jury strut installation surface C_p (Mach = 0.80, C_L = 0.695, Re_{mac} = 14M). 115
Figure 126 – Nacelle Shape and Rigging were optimized using MDOPT to reduce installed drag (Mach = 0.80, C_L = 0.695, Re_{mac} = 14M). 116
Figure 127. Configuration 1104-001-RG: Final Wing Twist Distributions. 117
Figure 128 – Configuration 1104-001-RG (WBS) Spanload at the Cruise Design Point (α = 1.51°). 118
Figure 129 – Comparison of wing-strut overlap regions for M=0.745 design vs. M=0.80 design. 119
Figure 130 – Wing and Strut surface C_p results from OVERFLOW for WBS Configuration at Mach = 0.80, C_L = 0.695, Re_{mac} = 14M. 119
Figure 131 – Drag Polar for 1104-001-RG (WBS) at Mach = 0.80, Re_{mac} = 14M. 120
Figure 132 – L/D for 1104-001-RG (WBS) at Mach = 0.80, Re_{mac} = 14M. 120
Figure 133 – Configuration 1104-001-RG Spanload - Effects of engine and pylon installation (Mach = 0.80, C_L = 0.695, Re_{mac} = 14M). 121
Figure 134 – Configuration 1104-001-RG – Effects of engine installation on the vehicle Drag Polar (Mach = 0.80, Re_{mac} = 14M). 122
Figure 135 – Configuration 1104-001-RG – Effects of engine installation on the vehicle L/D (Mach = 0.80, Re_{mac} = 14M). 122
Figure 136 – Configuration 1104-001-RG - Effect of engine installation on wing and strut surface pressure contours at Mach = 0.80, Re_{mac} = 14M. 123
Figure 137 – Configuration 1104-001-RG Spanload - Effects of FHF and jury strut installation (Mach = 0.80, C_L = 0.695, Re_{mac} = 14M). 124
Figure 138. Configuration 1104-001-RG – Effects of FHF and jury strut installation on the vehicle Drag Polar (Mach = 0.80, Re_{mac} = 14M). 124
Figure 139 – Configuration 1104-001-RG – Effects of FHF and jury strut installation on vehicle L/D (Mach = 0.80, Re_{mac} = 14M). 125
Figure 140 – Configuration 1104-001-RG – Effects of FHF and jury strut installation on vehicle Aerodynamic Performance (Mach = 0.80, Re_{mac} = 14M). 125
Figure 141 – Configuration 1104-001-RG - Wing Pressures (WBSNFJ) M=0.80, C_L=0.695, Alt=40kft, Re_{mac} = 14M. 126
Figure 142 – Configuration 1104-001-RG - Effect of FHF and jury strut installation on wing and strut surface pressure contours (M=0.80, C_L=0.695, Re_{mac} = 14M). 127
Figure 143 – Configuration 1104-001-RG Long-Range Cruise (LRC) Estimates (C_L = 0.695, Re_{mac} = 14M). 128
Figure 144 – Configuration 1104-001-RG Drag Rise Component Buildup (C_L = 0.695, Re_{mac} = 14M). 128

Figure 145 – Buffet analysis of wing upper surface at high lift coefficient (Mach=0.80, C_L = 0.91, Re_{mac} = 14M). 129
Figure 146 – Buffet analysis of strut lower surface at low lift coefficient (Mach=0.80, C_L = 0.50, Re_{mac} = 14M). 129
Figure 147 – Configuration 1104-001-RG – Trimmed Vehicle L/D (Mach = 0.80, Re_{mac} = 14M). 130
Figure 148 – Configuration 1104-001-RG – Trimmed Vehicle Drag Polar (Mach = 0.80, Re_{mac} = 14M). 130
Figure 149 – CASES Standard Buildup. 132
Figure 150 – 1104-001-RG – Wing NLF Drag Improvement (C_L = 0.695, Re_{mac} = 14M). 134
Figure 151 – 1104-001-RG – M(L/D) Total. 134
Figure 152 – 1104-001-RG – Low Speed Lift Curve, Free Air at Mach = 0.20, Re_{mac} = Flt Re. 135
Figure 153 – 1104-001-RG – Low Speed Polar, Free Air (Mach = 0.20, Re_{mac} = 9.8M). 136
Figure 154 – 1104-001-RG – Low Speed Lift / Drag, Free Air (Mach = 0.20, Re_{mac} = 9.8M). 136
Figure 155 – 1104-001 Preliminary Vehicle Balance Diagram. 139
Figure 156 – 1104-001-RG Scissors Plot. 141
Figure 157 – Candidate Wing Control Surface Layouts. 143
Figure 158 – Control Surface Layout Similarity. 144
Figure 159 – Airplane Sizing Using CASES / ModelCenter. 148
Figure 160 – Payload-Range Requirements. 149
Figure 161 – 2035 Mission Profile with NextGen Air Traffic Management. 150
Figure 162 – 765-095-RJ and 1104-001-RG Sized Payload-Range Curves. 153
Figure 163 – Block Fuel Reduction Compared to NASA Goal. 154
Figure 164 – Fuel Consumption per Segment. 154
Figure 165 – Block Fuel vs. Range between SUGAR FREE (2005 Best-in-Class), 765-095-RJ Sized, and 1104-001 Sized. 155

Special Data Rights Assertion

Boeing and NASA have agreed to restrict certain intellectual property created during this design effort as Boeing Special Data Rights (SDR). In particular, data shedding light on airfoil, wing, or high lift system design methods and geometry as well as pressure data plotted with scales are considered sensitive. As a result, a number of the figures generated during the aerodynamic design process described in this report are considered as part of the Special Data Rights. The figures identified under that classification are included in a separate special data rights appendix; Boeing has agreed to share those figures with NASA under the Special Data Rights classification and they are not intended for distribution to the broader public. Figures in the SDR appendix will

be labelled with a separate numbering scheme from those in the main body of the report. In the instance that there is both an unlimited rights version of a figure in the main report and a corresponding special data rights version of the same figure in the appendix then that will be noted in the accompanying text in this report.

Nomenclature

AC	Aerodynamic Center
b	Wingspan
BET	Boeing Equivalent Thrust
BMAP	Boeing Mission Analysis Program
c	Local chord
C_D	Vehicle Drag Coefficient
C_L	Vehicle Lift Coefficient
C_l	Sectional Lift Coefficient
C_M	Vehicle Pitching Moment
c_{ref}	Wing reference chord
CASES	Computer Aided Sizing and Evaluation System
CFD	Computational Fluid Dynamics
DF	Ducted Fan
DTE	Divergent Trailing Edge
EC	Economy Class
eTAPS	Efficient Twin-Annular Premixing Swirler
FC	First Class
FEA	Finite Element Analysis
FHF	Flap Hinge Fairing
Fn	Engine Reference Thrust
gFan+	A General Electric Gas Turbine Defined in Phase II
HLFC	Hybrid Laminar Flow Control
HPT	High Pressure Turbine
ICAC	Initial Climb Altitude Capability
ICAO	International Civil Aviation Organization
ISA	International Standard Atmosphere
LE	Leading Edge
LEMAC	Leading Edge of the Mean Aerodynamic Chord
LH	Horizontal tail arm
LOPA	Layout of Passenger Accommodations
LP	Low Pressure
LPT	Lower Pressure Turbine
LRC	Long Range Cruise
LV	Vertical tail arm
MAC	Mean Aerodynamic Chord
MDO	Multidisciplinary Optimization
MEW	Manufacturers Empty Weight

MLG	Main Landing Gear
MLW	Maximum Landing Weight
MRC	Maximum Range Cruise
MTOGW	Maximum Takeoff Gross Weight
MTOW	Maximum Takeoff Weight
MZFW	Maximum Zero Fuel Weight
N&P	Nacelle and Pylon
NASA	National Aeronautics and Space Administration
NLF	Natural Laminar Flow
NLG	Nose Landing Gear
OD	Outside Diameter
OEI	One Engine Inoperative
OEW	Operating Empty Weight
OML	Outer Mold Line
OWE	Operating Weight Empty
PAX	Passengers
PR	Pressure Ratio
Re	Reynolds Number [per unit length]
Re_{mac}	Reynolds Number based on MAC
ROC	Rate of Climb
SFC	Specific Fuel Consumption
SOB	Side-of-Body
STA	Fuselage Station
SUGAR	Subsonic Ultra-Green Aircraft Research
TDT	Transonic Dynamics Tunnel
TE	Trailing Edge
TOFL	Takeoff Field Length
TOGW	Takeoff Gross Weight
TTBW	Transonic Truss-Braced Wing
UDF	Unducted Fan
WB	Wing-Body
WBS	Wing-Body-Strut
WBSN	Wing-Body-Strut-Nacelle (incl. pylon)
WBSNF	Wing-Body-Strut-Nacelle (incl. pylon)-Flap Hinge Fairing
WBSNFJ	Wing-Body-Strut-Nacelle (incl. pylon)-Flap Hinge Fairing-Jury Strut
WBSNFJHV	Wing-Body-Strut-Nacelle (incl. pylon)-Flap Hinge Fairing-Jury Strut-Horizontal and Vertical Stabilizers
Y	Span station (inches)
α	angle of attack [deg]
η (eta)	Percent wing semi-span [Y/(b/2)]

1.0 Introduction

In 2009-2010, Boeing conducted the Subsonic Ultra-Green Aircraft Research (SUGAR) study for NASA. In this study, Boeing identified and analyzed advanced concepts and technologies for aircraft that would fly in the 2030-2035 timeframe. Large possible improvements in fuel consumption, emissions, and noise were identified and roadmaps developed for key technologies. Recommendations for future work were made in the Boeing Phase I Final Report (1), including a more detailed consideration of hybrid-electric gas turbine propulsion and a comprehensive, multidisciplinary study of the high aspect-ratio transonic truss-braced wing (TTBW) configuration. These research objectives were pursued during subsequent, focused Phase II efforts addressing TTBW design space exploration (2), hybrid-electric propulsion evaluation (3), and aeroelastic analysis and test (4).

After multidisciplinary optimization using a design environment developed by Phase II partner Virginia Tech, a TTBW configuration was selected promising significant reductions in fuel consumption relative to the present industry standard identified in the Phase I report. The selected design had a maximum range cruise Mach number of 0.70 as it was optimized for fuel reduction without regard to the economic benefits of productivity. It was also determined that airport compatibility could be achieved even for very high-span designs through the use of a folding wing. Detailed aeroelastic analysis and test in the NASA Transonic Dynamics Tunnel (TDT) determined that aeroelastic impacts to TTBW designs are both manageable and analytically predictable, and that the wing weight necessary to prevent flutter does not significantly erode the aerodynamic benefit of increased span.

The conclusion of the Phase II activities spawned several new research areas that would further mature the TTBW. These included a detailed, high-fidelity aerodynamic design effort to determine achievable levels of interference between the primary components and to reduce uncertainty in configuration performance estimates. In addition, preliminary analysis was proposed to extend research up to Mach 0.80. These tasks were the formulation of a Phase III effort.

In Phase III, high speed lines were developed for Mach 0.745. High fidelity analysis, results validation via a wind tunnel test at the NASA Ames Research Center Unitary Plan Wind Tunnel (UPWT) 11-Foot Transonic Wind Tunnel (11-ft TWT) aided in reducing the uncertainty of predicted aircraft performance. The interference drag of the wing-strut join was determined to be three counts (approximately 1% of total drag at cruise). The performance of the Mach 0.745 vehicle exceeded preliminary estimates by two counts while demonstrating an operable concept across a range of lift coefficients and Mach numbers. In addition to a baseline strut, an alternate strut concept was investigated. The alternate strut included an offset pylon to mitigate

aerodynamic interference in the channel flow formed between the wing and strut. This alternate strut appears to have improved buffet margin as compared to the baseline strut concept. However, uncertainty in buffet prediction methods, and the low maturity of a structural attachment concept have thus far prevented the adoption of this concept.

While the Mach 0.745 design was being finalized, a Mach 0.80 preliminary design was developed using conceptual methods. The Mach 0.80 configuration did show slightly higher block fuel per seat than the slower aircraft as was expected. The execution of the Phase III activities culminated with the following recommendations for future work:

1) Conduct high-fidelity aerodynamic design for a Mach 0.80 transonic truss-braced wing to enable increased fleet productivity.
2) Undertake a dedicated buffet analysis and test effort to increase understanding and collect data for transonic buffet in truss-braced wing configurations.
3) Investigate stiffness requirements for the strut-wing connection.
4) Conduct initial planning for a possible transonic truss-braced wing demonstrator aircraft.

A Phase IV effort was initiated in July 2017 that focused on the development of a Mach 0.80 TTBW design (item one above). This study included the maturation of a Mach 0.80 high-speed outer mold line, as well as vehicle structural concept development. In addition, the study also included updates to the aerodynamic performance predictions of the TTBW concept and a preliminary assessment of high-lift performance. This material is presented in this technical volume.

In addition to the tasks described above, Phase IV funding was increased beyond the initial baseline task to include two transonic wind tunnel tests at the NASA Ames 11-ft TWT. The first of these tests was designed to provide risk reduction for the M=0.80 testing by addressing model roughness-related challenges experienced during the first M=0.745 transonic wind tunnel test. The second test was used for aerodynamic validation of the Mach 0.80 OML (completed in August 2019). Phase IV funding was also increased to perform a detailed high-lift system design task, and conduct a high-lift performance validation test in the NASA LaRC 14- by 22-Foot Subsonic Tunnel (completed in November 2019). Documentation of the funded tasks in the project's final reporting will be delineated as follows:

- Volume I: High-Speed Design Report
- Volume II: High-Speed Test Report
- Volume III: High-Lift System Design Report
- Volume IV: High-Lift System Test Report

The material presented in this report summarizes the high-speed design the Mach 0.80 TTBW configuration. This includes detailed aerodynamic development of a M=0.80 TTBW loft, configuration design, structural design (including aeroelastic assessment), and aerodynamic performance quantification. The results of this design work was used for the definition of a transonic wind tunnel model which was tested in the NASA Ames 11-ft TWT located at Moffett Field, CA. The results of that wind tunnel test will be documented in Volume II of the Phase IV final report series. In addition, the loft developed in this task served as the basis for the definition of a TTBW high-lift system, as documented in Volume III of the Phase IV final report series.

2.0 Transonic Truss-Braced Wing Configuration Design

A preliminary layout (Model 1104-001-NEW) was developed under Phase III (5). This configuration was further refined in the phase IV effort. This section will detail the finalized 1104-001-RG configuration.

2.1 SUGAR TTBW Configuration Evolution

The evolution of the Mach 0.80 TTBW (Figure 1) began with a preliminary layout developed in the Phase III effort that pivoted from the Mach 0.745 vehicle knowledge. Only sweep and thickness changes were made to the planform and all other variables were held constant for consistency. The figure and following paragraphs summarize the work performed and the configuration evolution executed in this effort.

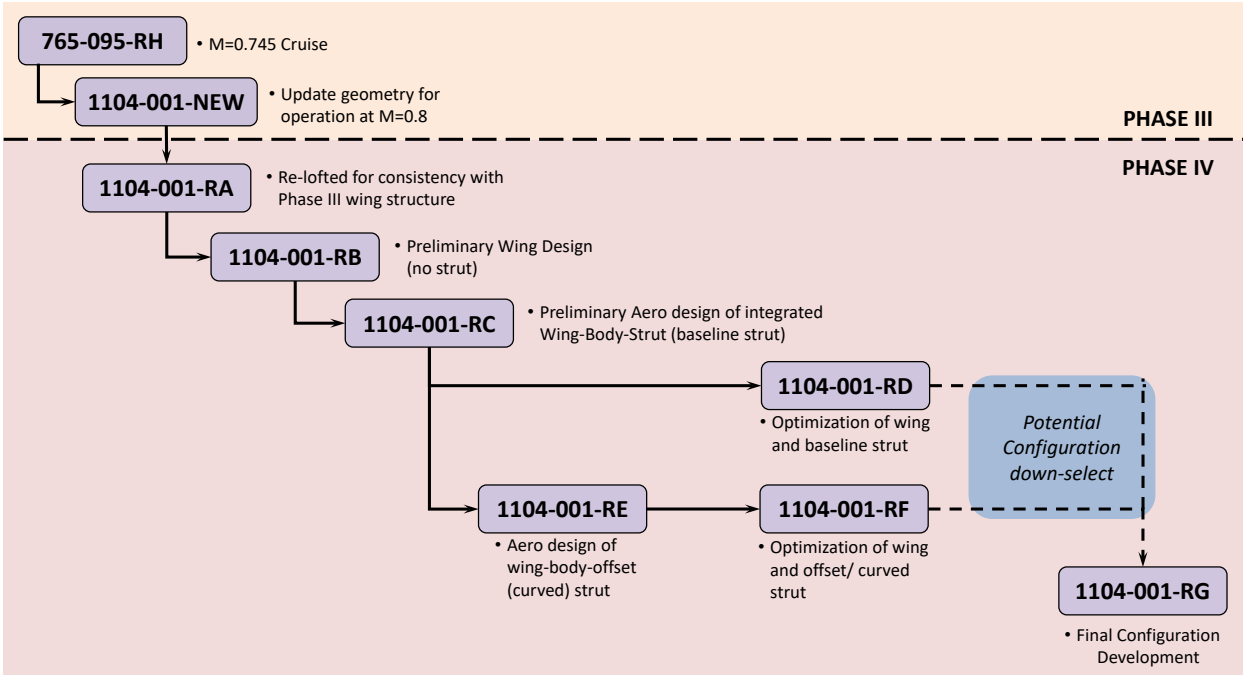


Figure 1 - Phase IV Configuration Evolution.

The initial release of the 1104-001 configuration was based primarily on the 765-095-RH. The wing sweep was increased and it utilized reduced thickness-to-chord airfoils. The wing was lofted with new airfoils optimized for the Mach 0.80 cruise condition. The main and jury struts were initially lofted with chordwise scaled Mach 0.745 (Revision H) airfoils and then optimized for the Mach 0.80 condition.

Other than higher design speeds, all other requirements are identical for the two configurations. To provide reasonable commonality between designs, the wing planform remains unchanged other than sweep. Additionally, because two passenger aircraft with the same payload layout will tend to load the same (ignoring fuel load vectors), the aerodynamic center (AC) of the wing and the location of the landing gear are maintained at common fuselage stations relative to the Mach

0.745 configuration. No additional sweep was required for the horizontal and vertical, so the empennage is also common.

Revision A was developed bringing the aircraft to consistency with the 765-095-RJ OML and structural layouts. This was a minor change relative to the initial release. Following the Revision A update, the wing was designed in isolation (configuration 1104-001-RB), which provided a solid starting point with which to design the wing and strut in parallel. The development of the wing and strut design continued with manual revisions to the aircraft geometry to prepare the configuration for optimization. The final geometry from Revision C was used as the preliminary seed geometry for aerodynamic and aerostructural optimization, which constituted the majority of Revision D design investigations.

In addition, after the release of the Revision C geometry, a parallel design task was kicked off to investigate various high-lift system architectures. This study was the basis for a more detailed study of the TTBW's high-lift system development, which will begin in earnest following the completion of the final high-speed OML.

Following the completion of the Revision C seed geometry, the high-speed lines development also examined an offset/curved strut concept, referred to as configuration 1104-001-RE. Investigations focused on both aerodynamic and structural design concepts. At the onset of the program planning, a design optimization task was laid out for the offset strut concept. This configuration (referred to as Revision F) was not initiated.

2.2 SUGAR Mach 0.80 Configuration Description

The final release of the Mach 0.80 aircraft geometry is referred to as configuration 1104-001-RG. This geometry represents a single member of a 737-class airplane family. It is a tube and wing configuration with a high mounted truss-braced wing, twin wing mounted engines, a T-tail empennage, and pylon mounted main landing gear. The 154 passenger dual class fuselage is a 6-abreast seating arrangement, and the lower lobe is bulk loaded.

2.2.1 Integration

The Mach 0.80 configuration walk-around, general arrangement drawing, and principal characteristics are shown in Figure 2, Figure 3, and Table 1, respectively. Table 2 shows the component axis system origins relative to the body axis.

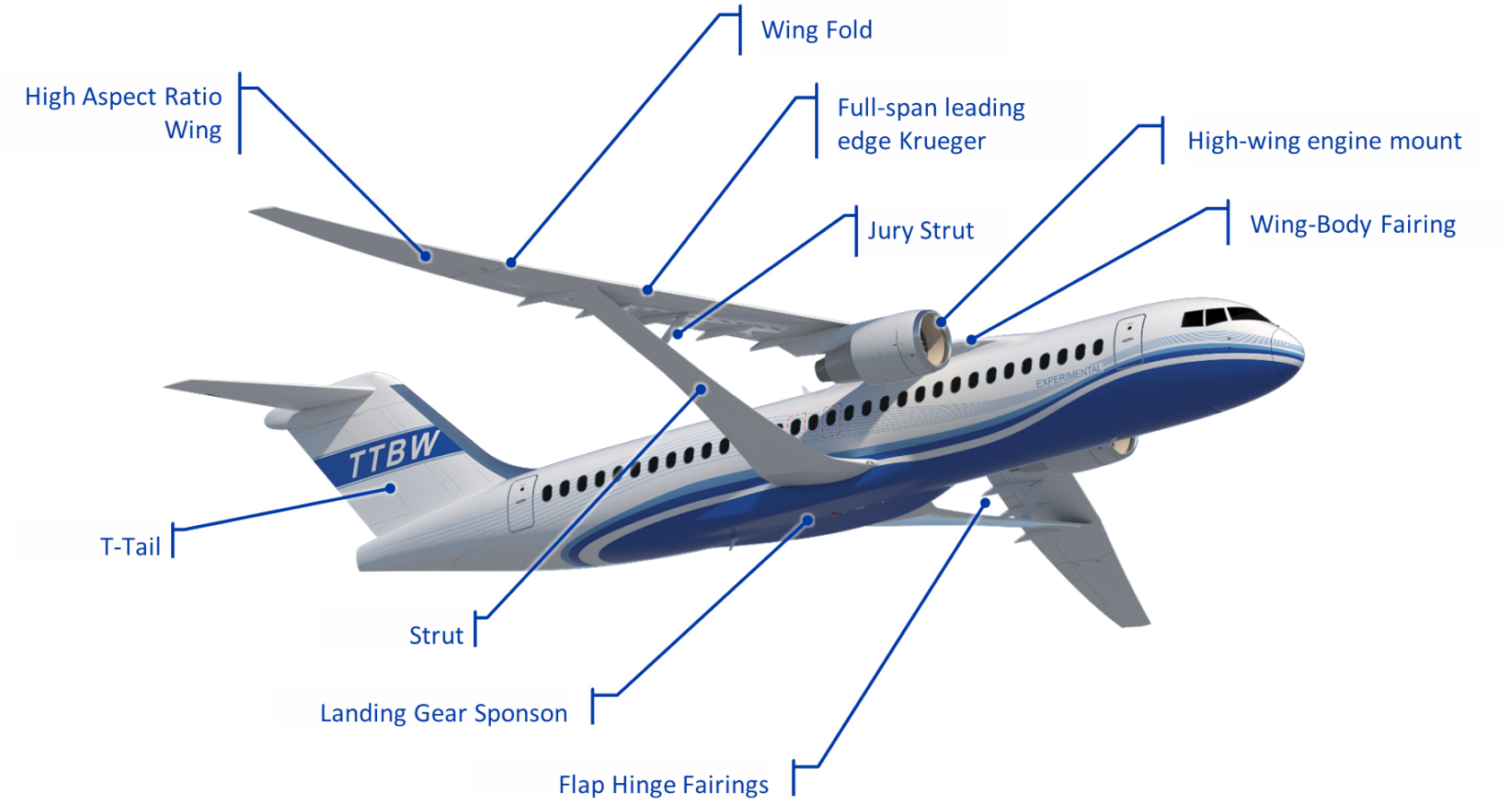


Figure 2 – SUGAR TTBW Mach 0.80 Configuration (1104-001-RG).

Projected Characteristics			
	WING TOTAL	V-TAIL TRAP	H-TAIL TRAP
AREA (SQ FT)	1477.109	292.990	276.942
ASPECT RATIO	19.565	0.825	4.928
SPAN (IN)	2040.000	186.562	443.322
TAPER RATIO	0.346	0.801	0.352
MAC (IN)	110.246	227.070	96.833
DIHEDRAL (DEG)	-1.500	--	-3.000
1/4 CHORD SWEEP (DEG)	22.470	43.500	31.600
ROOT CHORD (IN)	130.214	251.158	133.037
TIP CHORD (IN)	45.100	201.137	46.876
TAIL VOLUME COEFFICIENT	--	0.069	1.502
YMAC / ZMAC / YMAC (IN)	444.763	355.052	93.138
-- / LV / LH (IN)	--	668.937	843.661

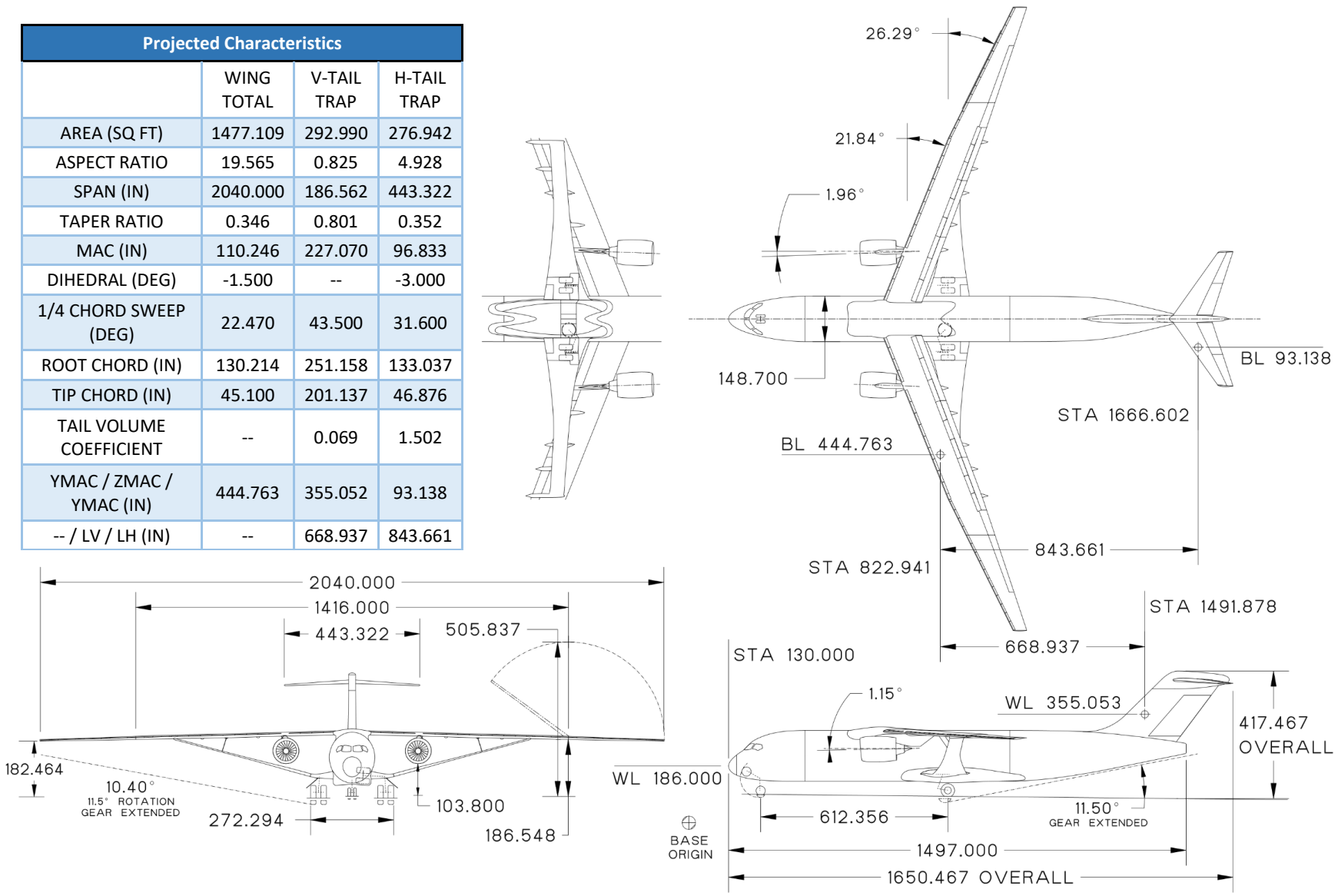


Figure 3 – SUGAR TTBW Mach 0.80 (1104-001-RG) General Arrangement (3-view).

Table 1 - Mach 0.80 Configuration (1104-001-RG) Principal Characteristics.

Model 1104-001 RG (As Drawn)	
Maximum Takeoff Weight (MTOW)	145,000 lbm
Maximum Landing Weight (MLW)	139,000 lbm
Maximum Zero Fuel Weight (MZFW)	131,000 lbm
Operating Empty Weight (OEW)	85,000 lbm
Manufacturer's Empty Weight (MEW)	78,000
Engine Type	gFan+
Boeing Equivalent Thrust	23,000 lbf
Fan Diameter	71 in
Overall Dimensions	
Length	137.5 ft
Height	34.4 ft
Fuselage Length	124.8 ft
Fuselage Cross Section (Height x Width)	166.5 x 148.7 in
Passenger Cabin Length	1127 in
Wing	
Reference Area	1477.109 ft^2
Span	170.000 ft
Projected Sweep	22.47 deg
Passenger, Baggage, Fuel Capacities	
Passenger Count (Dual Class)	154
Class Distribution (FC / EC)	12 / 142
Cargo Capacity	Bulk
Fuel Capacity	4,595 USG
Landing Gear	
Wheel Base	637.20 in
Main Track	272.29 in
Main Tire Size	45x17R21
Nose Tire Size	30x10.5R15

Table 2 – Mach 0.80 Configuration (1104-001-RG) Body Axis Component Origins (units are inches).

Component	X	Y	Z
Fuselage	0.00	0.00	0.00
Wing	611.53	0.00	299.12
Vertical Fin	1,356.02	0.00	281.49
Horizontal Stabilizer	1,575.97	0.00	468.05
Main Strut	842.20	67.13	144.10
Jury Strut	857.13	424.52	241.26
NLG*	235.00	0.00	92.34
MLG*	872.20	110.00	87.00

* To Centroid of the Bogie Contact Patch

2.2.2 Wing

The wing is high aspect ratio, truss-braced, and designed for a 0.8 cruise Mach number. The wing is derived from the Mach 0.745 wing by adding 10 degrees sweep (refer to Figure 4) and reduced thickness-to-chord ratio. The chord distribution is identical to the Mach 0.745 wing. Like the Mach 0.745 wing, turbulent supercritical airfoils are used while natural laminar flow is bookkept in the conceptual aerodynamic buildup. The wing layout incorporates a fold at 118 feet of span to accommodate existing Code C gate and taxiway infrastructure.

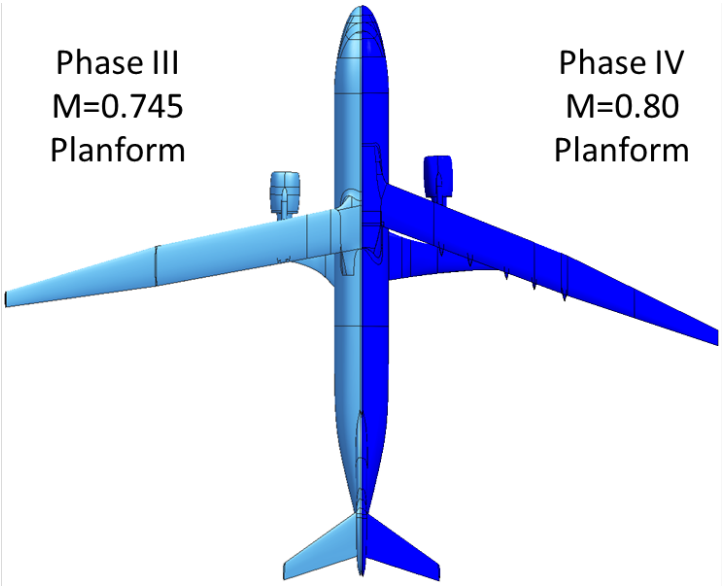


Figure 4 – Planform Change from Phase III to Phase IV.

The leading edge is populated with full span Krueger flaps broken by the engine pylon. The front spar accommodates a leading edge device chord ratio ranging from ten percent at the root to fifteen percent at the tip. The trailing edge of the wing is fitted with single slotted flaps extending from the side of body, past the outboard planform break, to the inboard side of an all-speed aileron. The all-speed aileron extends outboard to the wing fold. Outboard of the wing fold there is a low speed aileron, which is locked out at high speed. Spoilers are assumed to cover the entire flapped span. The control surface and high lift system layout is the result of trade-offs between low speed aerodynamics and stability and control. The Mach 0.80 planform is illustrated in Figure 5, and the projected reference quantities are shown in Table 3. It should be noted that the reference quantities are displayed for a planform with no leading or trailing edge breaks at the side-of-body.

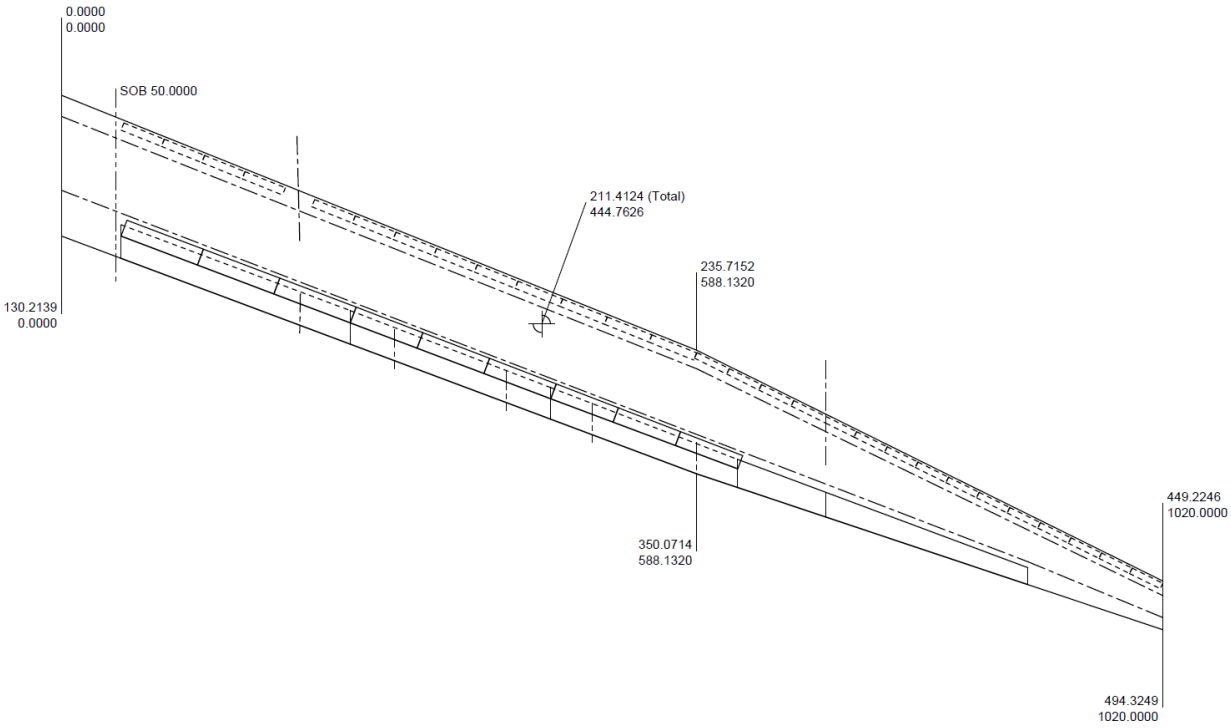


Figure 5 – SUGAR Mach 0.80 (1104-001-RG) Wing Planform (Projected view, units are inches).

Table 3 – Wing Reference Geometry.

Parameter	Units	Total (Projected)	Parameter	Units	Total (Projected)
Area	ft^2	1477.109	MAC	in	110.246
Aspect Ratio		19.565	Y_{MAC}	in	444.763
Span	in	2040.000	$X_{LE\ MAC}$	in	795.380
Taper Ratio		0.346	$X_{C/4\ MAC}$	in	822.941
Root Chord	in	130.214			
Tip Chord	in	45.100			Total (Reference)
SOB Chord	in	1289.289	Krueger Area	ft^2	88.640
Sweep LE	deg	23.32	High Speed Aileron (Flaperon) Area	ft^2	27.738
Sweep 25%	deg	22.47	Single Slot Flap Area	ft^2	237.348
Sweep TE	deg	19.85	Low Speed Aileron Area	ft^2	50.033
Dihedral	deg	-1.50	Spoiler Area	ft^2	126.787

2.2.3 Main Strut and Jury Strut

The strut integration concept is shown in Figure 6. The landing gear is integrated into a landing gear pylon that protrudes rigidly from the fuselage. With the landing gear retracted, a sponson fairs over the landing gear. A strut is attached to the outboard end of the gear pylon and is affixed by pin joints. The outboard end of the strut element is attached primarily to the wing front spar also through a pinned attachment. The main strut element is stabilized under buckling load via a jury strut.

The MLG location is the same as the Revision J Mach 0.745 configuration, but the strut attachment at the wing is swept further aft. The resultant strut sweep is 2.88 degrees (aft), and the dihedral is 14.43 degrees. The main strut spar locations are defined in Table 4 and the corner points are shown in Figure 7.

The jury strut location relative to wing span has been updated from the previous phases of study (Section 4.1.3.4). The dihedral of the jury strut was updated to -72.6 degrees (outboard cant relative to wing). The attachments at the wing and main strut are pinned joints (axis aligned streamwise). The jury strut spar locations are defined in Table 5 and the corner points are shown in Figure 8. The jury strut attachments are also pinned connections with the pin axis aligned spanwise.

The jury strut has a linear chord distribution between defining airfoils. The defining airfoils for the jury strut are at Y locations, which correspond to the spar stations in Table 5. These locations are defined in the jury strut reference plane (see Figure 8). The defining airfoils for the main strut are at specified Y locations in the main strut reference plane (see Figure 7). Specified planform breaks in the main strut are defined in Table 4.

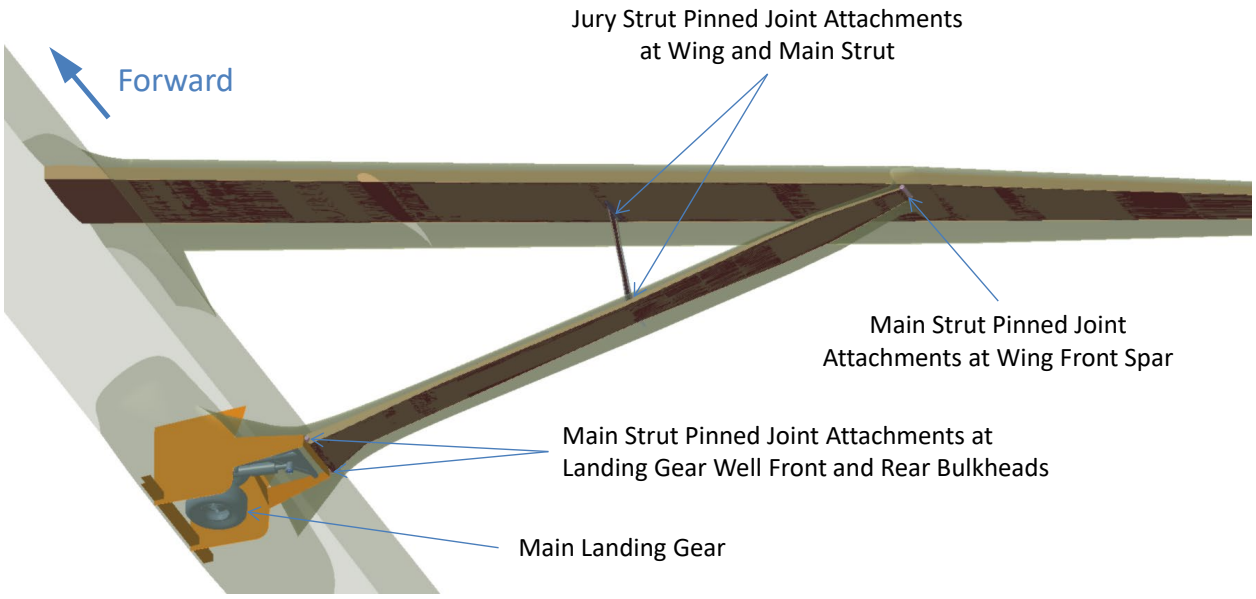


Figure 6 – SUGAR Mach 0.80 Main Strut Structural Concept.

Table 4 – Main strut spar centerline locations (Strut Reference Plane).

Y (in.)	Front Spar x/c	Aft Spar x/c
47.184	0.150	0.700
72.708	0.150	0.700
152.098	0.150	0.700
363.826	0.150	0.700
518.164	0.150	0.700

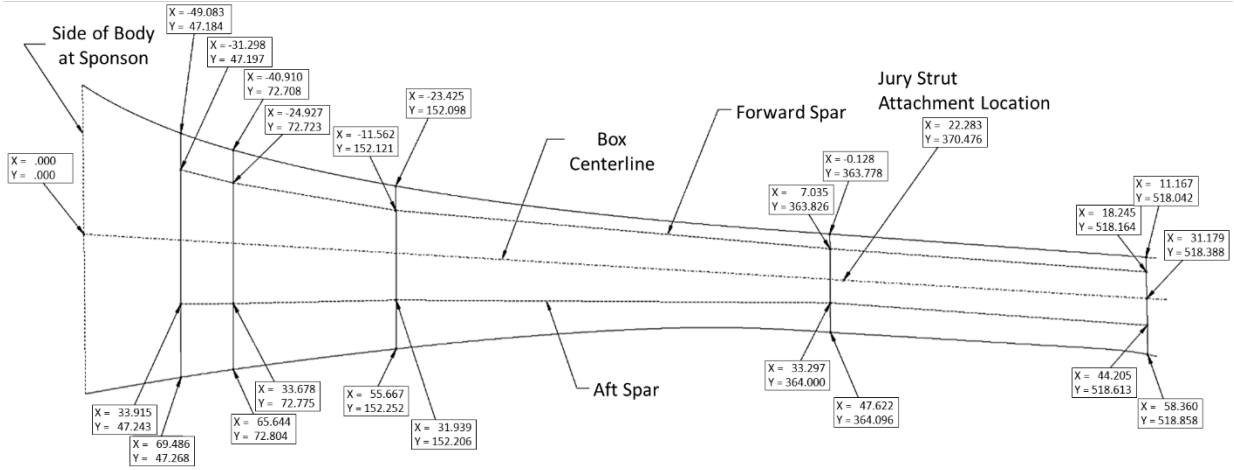


Figure 7 – SUGAR Mach 0.80 (1104-001-RG) Strut Reference Plane Corner Points.

Table 5 – Jury strut spar locations (Jury Strut Reference Plane).

Y (in.)	Front Spar x/c	Aft Spar x/c
0.000	0.100	0.800
45.450	0.100	0.800

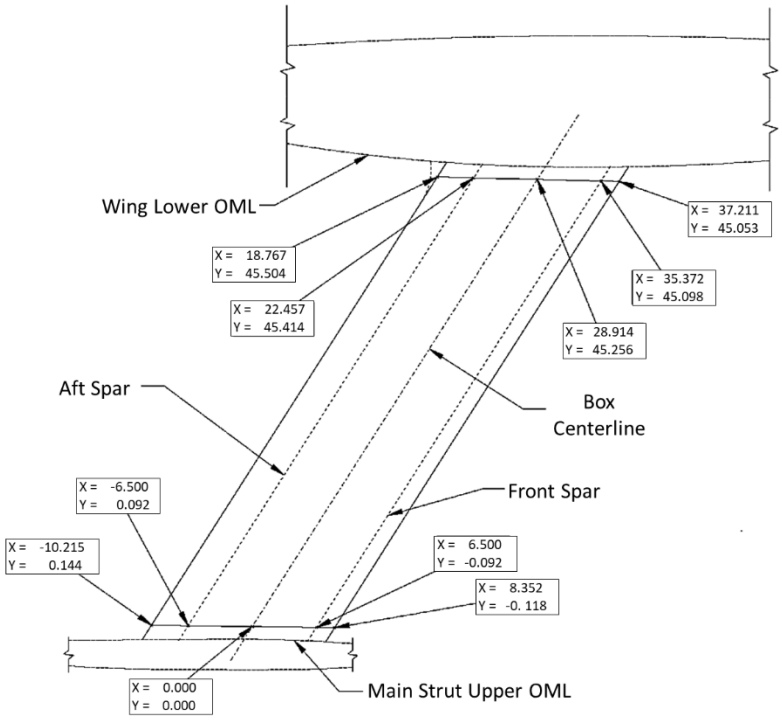


Figure 8 – SUGAR Mach 0.80 (1104-001-RG) Jury Strut corner point drawing (jury strut reference plane).

2.2.4 Vertical Fin

The vertical tail planform is identical to that of the Mach 0.745 Revision J aircraft. It is a 134.67% scale version of a DC-9 twin-jet tail and is sized to provide a tail volume coefficient of 0.066. It is a two spar layout with a two surface simple hinged rudder. The front spar breaks and converges on the rear spar at the vertical tip where the horizontal stabilizer pivot is mounted. The horizontal jack screw mechanism is above the front spar. The vertical planform is illustrated in Figure 9, and the reference planform parameters are shown in Table 6.

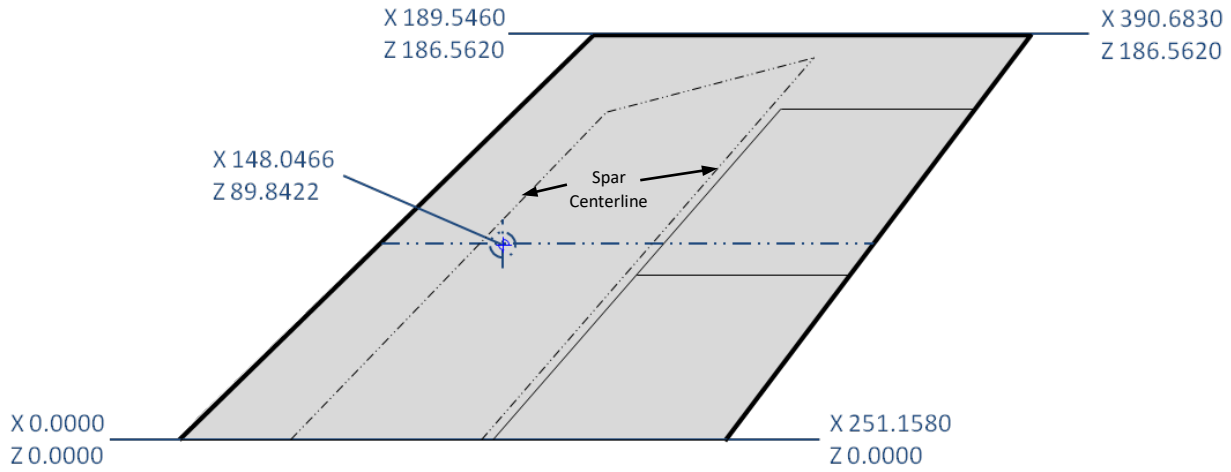


Figure 9 – 1104-001-RG Vertical Tail Planform (units are inches).

Table 6 – 1104-001-RG Vertical Tail Planform Parameters.

Parameter	Units	Total (Projected)
Area	ft^2	292.990
Aspect Ratio		0.825
Span	in	186.562
Taper Ratio		0.801
Root Chord	in	251.158
Tip Chord	in	201.137
Sweep 25%	deg	43.50
MAC	in	227.070
Z_{MAC}	in	89.842
$X_{C/4\ MAC}$	in	148.047

2.2.5 Horizontal Stabilizer

The horizontal stabilizer planform is identical to that of the Revision J Mach 0.745 aircraft. It is a 100.25% scale version of a DC-9 twin-jet tail and is sized to provide a tail volume coefficient of 1.43. The stabilizer is trimmable with a pivot behind and below the rear spar and a jack screw acting in front of the front spar. The elevator is split into two separate segments spanwise. The horizontal planform is depicted in Figure 10, and the projected planform parameters are shown in Table 7.

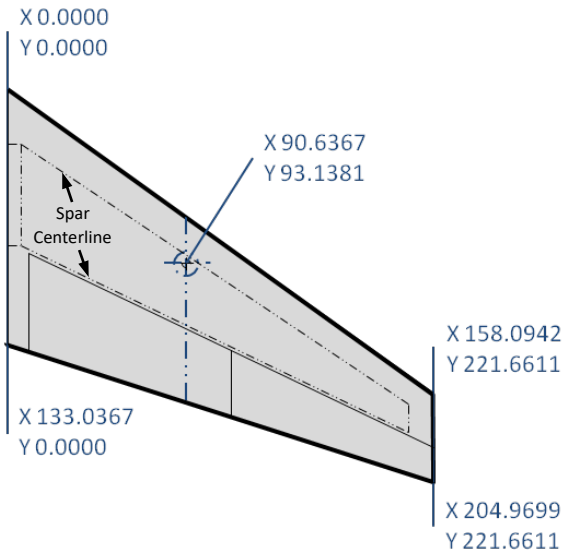


Figure 10 – 1104-001-RG Horizontal Planform (units are inches).

Table 7 – 1104-001-RG Horizontal Planform Parameters.

Parameter	Units	Total (Projected)
Area	ft^2	276.942
Aspect Ratio		4.928
Span	in	443.322
Taper Ratio		0.352
Root Chord	in	133.037
Tip Chord	in	46.876
Sweep 25%	deg	31.60
Dihedral	deg	-3.00
MAC	in	96.833
Y_{MAC}	in	93.138
$X_{C/4\ MAC}$	in	90.637

2.2.6 Fuselage

The SUGAR TTBW fuselage is a single-aisle layout with three-by-three seating. The cargo compartment is bulk loaded and is not designed for containerized cargo. The cross-section is illustrated in Figure 11 and a Layout of Passenger Accommodations (LOPA) is shown in Figure 12. The LOPA and cross-section were defined in Phase I and have not changed.

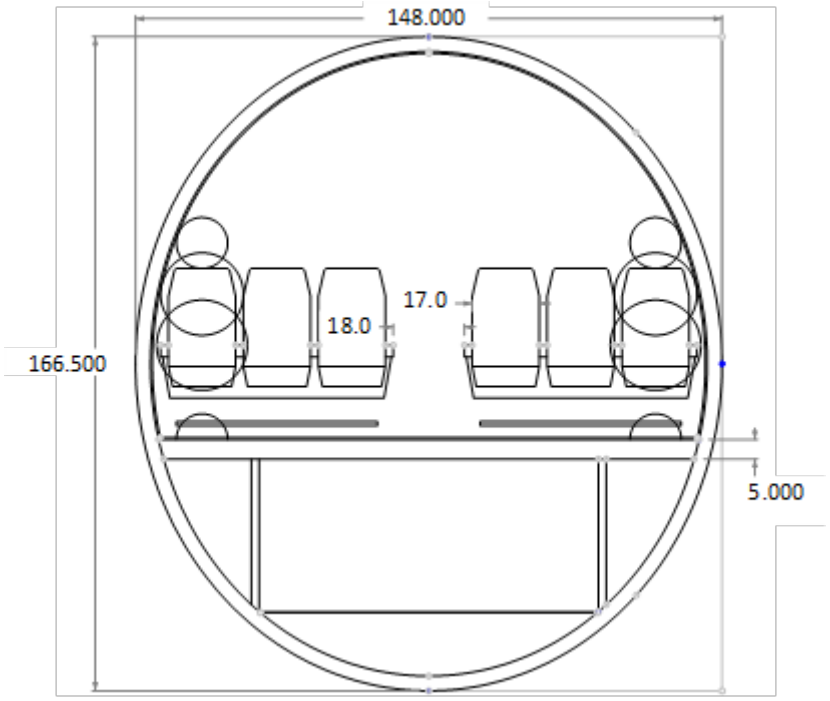
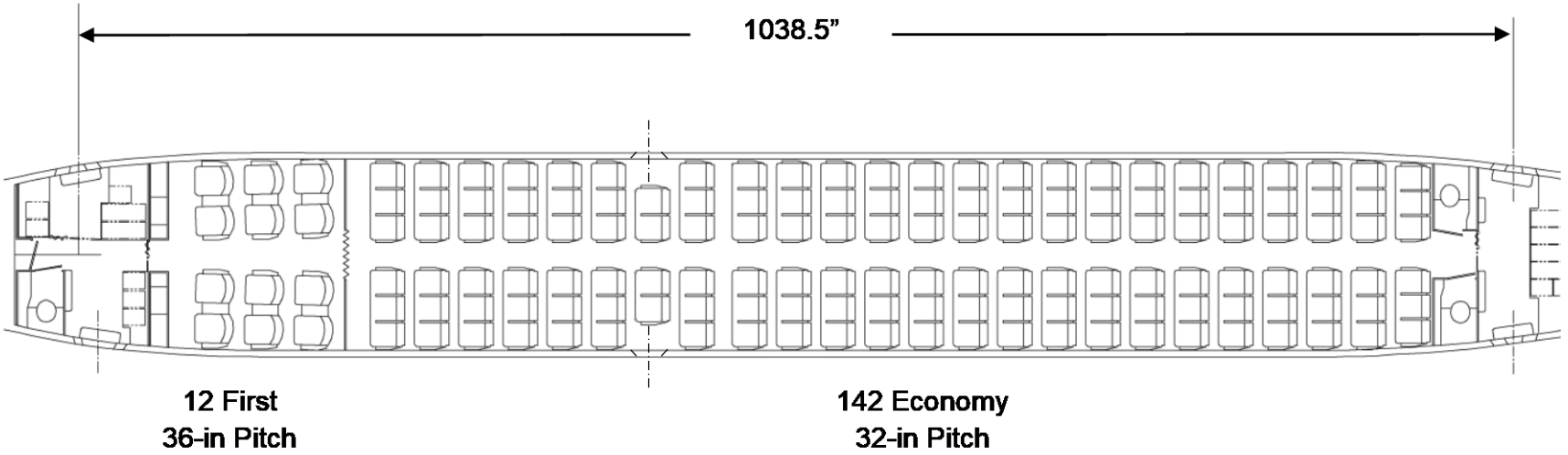


Figure 11 – 1104-001-RG Fuselage Cross Section, common for both Mach 0.745 and Mach 0.80 configurations (units are in inches).

Interior Arrangement

SUGAR

IAC Short / Medium Range – Dual Class



	Class (%)	Carts (qty)	Cart Ratio (Carts/Pax)	Lavatory Ratio (Pax/Lav)	Closet Ratio (Rod-in/Pax)
First	7.79	3.0	0.250	12	4.00
Economy	92.20	7.0	0.049	71	0.00
Total	100.00	10.0	0.065	–	–

Figure 12 – 1104-001-RG Layout of Passenger Accommodations, common for both Mach 0.745 and Mach 0.80 configurations.

2.2.7 Landing Gear

The Mach 0.80 aircraft landing gear design is identical to that of the Mach 0.745 aircraft. The high aspect ratio, high lift-curve slope SUGAR TTBW configuration allows for a low static ground line. The configuration uses a levered landing gear arrangement to enable this low stance. The landing gear attaches to the gear pylon, a stub wing-like structure that carries landing gear and strut loads. The gear pylon OML was updated to a lower profile, lower drag design that more closely encloses the main gear system and primary structure.

The Phase IV landing gear design is unchanged from Phase III. An overview of the kinematic arrangement is illustrated in Figure 13, and the ground footprint is shown in Figure 14 (not to scale).

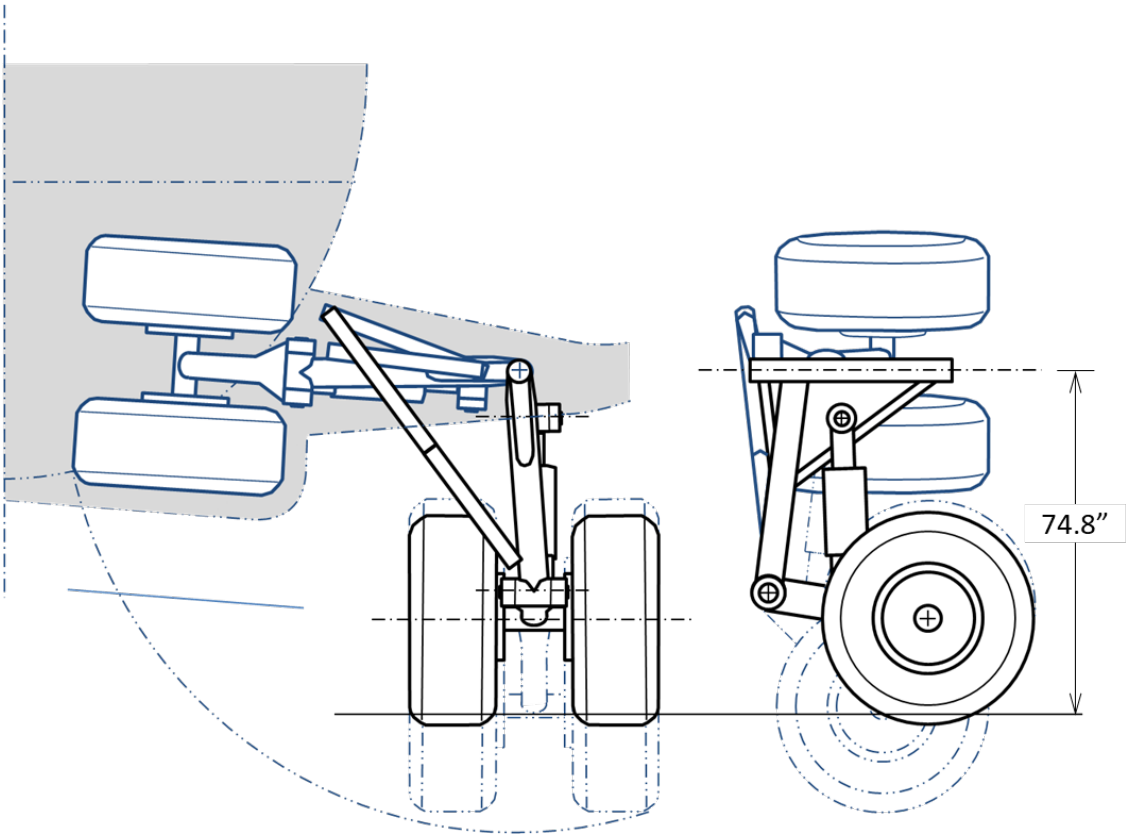
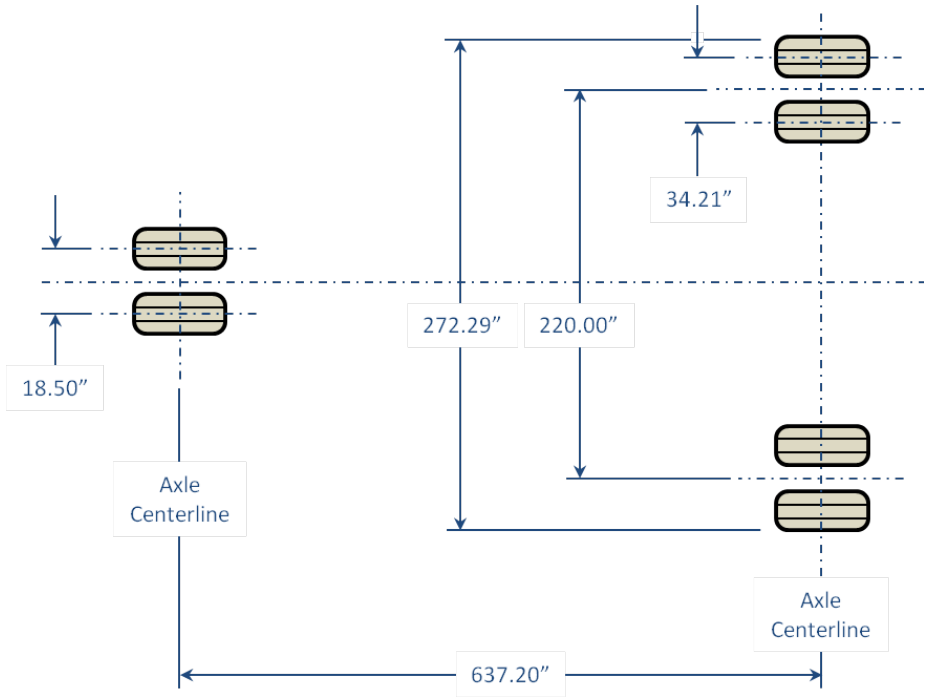


Figure 13 – SUGAR TTBW Landing Gear Layout, common for both Mach 0.745 and Mach 0.80 configurations (765-095 RJ shown).



	Tire Size
Main	45x17R21
Nose	30x10.5R15

Figure 14 – SUGAR TTBW Landing Gear Arrangement.

2.2.8 Propulsion

The SUGAR TTBW propulsion system design was not modified during the Phase IV effort. The Phase II gFan+ engine features a pressure ratio of 1.46, which was selected from a GE parametric study accounting for vehicle-level sensitivities. The selected pressure ratio sacrifices specific fuel consumption (SFC) but achieves a lighter weight, lower drag design relative to a higher bypass ratio engine. A conceptual layout of the Phase II gFan+ is shown in Figure 15, and a summary of the propulsion system key characteristics is provided in Table 8. The maximum range cruise Mach number of the Phase IV 1104-001-RG configuration is higher than the Phase III configuration by approximately 0.055 Mach. An SFC factor was applied to the engine dataset within the performance routine to adjust the design point of the engine accordingly.

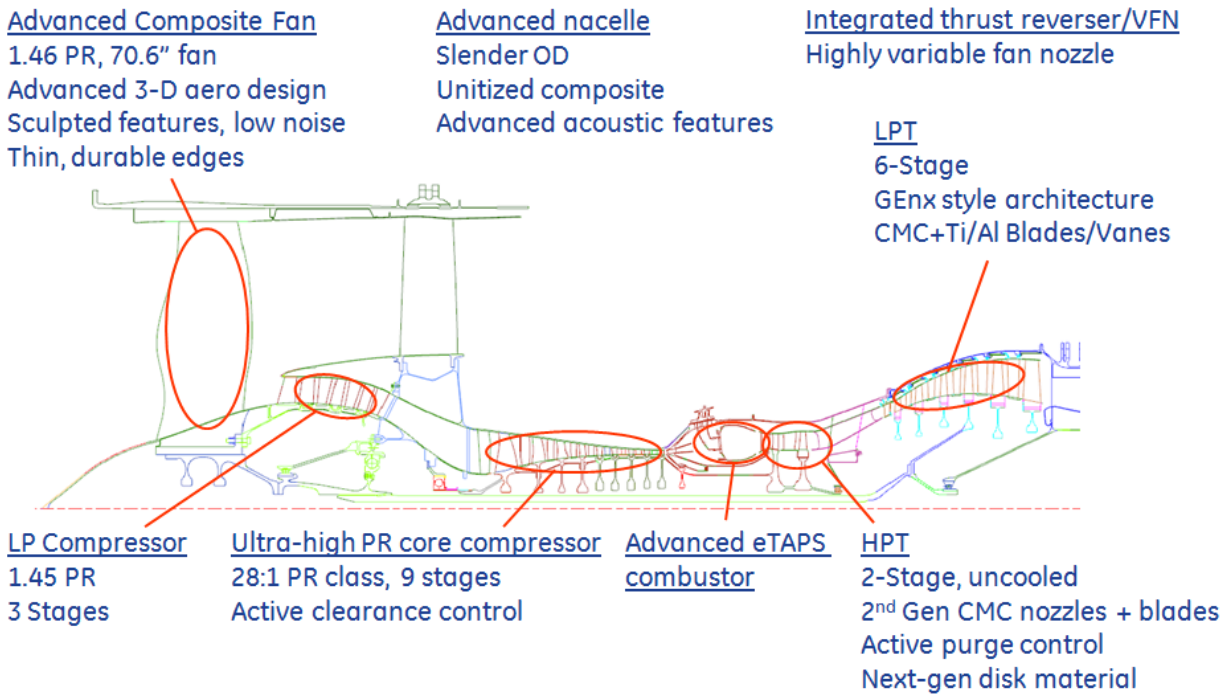


Figure 15 – gFan+ Concept Layout.

Table 8 – gFan+ Key Characteristics.

JP+2035GT+DF	
Fan Diameter	70.6 in
Length	129 in
Propulsion System Weight	6,335 lbm

Performance	Thrust (lbf)	SFC (lbm/lbf/hr)
Sea Level Static	21,943	0.220
Takeoff	16,592	0.295
Top of Climb	3,931	0.467
Cruise	3,145	0.455

3.0 Structural Analysis

Phase IV structural analysis work focused on two areas: 1) the development of design concepts for connections between the main strut and the sponson and wing to meet fail-safe and structural load requirements, and 2) refinement of the aeroelastic finite element model (FEM) for use in assessing joints and other structural features and for estimating structural weight.

3.1 Structural Fittings/Joints

A design concept was developed for a fail-safe swivel joint connection (shown in Figure 16) at the inboard end of the main strut, and for associated backup structure at the sponson. An offset attachment concept was developed for the outboard end of the main strut. The concepts are described in the following sections. The next step to mature the concepts will be to evaluate them in the vehicle FEM, and analyze them in more detail.

3.1.1 Inboard – Strut to Sponson

The Mach 0.80 main strut design methodology is similar to that of the Mach 0.745 configuration. For the Mach 0.745 configuration, the main strut front spar plane was aligned with the main landing gear (MLG) front bulkhead. The strut rear spar kicked aft in the strut-sponson fairing region to align with the MLG rear bulkhead.

For the Mach 0.80 configuration, the strut spars (shown in Figure 6 and Figure 7) remain nearly parallel for the entire length of the strut, except at the inboard end, where the spars are spliced with back-to-back (fail-safe requirement) triangular transition lug fittings and a pair of lug straps that are external to the triangular lug fittings. These lugs attach to a single swivel fitting that allows rotation about three axes, thus allowing the strut to carry axial loads while avoiding strut bending induced from wing twist as the wing lifts during flight, and simplifies the construction of the main strut.

The swivel joint is tied to a single set of continuous inboard/outboard oriented nested backup tension fittings that attach to a shear panel and doubler (fail-safe requirement). The shear panel extends inboard to the side of the fuselage. A fore-aft torque box interfaces with the inboard side of the strut swivel fitting and causes the strut fore-aft load component to react at the swivel joint. The torque box will also be used to house the MLG door hinge fittings.

The bending moment induced as the result of the offset between the vertical pivot of the swivel joint and the end pad of the backup primary tension fitting, the inboard/outboard axis double bolt reacts by extending inboard where it attaches to an integral rib on the outer (primary) tension fitting and to the nested inner tension fitting end pad. The rib/end pad vertical load causes a longitudinal beam that is located between the shear panel and the sponson upper fairing panel to react. The longitudinal beam extends forward to the MLG-well forward bulkhead, and aft to the MLG-well aft bulkhead.

Due to the critical nature of the swivel joint to flight safety, a bird splitter located on the forward side of the swivel joint, will be used to protect the joint integrity during a bird strike event.

To ensure the integrity of the swivel joint to carry the limit load in case of failure of any one of its component parts, illustrated in Figure 16, the following provisions are made:

- The three swivel pivot joints each have one outer bolt and one inner bolt, with each bolt capable of carrying shear and bolt bending limit loads independent of the other.
- The three swivel pivot joint inner and outer bolts have separate nuts that are safety wired together to prevent the nuts from backing off.
- A main swivel lug fitting and swivel clevis fitting are the primary components that transfer the strut axial load from the strut transition fittings and lug straps to the pivot cup vertical double bolts.
- The pivot cup vertical double bolts then transfer the load through the inner and outer pivot cups into the inboard/outboard pivot cup double bolts.
- The inboard/outboard pivot cup double bolts transfer axial and bending loads to the backup nested tension fittings and then into a shear panel that closes out the top of the MLG wheel well and to a longitudinal beam that spans between the MLG-well forward closeout bulkhead and the MLG-well aft closeout bulkhead.
- Due to the magnitude of the horizontal load component that needs to be reacted by the nested tension fittings, the nested tension fittings are continuous, interrupting the longitudinal torque box.

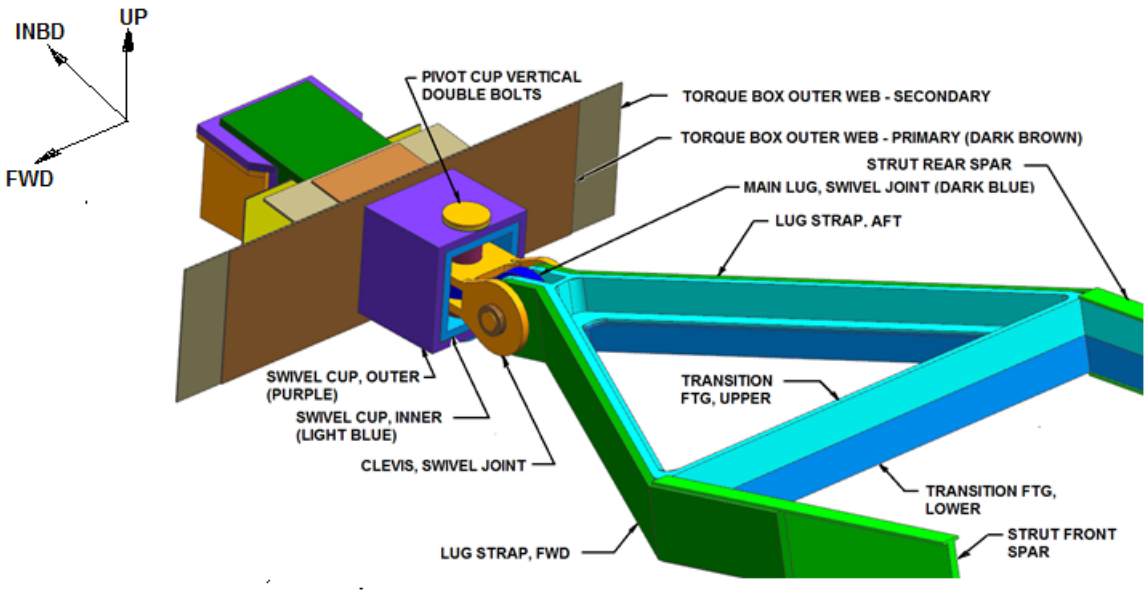


Figure 16 – Main Strut Swivel Joint at Sponson.

3.1.2 Outboard – Strut to Wing

The baseline sponson-strut-wing concept for the Mach 0.80 configuration, developed during SUGAR Phase III is shown in Figure 6. At the wing-strut intersection, the baseline strut axis aligns with the wing front spar at the wing planform break (the strut spars straddle the wing front spar). Also, the outboard end of the main strut incorporates lug fittings attached at the end of the straight strut front and rear spars. The baseline strut centerline intersects the wing lower surface at a shallow angle. The main strut attachments at the sponson and wing are pinned joints (axis aligned streamwise).

Due to the sensitivities of the vehicle performance to wing-strut aerodynamic interference and the higher cruise Mach number of 0.8, a trade study was initiated to further investigate the structural design of a curved beam (offset) strut attachment concept (Figure 17). This concept could potentially alleviate some of the aerodynamic interference resulting from the closer aerodynamic coupling present in the baseline strut attachment concept. The offset structural concept is synergistic with the aerodynamic investigations of an offset strut (configuration 1104-001-RE) as detailed in Section 4.1.2.6. In addition to the aerodynamic benefits of the concept, the offset strut enables a more continuous wing structure as the baseline strut attachment concept requires a local 'scalloping' of the wing to reduce aerodynamic interference between the wing and strut. Since the offset strut concept is likely to have a higher component weight than the baseline strut, a detailed trade analysis will be required in the future to quantify the benefit at a system level.

In the offset strut attachment configuration the strut axis is repositioned so the strut spars align with the wing lower skin positioned between the wing front and rear spars. The strut incorporates curved lug fittings with lugs that interface with clevises attached to the wing lower surface. The interface of the strut with the wing is at a more vertical angle. The wing mounted clevises are fastened with tension bolts through the wing lower skin into wing internal backup structure. The resultant pinned joint with the axis aligned streamwise will require a very minimal fairing to cover the joint.

The curved beam configuration allows the fitting section to be minimal just below the lug, increasing in frontal width until the transition point (where the strut bending moment is highest). The strut section height of the spanwise section gradually tapers down to the attach pin joint located just outboard of the intersection of the jury strut with the main strut.

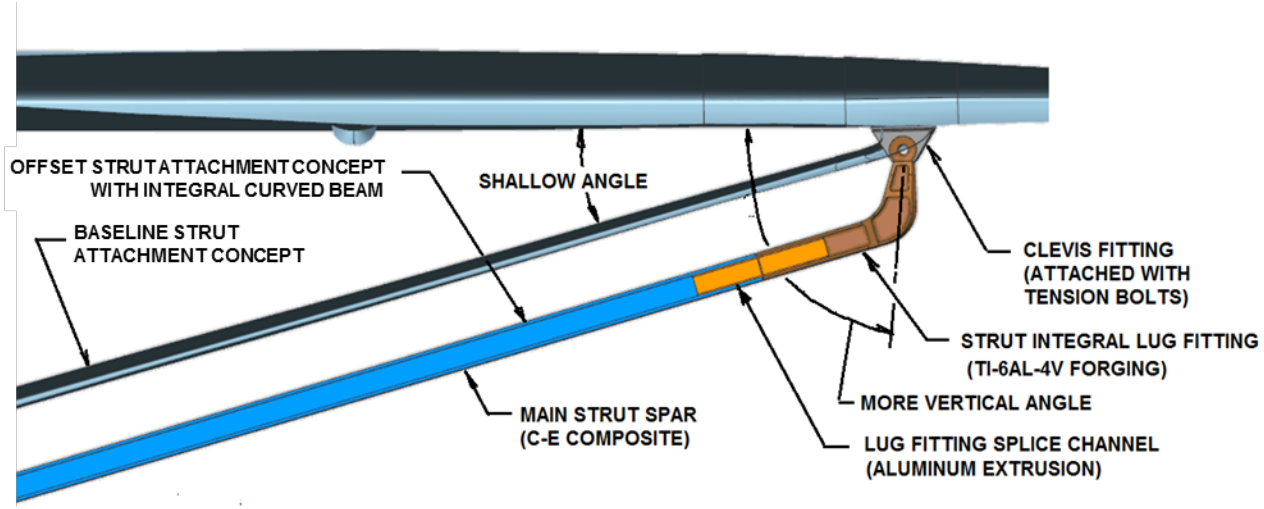


Figure 17 – Main Strut Outboard Attachment Configuration.

3.2 Aeroelastic Analysis

A detailed FEM of the Mach 0.80 Transonic Truss-Braced Wing (TTBW) aircraft was produced. It was prepared for aeroelastic analysis, and sized for typical maneuver load conditions. Gust and flutter analyses were also considered since aeroelastic stability drove final sizing in previous phases of design.

3.2.1 Background

The structural design task for the Phase IV Mach 0.80 TTBW includes a refinement of the aeroelastic FEM, previously constructed using Boeing internal funds, for use in determining joint structural sizing and weight estimates. A brief description of the work completed using the previous FEM is provided in the following paragraphs.

Preliminary design of the Mach 0.80 TTBW aircraft was performed during Phase III of the SUGAR program. Leveraging this design, FEM-based aeroelastic and structural analyses were completed between July 2014 and January 2016 under Boeing internal funding. The results showed a moderate weight increase compared to the Mach 0.745 TTBW results from SUGAR Phase II, driven by a reduction in wing thickness associated with the higher cruise Mach number. The results represented early conceptual design estimates subject to change during subsequent detailed, coupled aerostructural design of the Mach 0.80 aircraft. The Mach 0.80 TTBW flutter speed was found to exceed minimum requirements, with no weight increase for flutter.

Under Phase IV, enhancements to the structural FEM focused on upgrades to the prior 2016 model. However, it was determined that the model lacked the integrity required to perform the analyses to Boeing standards. Therefore, Boeing took on the task of developing a new FEM for use in subsequent studies.

To complete the aeroelastic model for the enhanced FEM, updates were made to the Doublet Lattice Model (DLM), and mass properties. Initial aeroelastic analyses to check out the model were executed in parallel with the application of mass to the FEM, which was completed in June 2018. The details of the FEM enhancements are discussed next, and results of aeroelastic analysis and sizing optimization performed are presented.

3.2.2 Phase IV FEM Refinement

The improvements to the TTBW FEM included updating the wing and strut geometry to a recent configuration, the use of a detailed strut model, additions to the doublet lattice aerodynamic model and refinement of aerodynamic panels, application of new mass properties, an updated optimization setup, and better model organization to facilitate future studies in which components are modified. While more refined than the previous Mach 0.80 FEM, the new FEM is the next step, rather than the final stage of refinement. As the structural design and configuration mature, the FEM can evolve to be more accurate.

3.2.3 Configuration Geometry and Data

The structural model of the wing, strut, and jury was created using the 1104-001-RC_des05 configuration geometry. This configuration was selected based on the work schedule in 2017. Waiting for the finalized 1104-001-RC geometry would have been too much of a delay. The differences in the two configurations are structurally insignificant. The configuration geometry specified the OML and major features; the internal structure was defined by the analyst based on a typical rib spacing, and percent-chord locations of spars provided by the configuration designer.

The FEM updates ensured that the aerodynamic model matched the 1104-001-RC_des05 geometry of the wing, strut, and jury structure. The fuselage structural and aerodynamic models were not changed from the previous 2016 FEM, and were integrated with the new model of the wing and strut. The mass properties provided in 2018 were for the 1104-001-RC configuration.

3.2.4 Structural Idealization and Optimization Model

All structural elements of the wing, strut, and jury are of composite material except the titanium splitter plate in the strut. The material properties are listed in Table 9. The spar and rib caps, as well as spar stiffeners, are modeled with beam elements (Nastran PBEAM) to enable nonlinear analysis. The composite beam material has a Young's modulus (E) of 10,500,000 lbs/in^2, a shear modulus (G) of 4,038,500 lbs/in^2, a Poisson's ratio (ν) of 0.3, and a density of 0.067 lbs/in^3. The skins, spar and rib webs, and spar intercostals, are laminates of composite material (Nastran PCOMP), with each ply consisting of orthotropic material with a modulus of elasticity in the fiber direction (E1) of 23,500,000 lbs/in^2, a modulus across the fiber direction (E2) of 1,600,000 lbs/in^2, a Poisson's ratio of 0.34, an in-plane shear modulus (G12) of 800,000 lbs/in^2, and a density of 0.067 lbs/in^3.

Table 9 – Composite Material Properties.

1D Beam Laminate Stiffness		
E	10,500,000	lb/in^2
ν	0.30	
G	4,038,500	lb/in^2
ρ	0.067	lbs/in^3

2D Element Lamina Stiffness		
E1	23,500,000	lb/in^2
E2	1,600,000	lb/in^2
ν	0.34	
G12	800,000	lb/in^2
ρ	0.067	lbs/in^3

The skin laminates consist of plies in the 0, +/-45, and 90 degree directions with a stacking sequence of +45/-45/90/0/90/-45/+45, which represents a balanced and symmetric layup. The intent is not to capture the actual layup, which would have many more plies in each orientation, but to model the total thickness of plies in each orientation, while maintaining symmetry and balance. Therefore, plies in the laminate model are equivalent to groups of plies in reality. In addition to the skin plies, the laminates for the stiffened panels of the wing, strut, and jury, include plies representing the panel stiffeners. The stiffeners or stringers consist of base flanges and webs forming a 'T' or blade stringer cross-section. The bases are represented by one ply, and the webs by another ply, in the laminate, as illustrated in Figure 18. In each of these plies, the discrete bases or webs are smeared into the homogenous ply by adjusting the orthotropic material properties of the ply to match the in-plane stiffness in each direction. The thickness of the ply matches the thickness of the base or height of the web, and the density of the material is adjusted so that the weight of the homogeneous ply matches that of the discrete members it represents.

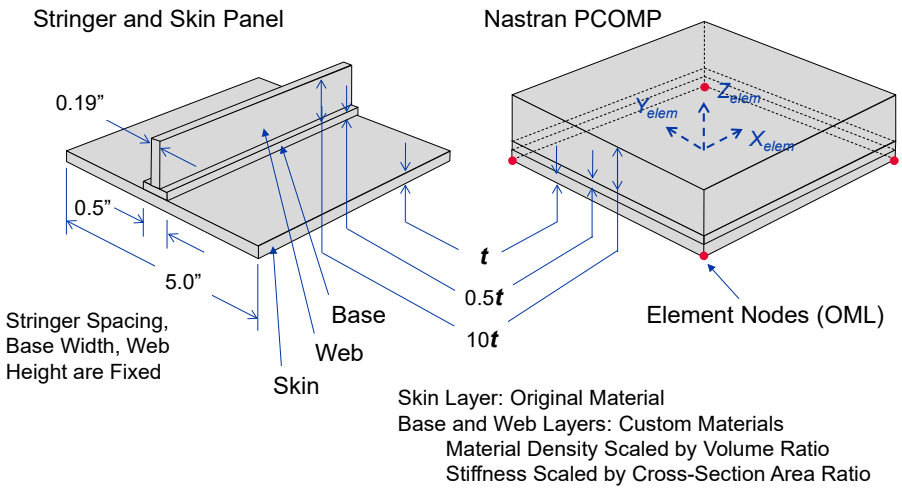


Figure 18 – Composite Laminate Representation of Stiffened Panels.

For the wing, strut, and jury, the stringer geometry was assumed to be the same, with a base width of 0.5 inch and a base thickness equal to half the thickness of the skin. The stringer web has a fixed thickness of 0.19 inch, and its height equals ten times the thickness of the skin. Stringer spacing is 5.0 inches, measured from center to center. This arrangement means that the stinger

cross sectional area scales up with skin thickness, keeping the stringer area equal to half the skin area, or equal to one third of the total area of the stringer and skin cross sections. The stringer area ratio is consistent with the Phase II study, but the stringer base width has been reduced while the stringer height has been increased from three times skin thickness to ten times skin thickness. This is more consistent with an optimized stringer as determined by the high fidelity buckling study completed for the Mach 0.745 vehicle. That this one stringer geometry is applicable to the wing, strut, and jury, and to skin panels, spar webs, and rib webs, is a simplifying assumption for the present maturity of the structural design. Other factors, like depth of the wing box, rib cutouts at stringer intersections, the concept for attaching the stringers to the skin, and stringer web crippling, may require different proportions for the stringer cross section, as well as different stringer spacing. For this stringer geometry, the material properties of the base ply are E1 = 2,350,000 lbs/in^2, E2 = 0.0001 lbs/in^2, ν = 0.34, G12 = 800,000 lbs/in^2, and density = 0.0067 lbs/in^3, and for the web ply are E1 = 893,000 lbs/in^2, E2 = 0.0001 lbs/in^2, ν = 0.34, G12 = 800,000 lbs/in^2, and density = 0.00255 lb/in^3.

Table 10 – Custom Material Properties for Stiffener Layers.

Stringer Base		
E1	2,350,000	lb/in^2
E2	0.0001	lb/in^2
ν	0.34	
G12	800,000	lb/in^2
ρ	0.0067	lbs/in^3

Stringer Web		
E1	893,000	lb/in^2
E2	0.0001	lb/in^2
ν	0.34	
G12	800,000	lb/in^2
ρ	0.00255	lbs/in^3

The control surfaces on the wing are not sized, and are modeled only to transfer loads from the aerodynamic model into the wing box. They use a laminate similar to the stiffened panels of the wing skin, with fixed ply thicknesses for a total skin thickness of 0.1 inch, a stringer base thickness of 0.05 inch, and a stringer web height of 1.0 inch. The material properties are the same as those for the wing skins, except that density is zero for all the plies. The mass of the control surfaces is represented by nonstructural mass provided in the mass properties statement.

To represent the structural elements within the structural OML, correct element offsets are required. For the beam elements of the rib and spar caps, areas are small, so it is a reasonable simplification to neglect the offset, placing the neutral axis of the beam at the OML. In addition, the cross sectional geometries of the caps are not yet defined, without which the correct offset cannot be determined. Including beam offsets requires that the optimization model include links between beam cross-section design variables and the beam offsets, so that the offsets remain correct as the beam sizing changes. When the structural design has matured further, the beam offsets and other details can be included in the FEM. For the stiffened laminates of the skin panels, the presence of the smeared stiffener plies makes the laminate quite thick, so that if its thickness is centered on the OML plane, then the structure protrudes significantly past the OML.

Therefore, the skin panel elements are modeled with their normals pointing inward from the OML, and the offset is defined so that the bottom of the first ply in the laminate rests on the OML. From this location, the plies stack up in the direction of the element normal, that is, inward. In Nastran, this arrangement is achieved by specifying the Z0 offset as 0.0 on the PCOMP entries. The approach is illustrated in Figure 19 and Figure 20.

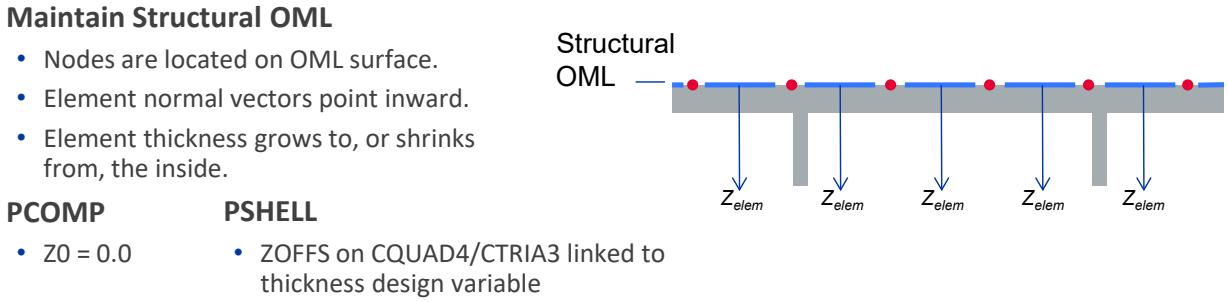


Figure 19 – Offsets for Nastran PCOMP and PSHELL Entries to Maintain OML during Sizing.

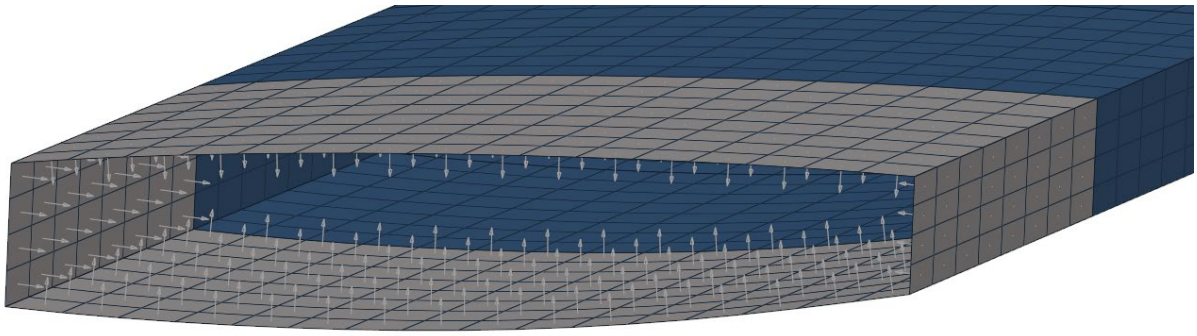


Figure 20 – Element Normal Directions in the Wing Box.

The structural optimization model uses four types of design variables. For beam elements, the beam cross-sectional area is the design variable. The lower bound is 0.01 in^2 and the upper bound is 5.0 in^2. For composite laminates, the design variables are the thicknesses of the 0, 45, and 90 degree plies, each bounded between 0.001 inch and 3.0 inches. Since the design variable for each orientation is the thickness of one ply, and the aforementioned stacking sequence includes one ply of 0-degree material, four plies of +/- 45-degree material, and two plies of 90-degree material, the total skin thickness is the sum of the 0-degree design variable, four times the 45-degree design variable, and two times the 90-degree design variable. Figure 21 illustrates the total laminate thickness. The thickness of the stringer base ply is half of the total skin thickness, and the thickness of the stringer web ply is ten times the total skin thickness. For example, with a skin thickness of 0.2 inch, the total laminate thickness is 2.3 inches. The ply thickness design variables are continuous, while in reality, the laminate grows thicker by the addition of a discrete number of plies. Ideally, a scheme for 'ply integerization' should be applied during optimization, or as a correction after sizing, but this adds complexity and effort to the optimization process that may not be appropriate for the present maturity of the structural design. The assumption implicit in

omitting ply integerization is that the skins are thick enough that rounding up to the nearest integer multiple of ply thickness will not be a significant impact on weight.

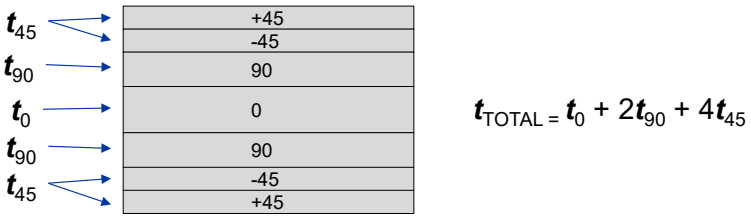


Figure 21 – Total Laminate Thickness for Balanced Stacking Sequence.

The responses and constraints for beam elements are the axial stress at each end of the beam. The stresses are constrained to 90,000 psi in compression and in tension. For composite laminates, the responses are major and minor composite strains at the extreme plies of the skin (plies 1 and 7 in the stacking sequence). These strains are constrained to 4500 microstrains (0.0045) in tension and in compression. In addition, the total laminate thickness is constrained to be above 0.16 inch, and the thickness of skin ply material in each orientation is constrained to be at least ten percent of the total skin thickness. These responses and constraints represent a basic set of checks for structural integrity, for an initial estimate of structural weight. As an aircraft design matures, many more checks are required.

In addition to the strength sizing described above, the wing, strut, and jury are optimized for buckling loads. The first nine buckling modes are constrained to have eigenvalues above 1.0, which means there is to be no buckling below the applied loads, which are ultimate loads. This constraint is intended for global buckling modes, as opposed to local panel or stiffener buckling, but because it is applied to all modes detected in the FEM, it can be conservative if local buckling modes are present. Some effort was put into the FEM development to eliminate local buckling modes, especially in structures that are not being sized, such as the titanium splitter and the sponson structure. In many aircraft, some structural members are allowed to be locally buckled at limit load. For the TTBW, global buckling of the strut and jury is the focus, and neither of these members should buckle below ultimate load. To properly address the issue of buckling at the local and global levels, the structural design criteria for the TTBW should be defined in greater detail.

The FEM is divided into design zones or property regions corresponding to the bays formed by ribs and spars. This allows panel thickness or beam cross sectional area to vary for each bay. The property regions in the wing, strut, and jury are indicated by different colors in Figure 22. The patterns are the same for the upper and lower sides of the structure. A good number of property regions allows the sizing to be tailored to the internal loads of each region, saving weight. As the structural concept matures, manufacturing considerations need to be included to ensure that variations between adjacent bays don't result in unbuildable structure.

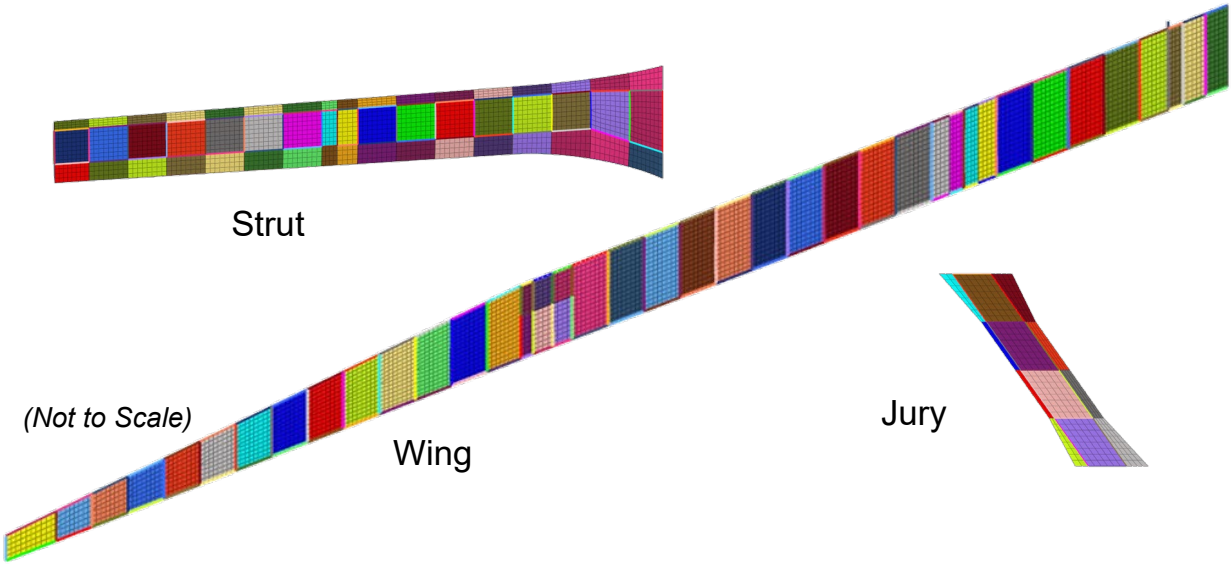


Figure 22 – Property Regions of the Wing, Strut, and Jury.

For the Mach 0.80 TTBW, the structural optimization is done entirely in Nastran. No local optimization is performed in HyperSizer, as was done for the Mach 0.745 TTBW in Phase II. This approach reflects the maturity of the Mach 0.80 structural design relative to the Mach 0.745 design. More work is needed on the Mach 0.80 design to refine structural concepts, practical limits on panel geometries, manufacturing approaches, and constraints at the global level, before detail is added at the local level through application of HyperSizer or other panel optimization tools. To move to the next level of refinement, design development is needed for the wing, strut, and jury, to identify the concepts and restrictions that apply to each of them. For future evolution of the TTBW FEM and optimization process, definition of the design and sizing criteria is critical.

3.2.5 Wing, Strut, and Jury Features in the FEM

The wing was modeled with a conventional layout of two spars, and streamwise ribs spaced at 30 inches. The rib spacing was adjusted to accommodate key features like the jury and strut attachments, the outboard wing fold, the front spar break, and the engine pylon attachment. Figure 23 shows a planform view of the wing structural layout. The front spar location was defined as 15 percent chord from the wing root to the front spar break, and then increasing linearly from 15 percent to 30 percent chord from the break to the wingtip. The rear spar was defined at 68 percent chord from the wing root to wingtip. The strut was modeled with a similar layout, shown in Figure 24, with streamwise ribs spaced at 30 inches, a front spar at 15 percent chord, and a rear spar at 70 percent chord. The front spar of the jury was defined at 10 percent chord and the rear spar at 80 percent chord, with streamwise (horizontal) ribs spaced at 13.75 inches. Figure 25 shows the structural layout of the jury.

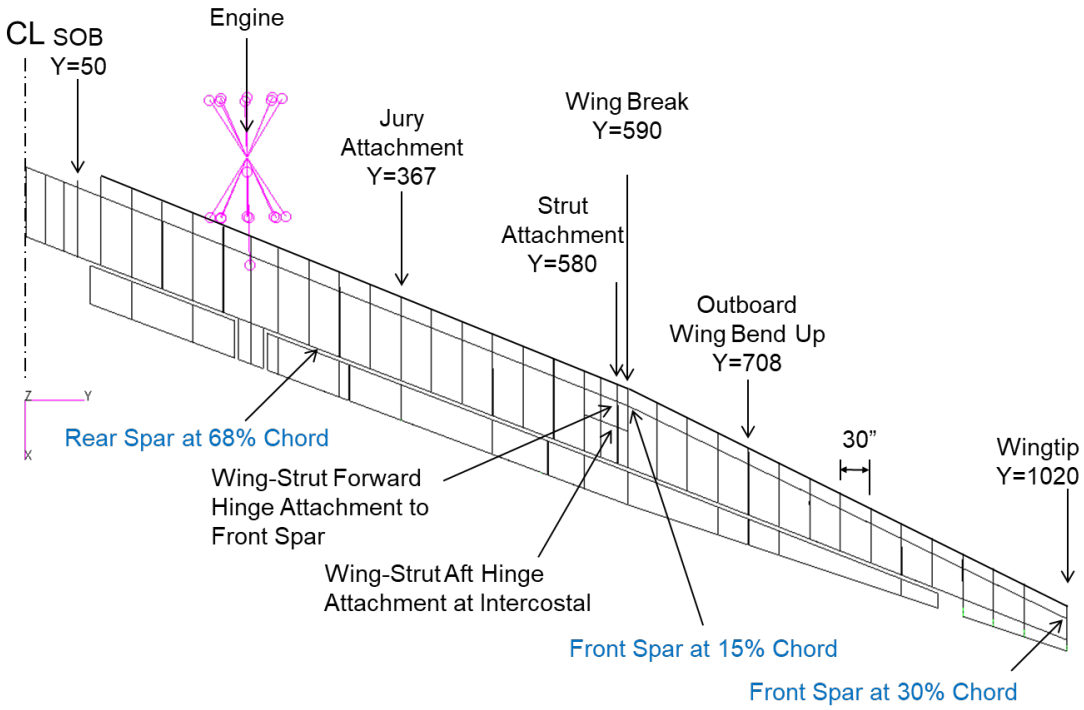


Figure 23 – Wing Structural Layout.

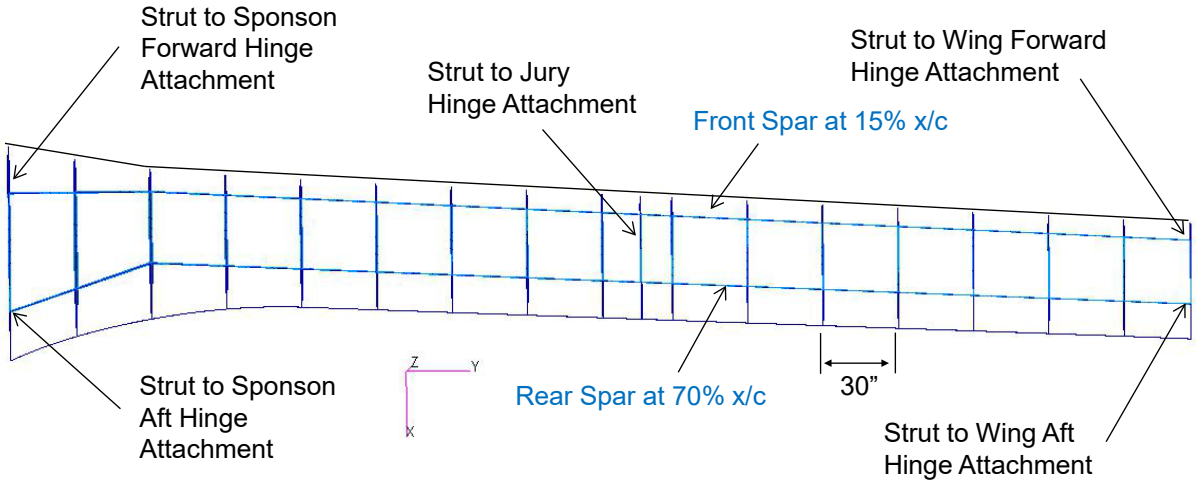


Figure 24 – Strut Structural Layout.

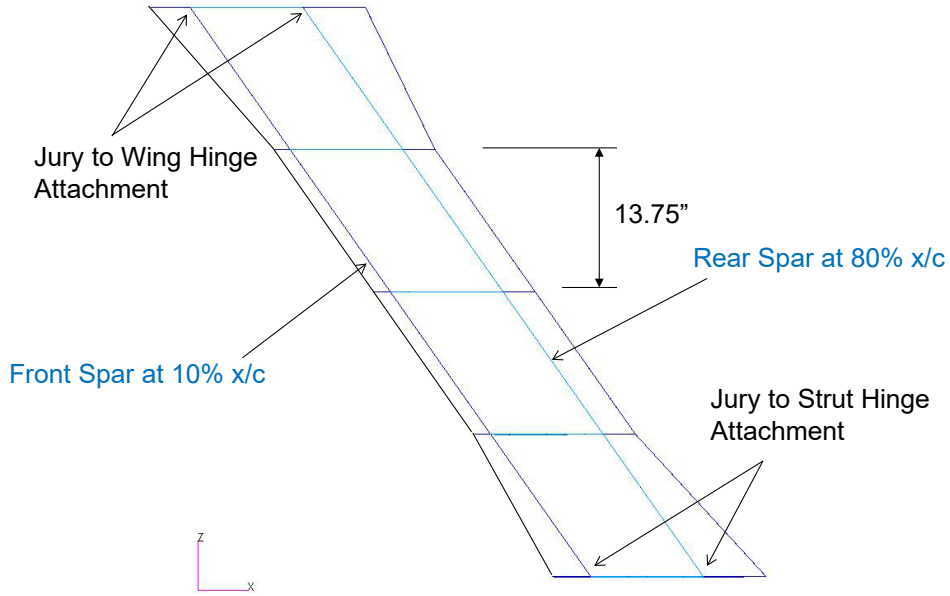


Figure 25 – Jury Structural Layout.

The spar locations and rib spacing in the wing, strut, and jury, are initial estimates, and require a design layout effort to better establish them. In fact, the internal structural layout itself would benefit from a structural and manufacturing study, as unconventional layouts (like a multispar arrangement) may have advantages for the unusually long and thin wing box of the TTBW, and the thin structures of the strut and jury.

The FEM representations of the connections of the strut to the sponson and wing do not reflect the latest designs described in the previous section, as these designs were developed after the structural FEM, and at the same time when the FEM was being developed for aeroelastic analysis. The modeling of the new joint concepts in the FEM, and the assessment of their impact on the sizing of the strut and other parts of the airframe, is a future task. The descriptions below are of the current structural connections in the FEM.

At the connection of the strut to the wing, auxiliary ribs and an intercostal spar were added to reinforce the wing. The connections link the front and rear spars of the strut to a wing rib, the strut front spar connecting between the wing front spar and the intercostal spar, and the strut rear spar attaching just aft of the intercostal spar, as shown in Figure 26. The attachments are modeled with multipoint constraints (Nastran RBE2 entries) and are aligned to form a pinned connection. The forward attachment links the fore-aft, lateral, and vertical translations, and the aft attachment links only the lateral and vertical translations. All rotations are free, however, the presence of two attachment points at each end of the strut prevents torsional rotation of the strut. Care was taken to ensure that the axis of the pinned connection between the strut and wing is parallel to the axis of the pinned connection between the strut and sponson, so that no bending loads are transmitted to the strut. The connection of the strut to the sponson is similar

to that of the strut to the wing, as shown in Figure 27, and the front and rear spar of the strut are connected to the front and rear spars (or bulkheads) of the sponson.

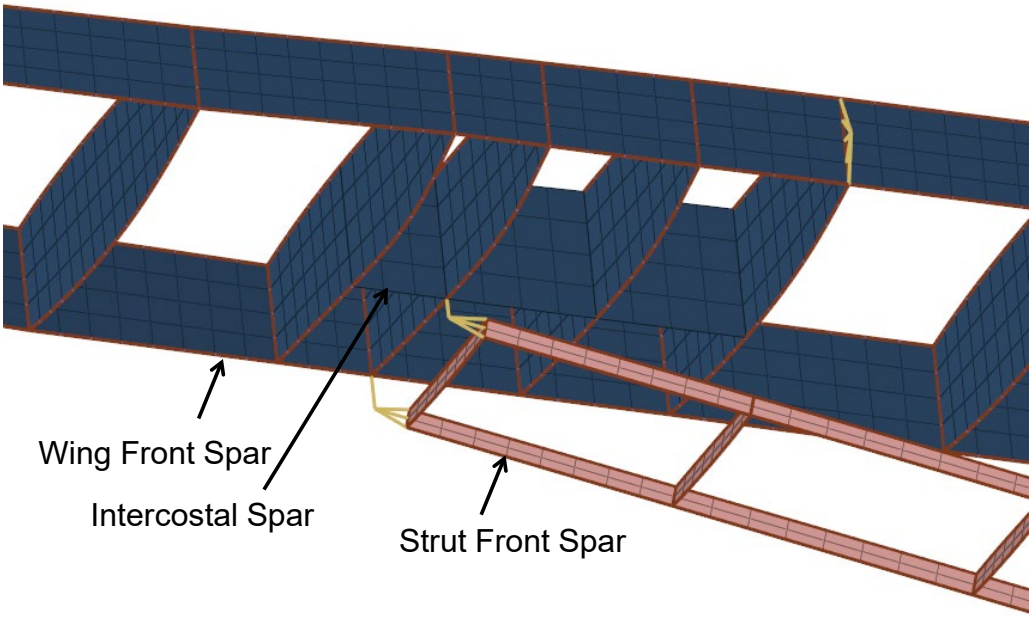


Figure 26 – Connection of Strut to Wing (Skins Removed for Clarity).

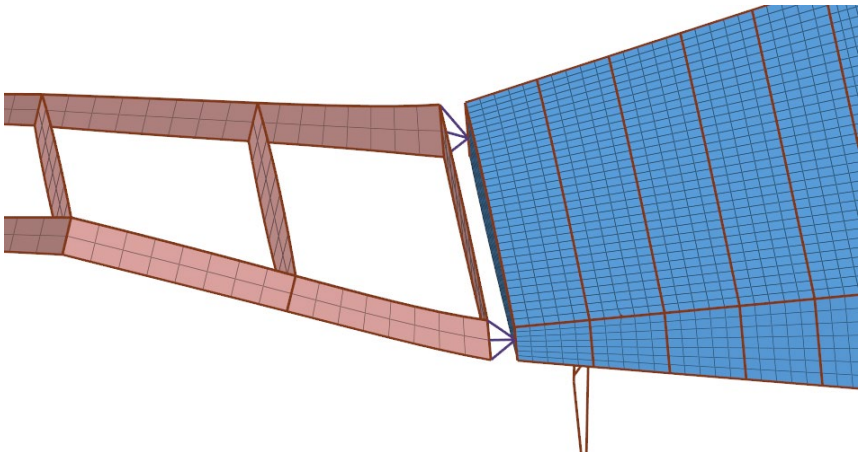


Figure 27 – Connection of Strut to Sponson (Strut Skin Removed for Clarity).

The connection of the jury to the wing links the front and rear spars of the jury to a single point on a wing rib, as shown in Figure 28. The attachment links three translations, fore-aft, lateral (normal to the plane of the jury, which is slightly canted), and vertical (in the plane of the jury), as well as rotation about the vertical axis (in the plane of the jury). Rotations about a fore-aft axis, and rotations in the plane of the jury, are free. The connection of the jury to the strut is similar, attaching the front and rear spars of the jury to a single point on an auxiliary rib in the strut. This attachment links the three translations, along axes parallel to that of the jury-wing connection, but leaves all rotations free. The effect of the attachments at the ends of the jury is

to prevent any bending or torsional loads from entering the jury, but without leaving the jury free to twist about its lengthwise axis.

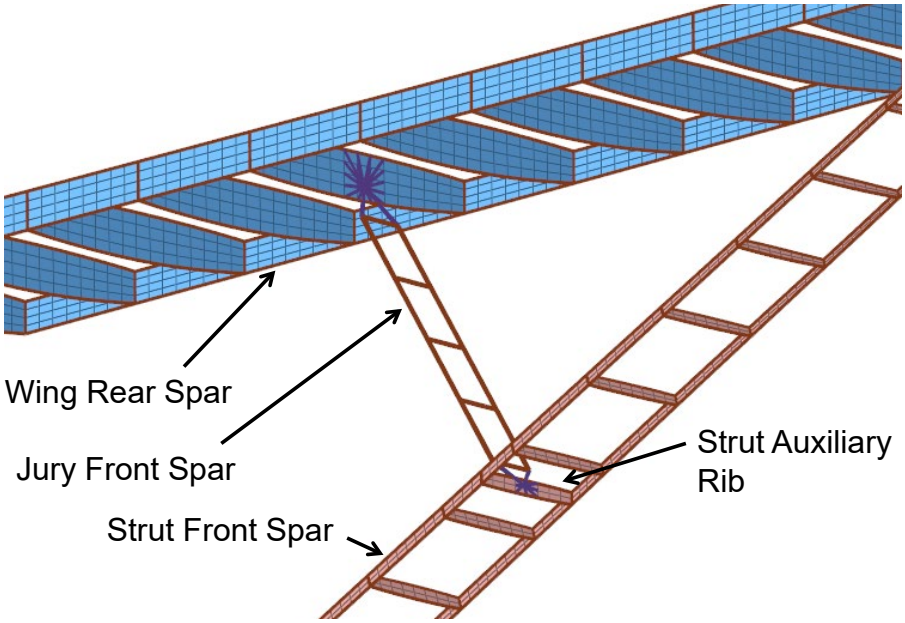


Figure 28 – Connections of the Jury to the Strut and Wing (Skins Removed for Clarity).

The control surfaces - flaps, flaperon, aileron - are modeled as three-dimensional structures but they are not realistic and only serve to transfer loads from the aerodynamic control surfaces in the doublet lattice model into the wing box. In the aerodynamic model, the control surfaces are accurately modeled, with correct dimensions and hinge lines in the correct locations. The structural control surfaces were modeled somewhat arbitrarily within the OML of the wing. The control surfaces are connected to the wing box at inboard and outboard hinges, which are modeled with RBE2 entries, as shown in Figure 29. The inboard hinge rigidly links all six degrees of freedom, while the outboard hinge leaves translation along the hinge line, and rotation about the hinge line, free. The effect is that control surface hinge moments are reacted at the inboard hinge. There is no flexibility in the hinge model, as such, data were not available during model development. Therefore, dynamic modes of vibration or flutter, which include control surface movements due to hinge flexibility, will not be correctly captured by this model. This is yet another feature that can be refined when the vehicle design matures and the required data are available.

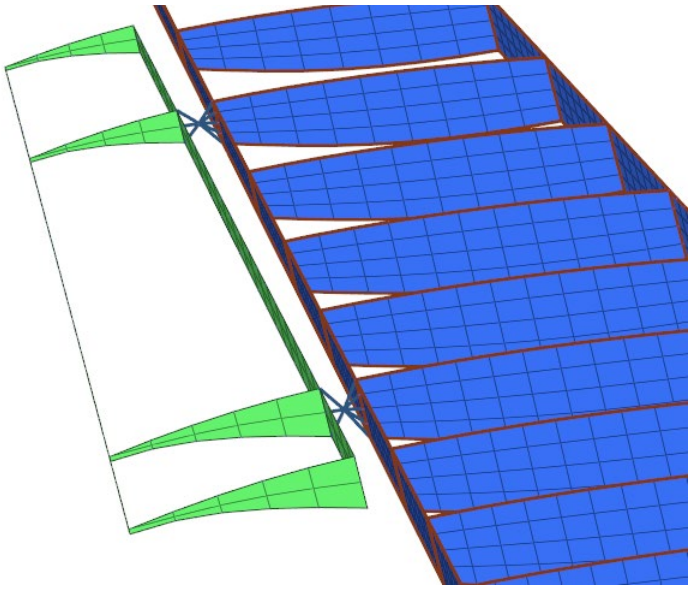


Figure 29 – Control Surface Hinge Connections (Upper Skins Removed for Clarity).

For the engine, nacelle, and pylon, grid points at which weight and aerodynamic loads are applied are connected to the wing using interpolation constraint elements (Nastran RBE3 entries). The RBE3 element attaches to wing grids located at skin and rib intersections, between the front spar and rear spar. The RBE3 element reacts with all rigid body deflections at the independent grid, where loads are applied, but adds no stiffness to the model at the dependent grids.

The wing fold is not represented in the structural FEM. Because the joint needs to carry the same loads as the wing box, the load paths are unchanged by omitting the joint. The weight impact of the joint is captured by adding nonstructural masses at the fold location to represent the joint. When the detailed design of the joint is defined, a better representation can be added to the FEM.

To protect the strut from a bird strike, a titanium splitter is formed at its leading edge by two surfaces extending from the top and bottom of the front spar to a line offset one inch aft of the leading edge of the strut. The titanium panels of the splitter are not optimized, and their fixed sizing was given enough stiffness to prevent local buckling below the applied loads. It is assumed that the jury strut will withstand a bird strike without a splitter due to its narrow leading edge.

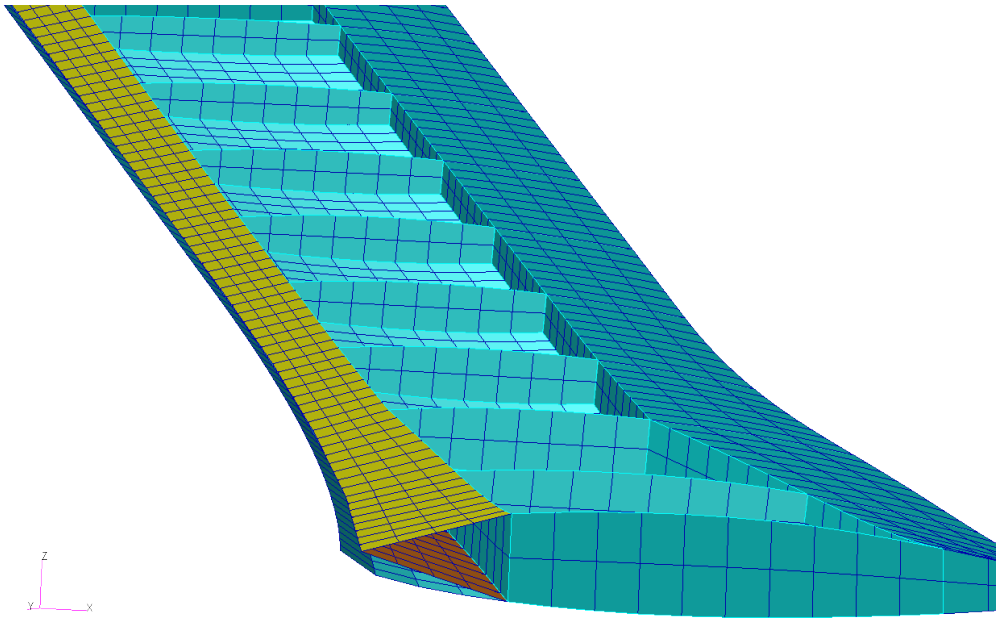


Figure 30 – Titanium Splitter (Yellow/Brown) in Strut Leading Edge (Upper Skin Removed for Clarity).

3.2.6 Center Body/Sponson FEM

The sponson connects the root of the strut to the fuselage. It includes upper skin, two spars, ribs, and a fuselage bulkhead, as shown in Figure 31. These members are not included in structural sizing optimization. The sponson is modeled with representative properties, including stiffened panels modeled as composite laminates similar to those in the wing. Although no gear loads were included in the current study, the sponson also reacts gear loads and a gear beam model is attached to the sponson. Gear conditions are not critical for the structure sized in the current study and are not expected to impact results. The properties in the sponson structure were adjusted to avoid local buckling modes under the applied loads.

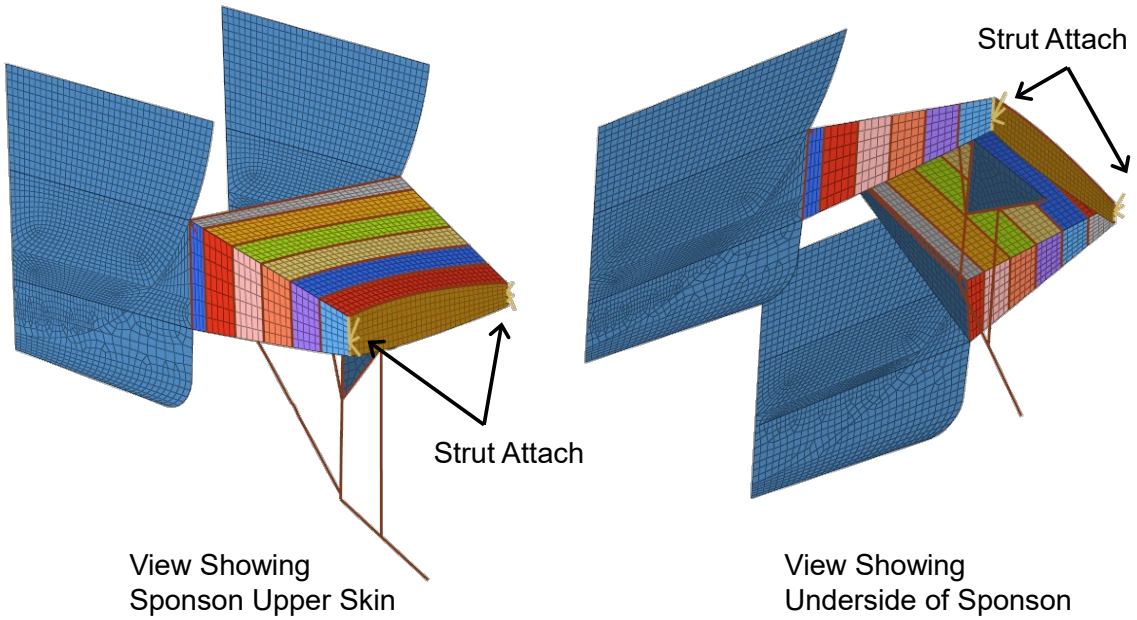


Figure 31 – Sponson Structural Model.

In the present study, as in past TTBW aeroelastic studies, the focus is on the wing, strut, and jury, with the fuselage providing structural support, carrying payload and other weight, and the tail trimming the vehicle. As structural concepts are developed for strut-to-sponson joints, and design details are defined to accommodate the joints, landing gear, and associated back up structure, the sponson and center fuselage structure will need to be included in structural optimization.

3.2.7 Finite Element Model Integration

The fuselage and tail model from the 2016 FEM was used in the refined FEM. It consists of beam models of the forward fuselage, aft fuselage, and empennage, with a three dimensional barrel section model of the center fuselage to support the wing and strut models with the correct boundary conditions. The forward fuselage and aft fuselage attach to the barrel section using an RBE3 elements, which add no stiffness to the centerbody. The beam models are nearly rigid, and serve to support the aerodynamic surfaces of the fuselage and empennage, and transfer loads into the barrel section of the center fuselage. The goal of the finite element analysis was to size the wing, strut, and jury; hence the assumption was made that the dynamics of the forward and aft fuselage and tail would not significantly impact the wing dynamics. The barrel section, shown in Figure 32, is modeled with representative properties for aluminum structure. The fuselage and tail beams, as well as the barrel section, have no material density, and their mass properties are represented by concentrated masses derived from the vehicle weight statement. Neither the beam nor barrel sections of the fuselage are included in structural sizing optimization.

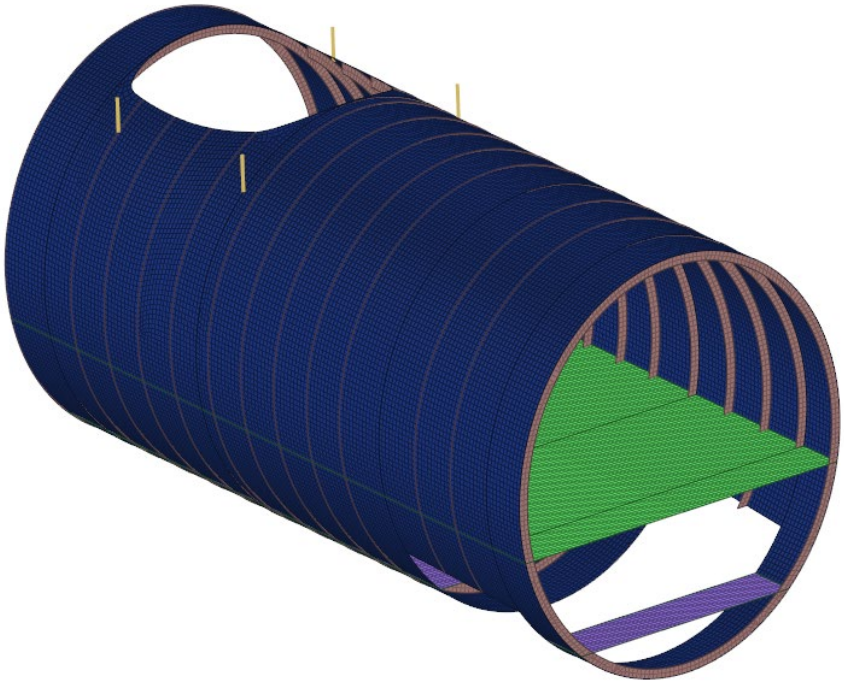


Figure 32 – Fuselage Barrel Section Structural Model.

In the development of the 2016 FEM, the barrel section was lengthened to accommodate the wing and strut positions for the Mach 0.80 vehicle. During development of the refined FEM, the tail model was adjusted to match the geometry of the 1104-001-RC configuration. The integrated FEM is shown in Figure 33.

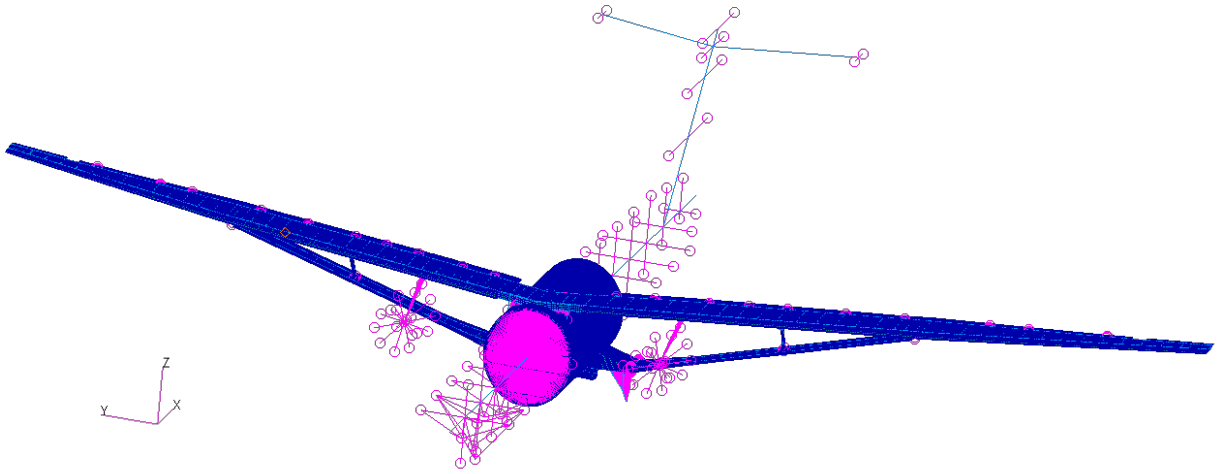


Figure 33 – Integrated Vehicle Finite Element Model.

The wing is attached to the centerbody in three ways. The first is the primary vertical connection between the wing and fuselage, and occurs at the wing front and rear spars. Here, a frame-mounted post extends up from the fuselage and attaches to a trap panel. The trap panel extends from the post to the front and rear spars of the wing at the side-of-body rib.

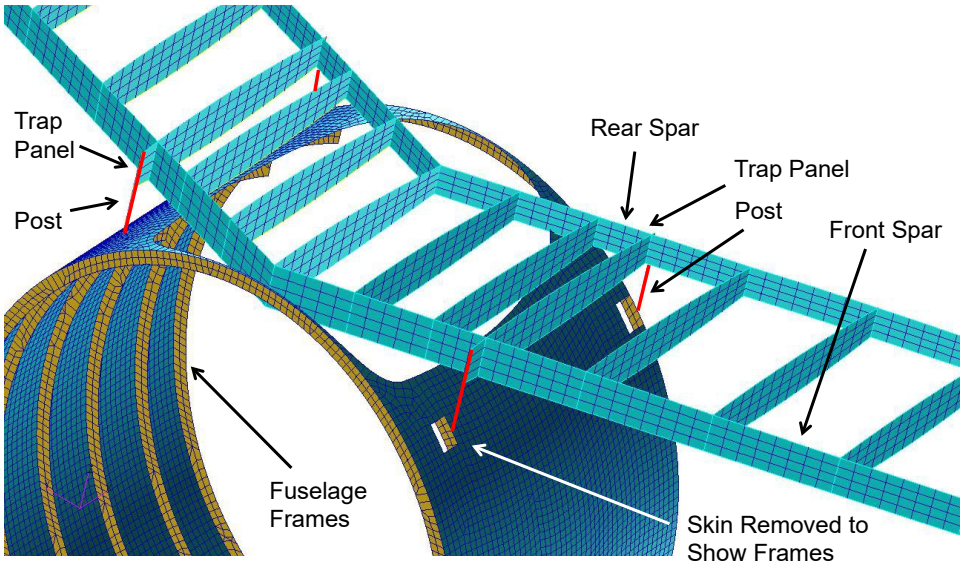


Figure 34 – Primary Vertical Connection between Wing and Body.

The second is the primary fore-aft connection between the wing and fuselage. Here, the grids along the fuselage wing cutout are connected, in the fore-aft direction only, to the closest grids on the wing's lower skin.

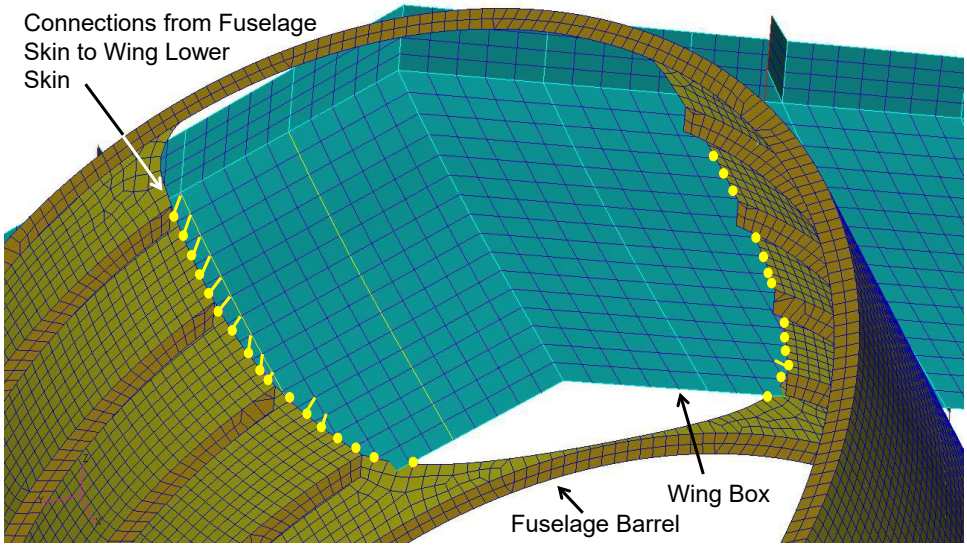


Figure 35 – Primary Fore-Aft Connection between Wing and Body.

The third is the primary lateral connection between the wing and fuselage, where the end grids of three fuselage frames are connected, in the inboard-outboard direction only, to grids on the wing lower skin.

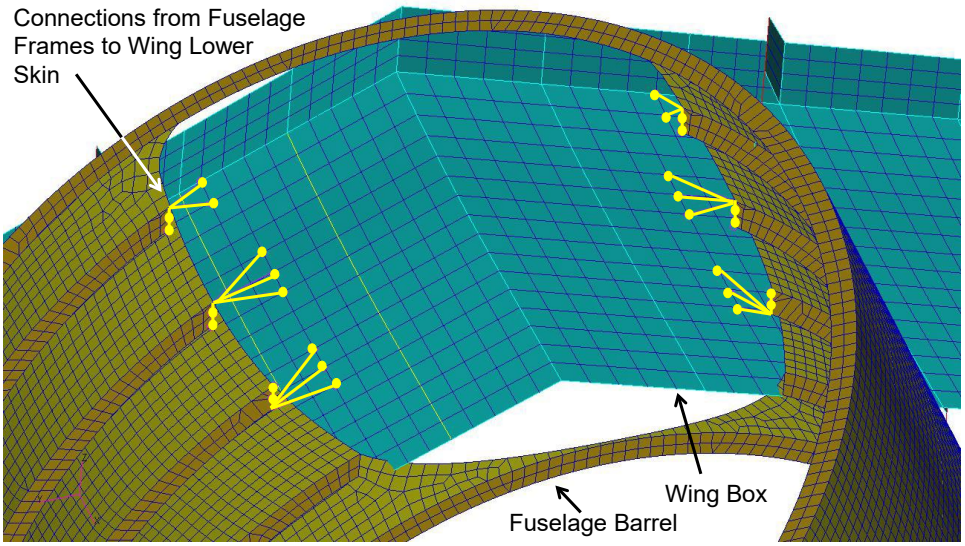


Figure 36 – Primary Lateral Connection between Wing and Body.

3.2.8 Nonstructural Mass and Fuel/Payload Cases

Material density of structural elements in the FEM determines the weight that is optimized during structural sizing. As in previous TTBW studies, an increased density for the composite material is used to represent cutouts, fasteners, and other unmodeled features. Density weight, or structural weight, applies to the wing, strut, and jury. All the remaining weight is applied to the FEM to match the vehicle weight statement, and is spread on the model as concentrated mass items. The weight statement specifically breaks out the structural, or load bearing material, weight for the wing, strut, and jury, so that these values can be replaced by the density weight from the FEM. For the other components, including the fuselage, tails, and control surfaces, the entire mass of each item is applied by spreading concentrated masses over the component in the FEM. For the engines, nacelles, and pylons, single-point concentrated masses with inertia terms were used. For other discrete items, like the wing fold joint, landing gear, and auxiliary power unit, the concentrated masses were spread over multiple grids in the locality of the item.

In the present FEM, the weights of joints and splices are captured in either the increased density of composite material, or in the general nonstructural mass spread over each component. As the structural concepts and designs develop, the locations and design details of joints and splices will be defined well enough to be represented by discrete masses in the FEM. Such refinement will reveal any impacts to the local structure surrounding these features.

To represent a range of flight weights, five fuel and payload combinations were defined. They are listed in Table 11. Concentrated masses were spread in the regions of the payload bay, a forward and aft fuselage or body tank, a center tank in the wing box, and a main or outboard tank in each wing, to represent the mass conditions.

Table 11 – Payload and Fuel Combinations.

Mass Case	Fuel	Payload
1	Fuel to reach MTOW from MZFW	Max to Reach MZFW
2	Full	Max to reach MTOW with Full Fuel
3	Full	None
4	Reserve	Max to Reach MZFW
5	Reserve	None

MTOW = Maximum Takeoff Weight; MZFW = Maximum Zero Fuel Weight

3.2.9 Aerodynamic Model

The doublet lattice aerodynamic model from the 2016 FEM was adjusted to fit the geometry of the refined structural FEM. The planforms of the horizontal and vertical tails, and the strut, were modified to fit the configuration geometry of the structural FEM.

Some refinements were made to improve the accuracy of the model, which is depicted in Figure 37. Various minor adjustments were made to aerodynamic panel coordinates to improve alignment and symmetry among panels. To improve the representation of the spanwise load distribution for the wing and strut, panels were added to extend the wing and strut to the vehicle centerline. These carry-through panels are visible in Figure 38. Small panels were added to connect the strut panel to the wing panel as shown in Figure 39. Aerodynamic panels for the jury strut were added to the model. The mesh density was increased to maintain the aspect ratio (span/chord) of the aerodynamic boxes between one and three, and to ensure that box chords were appropriate for the reduced frequencies involved in flutter analysis. Care was taken to ensure that the intersections of aerodynamic panels aligned with box edges.



Figure 37 – Doublet Lattice Aerodynamic Model with Refined Mesh and Updated Panels.

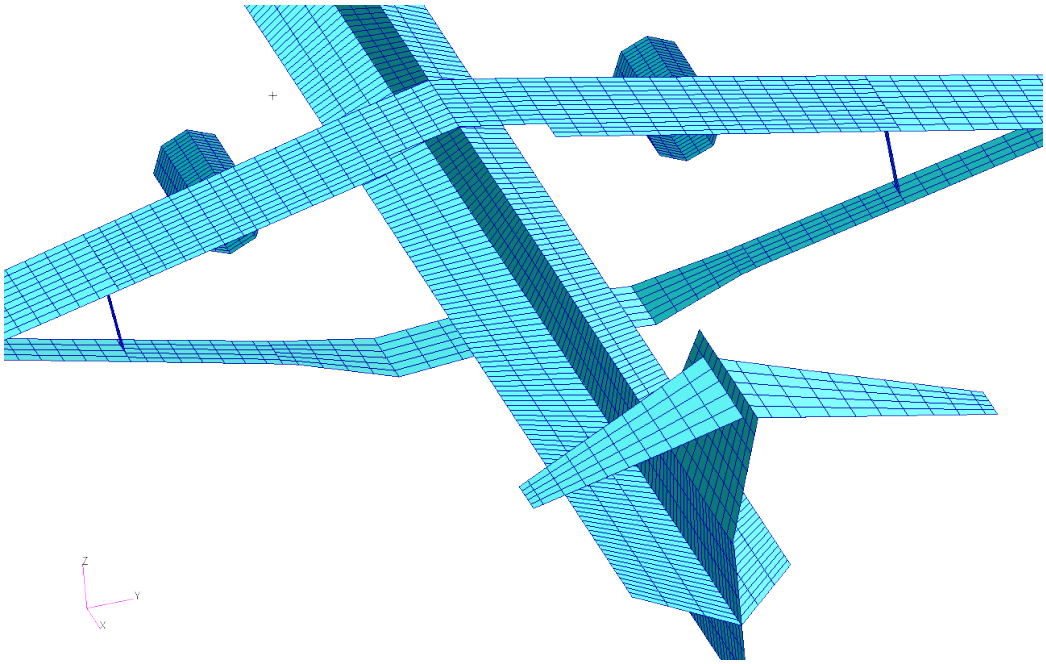


Figure 38 – Detail of Aerodynamic Model Showing Carry-through Panels and Updated Tail.

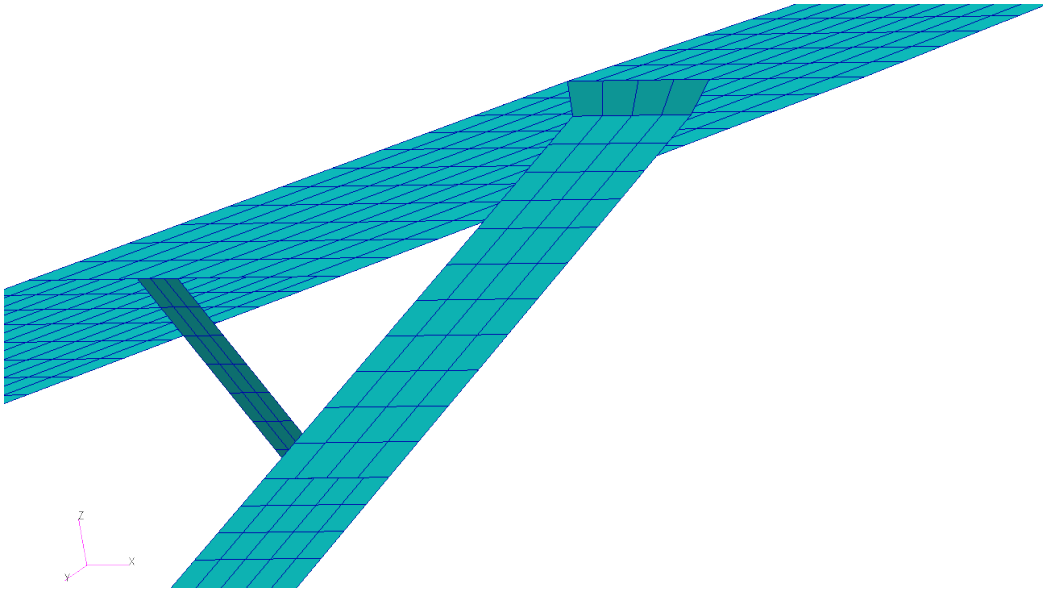


Figure 39 – Detail View of Aerodynamic Model of Jury and Strut-to-Wing Connection.

In the Phase III Mach 0.745 TTBW aeroelastic study, correction factors were calculated for the doublet lattice aerodynamics to match computational fluid dynamics (CFD) results. The 2016 FEM did not use aerodynamic corrections because CFD analyses had not been completed at the time. In addition, previous studies showed better correlation with the uncorrected analysis results. The present study was initially performed with theoretical doublet lattice aerodynamics.

3.2.10 Maneuver Load Conditions

Load conditions investigated include symmetric 2.5g and -1g balanced maneuver load conditions. Balanced maneuver load conditions are FAA-required symmetric pitch conditions with a specified load factor and tail loads calculated to produce zero pitch acceleration. Flight loads were calculated in Nastran Sol 144 with the horizontal tail used to trim the vehicle.

The external loads and the structural sizing are interdependent, so an initial sizing of the model was done with assumed load conditions. The wing, strut, and jury were sized for strength and buckling using 2.5g and -1g balanced maneuver conditions at a Mach 0.80 and dynamic pressures of 2.0 lb/in^2 and 4.0 lb/in^2. These initial cases were used to check out the model and the optimization parameters, and to provide a sized structure for subsequent maneuver loads analysis.

Next, a maneuver loads survey was performed to determine critical load conditions. A 2.5g pull up, a -1g push over, and 1g steady flight conditions were analyzed at the six flight conditions shown in Figure 40, and the five mass cases listed in Table 11.

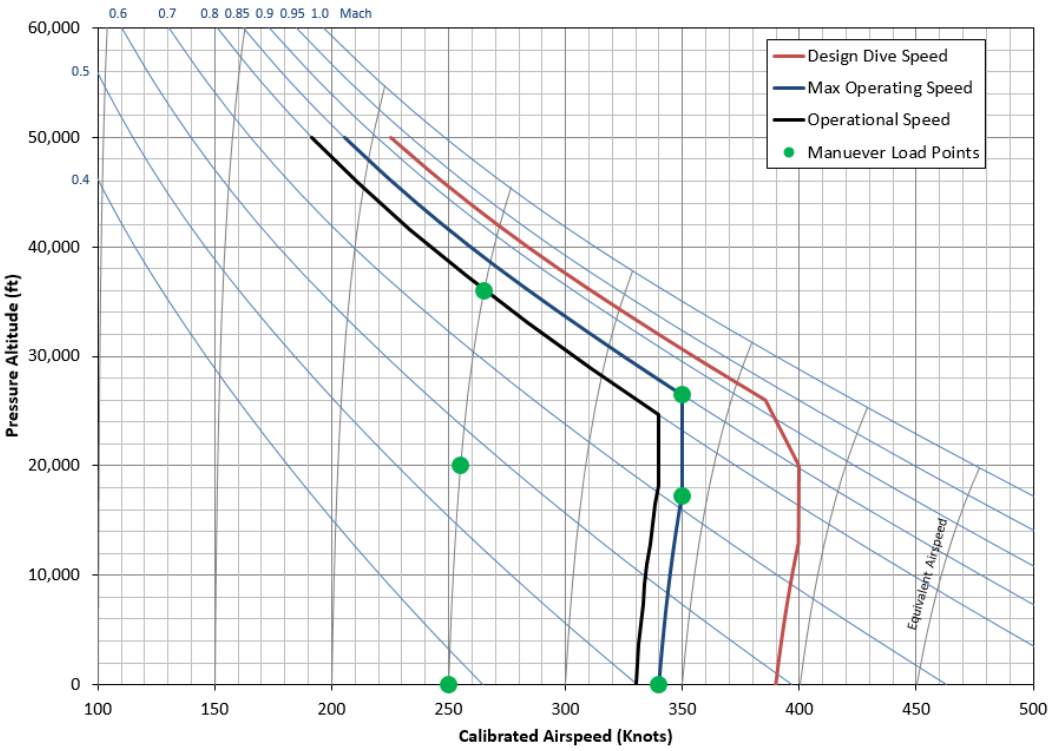


Figure 40 – Flight Conditions for Maneuver Loads Survey.

After running the analyses for the 90 load conditions, the loads at each of the wing and strut monitor points were analyzed for the maximum and minimum of shear load, vertical bending load and torsional load. For an intial selection of critical loads, a total of 30 conditions were identified that caused either a maximum or a minimum load at one or more monitor points.

Among them, four conditions were identified that were critical for the most monitor points. They were two pairs of 2.5g and -1g maneuvers. Both pairs occur at Mach 0.38, at an airspeed of 250 knots, at sea level, which was the slowest airspeed analyzed, and resulted in relatively high angles of attack and tail deflections for trim. One pair is for Mass Case 2, full fuel with payload to reach MTOW. For this pair, most of the critical loads are on the outer wing, probably a result of having the least local inertia relief despite the highest applied loads. The other pair is for Mass Case 5, reserve fuel with no payload. This case has the least weight, and most of the critical loads are on the strut. With no fuel in the wing there is less inertia relief, and the strut has to carry more load. To fully understand the interplay of competing factors that makes these load conditions the most critical would require more in-depth investigation than has been done as of this writing.

The deformation of the wing and strut under a 2.5g pull-up condition at Mach 0.85 and altitude of 26,468 feet is shown in Figure 41. The influence of the strut is clearly visible; inboard of the strut connection, the wing deforms relatively little, and the majority of the deflection is outboard of the strut. The wingtip deflections are about 6% of the semispan, suggesting that linear structural analysis is appropriate at least for preliminary sizing.

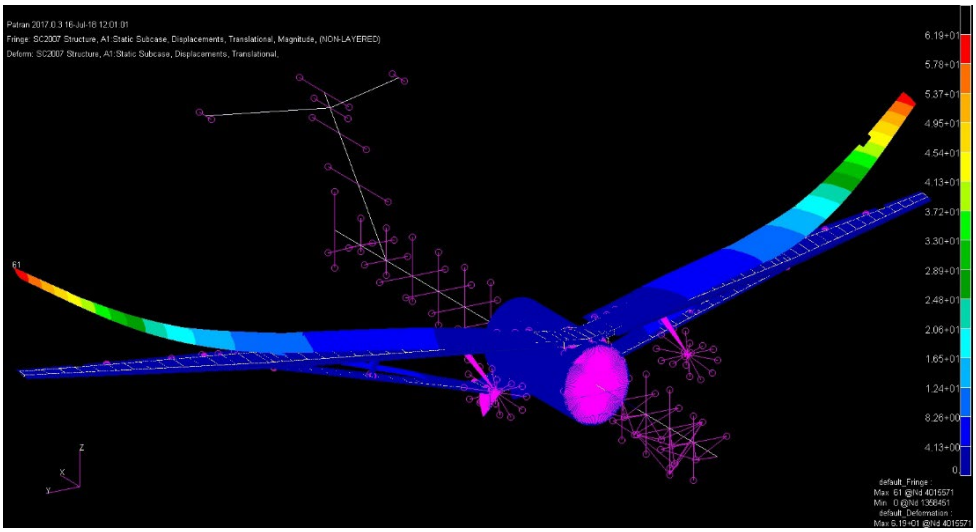


Figure 41 – Structural Deflection for a 2.5g Steady Pull-Up at Mach 0.85, Altitude 26,468 feet.

Aerodynamic pressures associated with rigid body motion are shown in Figure 42 and Appendix Figure A.1. The pressures match expectations for a symmetric pitch motion and provide verification of the doublet lattice model implementation. Incremental aerodynamic pressures associated with airframe flexibility are shown in Figure 43 and A.2. Negative lift on the outboard wings (indicated in blue) as is expected per swept wing aeroelastic effects, providing further model validation.

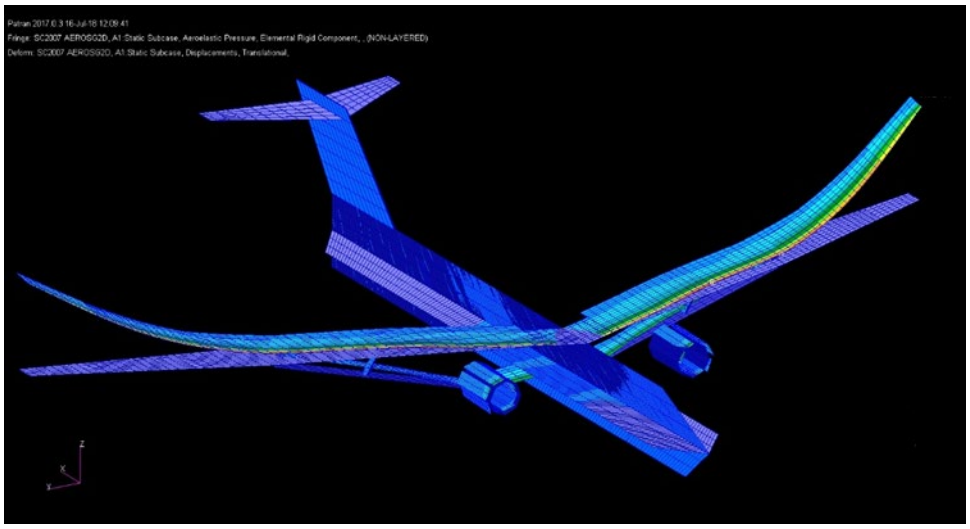


Figure 42 – Rigid Pressure Distribution for a 2.5g Steady Pull-Up at Mach 0.85, Altitude 26,468 feet.

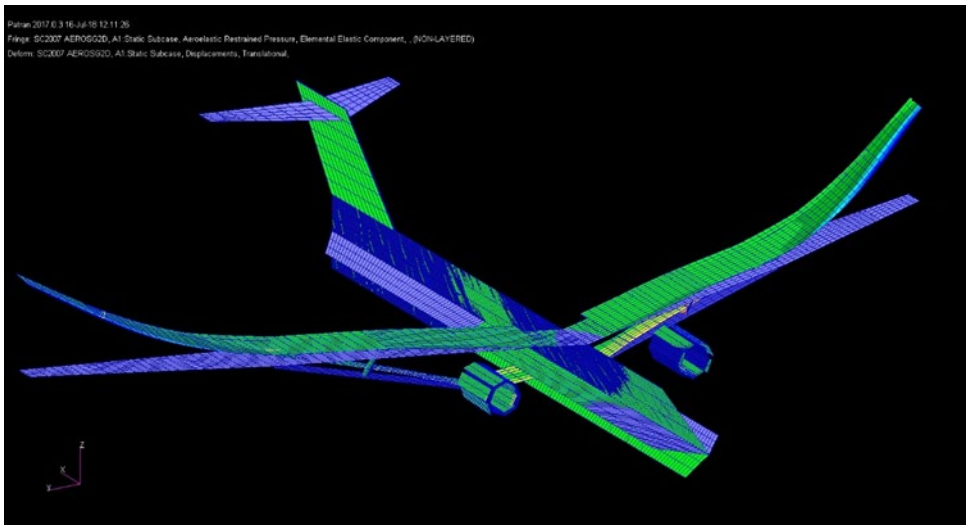


Figure 43 – Flexible Pressure Distribution for a 2.5g Steady Pull-Up at Mach 0.85, Altitude 26,468 feet.

Plots of internal loads for the aircraft configurations and flight conditions analyzed are shown for both wing and strut in Figure 44 and Figure 45. The loads plotted are limit loads for the 2.5g and -1g maneuvers. Inboard of the strut-to-wing connection, the wing and the strut react with the external loads together, and the monitor points integrate internal loads to properly identify the loads in each component. The large effect of the strut in reducing wing shear and bending loads is evident as expected. The significant effect of engine inertia loads on wing internal loads is also noted. The large tension and compression forces in the strut due to symmetric maneuvering are quantified in the plot. Just as the strut reduces wing shear and bending loads, the jury strut reduces strut shear and bending loads. The inboard strut bending loads arise due to the curved shape of the strut in the vicinity of the fuselage attach.

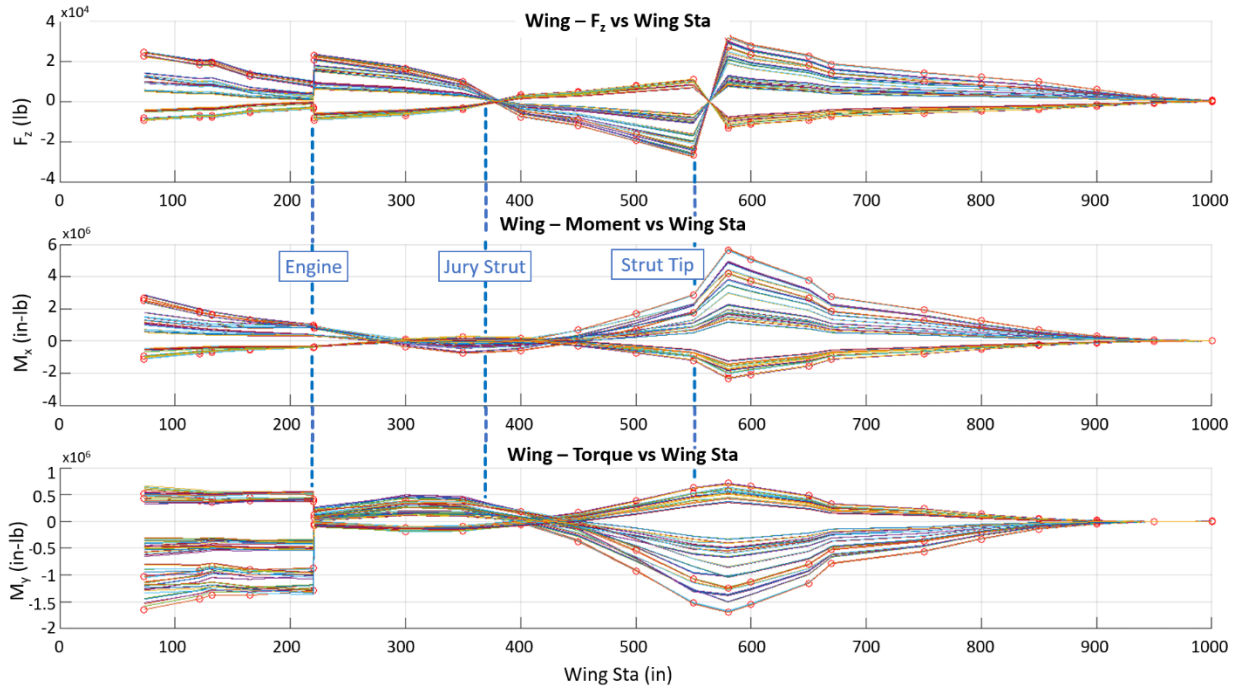


Figure 44 – Wing Critical Design Load Selection.

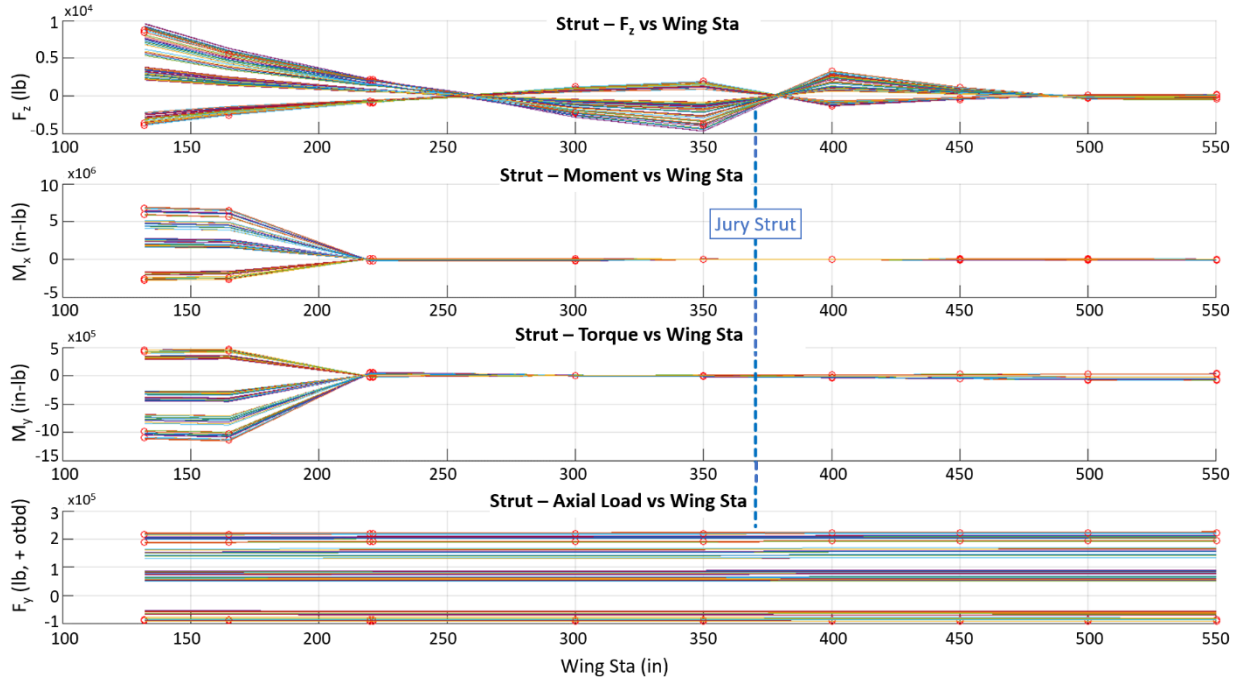


Figure 45 – Strut Critical Design Load Selection.

To select a manageable subset of design load conditions for structural sizing optimization, a combinatorial optimization problem is solved. This process identifies the N load cases that best capture the minimum and maximum loads at each of the monitoring points along the wing and strut. As can be seen in Figure 46, a particular combination of four load conditions was selected

because it captured the minimum and maximum of all 123 component loads for all aircraft mass conditions, flight conditions, and maneuvers to within less than 5%.

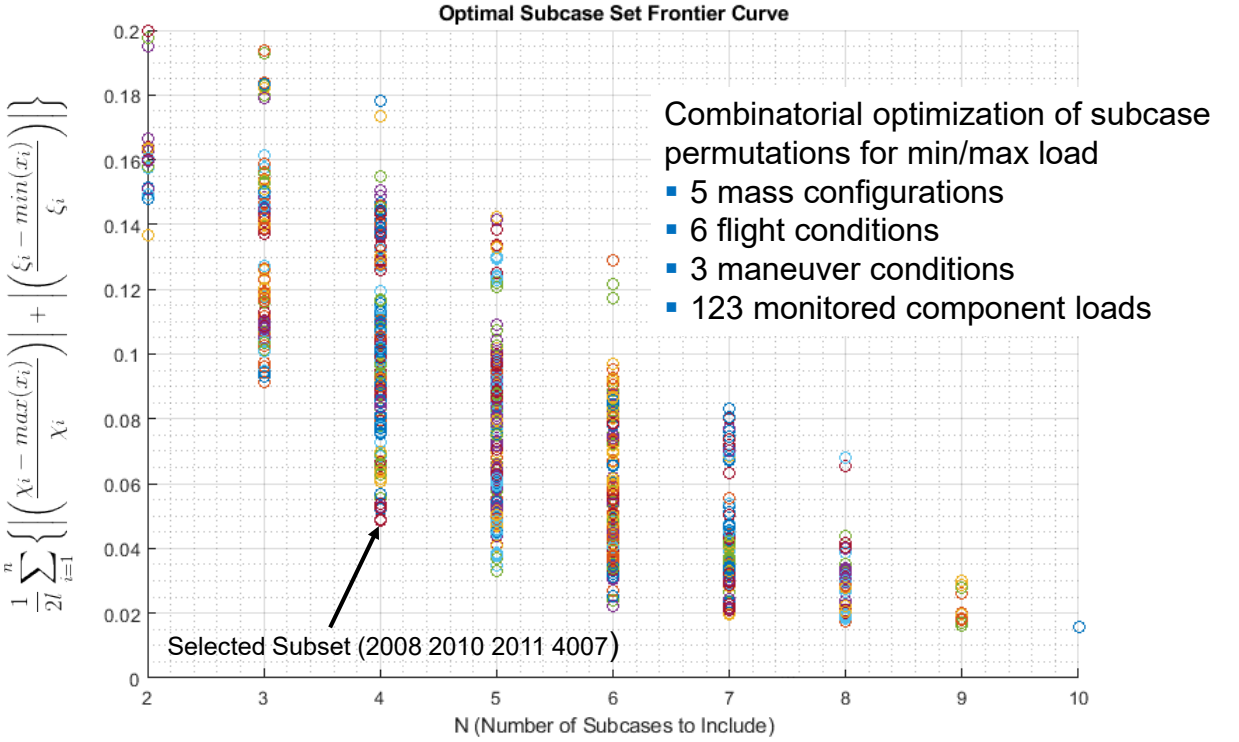


Figure 46 – Structural Sizing Critical Design Load Selection.

The aeroelastic load conditions for the present study are a limited initial set of conditions, representing the critical loads for most of the wing and strut structure. They are useful for establishing the overall structural weight. They do not necessarily produce critical internal loads for every structural part, and a broader loads survey is required to further refine the weight estimate. This is especially true as more of the airframe is included in the sizing optimization. Antisymmetric load cases, maximum control surface deflections, ground loads, crash loads, fuel overpressure loads, and more should be checked as the vehicle design matures. Any of these load cases have the potential to drive the sizing of particular regions of the airframe.

3.2.11 Preliminary Structural Sizing and Optimization

The wing, strut, and jury structure was optimized using Nastran Solution 200 to minimize weight and meet strength and buckling constraints, for the four most critical 2.5g and -1g balanced maneuver conditions from the initial selection of critical loads. The maneuver loads were scaled by a factor of 1.5 to represent ultimate load conditions. Forces from the Nastran aeroelastic loads analysis were extracted and applied as static loads for the optimization. This approach provides faster optimization and more reliable convergence than the ideal approach of performing the loads analysis within the optimization loop. The approach of including the aeroelastic loads analysis in the optimization loop is ideal because it allows the optimizer to change the design to

favorably redistribute internal loads, and to favorably reduce external loads. However, the ideal approach increases the optimization time significantly (by a factor of ten, in some cases), and makes convergence unpredictable. This approach is best used when there is plenty of time to nurse the optimizer to a converged solution. When using static forces to represent external loads, the loads analysis should be updated after the structure is sized, and the process should be repeated to convergence. As of this writing, a second loads cycle has not been performed.

For the four most critical load conditions, a converged solution was found that met all strength and buckling constraints. Table 12 shows a summary of overall weight, comparing the present Phase IV results to the 2016 Mach 0.80 vehicle study, and to Phase II and Phase III results for the Mach 0.745 vehicle. All the results compared in the table are from sizing analyses that did not include flutter. Overall, the new weights are similar to previous studies, indicating that the vehicle design is likely to close and a feasible structure can be achieved. These results should be considered preliminary. To draw further conclusions, gust loads and flutter need to be included in the sizing considerations, and results need to be compared with prior studies that included flutter.

Table 12 – Structural Weights Sized for Strength and Buckling at Critical Maneuver Loads.

			Mach 0.745		Mach 0.80	
			Phase II	Phase III	2016	Phase IV*
Wing			7420	7149	6782	5812
	Skins		5558	5439	5331	3662
	Spars		996	1095	671	767
		Webs	766	880	593	761
		Caps	230	215	78	6
	Ribs		866	615	780	466
		Webs	705	515	696	460
		Caps	161	100	84	6
	Leading Edge					916
Strut			787	1165	2578	2514
	Skins			914		1108
	Spars					110
	Ribs					101
	Edges					868
	Splitter			251		327
Jury			21	44	56	61
	Skins					38
	Spars					2
	Ribs					1
	Edges					20
TOTAL (lbs)			**8228**	**8358**	**9416**	**8386**

** Sizing results from 6/14/2018. Should be considered preliminary.*

The distribution of material in the optimized structure is illustrated by a plot of skin thickness in Figure 47. For this illustration, the stringer base and stringer web layers have been removed from the laminates, and the total thickness of only the skin plies has been plotted. The critical areas are where the strut connects to the wing, and the root of the wing and strut. Because the same scale is used for all components, the variations of thickness in the noncritical areas are obscured. The thickness plot is just an initial indication of material distribution.

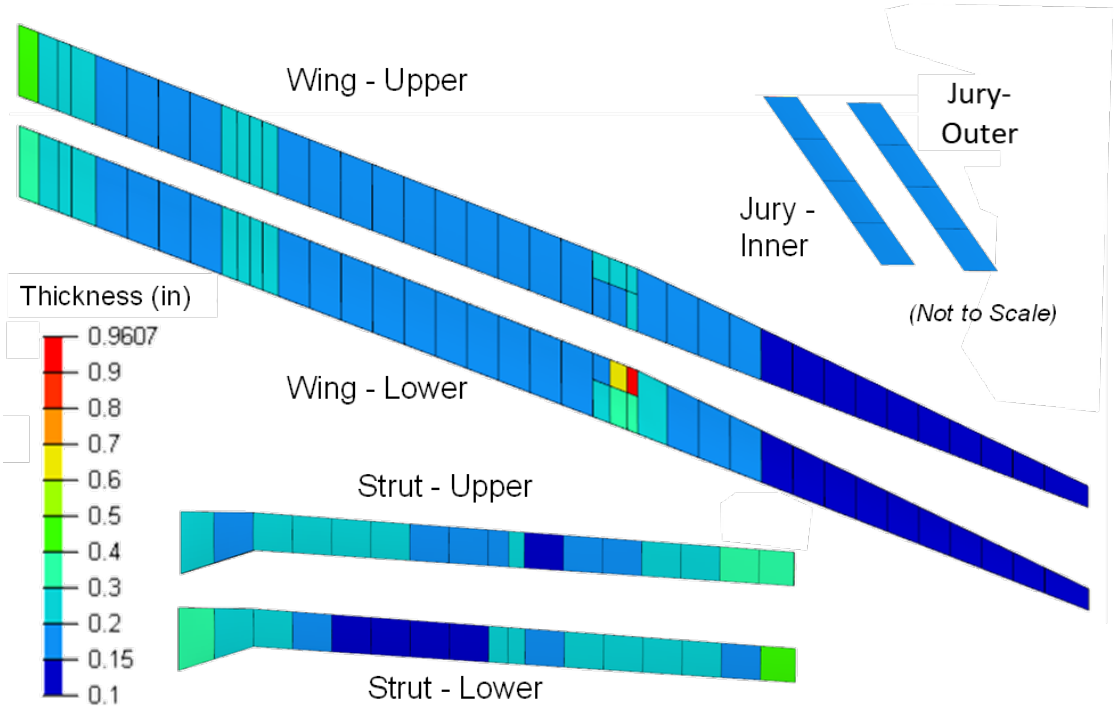


Figure 47 – Skin Thickness in Initial Optimized Structure.

An additional optimization run with different parameters indicated potential to reduce the weight of the structure, but more investigation is needed to understand if the solution is reasonable. In general, there is no way to guarantee a global minimum from the optimization process, and trying various optimization parameters (step sizes, convergence criteria, etc.), different starting designs, and different optimization sequences (such as sizing only the wing or strut before sizing the entire structure), can lead to different converged solutions. It is only after exploration of the design space that it becomes clear whether a particular design is among the best. Such exploration has not been done as of this writing.

A sizing optimization was attempted with all 30 critical load conditions from the maneuver loads survey, and it ran into cycle time and storage space issues. It is likely that optimizing for this many load conditions will need to be done a few conditions at a time.

The structural sizing from the initial optimization was used in the flutter assessment and gust loads analysis that are discussed next.

3.2.12 Initial Flutter Analysis

Flutter analysis was initially performed with the FEM wing, strut, and jury sized for the initial set of critical maneuver loads. The first step was a modal analysis (without aerodynamic effects). Modal analysis results for Mass Case 4 are given in Table 13. Because the TTBW configuration enables higher wing aspect ratio, the wing structural mode frequencies are low in general, and bending modes in both the normal and in-plane directions result. Among the list of flexible modes are several that are closely spaced in frequency, indicating a potential for the modes to coalesce under unsteady aerodynamic loading.

The six flight conditions selected for flutter analysis are shown on the flight envelope in Figure 48. At each condition, all five mass cases from Table 11 were evaluated for aeroelastic stability. The flutter analysis was performed using the Nastran Solution 145 p-k flutter method.

The results of the flutter analysis are summarized in Table 14. The reported flutter margins are based on modal damping of g=0.02, which is conservative based on decades of ground vibration test experience. At all flight conditions, and for all mass cases, adequate stability margins are predicted. Although the flight test required margin is 15 percent, at this early stage in the development and analysis of a new vehicle configuration, a margin of 25-30 percent is more appropriate.

The results of flutter analyses performed at the lower (below 0.92) Mach numbers are similar in the appearance of three critical flutter mechanisms, at roughly 3, 5, and 7 Hz. The 5 Hz mechanism is critical for mass configurations 1, 2, and 3. The 3 Hz mechanism is critical for mass configuration 5 and has slightly higher margins. The 7 Hz mechanism is critical for mass configuration 4 with yet higher margins. The results at 0.92 Mach are somewhat different, however. The 5 Hz mechanism is still critical for mass configurations 1, 2, and 3, but the 3 Hz mechanism is now critical for mass configurations 4 and 5, with configuration 4 now producing the lowest margins.

Table 13 – Modal Analysis Results – Mass Case 4.

Mode	Freq (Hz)	Shape
7	1.45	Wing 1st Bending - Symmetric
8	1.55	Wing 1st Bending - Antisymmetric
9	2.21	Wing 2nd Bending, 1st Bending In-Plane, Fuselage Pitch
10	2.50	Wing 2nd Bending, Fuselage Yaw
11	2.63	Wing 2nd Bending, 1st Bending In-Plane – Symmetric
12	2.81	Wing 2nd Bending, 1st Bending In-Plane, & Torsion, Fuselage Yaw
13	2.91	Wing 2nd Bending, 1st Bending In-Plane, Fuselage Yaw
14	3.20	Wing Torsion, 2nd Bending, Engine Pitch, Fuselage Pitch
15	4.18	Wing 2nd Bending - Antisymmetric
16	4.21	Wing 3rd Bending - Symmetric
17	5.55	Wing 4th Bending, 2nd Bending In-Plane - Symmetric
18	6.88	Wing 3rd Bending, 2nd Bending In-Plane - Antisymmetric
19	7.96	Wing 3rd Bending, 2nd Bending In-Plane, & Torsion - Antisymmetric
20	9.08	Wing 4th Bending, 2nd Bending In-Plane, Strut 2nd Bending - Symmetric

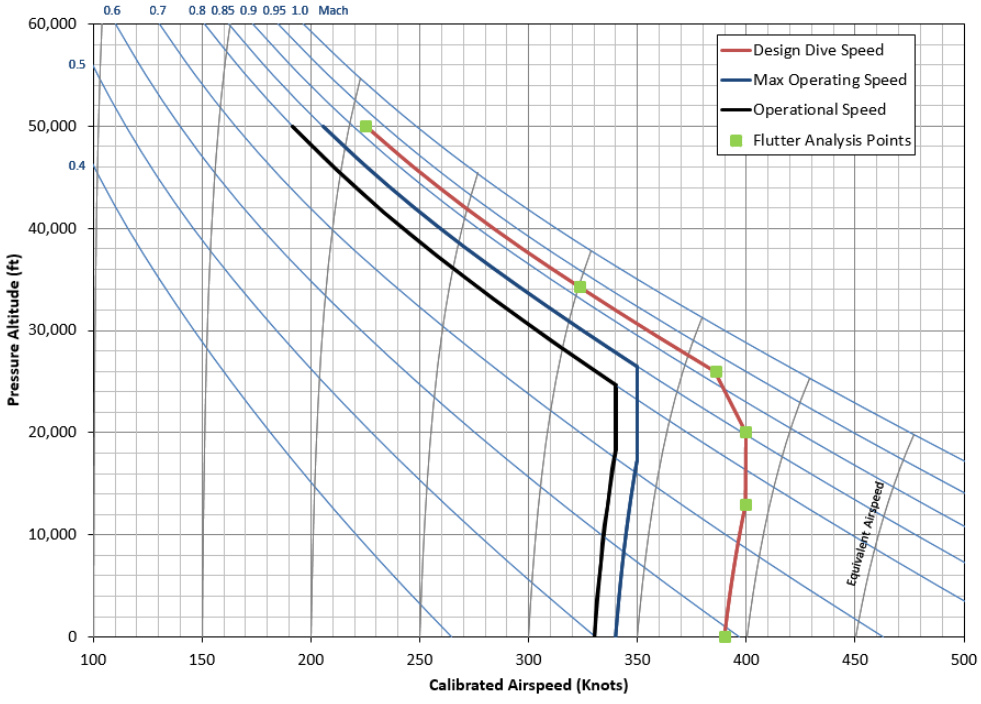


Figure 48 – Airspeed and Altitude Points for Flutter Analysis.

Table 14 – Initial Flutter Analysis Results.

Mach	Altitude (feet)	Mass Case	Frequency (Hz)	Airspeed (KCAS)	Margin (%)
0.92	50000	1	4.51	1142.6	116.4
0.92	50000	2	4.52	1143.8	116.6
0.92	50000	3	4.96	1149.0	117.6
0.92	50000	4	2.74	1071.2	102.9
0.92	50000	5	3.08	1192.1	125.8
0.92	34000	1	5.07	840.8	57.7
0.92	34000	2	4.65	845.1	58.5
0.92	34000	3	5.09	846.7	58.8
0.92	34000	4	2.76	791.1	48.4
0.92	34000	5	3.06	861.2	61.6
0.92	26000	1	4.68	747.7	35.5
0.92	26000	2	4.69	748.3	35.6
0.92	26000	3	4.76	752.9	36.4
0.92	26000	4	2.78	728.2	31.9
0.92	26000	5	3.05	764.7	38.6
0.85	20000	1	5.22	717.8	37.4
0.85	20000	2	4.85	722.4	38.3
0.85	20000	3	5.25	723.5	38.5
0.85	20000	4	6.26	754.6	44.4
0.85	20000	5	3.11	742.9	42.2
0.75	12923	1	5.34	671.0	41.6
0.75	12923	2	5.35	688.4	45.3
0.75	12923	3	5.36	676.2	42.7
0.75	12923	4	6.63	732.8	54.6
0.75	12923	5	3.13	702.9	48.3
0.59	0	1	5.51	596.0	52.6
0.59	0	2	5.51	612.7	56.9
0.59	0	3	5.53	601.5	54.0
0.59	0	4	6.95	641.5	64.3
0.59	0	5	3.14	619.3	58.6

Detailed flutter analysis results for the lowest margin case are given in Figure 49, where the variation of damping and frequency versus airspeed is given for each of the airframe vibration modes included in the analysis. The frequency and airspeed stability margin are noted for the five most critical flutter mechanisms. The most critical mechanism becomes slightly unstable and then regains stability at higher airspeed while the next four mechanisms are each more violently unstable.

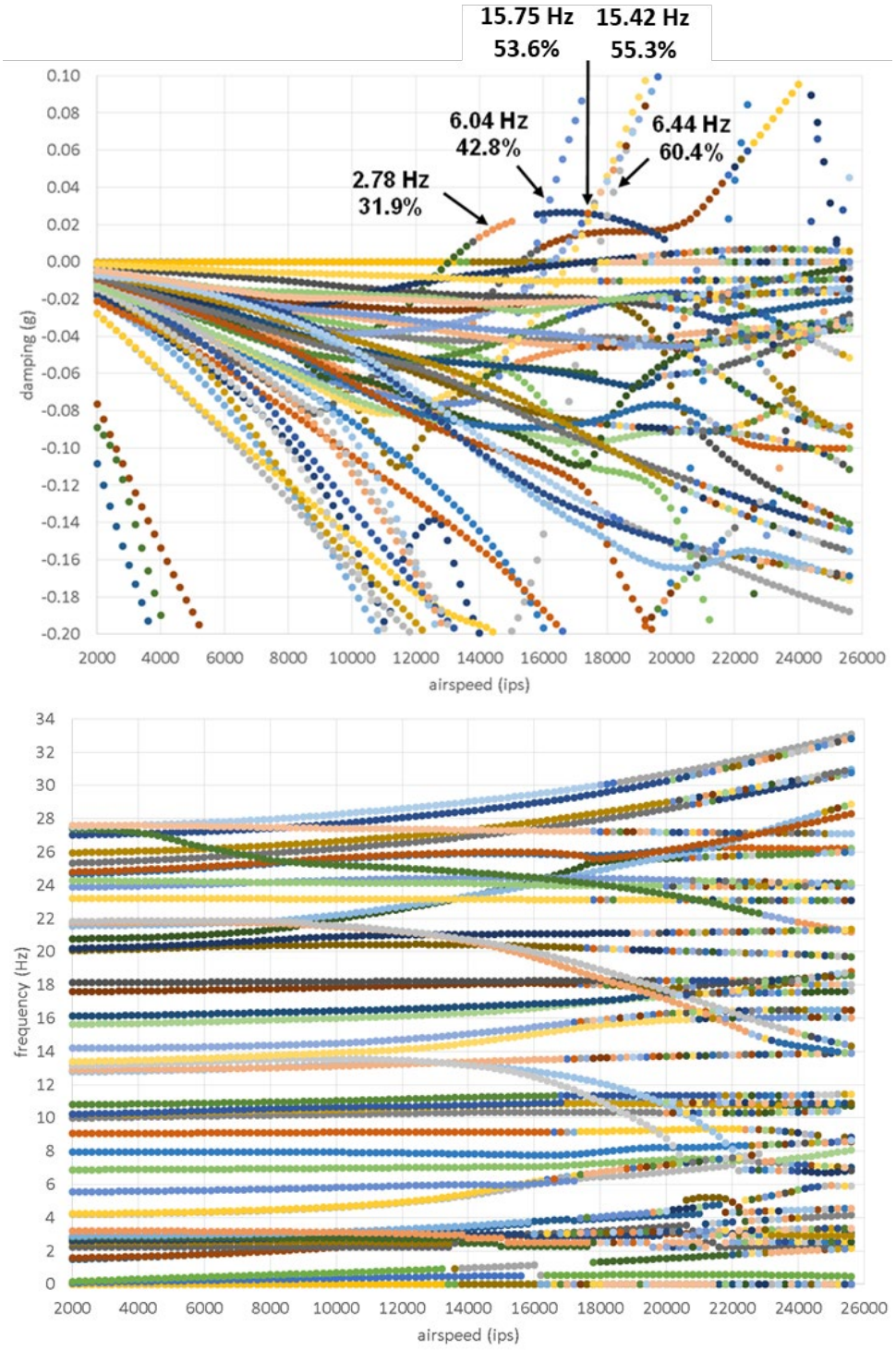


Figure 49 – Damping and Frequency Plots for Flutter Analysis at Mach 0.92, 26,000 feet, Mass Case 4.

Eigenvector analysis was performed on the critical mechanism to identify the constituent modes, and the results are given in Figure 50. Notable is the strong contribution of the rigid-body yaw mode (mode 5) and of multiple elastic modes (modes 7-13), which are both symmetric and antisymmetric, and yield a more complex flutter mechanism than the classical 2-mode bending-

torsion coupling. Mass and stiffness asymmetry built into the airframe FEM results in this case, in airframe vibration modes, which are not purely symmetric or antisymmetric, and thus an asymmetric flutter mechanism, a snapshot of which is given in Figure 51. The rigid-body motion of the fuselage is evident, and the motion of the right wing traces an ellipse as it moves both vertically and longitudinally.

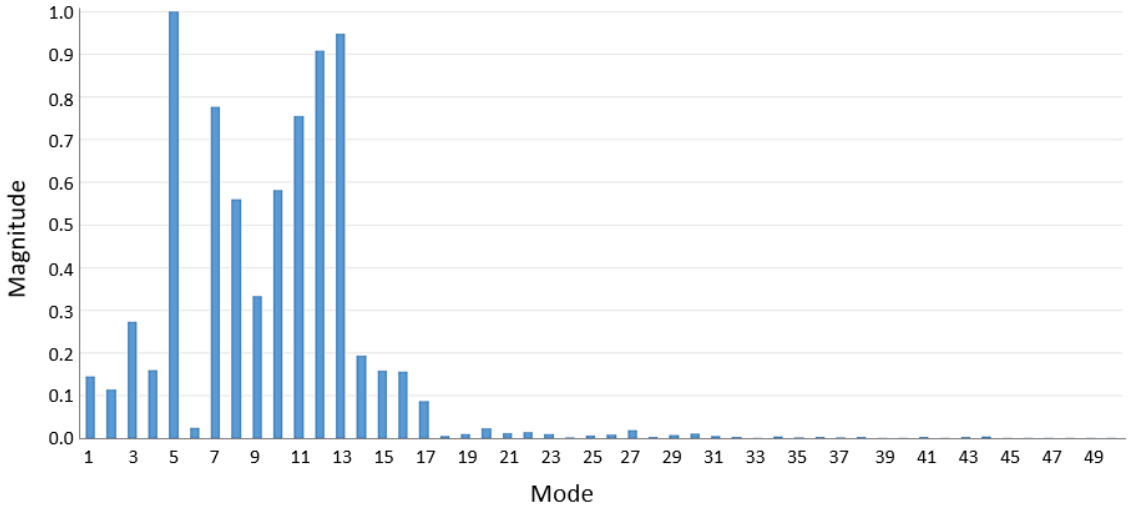


Figure 50 – Critical Flutter Mechanism Eigenvector Analysis at Mach 0.92, 26,000 feet, Mass Case 4.

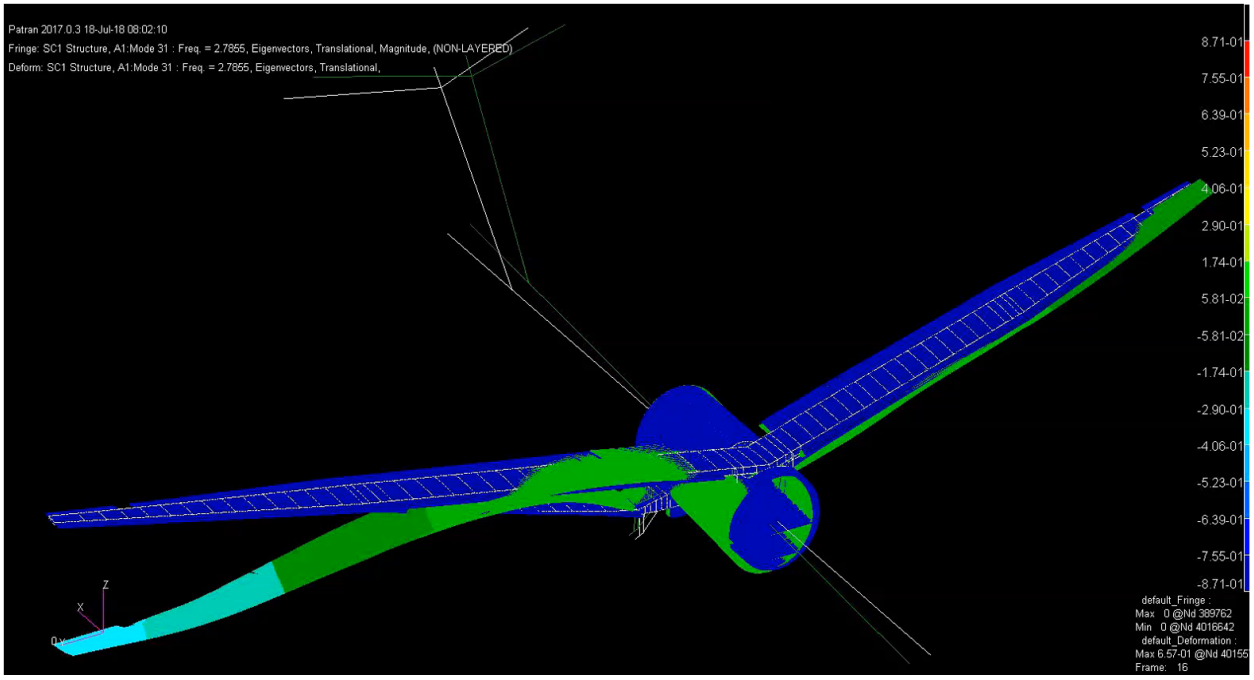


Figure 51 – Critical Flutter Mechanism at Mach 0.92, 26,000 feet, Mass Case 4.

These initial flutter analysis results suggested structural sizing for maneuver loads could also satisfy aeroelastic stability requirements, and this question was revisited as more comprehensive

and higher fidelity analyses were performed, the results of which are presented later in this report.

3.2.13 Gust Loads Analysis

A thorough investigation of gust loads was desired, as they are more likely significant on high aspect ratio wings, and had not been checked since the Phase II study, in which they were not found to be critical. Gust loads analysis began with the wing, strut, and jury sized for the initial set of critical 2.5g and -1g balanced maneuver conditions.

Gust loading is evaluated at critical conditions to capture the maximum vehicle response over the design flight envelope through tuned discrete gust (TDG) analysis in line with requirements of FAR 25.341. Analysis takes into account unsteady aerodynamic effects and all significant structural degrees of freedom contributing to the component loads of interest. Vertical gust loading is considered and the aircraft is assumed to encounter gusts of the shape defined by the following equation:

$$U = \frac{U_{ds}}{2}\left[1 - Cos\left(\frac{\pi s}{H}\right)\right] \quad (1)$$

$$for\ 0 \leq s\ \leq 2H$$

where: s = gust penetration distance in feet
U_{ds} = positive or negative design gust velocity in feet/second equivalent airspeed
H = the gust gradient, which is the distance in feet parallel to the airplane's flight path for the gust to reach its peak velocity

The critical dynamic response for each component load monitored is determined by evaluating gust gradient distances from 30 feet to 350 feet. This is done to ensure the gust wavelength producing maximum dynamic load is captured. Based on prior experience, 11 gradient lengths of 30, 35, 40, 50, 75, 100, 150, 200, 250, 300, and 350 feet were chosen to fully encompass potential vehicle response. Typical gust shapes are shown in Figure 52.

The design gust velocities are defined by the expression:

$$U_{ds} = U_{ref} F_g (H/350)^{1/6} \quad (2)$$

where: U_{ref} = the reference gust velocity in equivalent airspeed
F_g = the flight profile alleviation factor

Additionally, U_{ref} for positive and negative gusts is typically interpolated linearly from Table 15, which shows reference gust velocities for level flight maximum speed (V_H) and limit speed (V_L). At V_L, the gust velocities are reduced by half compared to their values at V_H. Whether critical gust loads are produced at V_H or V_L depends on the relative positions of V_H and V_L on the flight

envelope of the aircraft. For the TTBW aircraft, the operational speed is taken as V_H and the max operational speed as V_L. As these lines are relatively close together, V_H has been selected for the critical gust conditions. The reduced gust velocities at V_L, at which dynamic pressures would increase only about five percent, are unlikely to produce larger dynamic response than analysis along the operational envelope at an unscaled reference gust velocity. This approach has been verified on previous programs with similar flight envelopes.

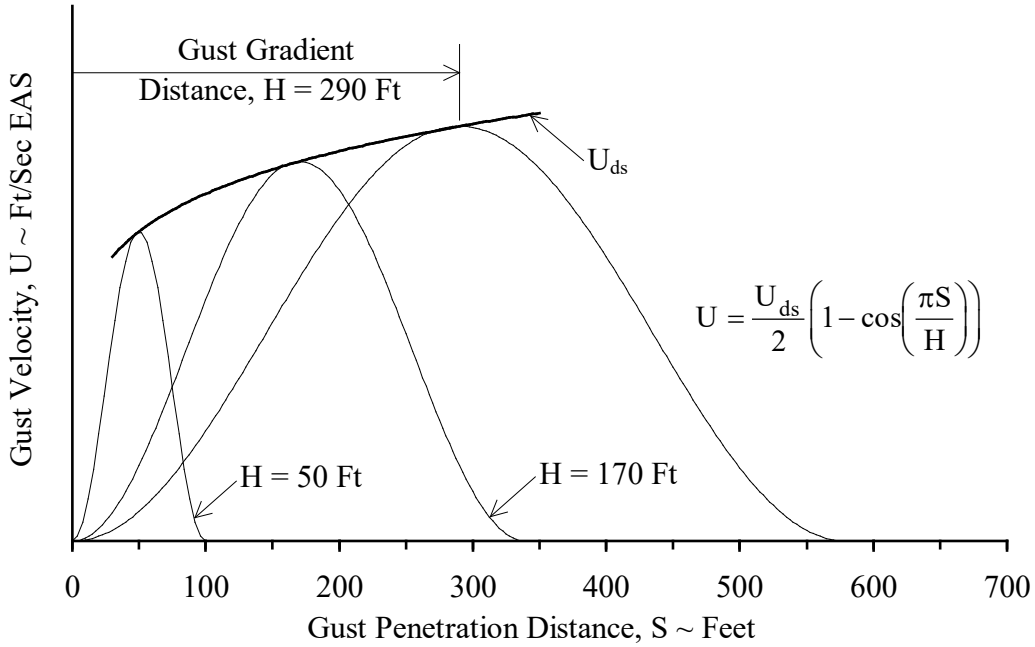


Figure 52 – Typical Gust Shapes.

Table 15 – Tuned Discrete Gust Reference Velocity as a Function of Altitude.

Altitude (ft)	U_{ref} (feet/second equivalent airspeed)	
	V_H	V_L
0	56.0	28.0
15,000	44.0	22.0
50,000	26.0	13.0

The flight profile alleviation factor, F_g, varies linearly from the value at sea level to a value of 1.0 at the maximum operating altitude of 50,000 feet. The sea level value of F_g is determined by the following equation:

$$F_g = \frac{1}{2}\left(F_{gx} + F_{gm}\right) \tag{3}$$

where:

$$F_{gx} = 1 - \frac{Z_{m0}}{250000};\ F_{gm} = \sqrt{R_2 Tan\left(\frac{\pi R_1}{4}\right)} \tag{4}$$

$$R_1 = \frac{Maximum\ Landing\ Weight}{Maximum\ Takeoff\ Weight} \tag{5}$$

$$R_2 = \frac{Maximum\ Zero\ Fuel\ Weight}{Maximum\ Takeoff\ Weight} \tag{6}$$

For the TTBW aircraft: Z_{mo} = Maximum operating altitude = 50,000 feet
Maximum Landing Weight = 145,000 lb
Maximum Takeoff Weight = 145,000 lb
Maximum Zero-Fuel Weight = 115,972 lb

Two weight configurations were selected for analysis to cover the effects of both wing loading and inertia relief: maximum payload with fuel to reach MTOW (Mass Case 1 from Table 11) and maximum payload with reserve fuel (Mass Case 4). Also, six points in the sky (PITS), were selected for evaluation, as shown in Figure 53.

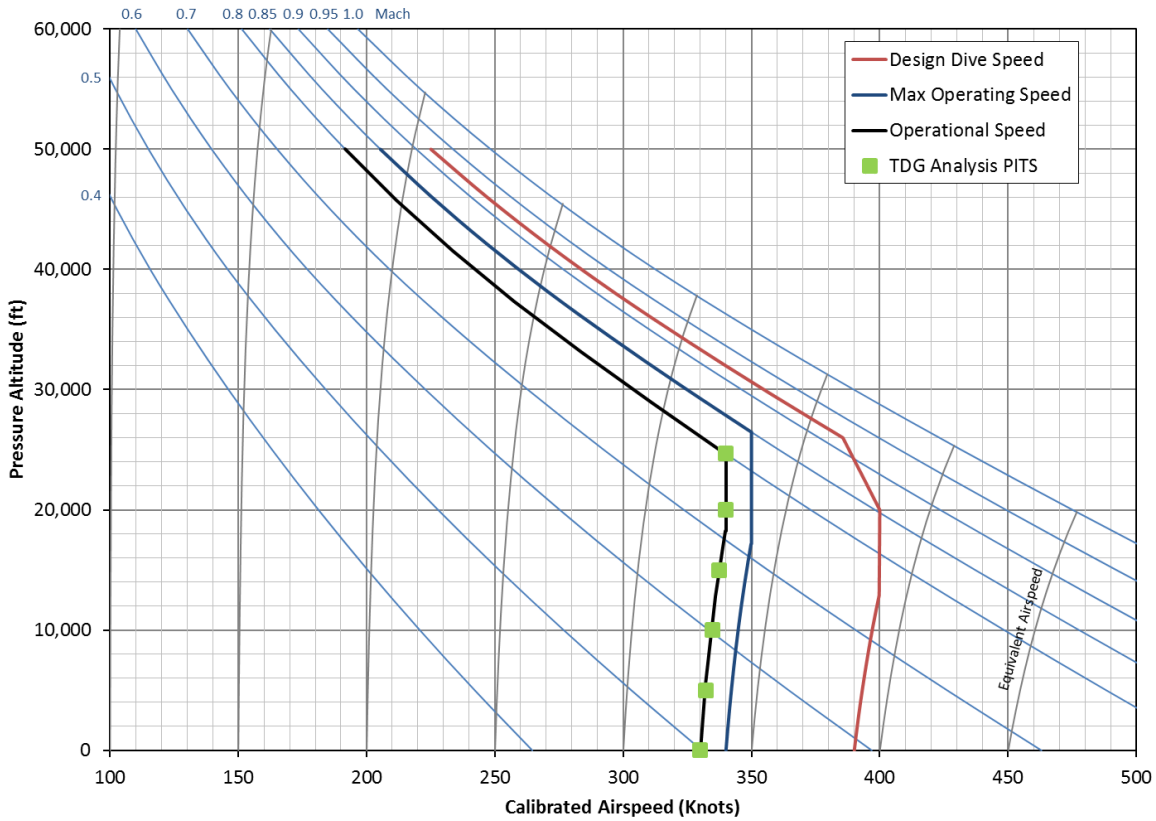


Figure 53 – Tuned Discrete Gust Analysis Points in the Sky.

Transient aeroelastic gust response analysis was performed in MSC Nastran and loading was tracked along the wing and strut at reference stations through monitored load sets (Nastran

MONPNT entries). Both positive and negative gust conditions were considered and superimposed with static loading corresponding to trimmed level flight. Component loads at each time point from these analyses were surveyed and considered for use in structural sizing.

The millions of potential load conditions associated with individual time points of the tuned discrete gust loads analyses were first filtered according to whether they produced a minimum or maximum component load. These results were then combined with critical maneuver load conditions and a combinatorial optimization problem was solved to identify the N conditions that would most closely approach the minimum and maximum component loads at all reference stations along the wing and strut, as shown in Figure 54. Nine gust conditions (all at sea level, four at Mass Case 1, and five at Mass Case 4) and two maneuver conditions were selected for use in structural sizing. For the gust conditions, balanced FEM load distributions were generated using inertia loads from modal accelerations associated with the critical gust response time point.

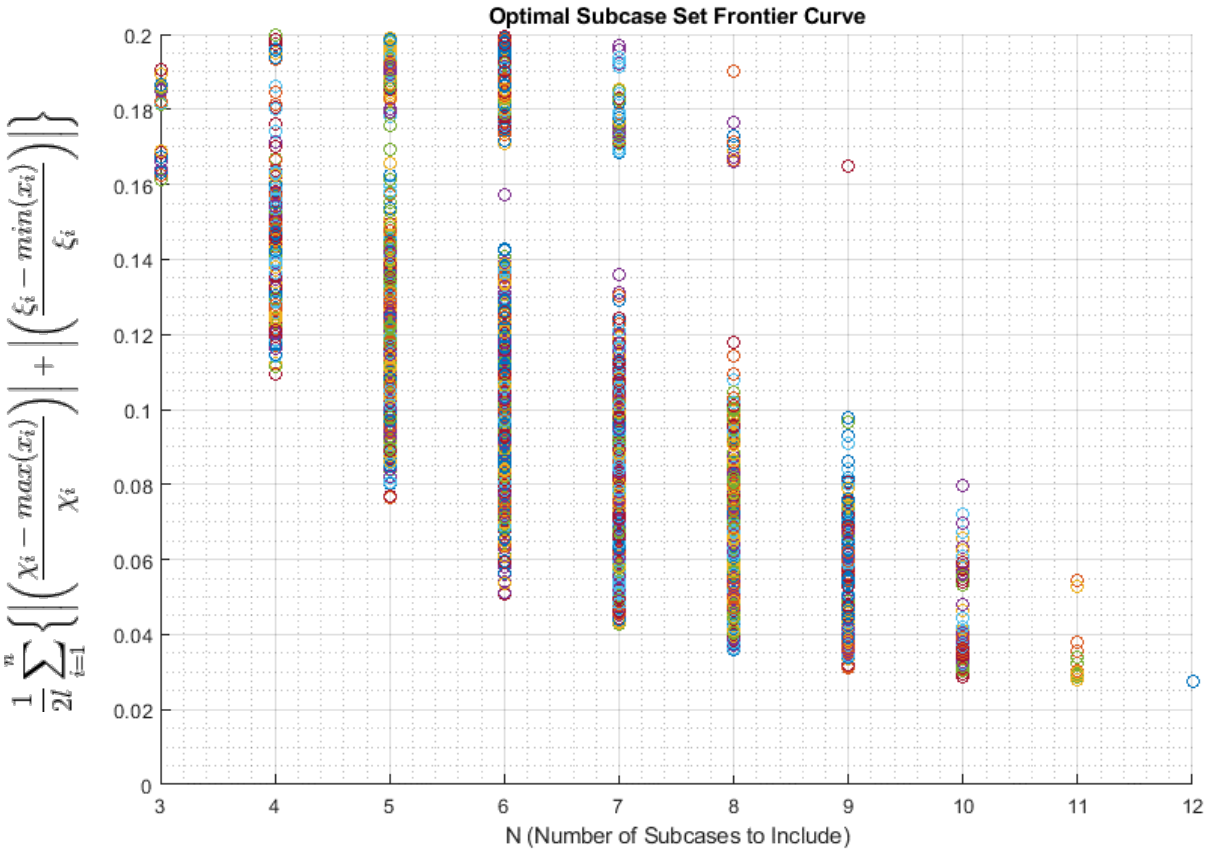


Figure 54 – Design Load Case Selection.

A skyline comparison of critical maneuver and gust loads is given in Figure 55. While the maneuver shear and bending loads are higher over portions of the outer wing, the gust loads are

dominant over most of the inboard wing. Overall, gust loads are more severe, and this is why more of the selected sizing conditions came from the gust loads analyses.

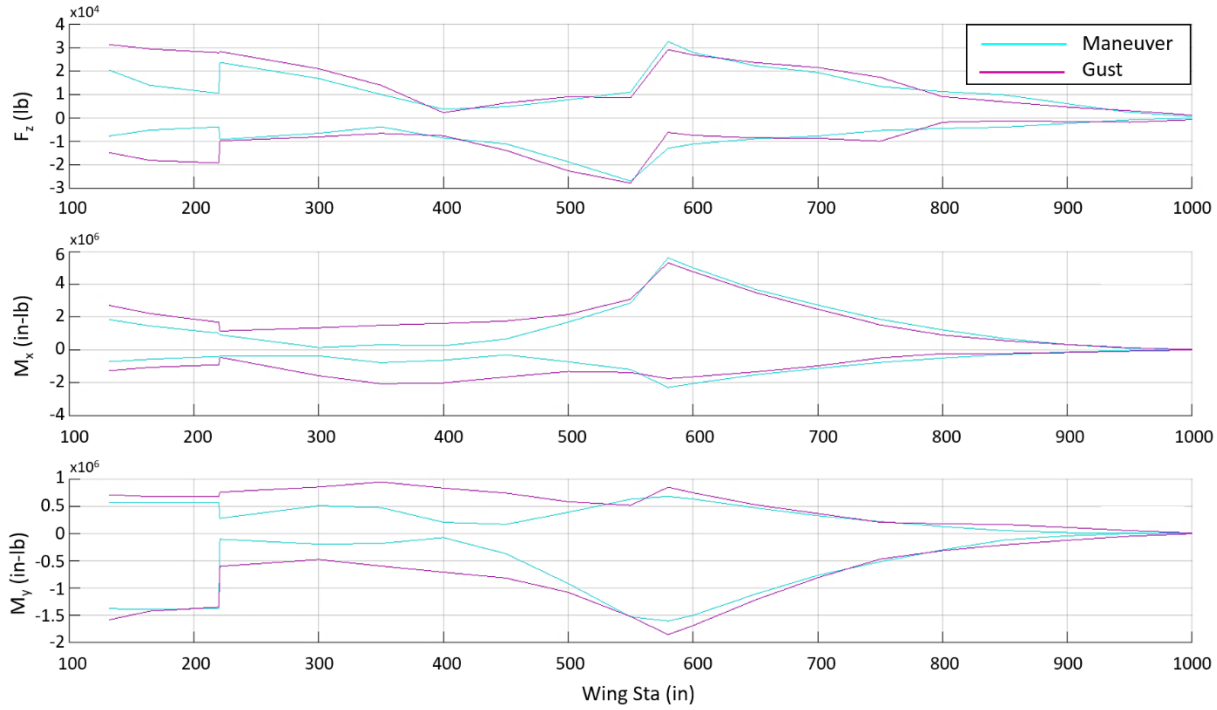


Figure 55 – Design Flight Loads Comparison.

3.2.14 Structural Sizing Optimization

The gust loads analysis resulted in a new set of critical load conditions for structural optimization, consisting of nine gust cases and two maneuver cases. The two maneuver cases were a pair of 2.5g and -1g maneuvers for Mass Case 2, full fuel with payload to reach MTOW. This pair was previously used in the preliminary structural optimization, along with another pair for Mass Case 5. Instead of the other pair of maneuver cases, the new set of critical loads included the nine gust cases. Forces from the Nastran aeroelastic loads analyses were extracted and applied as static loads for optimization with Nastran Solution 200. For optimization, both the gust loads and the maneuver loads were scaled by a factor of 1.5 to represent ultimate load conditions. As before, the wing, strut, and jury structure was optimized to minimize weight and meet strength and buckling constraints.

During the preliminary round of optimization, a set of optimization parameters was found that resulted in a lighter weight design. This set of parameters was used for the new optimization runs. With the number of load conditions for the optimization increased from four to 11, the run time increased from less than two hours per design cycle to nearly eight hours per cycle. Fortunately, the runs converged in six to eight cycles, and feasible designs were obtained. Runs

that started from different initial designs converged to optimum designs having weights within 100 pounds of each other, or less than one percent apart. This result gave confidence that the optimization was working properly.

Table 16 compares the structural weight breakdown from the initial optimization for maneuver loads only (see Table 12), to the updated optimization for maneuver and gust loads. The fact that the total wing weight decreased from 8,386 to 8,300 pounds, despite the addition of gust loads that were critical for the inboard wing, is probably due to the improved parameters providing better optimizer performance. It is noticeable that the wing skins got heavier and the strut got lighter with the new set of critical loads, which is consistent with the added gust loads being critical for the inboard wing.

Table 16 – Structural Weights Sized for Strength and Buckling at Critical Gust and Maneuver Loads.

			Mach 0.80	
			Phase IV*	
			Maneuver	Maneuver and Gust
Wing			5812	5917
	Skins		3662	3854
	Spars		767	702
		Webs	761	696
		Caps	6	6
	Ribs		466	473
		Webs	460	466
		Caps	6	6
	Leading Edge		916	889
Strut			2514	2323
	Skins		1108	959
	Spars		110	108
	Ribs		101	93
	Edges		868	837
	Splitter		327	327
Jury			61	60
	Skins		38	37
	Spars		2	2
	Ribs		1	1
	Edges		20	20
TOTAL (lbs)			**8386**	**8300**

** Sizing results from 6/14/2018 and 8/28/2018 should be considered preliminary.*

The distribution of material in the optimized structure is illustrated by a plot of skin thickness in Figure 56, which is comparable to Figure 47. The distribution from the new optimization closely resembles the previous one. Some increases in thickness are noticeable on the lower wing skin

where the engine and strut are attached. In other areas, the weight gain of the inboard wing skins that was shown in Table 16 probably corresponds to thickness increases that are within the resolution of the scale of the plot, and therefore appear the same in the two figures. The weight reduction in the strut can be observed by comparing the new plot to the previous one.

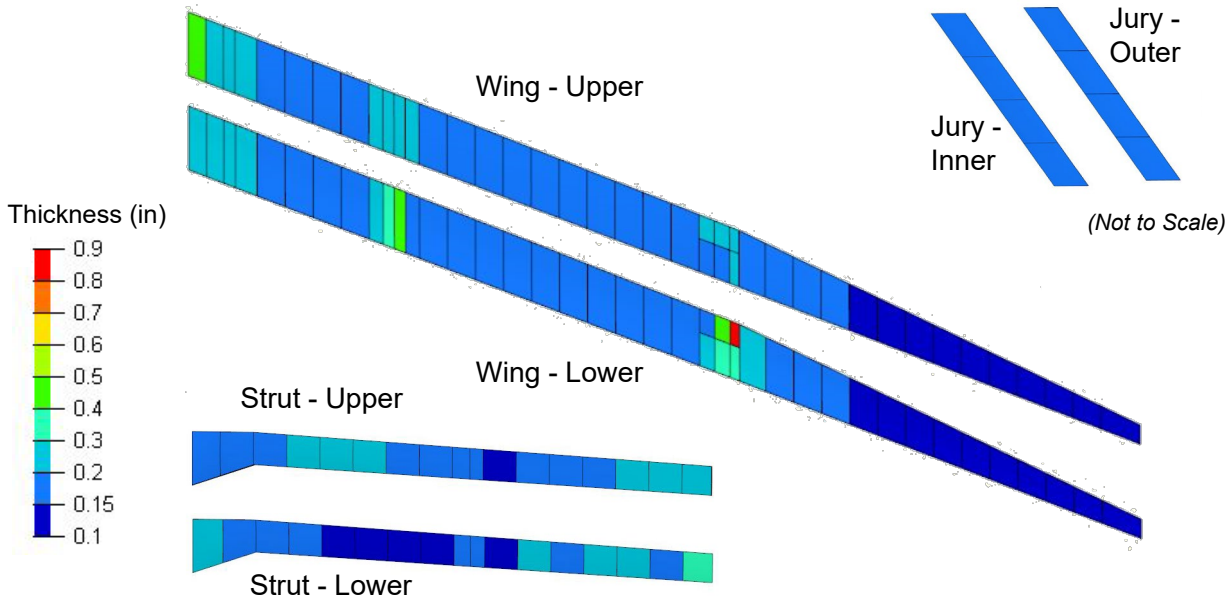


Figure 56 – Skin Thickness in Optimized Structure.

The thickness plot is just an initial indication of material distribution. In future rounds of optimization, the critical constraint for each design zone should be checked as well, to identify the critical load case and failure mode. The running loads at interfaces, such as the wing to strut connection, are also important to check, relative to the load limits of joint designs. Many refinements to the structural definition, load conditions, and optimization process are possible. For the present effort, the purpose was to provide an updated weight for the wing and strut, so further refinements were not pursued.

The structural sizing from the updated optimization was used in subsequent aeroelastic analyses, which are discussed next.

3.2.15 Aerodynamic Adjustments

In order to improve flutter analysis fidelity, aerodynamic adjustments based on CFD analyses were developed and applied to the unsteady aerodynamic wing loads predicted by the doublet lattice model. The improved analysis enabled a more accurate capture of compressibility effects and flow separation that can have a significant effect on overall spanload (defined herein as C_l*c/c_{ref}). This is particularly important in regions of the flight envelope where these factors play an increasingly important role in determining accurate estimates of aerodynamic loads. An outline of the process used is as follows:

1) For a given flight condition, calculate DLM wing loads for unit angle-of-attack (angle of attack)
2) Calculate strip normal force and pitching moment coefficients from DLM wing loads
3) Perform CFD analysis at the same flight condition at two selected values of angle of attack
4) Calculate strip normal force and pitching moment per unit angle of attack coefficients from CFD loads
5) Identify DLM strip load adjustment factors by comparing DLM and CFD results
6) Resolve DLM strip load adjustment factors into DLM box load adjustment factors

An example of the CFD analyses mentioned in Step 3 is shown in Figure 57 and A3. The difference in the solutions from two different angle of attacks is used to estimate the sensitivity of loads to angle of attack variation.

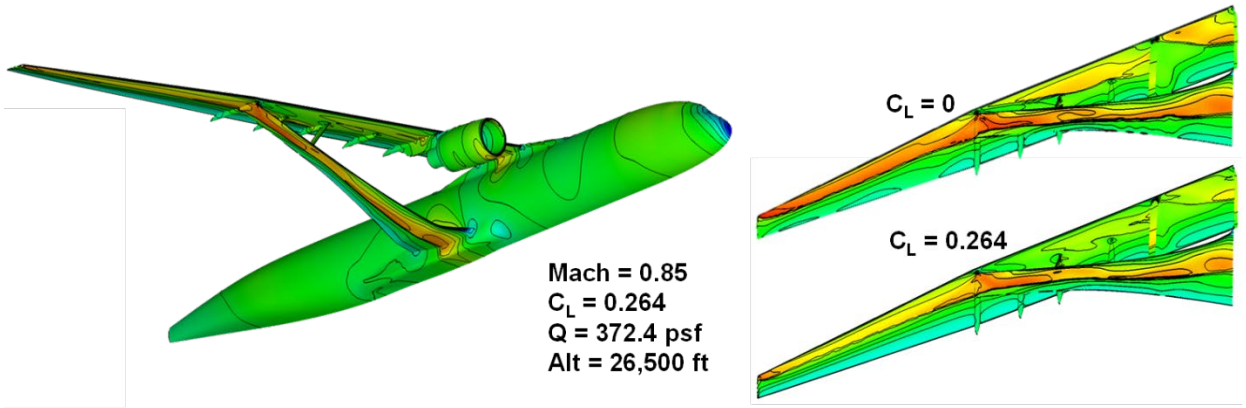


Figure 57 – Aerodynamic Pressures from CFD Analysis (M=0.85, C_L=0.264, Re_{mac} = 25.0M).

A complete list of all CFD analyses performed for development of DLM aero adjustments for loads and dynamics analyses is given in Table 17. Cases 1-12 were generated for loads analysis aero adjustment development, and the angle of attack increment between these pairs of solutions at each flight condition is larger, roughly consistent with the load factor range to be evaluated with the design maneuvers selected. Cases 13-20 were generated for flutter analysis aero adjustment development, and are relevant to the present discussion. Note the angle of attack increment between these solution pairs at each flight condition is smaller, as flutter is essentially a small perturbation problem.

Because the CFD analyses were performed on a multizone overlapping grid resulting in nonunique surface load distributions, some post-processing of the solutions was required. Surface pressures from the Overflow structured overlapping solution were mapped to the unstructured grid shown in Figure 58 and then converted into force vectors for integration into strip load coefficients for comparison with DLM results.

Table 17 – CFD Analysis Conditions.

Case	Mach	Altitude (feet)	Lift (lbs)	Q (psf)	ANGLE OF ATTACK (deg)	C_L	Re	T (Rank)	Pres (psf)
1	0.3779	0	0	211.54	-2.021	0.0000	223601	518.7	2116.2
2	0.3779	0	145,000	211.54	1.434	0.4641	223601	518.7	2116.2
3	0.6000	23,456	0	211.60	-1.990	0.0000	176900	435.0	839.7
4	0.6000	23,456	145,000	211.60	1.077	0.4640	176900	435.0	839.7
5	0.8500	38,628	0	211.59	-1.807	0.0000	144338	390.0	418.4
6	0.8500	38,628	145,000	211.59	0.476	0.4640	144338	390.0	418.4
7	0.5140	0	0	391.36	-2.037	0.0000	304133	518.7	2116.2
8	0.5140	0	145,000	391.36	-0.287	0.2508	304133	518.7	2116.2
9	0.7187	17,420	0	391.34	-1.983	0.0000	256402	456.5	1082.3
10	0.7187	17,420	145,000	391.34	-0.537	0.2509	256402	456.5	1082.3
11	0.8500	26,468	0	372.38	-1.856	0.0000	227101	424.3	736.3
12	0.8500	26,468	145,000	372.38	-0.604	0.2636	227101	424.3	736.3
13	0.5896	0	120,000	514.96	-0.996	0.1578	348868	518.7	2116.2
14	0.5896	0	145,000	514.96	-0.777	0.1906	348868	518.7	2116.2
15	0.7571	13,200	120,000	514.98	-1.128	0.1578	307077	471.6	1283.5
16	0.7571	13,200	145,000	514.98	-0.949	0.1906	307077	471.6	1283.5
17	0.8536	20,000	120,000	496.01	-1.080	0.1638	280996	447.4	972.5
18	0.8536	20,000	145,000	496.01	-0.916	0.1979	280996	447.4	972.5
19	0.9200	26,000	120,000	445.33	0.495	0.1824	249633	426.0	751.6
20	0.9200	26,000	145,000	445.33	0.795	0.2204	249633	426.0	751.6

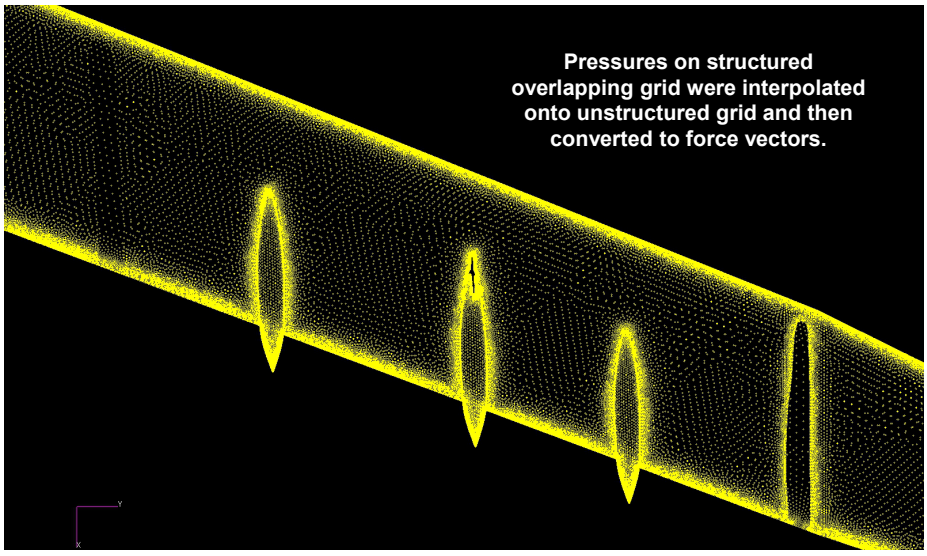


Figure 58 – CFD Results Processing.

DLM aerodynamic adjustment development results are presented herein for two of the four Mach numbers evaluated. The results given for Mach 0.76 are generally representative of those obtained at Mach numbers 0.59 and 0.85, while those given for Mach 0.92 will be shown dissimilar to those at the three other Mach numbers.

Wing pressure contours for the Mach 0.76 flight condition are shown in Figures 59 through 61 and Figures A4 though A6 for DLM and CFD analyses, and the integrated CFD strip load coefficients are given in Figure 62. The aerodynamic interference effect of the strut and the nacelle/pylon are evident in both the strip normal force and pitching moment distributions. In addition, the strip normal force is more sensitive to angle of attack variation than is the strip pitching moment. DLM and CFD strip load coefficients per degree angle of attack are compared in Figure 63. The DLM and CFD strip load distributions are of similar shape, with the CFD results again more clearly showing the aerodynamic interference effects of the strut and nacelle/pylon. The CFD strip normal force per degree angle of attack is greater than that predicted by the DLM, and this result is consistent with similar comparisons made previously on other aircraft programs. The strip pitching moments per degree angle of attack are small, with the DLM results more positive than those from CFD analysis.

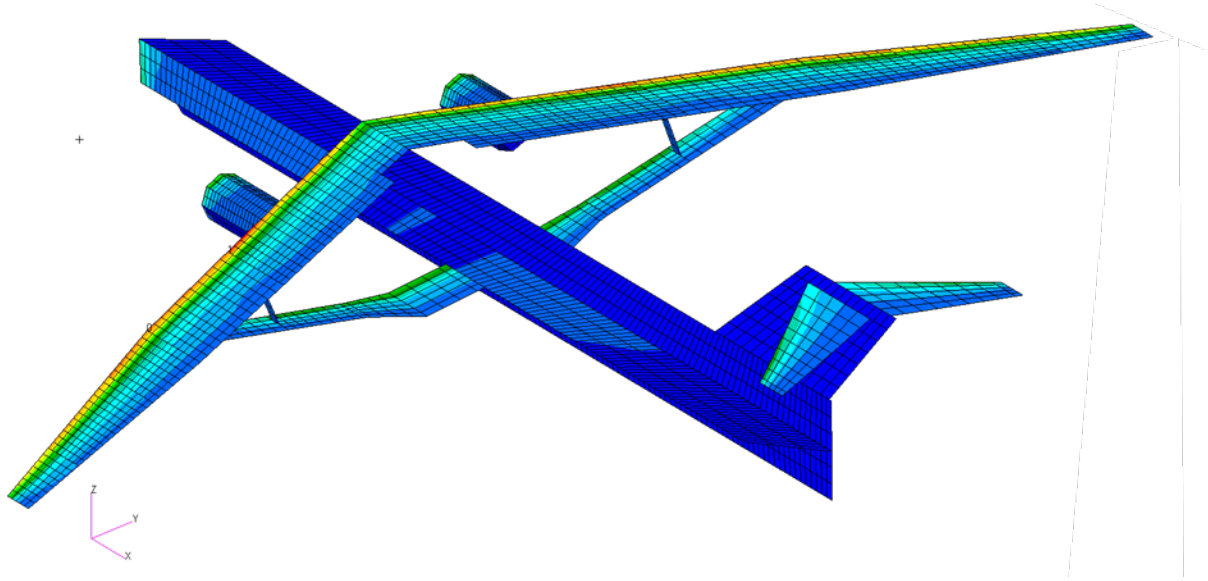


Figure 59 – Rigid Doublet Lattice Model Pressures at Mach 0.7571, 13,200 ft, Angle of Attack -1.128°.

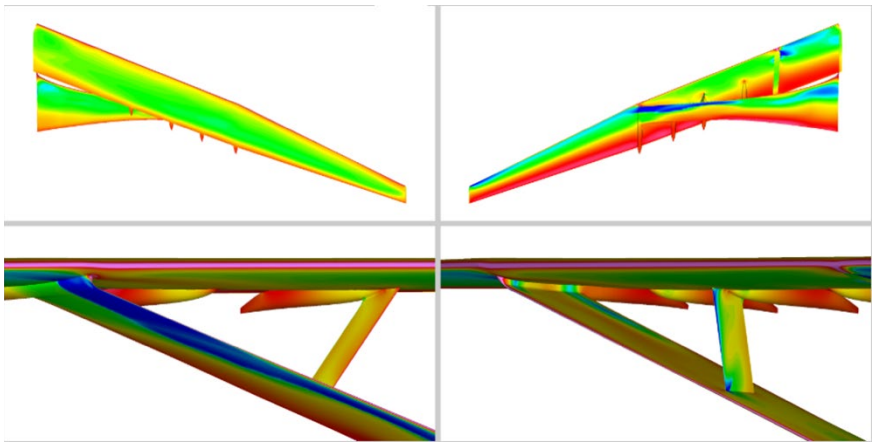


Figure 60 – CFD Solution for Case 15: Mach 0.7571, C_L = 0.158, q = 515.0 psf, Altitude = 13,200 ft, Re_{mac} = 33.9M.

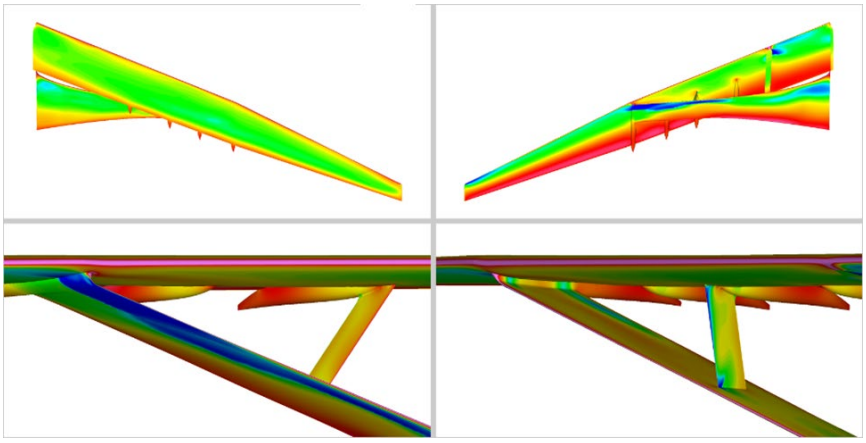


Figure 61 – CFD Solution for Case 16: Mach 0.7571, C_L = 0.191, q = 515.0 psf, Altitude = 13,200 ft, Re_{mac} = 33.9M.

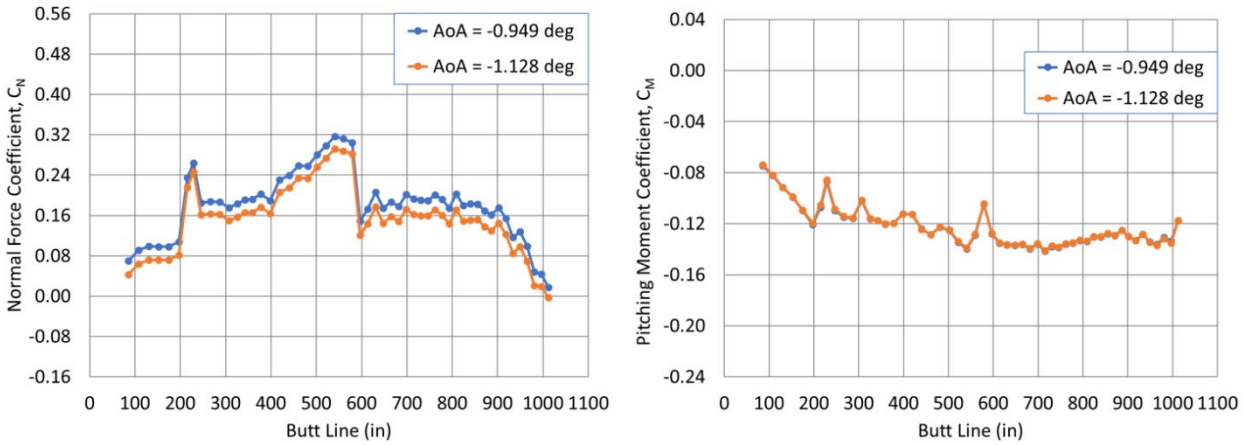


Figure 62 – CFD Strip Force and Moment Coefficients for Different Angles of Attack at Mach 0.7571, Altitude = 13,200 ft, Re_{mac} = 33.9M.

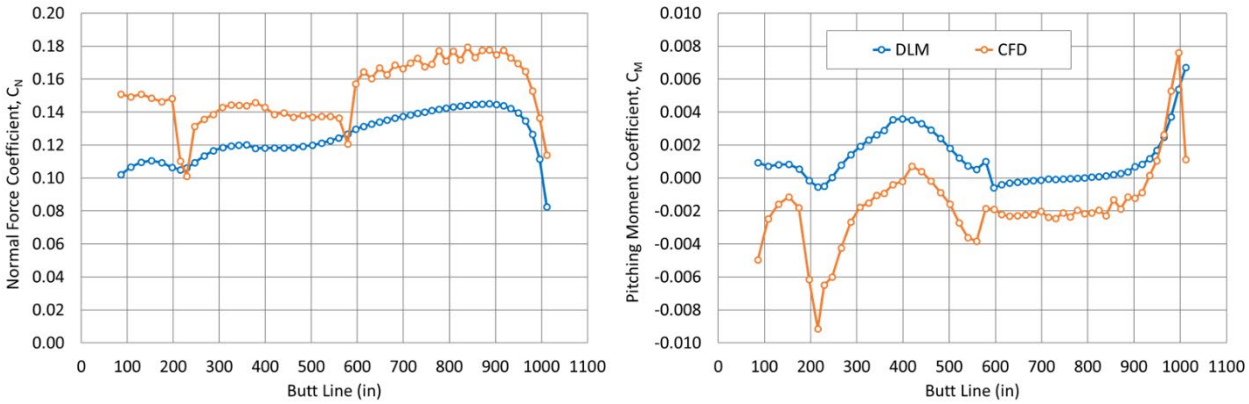


Figure 63 – Aerodynamic Strip Force and Moment Coefficients from DLM and CFD at Mach 0.7571, Altitude 13,200 ft, Re_{mac} = 33.9M.

The analysis results at the Mach 0.92 flight condition are markedly different from those at the three lower Mach numbers. Wing pressure contours are shown in Figures 64 through 66 and Figures A7 through A9 for DLM and CFD analyses. The integrated CFD strip load coefficients are given in Figure 67. Note the DLM pressures vary smoothly and are higher in value than those at Mach 0.76. The CFD pressures at both angle of attack conditions, however, exhibit abrupt changes on both upper and lower surfaces of the outer wing. The aerodynamic interference effect of the strut in particular is more dramatically evident in the strip normal force distribution. Note the wing, outboard of the strut juncture, is generating negative lift at both angle of attack conditions. DLM and CFD strip load coefficients per degree angle of attack are compared in Figure 68. The DLM and CFD strip load distributions clearly are no longer of similar shape. The DLM normal force per degree angle of attack is now larger than that predicted by CFD, and the CFD result drops sharply over the outer wing, where increasing angle of attack actually results in loss of lift in the 845-940 butt line region. The CFD results also predict a sudden increase in pitching moment due to angle of attack over the outer wing.

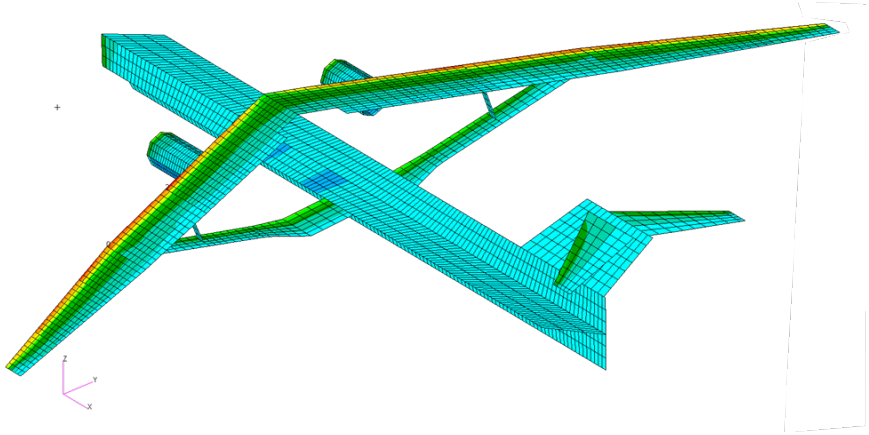


Figure 64 – Rigid Doublet Lattice Model Pressures at Mach 0.92, Altitude = 26,000 ft, α=1°.

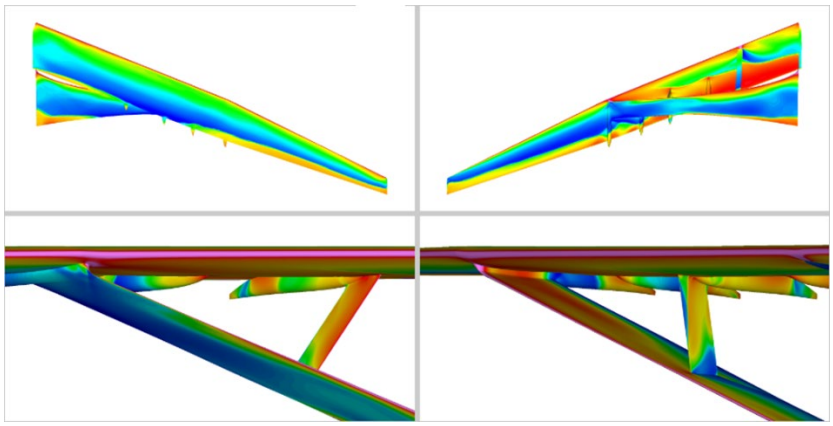


Figure 65 – CFD Solution for Case 19: Mach 0.92, C_L = 0.182, q = 445.3 psf, Altitude = 26,000 ft, Re_{mac} = 27.5M.

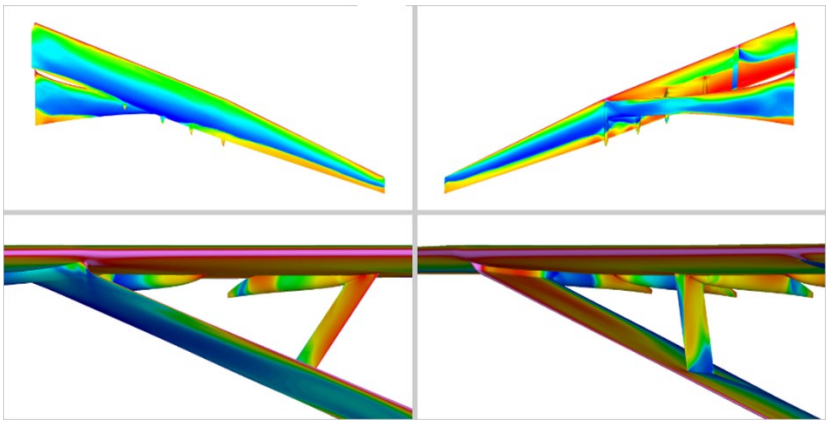


Figure 66 – CFD Solution for Case 20: Mach 0.92, C_L = 0.220, q = 445.3 psf, Altitude = 26,000 ft, Re_{mac} = 27.5M.

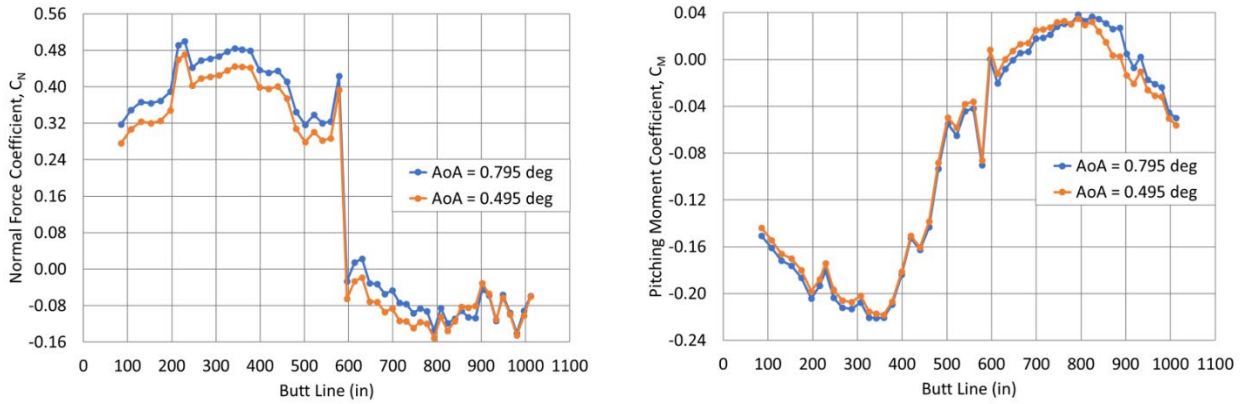


Figure 67 – CFD Strip Force and Moment Coefficients for Different Angles of Attackat Mach 0.92, Re_{mac} = 27.5M.

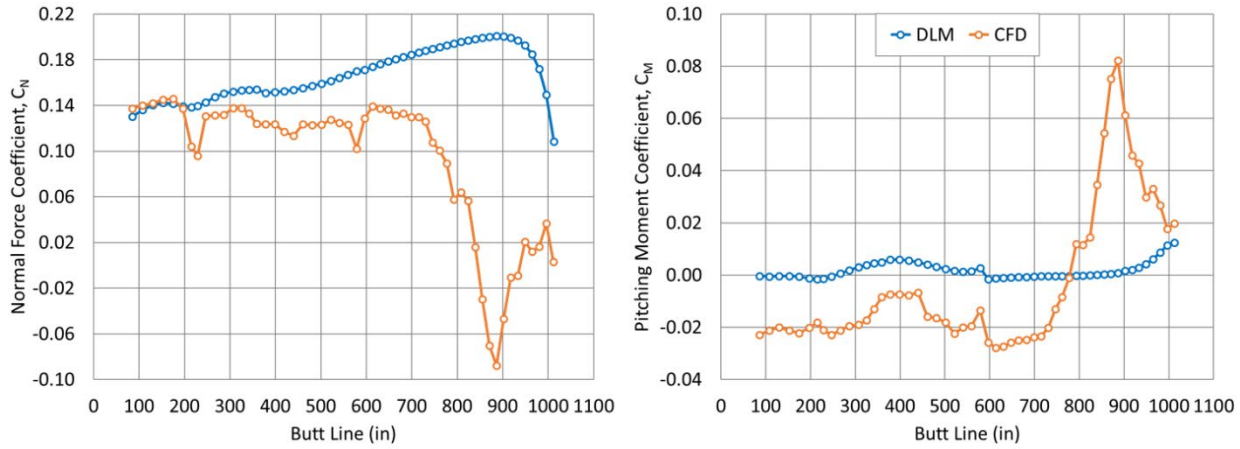


Figure 68 – Aerodynamic Strip Force and Moment Coefficients from DLM and CFD at Mach 0.92 , Re_{mac} = 27.5M.

CFD section cut pressures are shown in Figure 69 and appendix Figure A.10 for both the Mach 0.76 and 0.92 flight conditions at equivalent lift. The sharp pressure drops at roughly 75% chord on both upper and lower surfaces of the outboard wing at the higher Mach number flight condition are indicative of shock formation. The difference between the pressure distributions at the two Mach 0.92 angle of attack conditions as shown in Figure 70 and appendix Figure A.11 suggest the outer wing strip loads due to angle of attack are heavily driven by shock motion. Looking at the butt line 886 section cut pressure distributions of Figure 71 and appendix Figure A.12, we see the upper surface shock moves forward and the lower surface shock moves aft as angle of attack increases. The net effect of this shock motion is to increase lift somewhat over the forward 62% of the airfoil and to decrease lift much more over the aft 38%. This is the physical mechanism by which an angle of attack increase results in both lift loss and pitching moment gain for the outer wing at the Mach 0.92 flight condition. Due to the strong nonlinear flow features present at Mach 0.92, the DLM aerodynamic adjustment methodology employed here is not capable of improving analysis fidelity at this flight condition. This consideration will be discussed further in the next section.

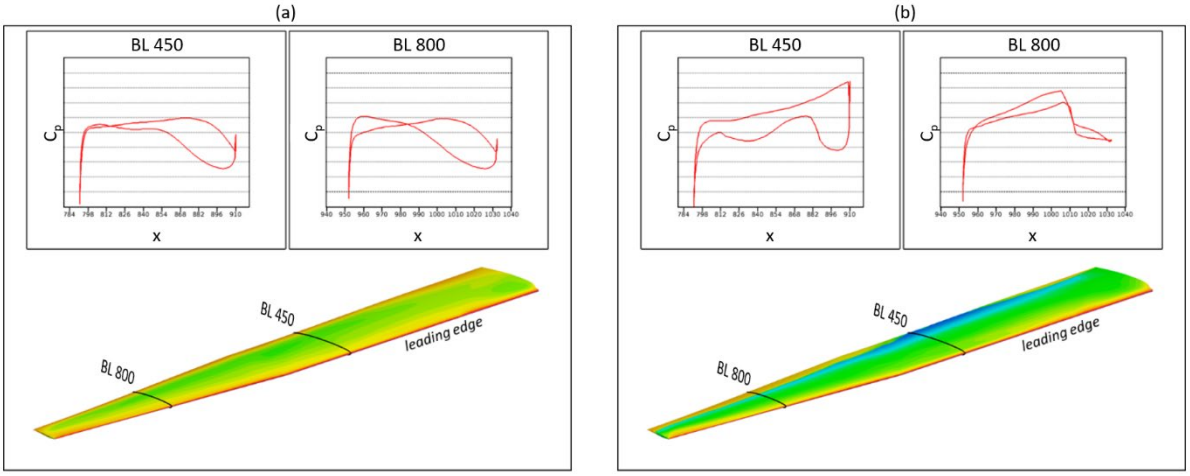


Figure 69 – Section Pressure Distributions (a) Case 16: Mach = 0.757, C_L = 0.191, Re_{mac} = 33.9M (b) Case 20: Mach = 0.92, C_L = 0.2204, Re_{mac} = 27.5M.

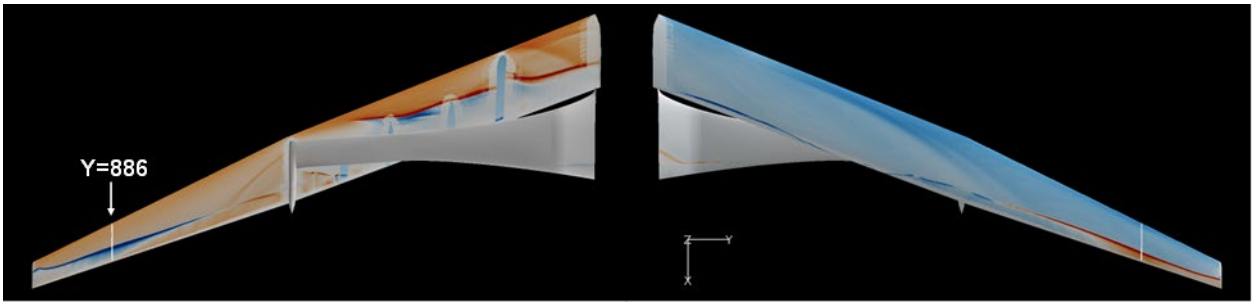


Figure 70 – Delta Pressure Distributions between α 0.795° and 0.495° at Mach = 0.92, Re_{mac} = 27.5M.

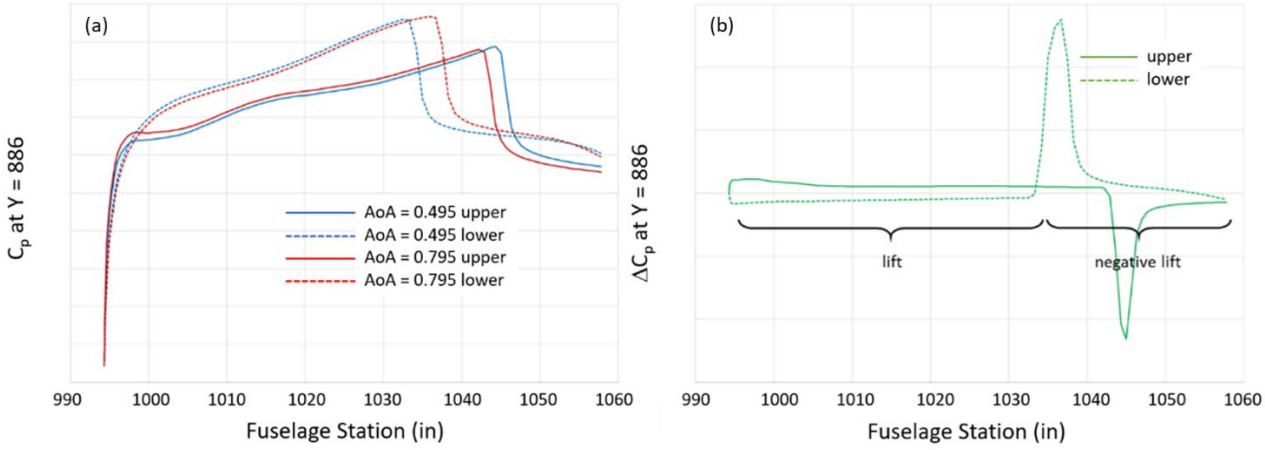


Figure 71 – Delta Pressure Distributions between α 0.795° and 0.495° at Station 886 at Mach 0.92, Re_{mac} = 27.5M.

As outlined at the beginning of this section, the last step in the aerodynamic adjustment process is to resolve DLM strip load adjustment factors into DLM box load adjustment factors. This is done to modify raw DLM predictions to match CFD results for strip normal force and pitching moment per unit angle of attack. Since there are typically more than two DLM boxes per strip, this is mathematically an underspecified problem, and the mimimum-norm least-squares solution is employed. Results are given for two strips at the Mach 0.76 flight condition in Figure 72. Note the box load adjustment factors are reasonable in both magnitude and distribution shape, and result in reasonable modification to the raw DLM pressure prediction. Results are given for the same two strips at the Mach 0.92 flight condition in Figure 73. The box load adjustment factors are no longer reasonable, with some actually being negative, and the resulting modification to the raw DLM pressure predictions is highly suspect. To resolve this discrepancy, future analysis should examine the use of unsteady RANS codes as a means for resolving the effects of unsteady shock-induced separation and its ssociated unsteadiness.

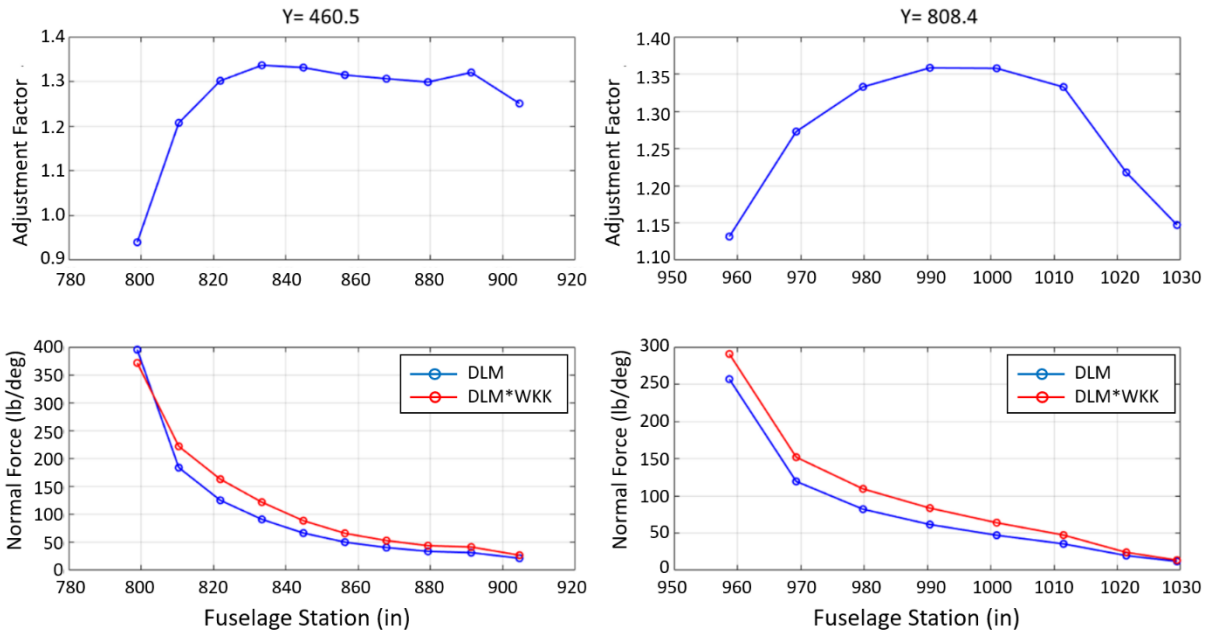


Figure 72 – Aerodynamic Box Force Adjustments at Mach = 0.76, Altitude = 13,000 ft, C_L = 0.2204, Re_{mac} =27.5M.

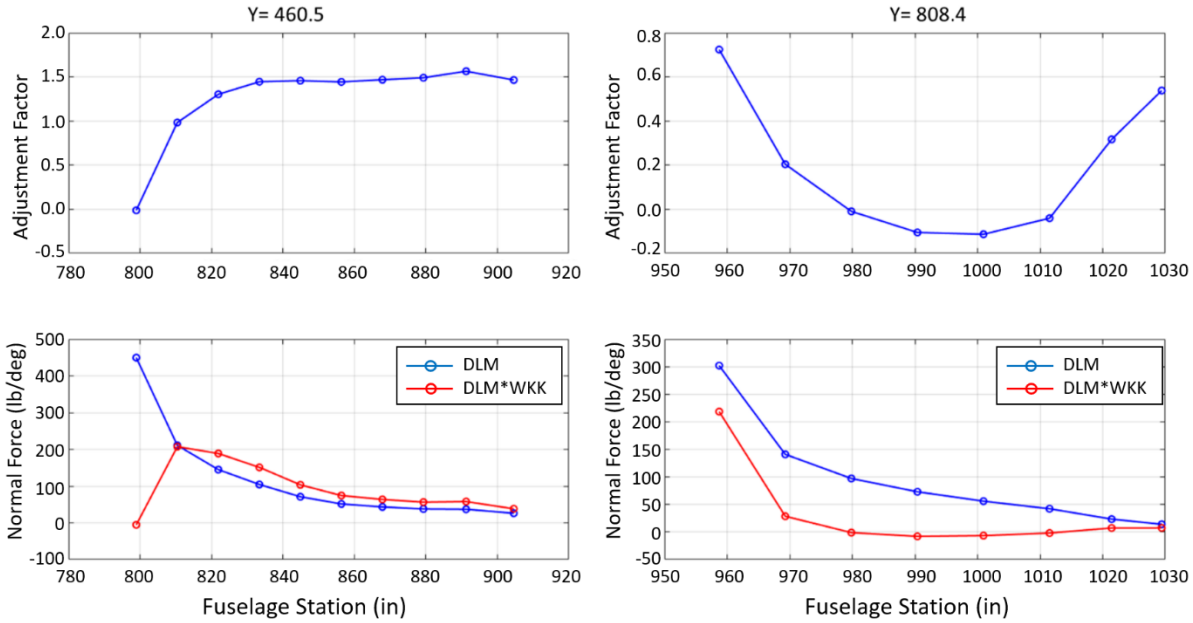


Figure 73 – Aerodynamic Box Force Adjustments at Mach 0.92, 26,000 ft, C_L = 0.2204, Re_{mac} = 27.5M.

3.2.16 Flutter Analysis

The DLM box load adjustment factors calculated were implemented in MSC/Nastran WKK format and the initial flutter analysis described in Section 3.2.12 was rerun. A basic assumption of this approach is that the aerodynamic adjustments calculated based on comparison of steady aerodynamic results may also be applied to unsteady DLM predictions at all reduced frequencies.

Results from flutter analyses performed both with and without aerodynamic adjustments are summarized for the three lower Mach number flight conditions in Table 18. Note first that in the majority of cases, the aero adjustments do not change the critical flutter mechanism. Furthermore, at Mach 0.59 and 0.76, the aero adjustments result in lower margins for the 5 Hz mechanism, but higher margins for the more critical 3 Hz mechanism. At Mach 0.85, the adjustments result in higher margins for both mechanisms. Overall, the aero adjustments raise the minimum aeroelastic stability margins by 10% for analyses conducted at the three lower Mach numbers of 0.59, 0.76, and 0.85.

Results from flutter analyses performed both with and without aerodynamic adjustments are summarized for the Mach 0.92 flight condition in Table 19. Clearly, the aero adjustments have completely changed the character of the analysis results with the introduction of multiple low and high frequency mechanisms, many of which have negative stability margins. The detailed flutter analysis results of Figures 74 and 75 support this conclusion. At Mach 0.76, the adjustments result in reasonable modifications to modal frequency and damping versus airspeed,

while at Mach 0.92, the raw and adjusted results differ significantly due to the inherent unsteadiness of the flow at this condition.

In conclusion, aeroelastic stability analyses performed with CFD-based DLM adjustments at flight conditions up through 0.85 Mach predict healthy airspeed margins, the minimum being 35% for the max payoad plus MTOW fuel configuration at the Mach 0.76 13,200 ft flight condition. Because the 0.92 Mach dive speed flight condition is well beyond the 0.80 wing aerodynamic design cruise Mach number, strong shocks on both upper and lower outer wing surfaces are predicted. The flutter analysis with raw DLM unsteady aerodynamics is therefore of limited value, and the CFD-based aerodynamic adjustment method employed herein is unable to improve flutter analysis fidelity at this transonic flight condition. A flutter analysis with the unsteady aerodynamic modal loads predicted with CFD directly is required to do this, but is beyond the scope of the work described herein.

Table 18 – Flutter Summary – Mach 0.59 to 0.85.

			Raw DLM			CFD Adjusted DLM			
Mach	Altitude (feet)	Mass Case	Freq (Hz)	Airspeed (in/sec)	Margin (%)	Freq (Hz)	Airspeed (in/sec)	Margin (%)	Delta (%)
0.5896	0	1	5.45	12108.1	53.2	5.51	11735.9	48.5	-4.7
0.5896	0	2	5.47	12262.4	55.1	5.53	11902.9	50.6	-4.5
0.5896	0	3	5.47	12200.8	54.4	5.53	11842.4	49.8	-4.6
0.5896	0	4	3.06	10952.6	38.6	3.07	11554.1	46.2	7.6
0.5896	0	5	3.11	11470.7	45.1	3.13	12356.8	56.3	11.2
0.7571	13,200	1	5.28	13839.5	43.0	5.40	13071.2	35.1	-7.9
0.7571	13,200	2	5.32	14065.1	45.3	5.43	13294.1	37.4	-7.9
0.7571	13,200	3	5.30	13914.6	43.8	5.42	13161.3	36.0	-7.8
0.7571	13,200	4	3.04	12487.7	29.0	3.07	13756.7	42.1	13.1
0.7571	13,200	5	3.10	12945.0	33.7	6.78	14401.4	48.8	15.1
0.8536	20,000	1	5.16	14868.4	39.9	5.60	17044.6	60.4	20.5
0.8536	20,000	2	4.83	15051.5	41.6	8.64	17711.2	66.6	25.0
0.8536	20,000	3	5.18	14940.3	40.6	5.64	17349.2	63.2	22.6
0.8536	20,000	4	3.01	13301.2	25.2	17.1	17374.7	63.5	38.3
0.8536	20,000	5	3.07	13921.0	31.0	17.01	16828.5	58.3	27.3

Table 19 – Flutter Summary – Mach 0.92.

			Raw DLM			CFD Adjusted DLM		
Mach	Altitude (feet)	Mass Case	Freq (Hz)	Airspeed (in/sec)	Margin (%)	Freq (Hz)	Airspeed (in/sec)	Margin (%)
0.92	26,000	1	5.09	15694.0	40.4	21.26	10342.8	-7.5
						1.33	11563.6	3.5
						1.16	11610.9	3.9
						19.83	12781.8	14.4
0.92	26,000	2	4.67	15758.4	41.0	1.17	10992.6	-1.7
						1.33	11380.6	1.8
						21.37	11506.3	2.9
						19.88	12841.0	14.9
0.92	26,000	3	5.11	15779.8	41.2	21.31	10578.7	-5.4
						20.56	10784.7	-3.5
						1.16	11576.9	3.6
						1.34	12064.6	7.9
0.92	26,000	4	2.95	13729.8	22.8	21.67	7011.8	-37.3
						21.41	8405.7	-24.8
						1.53	8824.4	-21.1
						1.39	10773.4	-3.6
0.92	26,000	5	3.00	14352.1	28.4	21.38	8098.5	-27.5
						21.44	8611.6	-23
						1.54	9206.7	-17.6
						1.39	10809.0	-3.3

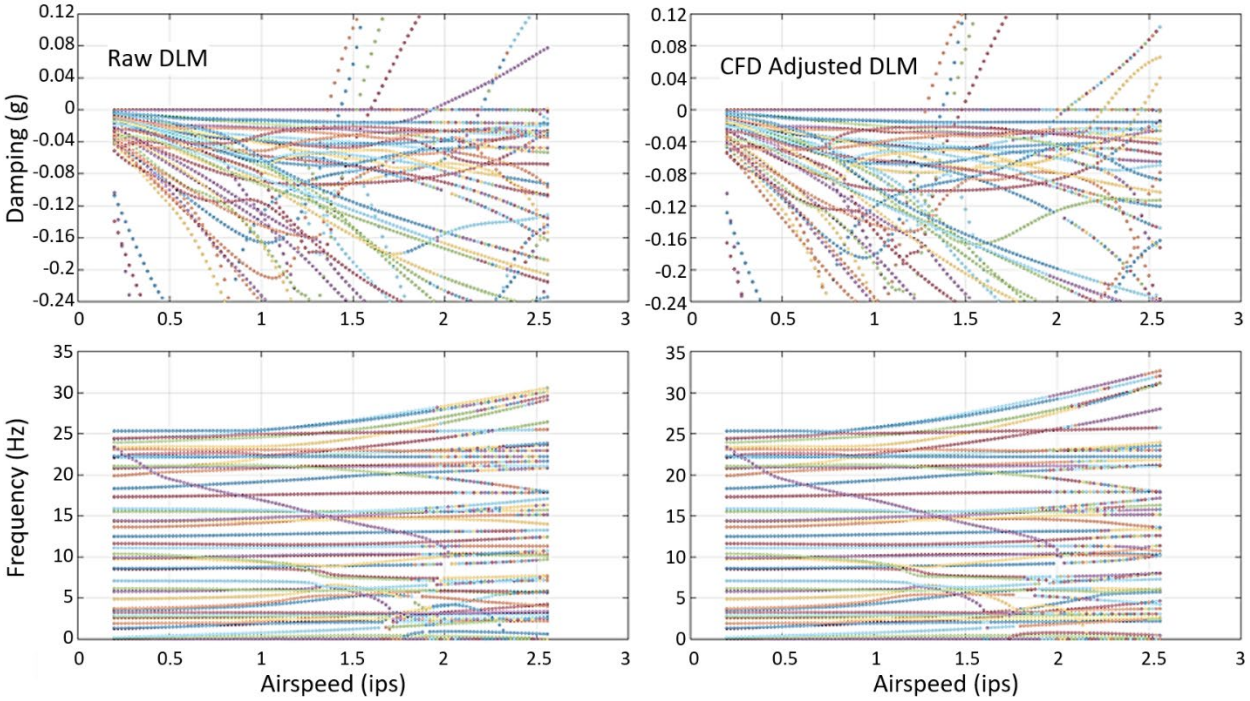


Figure 74 – Flutter Results for Mach 0.76, 13,000 feet, Mass Case 1, Re_{mac} = 33.9M.

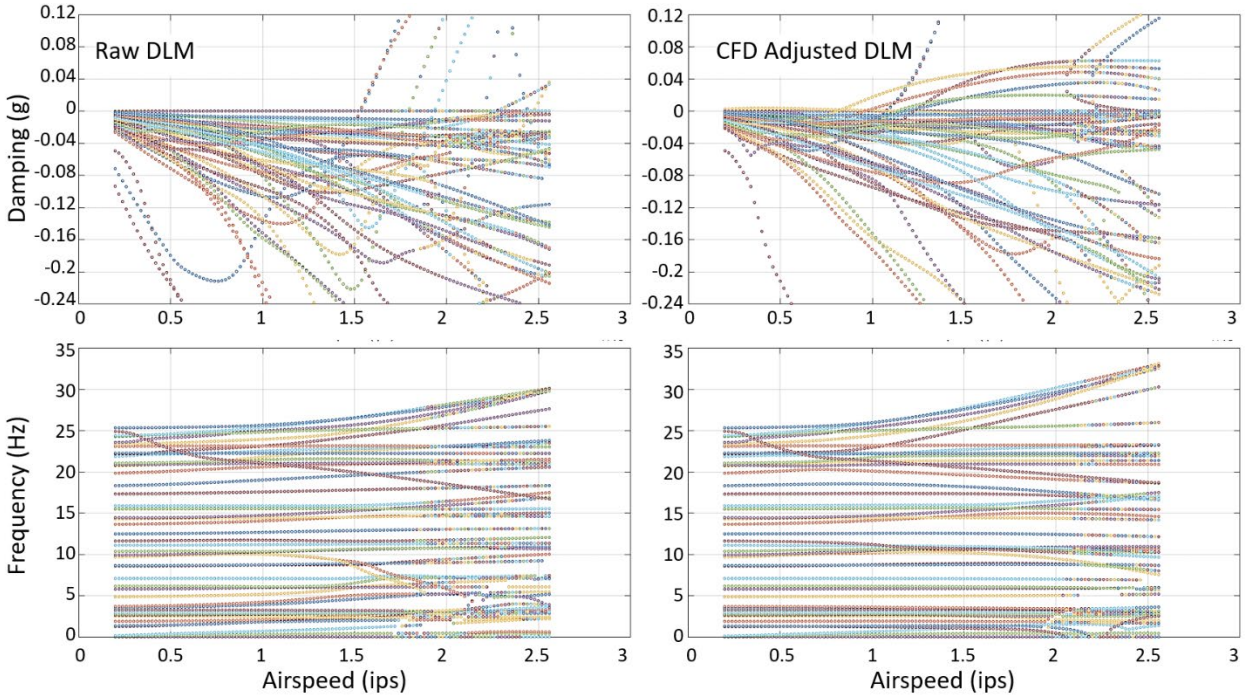


Figure 75 – Flutter Results for Mach 0.92, 26,000 feet, Mass Case 1, Re_{mac} = 27.5M.

3.2.17 Aeroelastic Analysis Conclusions

Loads and dynamics analyses performed thus far suggest the TTBW aircraft configuration is feasible. Due to the availability of geometry at the time of analysis, the aeroelastic FEM was updated to the 1104-001-RC configuration and used to generate a set of airframe structural design loads corresponding to critical maneuver and gust conditions. Structural sizing optimization using these design loads was performed and yielded reasonable wing and strut weights in line with the predictions of previous TTBW development work. Aeroelastic stability analyses incorporating CFD-based aerodynamic adjustments suggest healthy flutter margins at Mach numbers up through 0.85. This investigation should be revisited in a subsequent analysis to ensure that changes made to the final configuration (1104-001-RG) are still valid.

To complete this round of analysis with the current aeroelastic FEM, further work is recommended. As discussed at some length, the flutter analysis performed to date at the 0.92 Mach flight conditions is incapable of capturing for the nonlinear flow features predicted. To more confidently assess stability margins at this transonic flight condition, a flutter analysis employing CFD calculation of unsteady aerodynamic forces directly is required. In addition, because the TTBW configuration results in a redundant wing load path unlike that of a catilevered wing, flutter analysis should be performed with prestressed modes and potentially about a large deformation operating state. This has been investigated in the past, and should be revisited for the current TTBW configuration. Lastly, maneuver and gust loads analyses should be updated with CFD-based aerodynamic adjustments as was done for flutter analyses.

It bears noting that both the Mach 0.745 analyses and the current Mach 0.80 analyses are limited in scope. They are focused on the wing, strut, and jury structures only, use preliminary flight design load conditions, and size the structure to generic criteria. The structural layouts and constraints were created by structural analysts, with limited structural design development. To continue maturing the TTBW airframe, future work should include the following tasks:

- Design development to define structural concepts, manufacturing limits, and structural layouts of airframe components.
- Inclusion of more of the airframe in the aeroelastic sizing, particularly the gear pylon. This effort addresses the risk of unexpected weight increases late in airframe development, when key components are finally analyzed.
- Definition of more detailed airframe requirements and sizing criteria, and incorporation of these criteria into the sizing optimization. This effort addresses the risk of not knowing the weight impacts of criteria that may be unique to the TTBW airframe.
- Addition of more load conditions in the aeroelastic analysis, such as antisymmetric maneuvers, maximum control surface deflections, ground loads, crash loads, fuel

overpressure loads, and flap torsion loads. This work addresses the risk of missing critical conditions, and therefore the weight, of specific portions of the airframe.

4.0 Aerodynamic Design

4.1 High-Speed Aerodynamic Design

This section outlines the design process and results of a high-fidelity study aimed at maturing the TTBW concept for operation at a higher cruise Mach number than previously studied. Updating the design from the M=0.745 design (created in SUGAR Phase III) to a cruise Mach number of M=0.80 will enhance the commercial viability of a potential product by enabling an increase in fleet productivity. The primary design objectives of this study are consistent with the objectives from the Phase III aerodynamic design effort, such as efficient cruise operation, and minimizing wing-strut interference. However, the design effort also sought to increase the scope of the vehicle-level design considerations as compared to previous studies by tracking the implications of high-speed design changes on low-speed (high-lift) performance. This included items such as: low-speed (clean) aircraft performance, high-lift system compatibility, and the inclusion of flap hinge fairings into the high-speed design.

In addition to the similarities in design objectives, the M=0.80 design study also shares many of the same constraints as the M=0.745 design study. The configuration layout was frozen at the start of the study – wing sweep and planform remained unchanged throughout the design effort. The engine nacelle and pylon were modeled as a flow-through geometry, so power effects were not considered. Also, aeroelastic twist as a function of flight condition was not changed – rather, the geometry represents an ideal ‘1G’ geometry, which was used to determine the performance potential of a TTBW aircraft operating at transonic Mach.

Following the completion of a revised high-speed design, the geometry developed in this phase of work will be tested and validated in a transonic wind tunnel test at the NASA Ames 11-ft TWT beginning in January of 2019.

4.1.1 Design methodology

The design methodology used for the development of the M=0.8 high-speed lines is based on the experiences and lessons learned during the previous phases of the SUGAR program. Reliable tools and processes were used in the same capacity as previous design efforts, while tool improvements were made where a high return on investment was possible. For example, the 2D aerostructural strut optimization procedure used in Phase III was updated to a 3D procedure using the TRANAIR design tool. The new procedure allowed for design optimization across the wing and strut span (rather than at discrete 2D locations) and introduced 3D flow interactions into the optimization that were previously unaccounted. The results from the modified design tool was then validated in the RANS CFD code OVERFLOW to ensure design viability.

4.1.1.1 *Design and Analysis toolset*

Various software tools were used in the design, development, and analysis of the SUGAR TTBW concept. Key tools included but were not limited to FLO-22, CDISC, TRANAIR, OVERFLOW and BUFFET. Each tool is briefly described below with an explanation as to how it was used for the detailed SUGAR design:

- FLO-22 (6) is a full potential, 3D transonic flow code used for the aerodynamic analysis of wings modeled out of a wall. The code captures body effects by mathematically modeling the change in upwash as a function of span. It was used for initial wing design, wing-spanload evaluation and preliminary dragrise estimation of the SUGAR TTBW wing design.

- The TRANAIR (7) tool consists of a nonlinear, full potential compressible flow Newton solver with fully coupled 2D integral boundary layer (IBL) models for aerodynamic analysis at subsonic, transonic and supersonic freestream Mach numbers. Aeroelastic and powered propulsion models offer additional capabilities, as well as transpiration models to represent boundary layer displacement and design modifications. Structured surface grids represent the discretized model geometry (along with wakes) and output-based Cartesian mesh adaptation is used to generate the volume domain, as illustrated in Figure 76. A design mode is also available to model various surface modifications, such as twist, camber and thickness on lifting surfaces, dictated by a gradient-based optimizer. Numerous objective functions and inequality constraints are available for design across multiple design conditions that involve geometry assessments, solution features and functionals of various aerodynamic quantities.

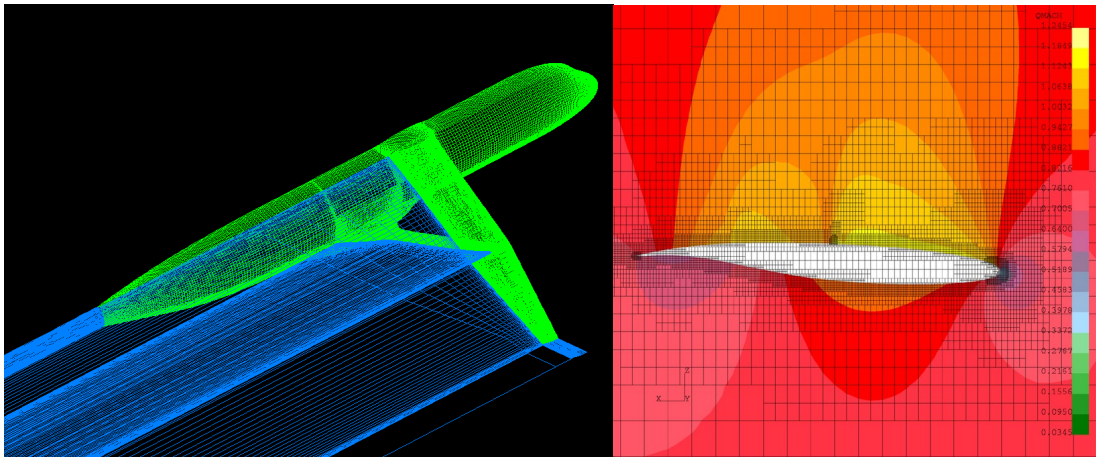


Figure 76 – TRANAIR surface and volume discretization.

- CDISC (8), which stands for Constrained Direct Iterative Surface Curvature, is an inverse design tool developed at NASA Langley for 2D or 3D configurations. This tool adjusts the geometry such that the resulting pressure distribution matches the distribution specified

by the designer. CDISC was used to reduce shock strength by smoothing pressure distributions throughout the SUGAR TTBW design.

- OVERFLOW (9) is a node-based RANS code specifically designed for structured, overset grid systems. It is capable of computing steady or unsteady flow about an arbitrary body across a wide range of Mach numbers using a number of different approaches. Depending on the type of simulation, the solver can be run in 2D or 3D, thin-layer or full Navier-Stokes, central or upwind differencing, static or moving body. OVERFLOW 2.2l was used to solve for the full 3D viscous solution over the entire SUGAR TTBW configuration and was the primary tool used to estimate the aerodynamic performance characteristics. A consistent solver setup was maintained throughout the project with the Spalart-Allmaras one-equation turbulence model, the Quadratic Constitutive Relation (QCR) and 5th-order HLLE++/SSOR differencing schemes employed.

- BUFFET is a Boeing-proprietary code that estimates a configuration's sensitivity to buffet by computing shock strength and position and comparing it against a database of 2D high Reynolds number data from conventional and supercritical airfoil tests. The method provides an indication of when shock-induced separation leads to buffet onset. The BUFFET program has been historically shown to be quite accurate for predicting buffet onset for T-tailed twinjet transport designs and was used to assess buffet characteristics for the TTBW wing and strut.

4.1.1.2 *CFD grid generation and post-processing*

CAD geometry was provided for grid generation using NX (Unigraphics). MADCAP, a Boeing proprietary grid generation code, and the Ansys ICEM CFD meshing software package were used to import the CAD surface definition and generate the necessary surface grids. Additional surface grid generation, volume grid generation and OVERFLOW input file creation was accomplished using scripts contained within NASA's Chimera Grid Toolset (CGT) (10). The CGT script BuildVol was used in conjunction with required input files to build all of the volume grids using one of two hyperbolic grid generators: HYPGEN (11) or LEGRID. All grids were built within a common model directory, which was broken up into subdirectories that were tied to the major components of the configuration. This use of the CGT script system facilitated configuration control throughout the SUGAR design process and provided a clear history of how each grid was built.

After the volume grids were built for each configuration, the BuildPeg5i CGT script was used to build a configuration-specific input deck for Pegasus5 (12). Pegasus5 was used to cut holes in grids that penetrate solid walls as well as to establish communication between the individual volume grids. This is a step in the process known as domain or grid connectivity. Next, a force and moment integration surface was created using an internal Boeing code called POLYMIXSUR. This program eliminates grid overlap on the surface and connects neighboring zones with zipper

grids comprised of triangles. POLYMIXSUR produces a closed integration surface used to compute forces and moments. Finally, the BuildOveri CGT script was used to create a configuration-specific input deck for OVERFLOW.

Both Tecplot and Fieldview were used for the generation of flow visualization images from the OVERFLOW results. A Boeing internal tcl script system facilitated the efficient generation of a common set of images across the entire polar. Common images were collected inside PowerPoint presentations and were viewed in flipbook mode in order to understand how the flow field changes as a function of angle-of-attack. These images helped to qualitatively explain the behavior of quantitative results and showed the designer where modifications were required to improve the design.

4.1.1.3 *Design Optimization using TRANAIR*

TRANAIR was used in several different modes during the design optimization process. The first mode was a purely aerodynamic-focused multipoint design optimization, while the second mode consisted of a detailed aerostructural design optimization. The latter mode was used to ensure that the aerodynamic loft had a viable structural solution and corresponding weight, and was used to investigate various general modifications to the strut structure as well as jury strut location.

Aerodynamic Optimization with TRANAIR

As the wing and strut lofts evolved throughout the SUGAR Phase IV tasks to improve aerodynamic performance, automated aerodynamic shape optimization was conducted using the TRANAIR tool to identify how additional performance improvements could be achieved. The goal for this effort was to increase maximum L/D at the vehicle cruise condition and ensure operability across the flight envelope. In addition, various constraints were included through the optimization process to address concerns over manufacturability.

A baseline Mach 0.80 wing-body-strut configuration resembling the updated Phase III model was provided as a seed for aerodynamic shape optimization. TRANAIR analysis settings for this model were determined using best practices and information from a grid refinement study. Small regions of complex geometry were not modeled with IBL to facilitate solver convergence to machine-zero, thus absolute drag measurements contained a small offset compared to 3D RANS simulations of the seed geometry. Nonetheless, performance improvements obtained in TRANAIR design translated into similar increment values when optimized geometry was analyzed with OVERFLOW.

The seed model was parameterized with surface deformation modes that accomplished both chordwise and spanwise camber, twist and thickness changes to the seed wing and strut grids. Only camber and twist deformation modes were used in the aerodynamic shape optimization

cases. The strut attachment location remained at the same wing spanwise station and was modified by the deformation modes while remaining attached to the wing. Both the wing and strut planforms did not change throughout the optimization studies. Instead of morphing the analysis grids, the designed deformation modes were transformed into transpiration boundary condition updates that affect the local flow field as if a new grid were used. Conservative bounds were chosen for the deformation modes to ensure transpiration errors did not accumulate substantially during an optimization case. A new loft of optimized geometry was generated for analysis to confirm transpiration errors were not exploited by the optimizer.

Gradient-based optimization was initially conducted at the design condition with fixed-lift coefficient. Numerous weighted combinations of drag functionals and boundary layer parameters were explored as the minimization objective to understand different objective spaces. The impact of constraining geometry or boundary layer parameters on the wing and strut were also studied. Multiple parameterization setups were also studied to understand the effect of twist, camber and thickness changes on the design trajectory taken by the optimizer. Figure 77 shows a typical drag history in the early design iterations taken by the optimizer. As expected, different levels of drag improvement were obtained depending on the problem setup. Close inspections of the resulting wing and strut pressure profiles and new deformation modes (Figure 78 and Appendix Figure A.13), as well as spanload and sectional lift distribution (Figure 79), were executed to understand how further drag improvements could be included in the CAD model.

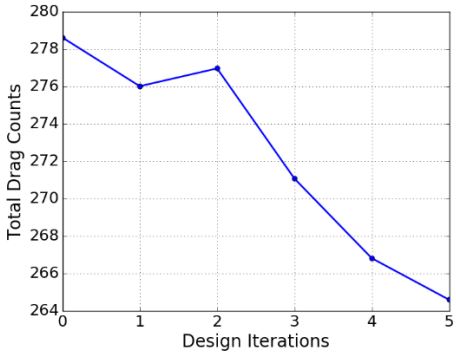


Figure 77 – Typical drag improvement seen in early design iterations for a single-point optimization.

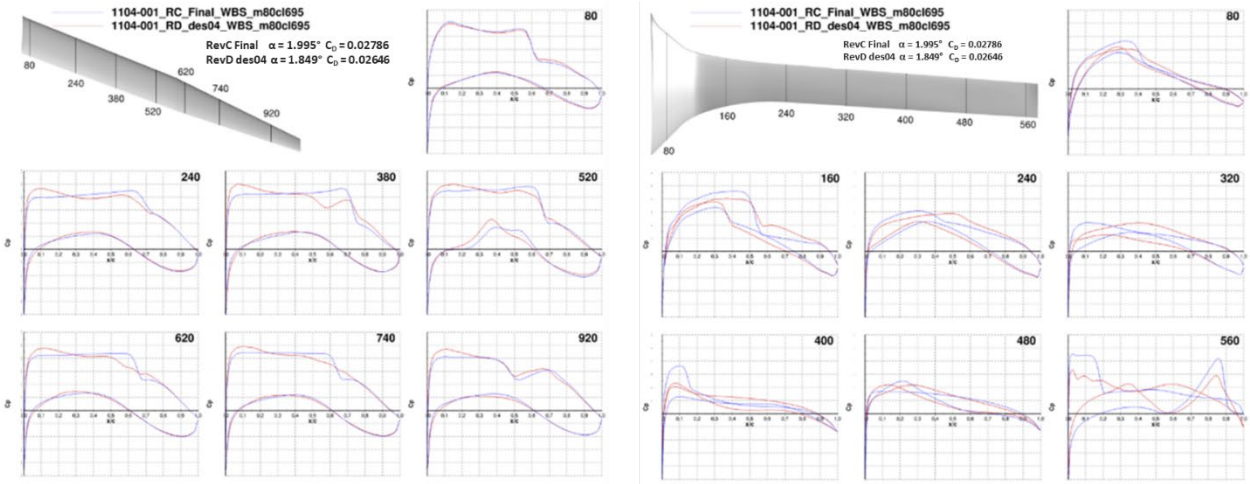


Figure 78 – Typical comparisons of seed and optimized results in relation to pressure profiles and deformation modes after single-point optimization at Mach = 0.80, C_L = 0.695, and Re_{mac} = 14M.

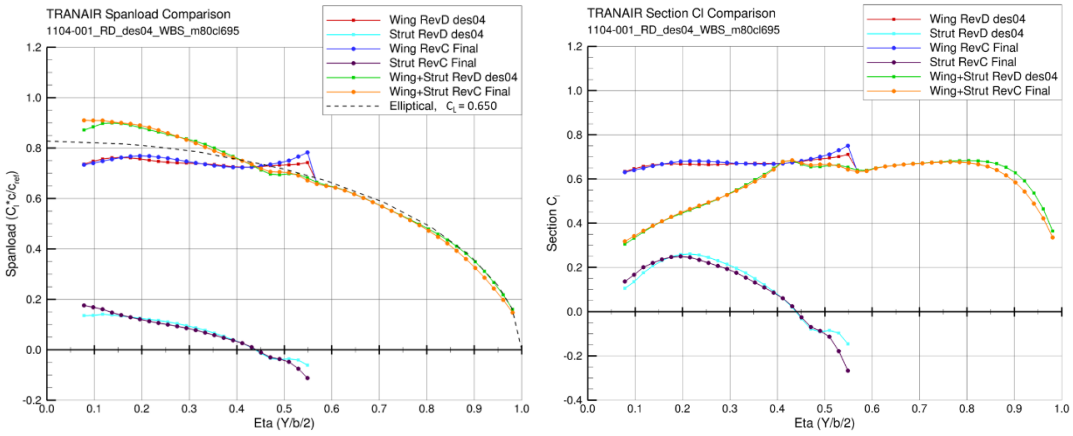


Figure 79 – Typical comparisons of seed and optimized spanload and lift-distribution after single-point optimization at Mach = 0.80, C_L = 0.695, Re_{mac} = 14M.

Note: the elliptical spanloads shown in Figure 79 are for C_L=0.650, which represents the wing-and-strut lift contribution for the vehicle. i.e. the body component of lift is removed from the vehicle total of C_L=0.695.

Multipoint optimization followed with an updated seed strut planform and the lessons-learned from design space studies with single-point optimization. With the design condition unchanged, various Mach and lift-coefficient pairs were added to the design problem across three, four or five total design conditions. Each condition contained a corresponding lift-coefficient constraint with angle of attack varying independently to satisfy it. The overall minimization objective was also defined in multiple ways to reflect different weightings of drag functionals in each design condition. Boundary layer parameters were investigated for some conditions as well, either as part of the objective function or as a constraint, in addition to surface geometry constraints. Figure 80 illustrates a drag history seen over 15 iterations for the last case influencing the high-speed design. Figure 81 shows a comparison of seed and optimized geometry for that case. As with the single-point optimization cases, inspections of the resulting wing and strut pressure profiles and new deformation modes (Figure 82 and Appendix Figure A.14), as well as spanload and lift distribution (Figure 83), were done to understand how further drag improvements could be included in the CAD model.

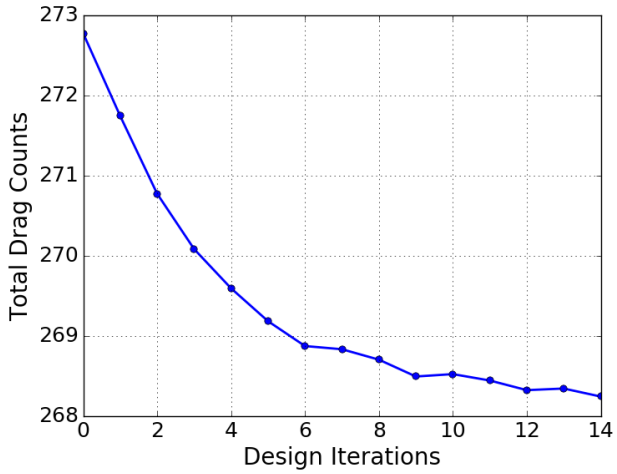


Figure 80 – Typical multipoint optimization drag history (Mach = 0.80, C_L = 0.695, Re_{mac} = 14M).

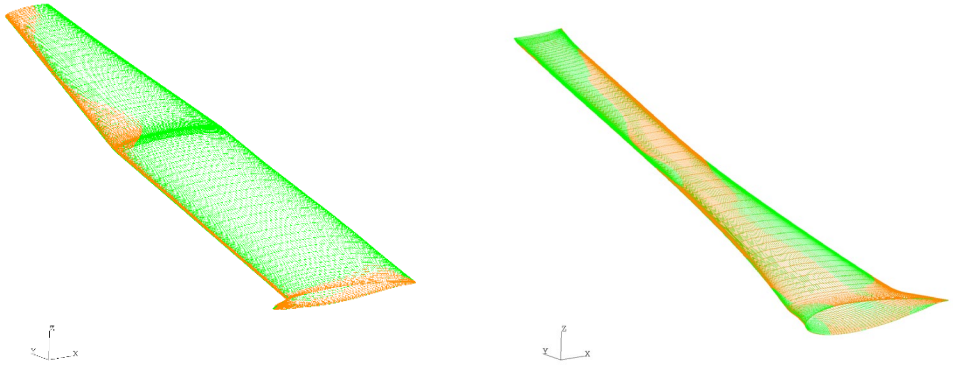


Figure 81 – Typical comparison between the seed (green) and optimized (orange) geometry after multipoint optimization.

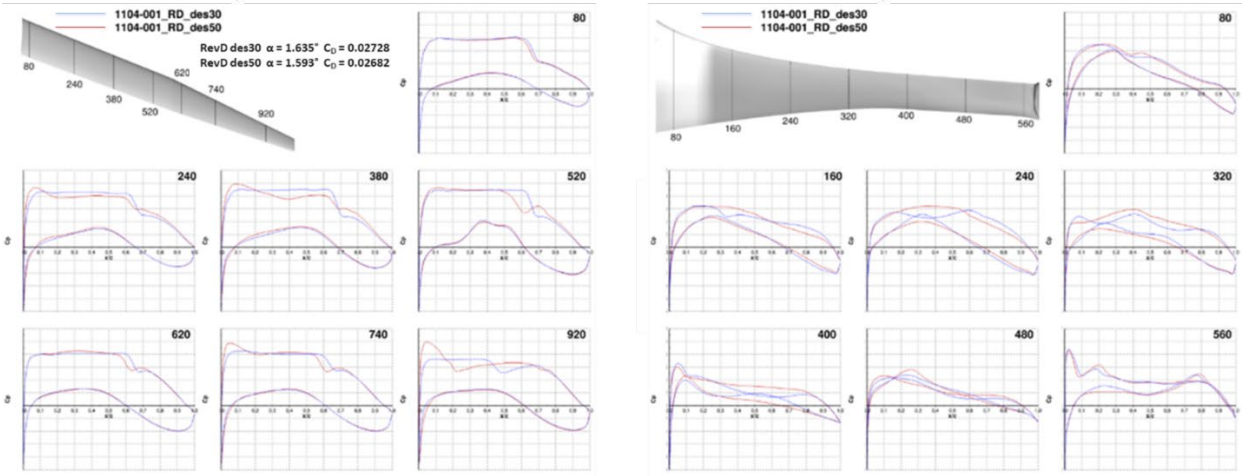


Figure 82 – Comparison between seed and optimized result pressure contours and deformation modes after multipoint optimization (Mach = 0.80, C_L = 0.695, Re_{mac} = 14M).

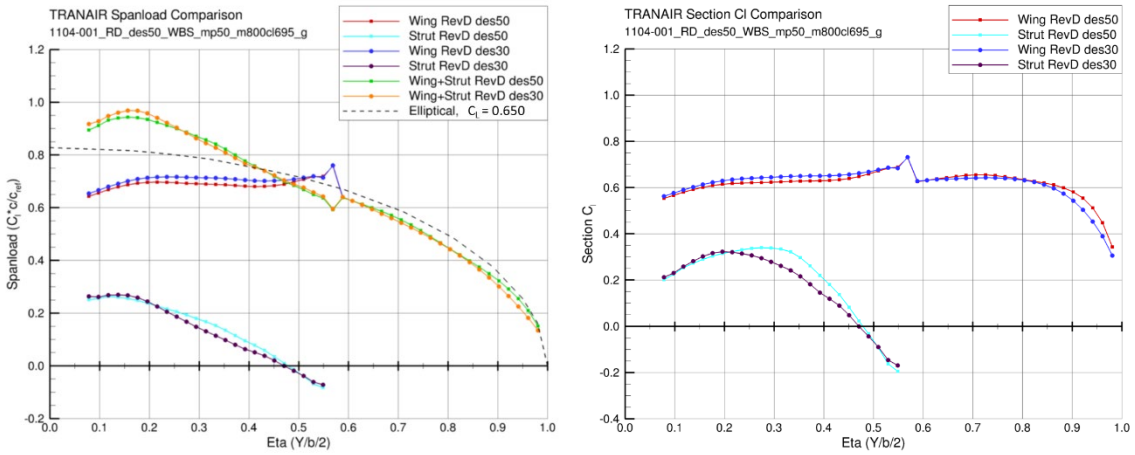


Figure 83 – Comparison of seed and optimized spanload and lift-distribution after multipoint optimization (Mach = 0.80, C_L = 0.695, Re_{mac} = 14M).

Aerostructural Optimization with TRANAIR

The TRANAIR tool suite was augmented with a low-fidelity structural sizing capability to conduct trade studies between aerodynamic drag and structural weight. The structural model consisted of airfoil-conforming spars and skin thickness components of arbitrary material properties. This simple structural box definition was automated within 2D airfoil slices at user-specified spanwise stations along the wing and strut planforms, as shown in Figure 84. With the addition of thickness deformation modes to the camber and twist modes in the design variable vector, the box definitions were sized with an inner-loop gradient-based optimization for each outer mold-line design iteration selected by the outer-loop aerodynamic optimizer. The fast structural optimizer minimized the local box weight by changing its component dimensions and enforcing local stiffness constraints for EI and GJ, as well as minimum and maximum gage limits. The spanwise distribution of EI and GJ constraints were inputs extracted from a high-fidelity FEM sizing study. The drag minimization objective functional used by the aerodynamic optimizer was penalized by a converted weight estimate for the combined wing and strut structural boxes. An additional penalty was appended for any spanwise stations where the structural box optimization was unable to meet stiffness constraints. Typically this occurred when the aerodynamics optimizer reduced airfoil thickness excessively. In this manner, a compromise between aerodynamic performance and weight could be studied, as depicted in the typical drag and feasibility history shown in Figure 85.

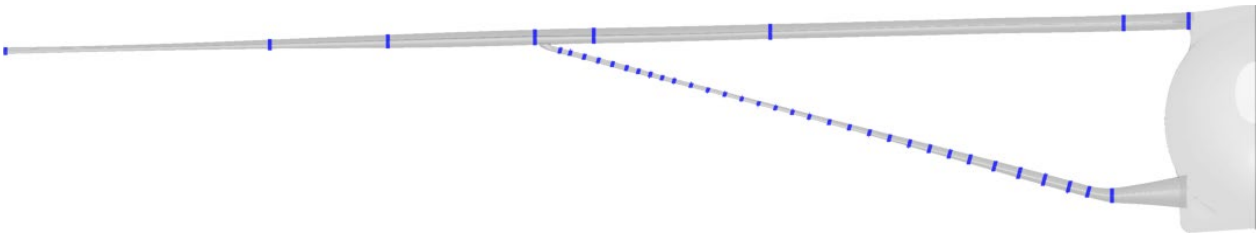


Figure 84 – Spanwise stations where structural box sizing was conducted during optimization.

Single-point aerodynamic optimization was conducted with the structural sizing inner-loop for a variety of minimization objective definitions that included structural penalty functions. The impact of different geometric and structural feasibility constraints were also investigated. General optimizer behavior included thickness increases in span locations where structural feasibility could become an issue, and thickness decreases in other locations where the stiffness constraints were less stringent and drag benefits could be obtained, as shown in Figure 86.

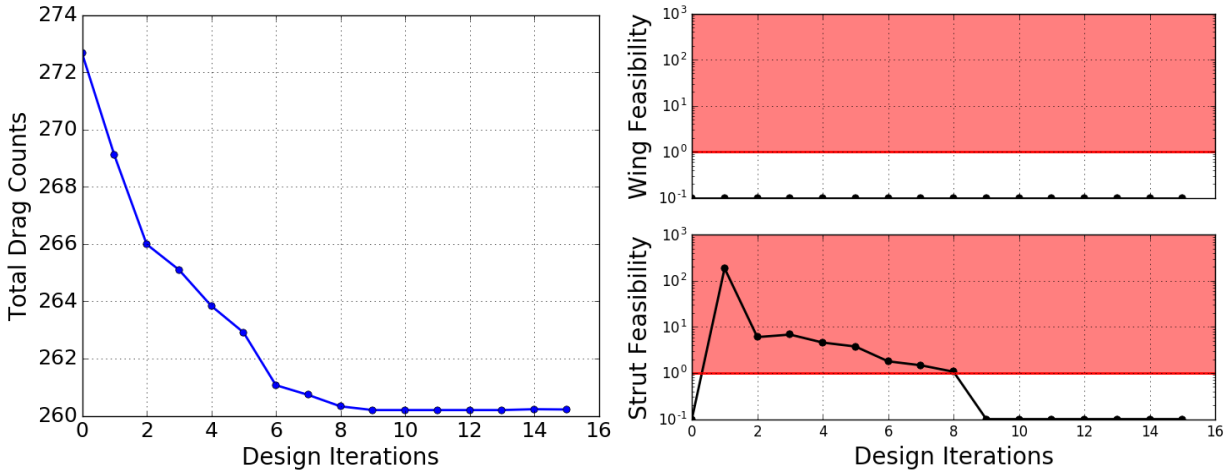


Figure 85 – Typical aero-structural optimization results showing drag improvements and structural feasibility maintained for a single-point case.

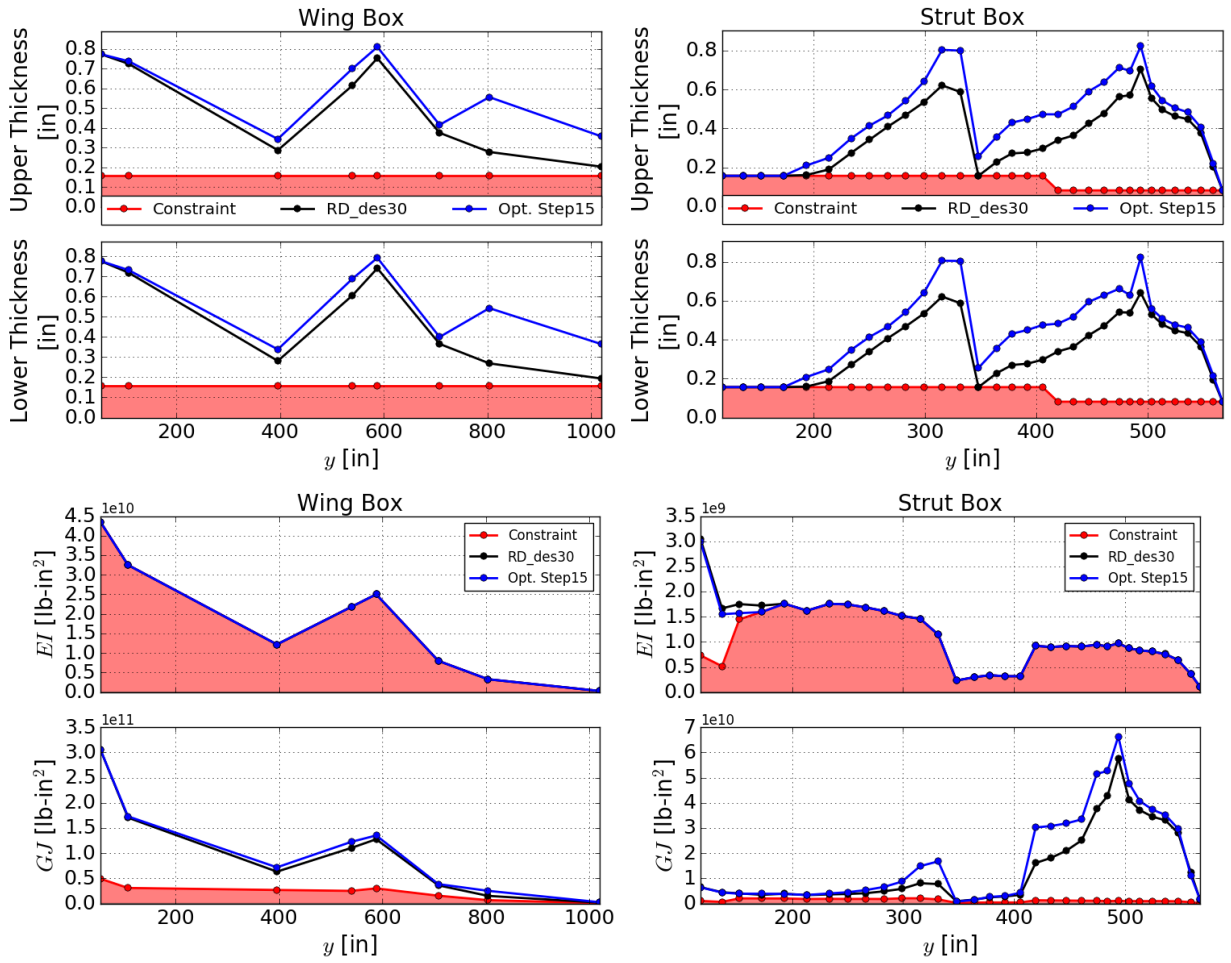


Figure 86 – The aero-structural optimization tracked the design progress for key design constraints.

4.1.2 Wing-Strut Design Overview

This section outlines the design progression from the starting M=0.8 conceptual geometry developed during Phase III up to the finalized 1104-001-RG high-speed lines.

4.1.2.1 *Configuration 1104-001-NEW*

The design of a M=0.8 variant of the TTBW concept began during SUGAR Phase III. In this phase of the program, the vehicle underwent a change from the M=0.745 design, and was adjusted using conceptual design methods. These methods adjusted the design by modifying wing sweep and thickness according to simple sweep theory.

4.1.2.2 *Configuration 1104-001-RA – Conceptual Design*

The –RA configuration was analyzed as a baseline for the current higher-Mach design effort using OVERFLOW. The results of the analysis, shown in Figure 87 and Appendix Figure A.15, show that while the basic features of the design have been updated, the preliminary layout was not intended to produce a high-performance design without additional design effort. The starting

design showcases the regions that will require the most attention to bring a higher-Mach design to fruition – the wing-strut juncture has a healthy shock, and the transition from the larger chord inboard strut (which houses the landing gear attachment) to the smaller-chord outboard strut is too heavily loaded. In actuality, the primary purpose of extending the high-speed design up to a higher Mach number (and up to a cruise Mach number that airlines are typically interested in) is largely based on the lack of available knowledge of strut-braced designs operating at high transonic Mach. It is therefore the objective of this design effort to determine the sensitivities and synergies of TTBW aircraft operating at more desirable cruise Mach numbers.

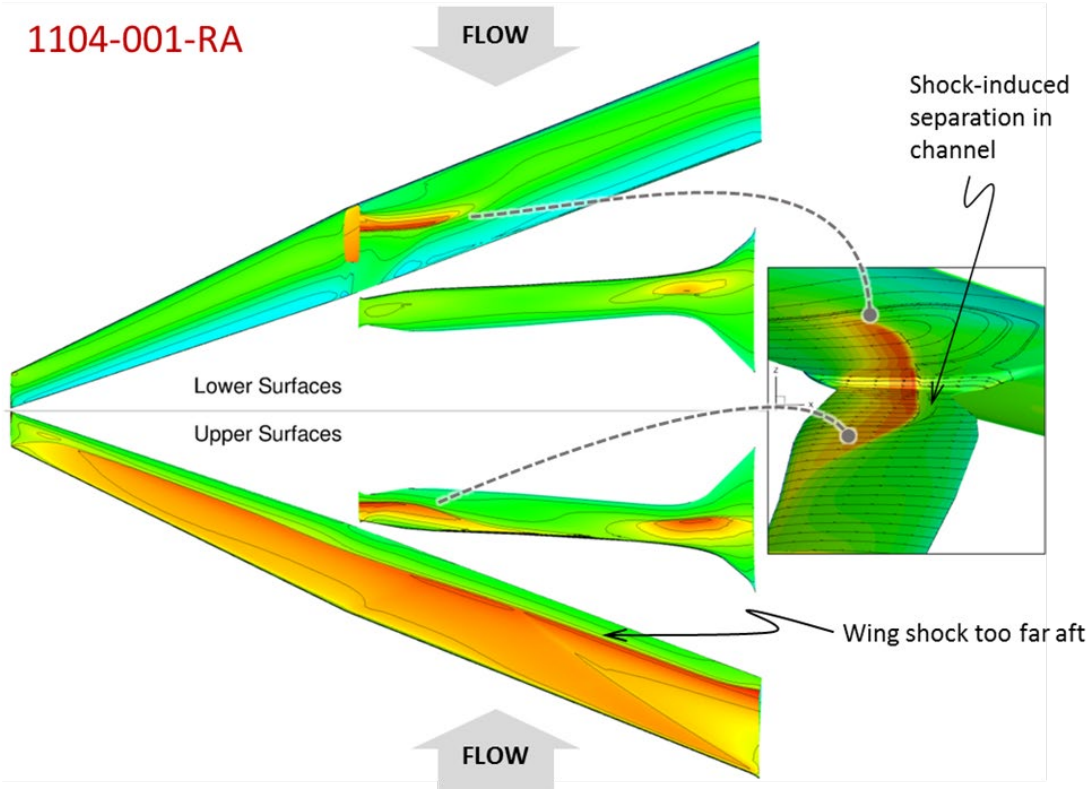


Figure 87 – Configuration 1104-001-RA, M=0.8, 40kft, C_L=0.695, Re_{mac} = 14M.

The starting point for vehicle spanload (shown in Figure 88), indicates a nonoptimal strut loading in which the inboard strut is not highly loaded, while the outboard strut is more heavily loaded than desired. In SUGAR Phase III, it was discovered that the optimal strut loading is higher inboard, and tapers to a negative sectional lift coefficient (and contribution to spanload) at the outboard end of the strut. This loading reduces the amount of aerodynamic interference between the wing and strut, and prevents the channel flow from resulting in a strong shock that severely limits vehicle performance (13).

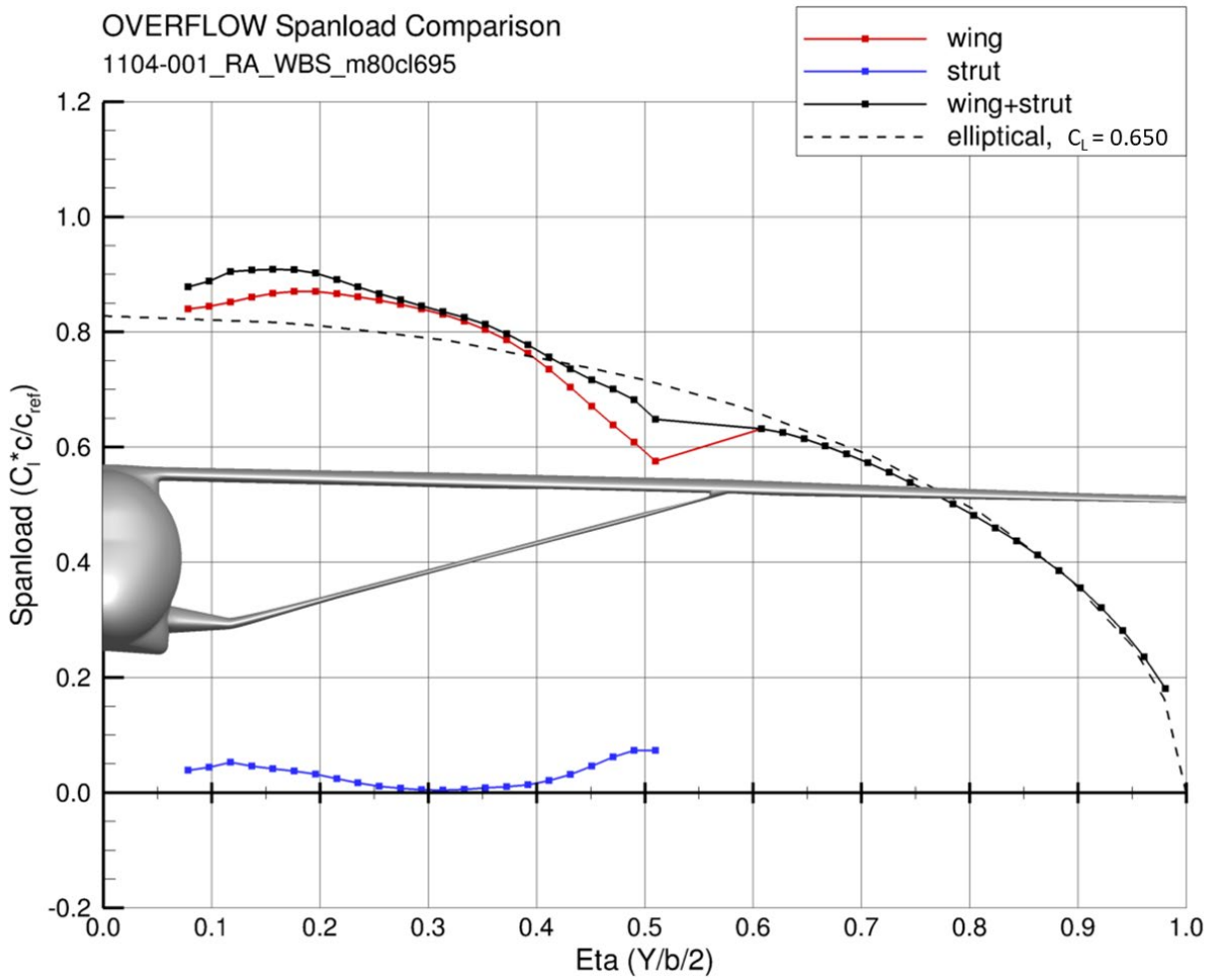


Figure 88 – Configuration 1104-001-RA Spanload, M=0.8, 40kft, C_L=0.695, and Re_{mac} = 14M.

Even though the optimal wing-strut combination would be designed in conjunction with each other, based on the analysis of the starting design point it was decided to focus initially on the wing design alone to ensure viability of the basic wing design.

4.1.2.3 *Configuration 1104-001-RB – Preliminary Wing Design*

Based on the OVERFLOW results of the –RA geometry, the wing underwent several modifications to update for the new design. First, the local modifications to the wing thickness distribution were removed, the wing thickness distribution was smoothed, and the outboard wing thickness was decreased slightly. Since the effects of the change in vehicle planform and the wing-strut channel's sensitivity to operation at higher Mach number was unknown, it was preferred to remove the local wing design tailoring and start from a geometrically continuous thickness distribution. A comparison of the wing twist distributions between the initial wing design (_NEW) and revised design (RB_FINAL) are illustrated in Figure 89 below; the corresponding changes to the wing thickness distributions are shown in appendix Figure A.16.

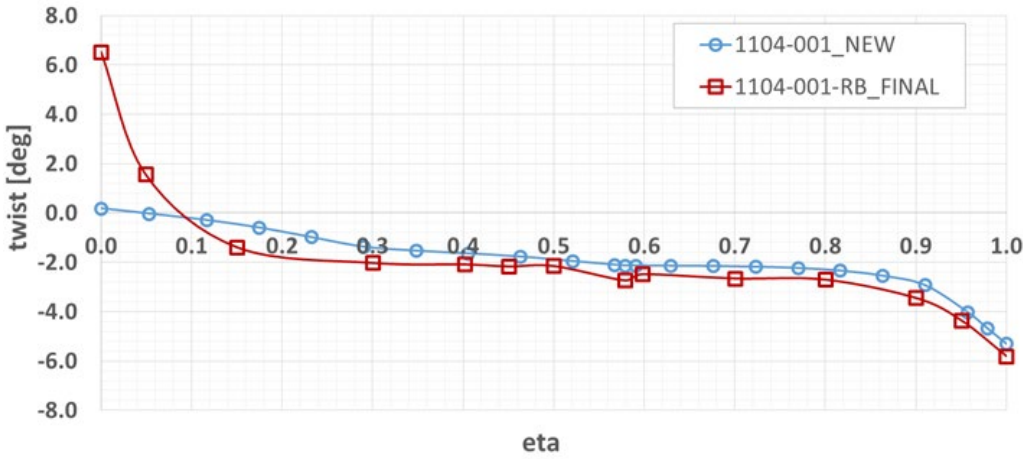


Figure 89 – Configuration 1104-001-RB Wing Twist Modification.

In addition, a significant feature of the airfoil – the divergent trailing edge (DTE) - was removed from the starting airfoil stack. The inclusion of the DTE in the previous wind tunnel model posed significant manufacturing challenges given the small chord of the model. In addition, the strong adverse pressure gradients in the airfoil cove posed design challenges during Phase III due to the structural necessity of full-chord engine pylon attachments. The combination of trying to close-out an engine pylon at the same chordwise locations as the wing airfoils required significant attention to prevent the formation of large regions of separation. The solutions to this problem likely had a locally-negative impact on wing spanload. It was therefore decided that the use of DTE airfoil technology would only be used on an as-needed basis, and would not be used if possible. This is not to say that DTE technology would not be potentially beneficial to the TTBW design, but rather that at present the design challenges associated with inclusion of a DTE outweighs the potential benefits.

The end result of the wing-alone design activity (shown in Figure 90 and Appendix Figure A.17) was a wing with acceptable performance across the design envelope and drag divergence Mach of 0.8. Modifications to the inboard wing airfoils and wing-body fairing (covered in more detail in Section 4.1.3.1) moved the inboard wing shock forward significantly. The angle of attack of the wing-body system increased from 2.25° (at the design condition) to 3.89° -- this would be rectified in subsequent designs by an alteration to the wing-body rigging angle.

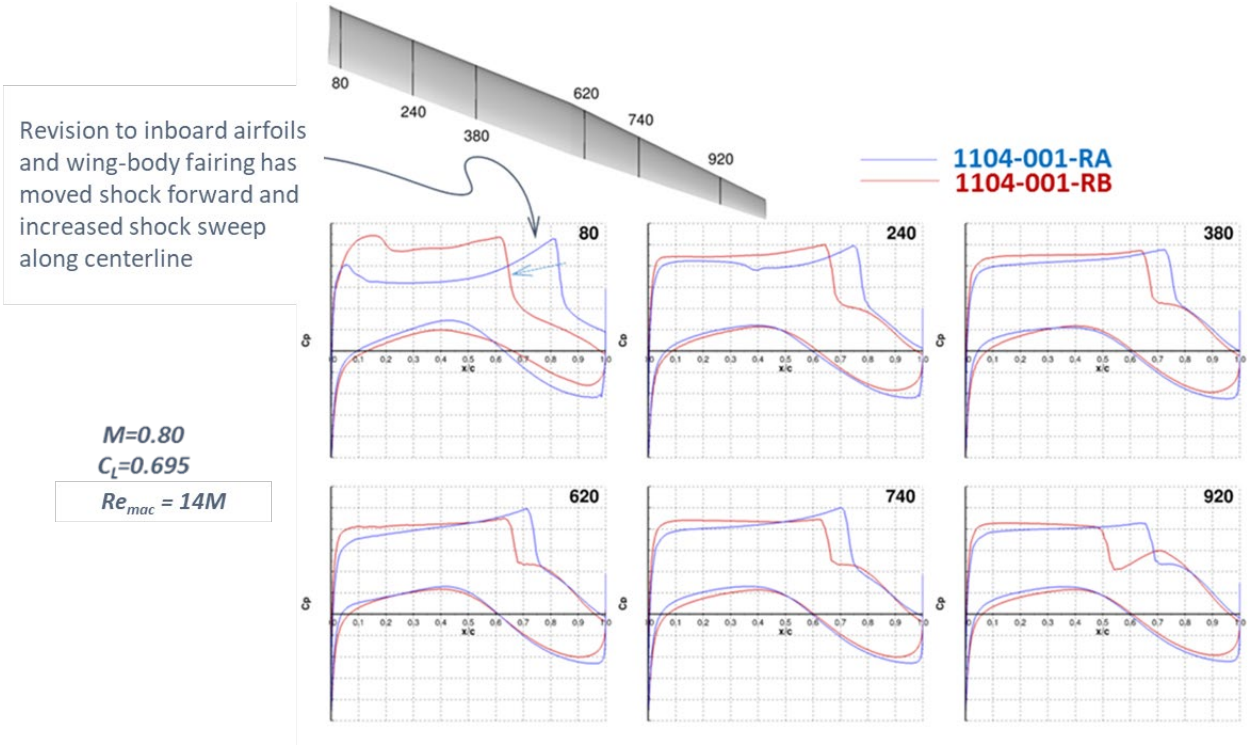


Figure 90 – Comparison of the 1104-001-RB wing-alone design wing pressures as compared to 1104-001-RA reference.

Upon completion of the wing-alone design activity a strut was added to the wing-body geometry to determine a new baseline for design activity. The focus of this design activity was primarily on the interaction between the wing and strut, and would ultimately culminate in the creation of a geometry (1104-001-RC) that could be used as a starting point for design optimization using the TRANAIR tool. This new configuration would also be used for flutter analysis.

Prior to the addition of the strut, strategic design decisions were made regarding the strut structure and desired aerodynamic loading. Previous design iterations of the TTBW concept utilized strut planforms that varied considerably in chord as a function of span. This was done primarily to limit the wetted area of the strut by reducing chord where structural requirements were less stringent. This followed the basic design observation that the strut was most critically loaded in the negative 1.0g-pushover maneuver, in which the strut became a column subjected to buckling loads. Since the strut attachment concept consisted of a pin-joint at either end of the strut, this meant that the strut structure could taper down significantly in size when approaching the pin joints. Minimizing the strut chord in this region thereby resulted in the characteristic ‘bow-tie’ strut planform found in the earlier phases of TTBW study. However, although the structural requirements were thereby significantly decreased near the pin joints, the severe changes in strut thickness and chord could lead to significant fluctuations in the strut’s contribution to vehicle spanload, and contributed to both additional complexity in the manufacture of the strut as well as in its cost. In addition, a component of the current TTBW design effort was to entail a significant amount of aero-structural optimization. This optimization

would have improved flexibility in design if the planform of the strut could be maintained throughout the study. Should the location of the jury-strut tie-in location be varied, the strut aerodynamic design could be considerably maintained. In addition, updated concepts of the strut-wing attachment suggested a larger spacing between the strut-wing attachment clevises, that would drive an increase in strut chord at the wing-strut attachment location. It was therefore decided that the strut planform would be significantly simplified from its earlier counterparts, with increased chord at the wing-strut attachment. The end result was a planform that remained relatively constant for much of its span.

The geometry made by combining the Revision B wing with the planform-modified strut design (which was at this point undesigned in an aerodynamic sense), referred to as 1104-001-RB, was analyzed in OVERFLOW. The results (shown in Figure 91 and Appendix Figure A.18) highlight general improvement in the wing design, but indicate that much improvement will be possible once detailed strut design begins. The two most obvious areas for improvement are the general strut loading and strong shock located in the wing-strut juncture. When examining the vehicle spanload Figure 92), it is clear that the strut has considerably too much load outboard near the strut junction, which is a significant contributor to the strong shock located in this region. The vehicle spanload is far from the idealized elliptical shape, which although the wing itself was twisted to produce this distribution on its own, has been strongly affected by the presence of the strut both inboard and outboard of the strut attachment.

It is worth reiterating herein that although the design effort began with a wing-alone study, the performance of the vehicle can only be refined when considering the wing-strut system as a whole. Consequently, the next step in the design process was to focus on wing-strut interactions.

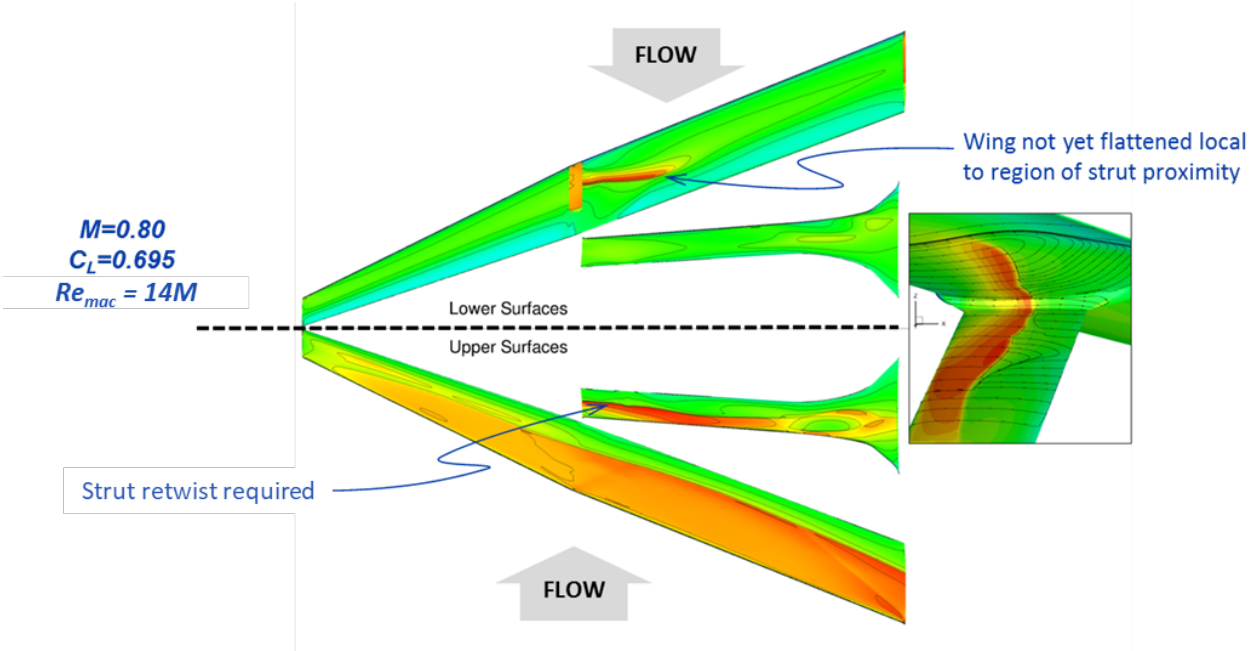


Figure 91 – OVERFLOW results for 1104-001-RB, M=0.8, 40kft, C_L=0.695, Re_{mac}=14M.

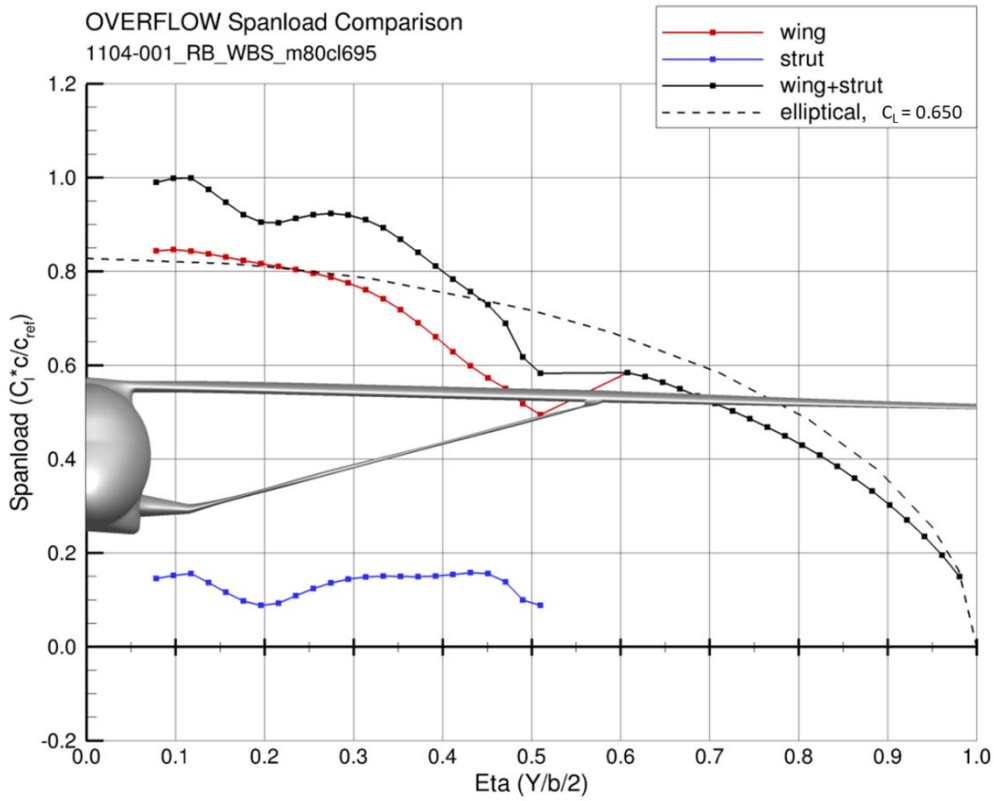


Figure 92 – 1104-001-RB Spanload at Mach = 0.80, C_L = 0.695, Re_{mac} = 14M.

4.1.2.4 *Configuration 1104-001-RC – Wing-Strut Interaction*

The design of the combined wing-strut system began with the 1104-001-RB geometry, which consisted of a designed wing and undesigned strut. As shown previously in Figure 91, the strut

was initially carrying too much load, particularly outboard where high strut loading led to the formation of a strong juncture shock. Through a series of design iterations in which strut thickness, twist, and camber were manually adjusted along with adjustments to wing twist, the system was substantially improved in performance.

In this configuration, a strategic decision was made regarding the strut loading – the inboard strut was intentionally aerodynamically loaded to a much greater extent than the previous designs. Since most of the strut sizing constraints are the result of structural considerations, it is not a trivial task to reduce it in size without adversely affecting the vehicle structure. The structural constraints have driven the strut to a considerable size; the inboard strut chord and thickness are sized primarily by the landing gear integration, while the outboard end of the strut is sized by failsafe spacing requirements of the strut-wing attachment. The gear constraint has driven the inboard strut to be greater in chord and thickness than the wing root, and therefore represents a significant lifting surface. While the previous design philosophy had sought to keep strut loading down in order to avoid interference with the lower inboard wing surface, the M=0.8 planform enabled a greater degree of loading without adversely affecting the inboard wing lift. This was primarily the result of a localized 'de-stacking' of the wing and inboard strut brought about by changes to the wing sweep. In so doing, the inboard strut was longer underneath the wing, and therefore able to carry significantly more load than the lower Mach TTBW designs without significant aerodynamic interference. It was therefore decided to make use of this structure to the extent that the strut could carry increased lift so long as it did not culminate in the creation of a significant amount of wave drag. This allowed the strut to contribute to the aircraft lift, rather than being a simply parasitic element. The ideal objective would be to reduce the loading required on the wing, and thereby reducing the strength of the wing shock, which would in turn reduce wave drag.

The wing thickness was changed only in the regions that had a direct impact on wing-strut interaction. The regions closest to the wing-strut junction were manually 'flattened' in curvature so that the flow acceleration through the channel could be limited, and the formation of a strong shock avoided. While this curvature change would ideally be completed without a net change to the wing thickness, it was found that both curvature manipulation and cross-sectional area progression control were both required to produce an operable design.

When placing the previously-designed wing in the proximity of the strut, twist changes (illustrated in Figure 93) were required to achieve the desired wing-strut loading balance. In this case, the wing loading was significantly increased relative to the strut loading. The corresponding wing $(t/c)_{max}$ distributions for the –RB and –RC configurations are compared in Appendix Figure A.19.

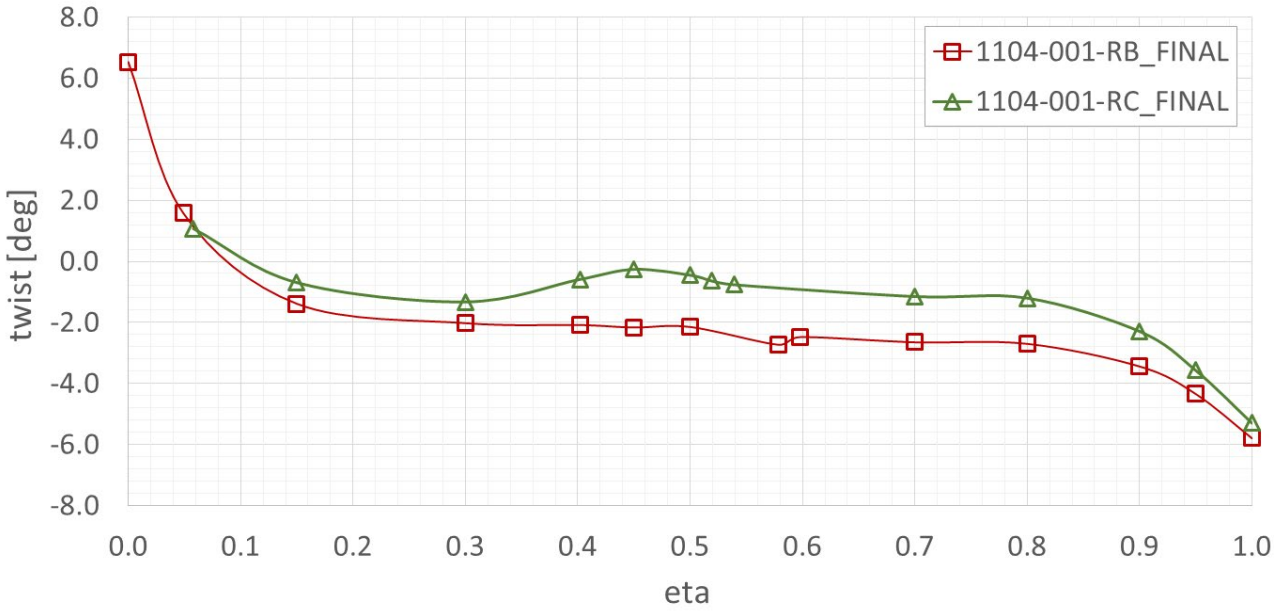


Figure 93 – Wing twist evolution from 1104-001-RB to 1104-001-RC Configuration.

Further to the point of strut planform normalization described in Section 4.1.2.3, in addition to the strut planform, the strut thickness and twist had to be normalized as the design moved away from the 'bowtie' planform concept as well. Therefore, as the design evolved from –RB to –RC configurations, the strut thickness was smoothed considerably. The remaining aspects of the bowtie planform were thereby removed.

Figure 94 shows the design evolution of the strut twist as the integrated effects of wing and strut were considered together. The dramatic decrease in strut incidence near the wing-strut juncture is evident outboard of eta=0.4. Here the strut is locally at a negative incidence angle so that the flow into the wing-strut channel is significantly reduced in speed. The design situation here is somewhat analogous to controlling mass flow into an engine by closing down the exit area of the nacelle. The strut airfoil sections are rigged about a common twist axis (at strut x/c=0.4) in order to keep the strut elastic axis straight so that eccentric loading of the strut can be minimized. Therefore, locally negative strut incidence angles drive the strut trailing edge up, rather than maintaining the strut trailing edge location and moving the leading edge down, which would open the channel capture area. The evolution of the strut $(t/c)_{max}$ distribution is illustrated in Appendix Figure A.20.

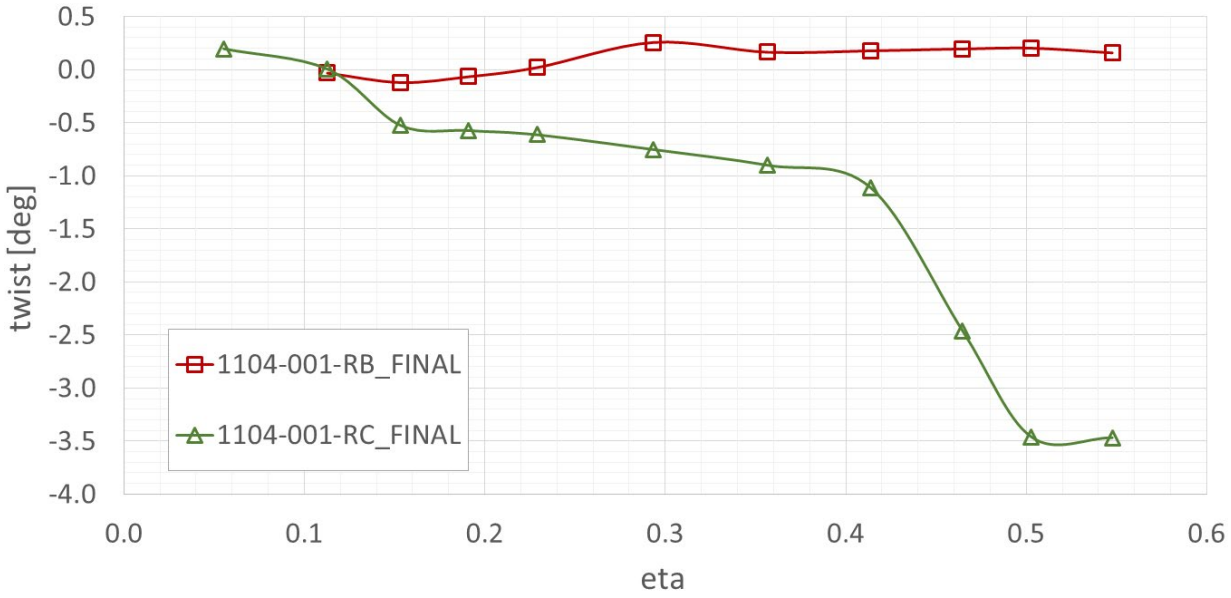


Figure 94 – Strut twist evolution from 1104-001-RB to 1104-001-RC Configuration.

The end result of the design changes made in configuration –RC are shown in Figure 95 and Appendix Figure A.21. The wing loading is more consistent across the span, the inboard wing shock weakened and the outboard strut loading has been reduced significantly. Also apparent is a visible increase in inboard strut loading, consistent with the strategic decision to carry a larger percentage of the aerodynamic load. Also of note, the shock in the wing-strut channel has been virtually eliminated at this flight condition.

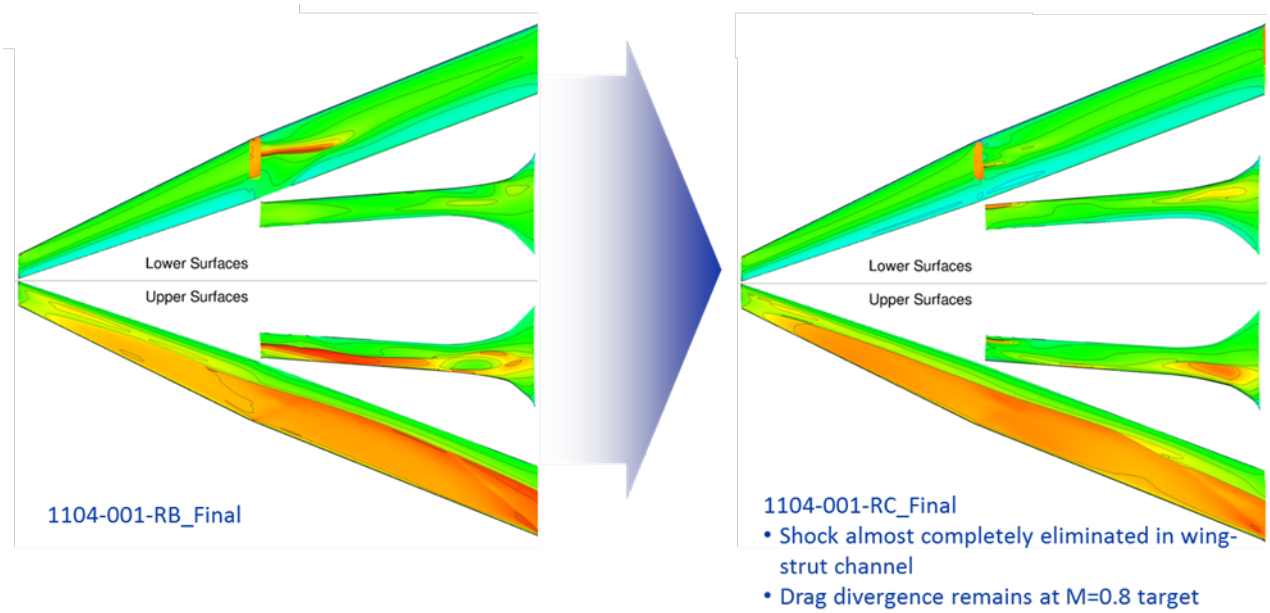


Figure 95 – Comparison of surface C_p contours from 1104-001–RB Configuration to 1104-001–RC (Mach = 0.80, C_L = 0.695, Re_{mac} = 14M).

Figure 96 shows the change in spanload as the design evolved to the –RC configuration. In this figure, the total spanload (black curve) has been substantially improved with a closer resemblance to the idealized elliptic shape. Strut loading inboard (blue line) has been maintained at a high level inboard but decreases as a function of span eventually reaching a locally downloaded state near the wing-strut juncture. This download is primarily the result of reducing curvature of the strut in the juncture region, which naturally results in an 'upside-down' airfoil camber. The red line, which denotes the wing contribution to spanload, shows a relatively flat loading on the inboard wing with a local increase in loading at the wing-strut juncture region in which the wing is used to offset the strut download. Similar to the strut, the wing experiences a local increase in lift coefficient as the underside of the wing airfoil is also locally flattened to reduce flow acceleration – these elements combine to create a local increase in wing lift.

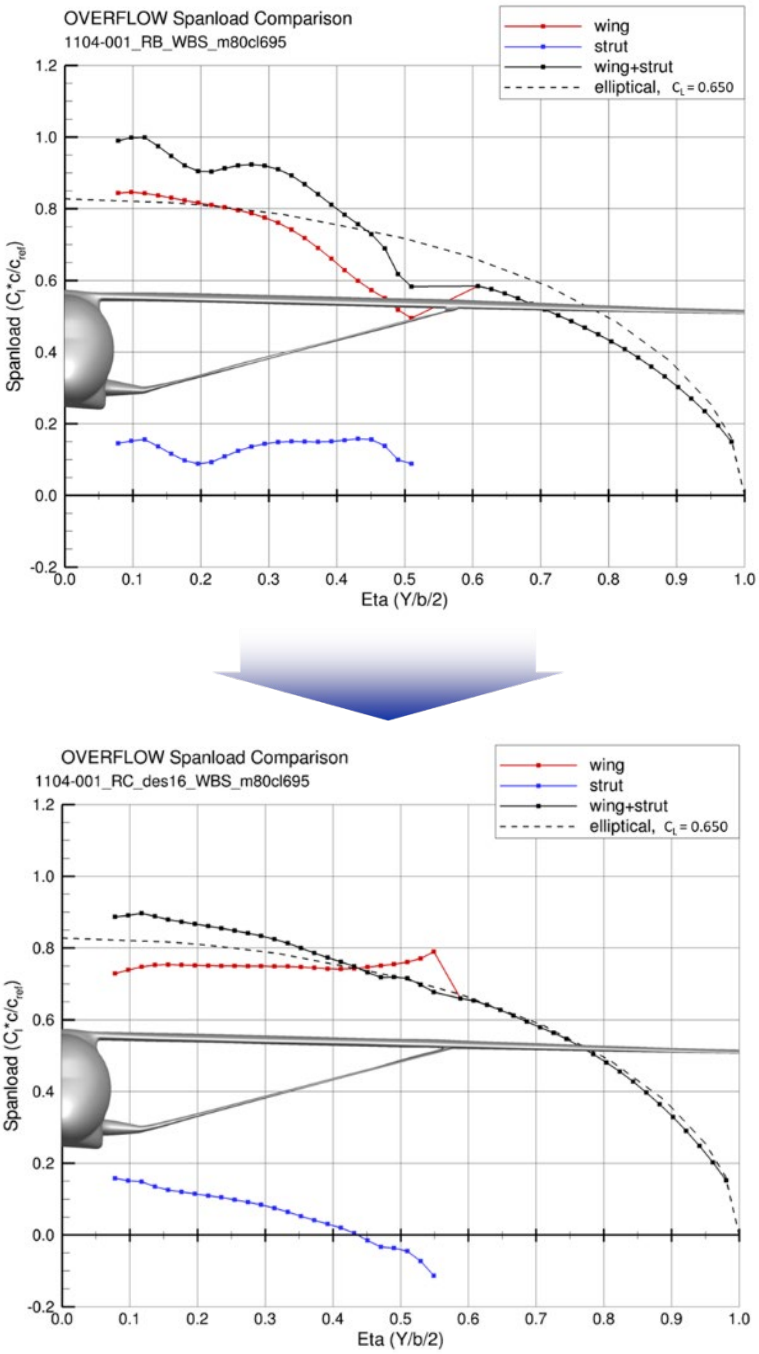


Figure 96 – Comparison of Spanload from 1104-001-RB Configuration to 1104-001-RC at Mach = 0.80, C_L = 0.695, Re_{mac} = 14M.

The net aerodynamic performance effect of the design activities for the –RC configuration are shown in Figure 97. The L/D of the configuration has been increased considerably from the starting design. Overall, the system is sufficiently well-behaved enough at this point to be used as a seed geometry for aerodynamic and aero-structural optimization efforts.

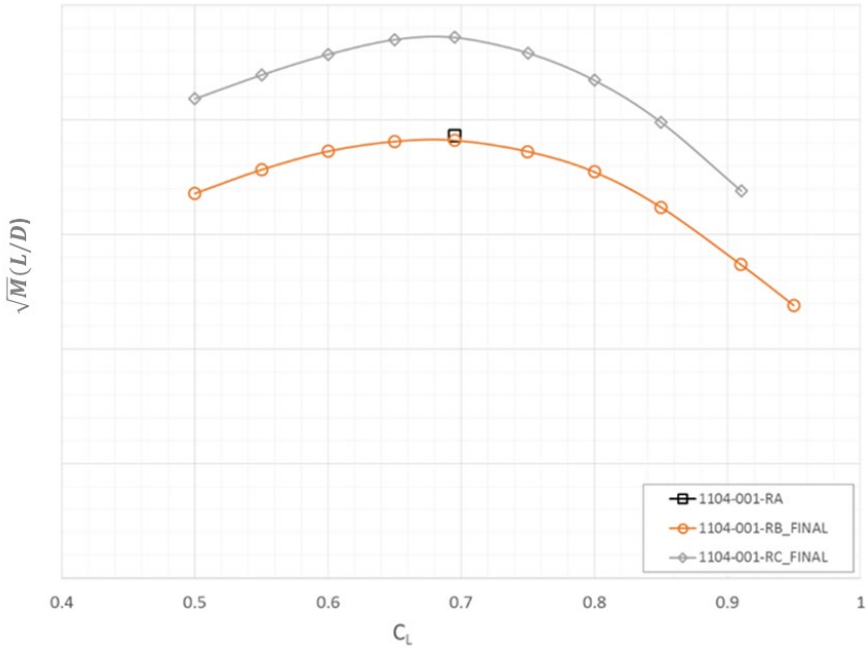


Figure 97 – Aerodynamic Efficiency changes as the design has evolved at Mach = 0.80, Re_{mac} = 14M.

4.1.2.5 *Configuration 1104-001-RD – Aerodynamic and Aerostructural Optimization*

This phase of the aerodynamic design effort utilized a combination of manual design adjustments and TRANAIR optimization. Results from the optimization studies completed in TRANAIR were validated for drag using OVEFLOW so that constant monitoring of the vehicle performance could ensure continual progress. Eventually a point was reached in which the differences in the flow physics being modeled between the two codes was not resolvable. These differences, however, constituted very small levels in drag and were most concentrated in areas in which there was a high degree of 3-dimensionality in the flow, such as in the wing-strut juncture and at the wingtip.

Initial optimization runs starting with the –RC geometry studied the varied effects of changing the physical design constraints and flow conditions to be used in the optimization. Flow conditions ranged from low-lift conditions to high-lift conditions near the required buffet boundary, and various weightings and combinations of these conditions. Both boundary layer and surface geometry limitations were also placed on the models. The effects of these types of modifications were described in Section 4.1.1.3.

Strut Planform Modification

In the course of the design optimization, structural models began to show that the outboard strut was not successfully meeting the EI and GJ structural design requirements determined by the FEM analysis. The aerostructural models determined a significant strut airfoil thickness change was required to meet the requirements. The bending and torsion structural requirements for the strut box and the required thickness changes to the strut necessary to meet the requirements are illustrated in Appendix Figure A.22.

Since the aerodynamic penalty for changing the strut thickness so close to the wing-strut juncture was so high, an alternate approach was used to reduce the strut load by moving the jury strut outboard to reduce the structural requirement (Figure 98). The outboard strut length L1 was reduced by 15%, resulting in a new outboard strut length L1A. Since buckling load is proportional to length squared, this resulted in a peak EI/GJ load reduction of ~40% for the outboard strut. The inboard strut length was increased by 15% from L2 to L2A, which increased inboard strut EI/GJ loads by ~32%. Since the jury strut would react to the column buckling loads as a column in buckling as well, the jury was mounted perpendicular to the strut to decrease the eccentricity of the loading. This had the additional benefit of keeping the channel area as high as possible since a vertical jury would enclose a smaller area between the wing-strut-jury channel.

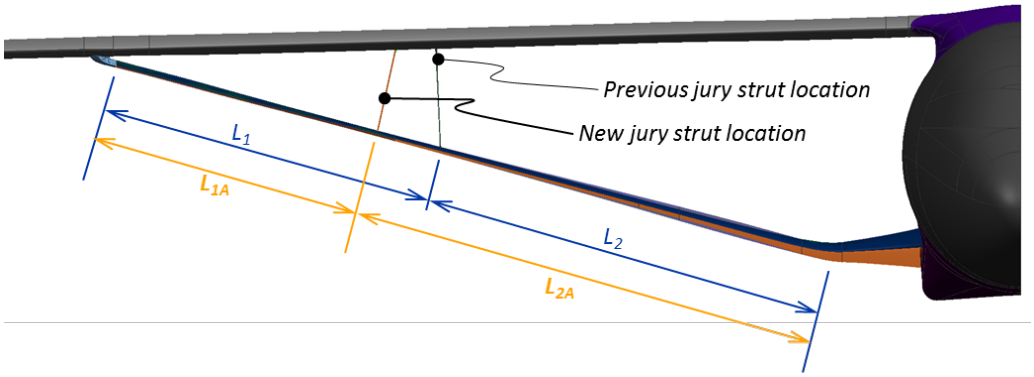


Figure 98 – Movement in the jury strut-to-strut connection was moved outboard to reduce the load on the outboard strut.

However, while the outboard jury strut movement decreased the load on the outboard strut, it increased the load experienced by the inboard strut. Therefore, the inboard strut was scaled with a combination of increased thickness and chord to provide required strength. In this process, there ended up being a large discrepancy in the chord requirements at the strut structural transition region where the landing gear enclosure meets the region of the strut dominated by buckling requirements. Since a rapid transition from a large to short chord in the transition region would result in a significant effect on spanload, it made sense from an aerodynamic perspective to blend the structure more continuously and take the opportunity to increase the sweep at the root of the strut. The planform view of the resulting modification is shown in Figure 99, and the resulting strut twist distribution is shown in Figure 100; the strut thickness distribution is shown in Appendix Figure A.23.

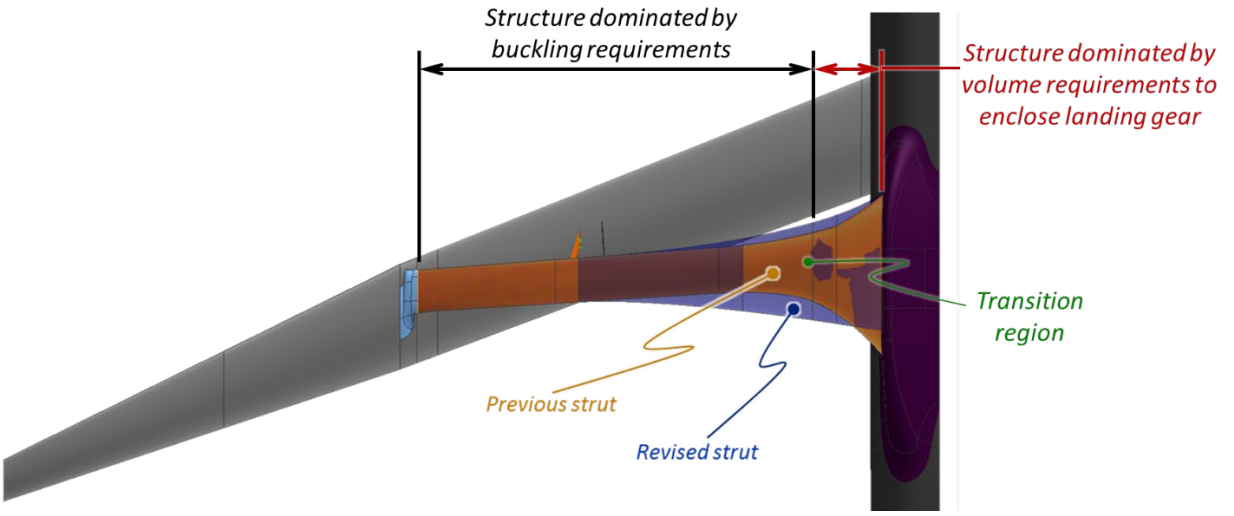


Figure 99 – Strut Planform Modification (1104-001-RD_des30).

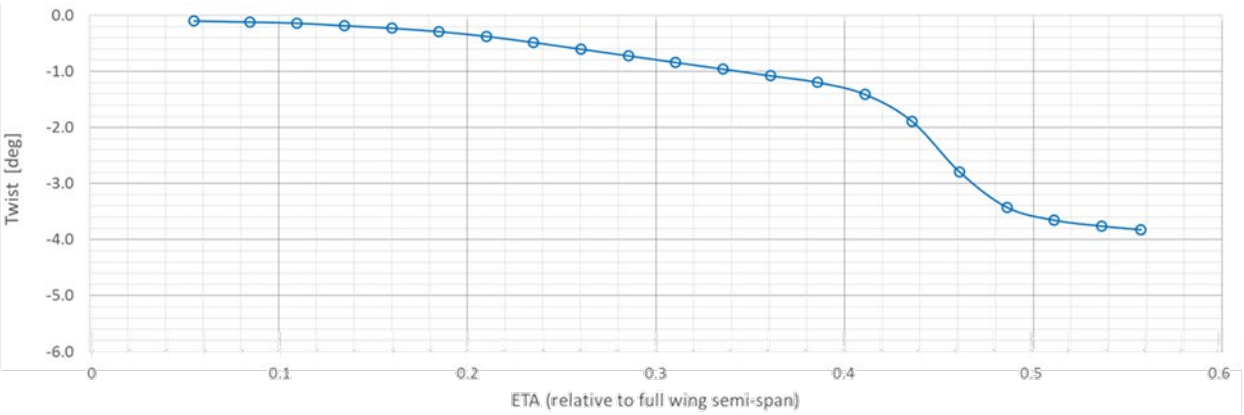


Figure 100 – Modified –RD_des30 strut twist distribution as a function of wing semi-span.

When the modified strut planform geometry was analyzed in OVERFLOW, the resultant effect on the strut loading was a significant reduction in the peak C_p levels in the structural transition region on the strut (Figure 101 and Appendix Figure A.24). While the manual modification of the strut did not have a significant impact on drag, the modified strut would benefit from subsequent aerodynamic design with –RD_des30 becoming the new seed geometry to be used in the TRANAIR optimization process.

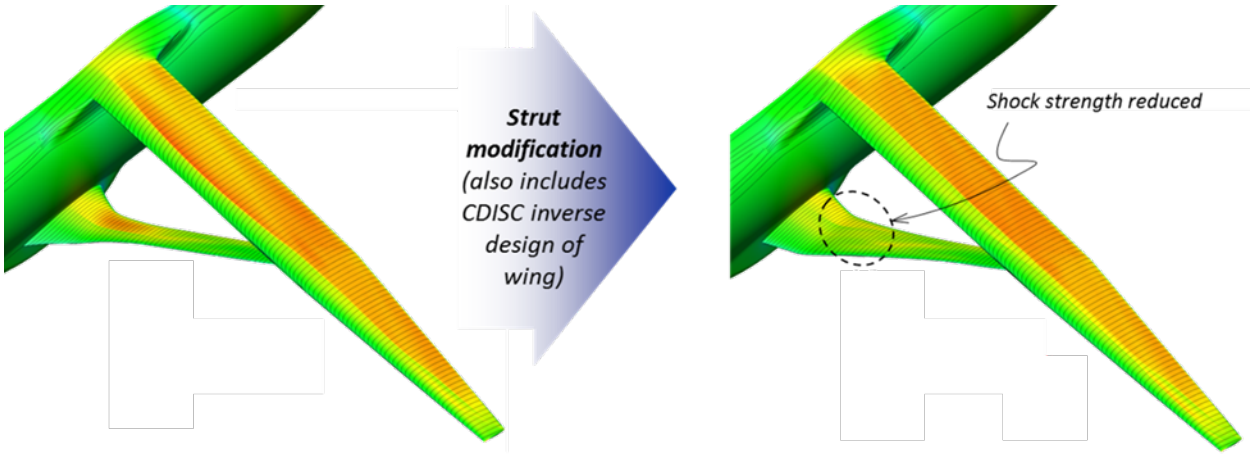


Figure 101 – Strut Planform Modification Reduced Peak Cp on Strut in Transition Region (1104-001-RD_des28 vs 1104-001–RD_des30) at Mach = 0.80, C_L = 0.695, Re_{mac} = 14M.

Aerostructural Investigation of Jury Strut Material

In the course of the –RD configuration optimization, a more detailed study of the strut structure was initiated in order to determine the impact on vehicle weight. In this study, the aerostructural sizing capability in TRANAIR was used to vary jury-strut spanwise location for a variety of different strut materials. EI and GJ stiffness constraints were updated from a baseline set as the jury-strut was relocated, then structural sizing was conducted throughout the span of the strut with different materials defined on each side of the strut to identify the lowest weight, stiffness-feasible jury-strut location. All composite, titanium, and steel structural boxes were analyzed outboard of the jury-strut. In addition, forward and aft spar locations were varied as well. Based on the results of the study (shown in Figures 102 and 103), an updated jury-strut location range was identified: an all-composite outboard strut had a feasible span location range from Y≈425” to 435”, while the steel outboard strut was feasible inboard of Y≈435”.

The finalized jury strut location (Y=425”) was determined based on a combination of the structural design requirements (detailed in this section) in combination with the aerodynamic design considerations detailed in Section 4.1.3.4.

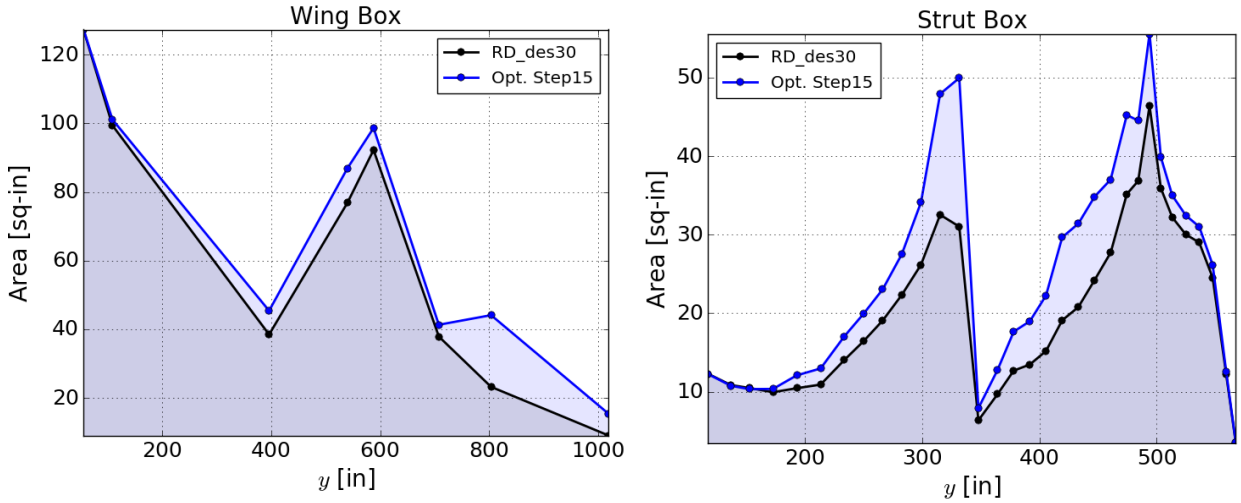


Figure 102 – Aerostructural optimization results for a composite-steel strut and composite wing comparing the seed and optimized geometry structural sizing.

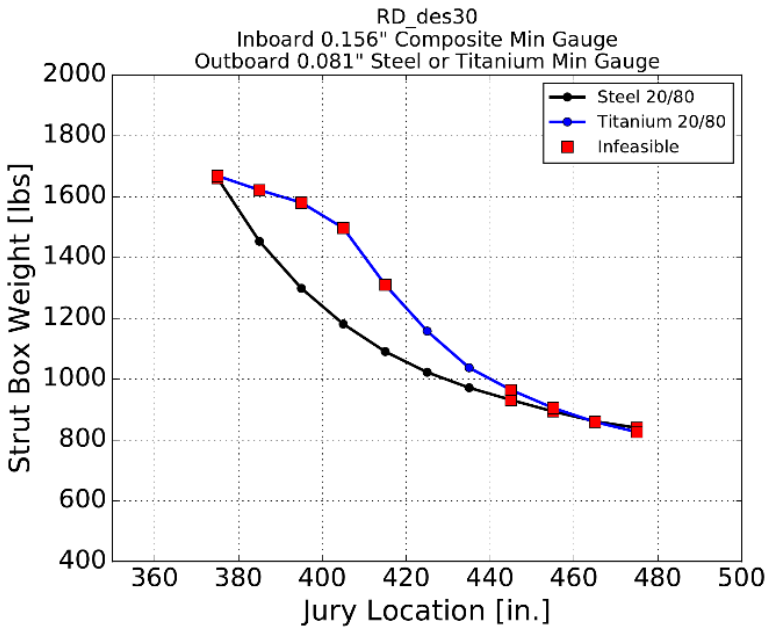


Figure 103 – Jury-strut location study results with multiple materials and structural box sizing. Weight and stiffness feasibility results are shown for forward/aft spar locations different x/c locations along the local chord.

4.1.2.6 *Configuration 1104-001-RE – Offset Strut Aerodynamic Design*

One of the most challenging aspects of the strut-braced wing design is the junction region between the wing and strut. The design challenges in this region are both aerodynamic and structural. From an aerodynamic perspective, at transonic cruise speeds, the high-velocity channel flow in the corner between the wing-strut juncture has a tendency to develop a strong shock. To mitigate this concern, the juncture is aerodynamically shaped in such a way as to reduce the flow velocity and acceleration within this channel. However, while the Baseline Strut concept

(Figure 104a) is the simplest and most light weight structural concept from a wing-strut attachment concept, the wing structure is locally compromised by a 'scalloping' of the lower wing surface proximate to the strut attachment. As a result, there are practical limits to how much wing scalloping is acceptable from a structural standpoint. An alternative concept to the straight (baseline) strut attachment concept would be to offset the strut from the wing and design a curved beam/fitting to transfer the strut load into the wing (Figure 104b). This concept would ideally preserve the continuity of the wing structure. However, the curved fitting required to transfer the load from the wing into the strut would have substantial strength requirements of its own. Therefore, it is necessary to investigate the implications of these attachment concepts from both a structural and aerodynamic perspective. The aerodynamic aspects of the offset strut design are described below.

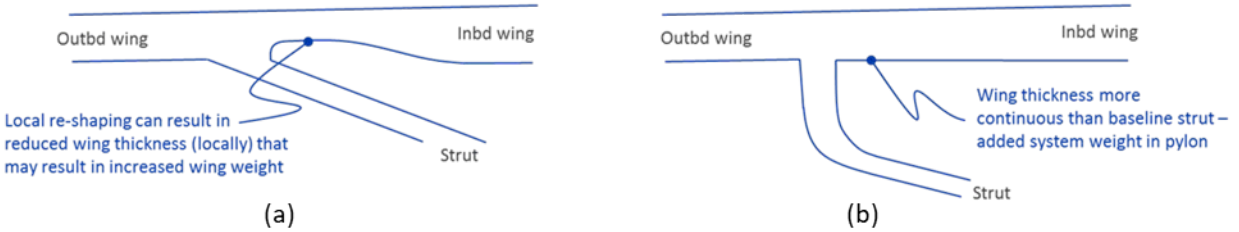


Figure 104 – Strut Concpt a) Baseline Strut and b) Offset Strut (cartoon)

In order to make a preliminary investigation of the offset strut's effect on the aerodynamic performance of a TTBW aircraft, a structure-generated volumetric constraint was required, around which an aerodynamic fairing could be sized and designed. The constraint used in the analysis was based on the working offset strut concept at that time, which was comprised of a standing leg that extended 9.1" below the wing surface, which then connected to a curved beam/fitting with a clevis located 20.0" below the wing surface. An aerodynamic fairing was tightly wrapped around this constraint (refer to Figure 105).

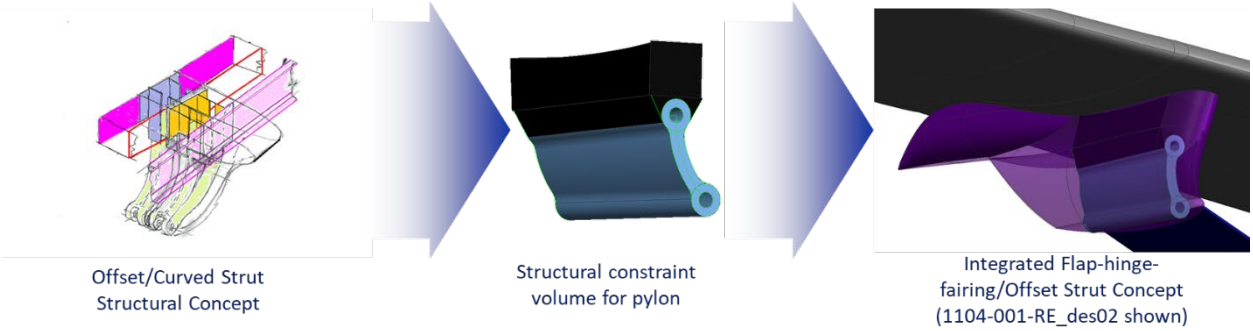


Figure 105 – Offset Strut Structural Requirement used in Design.

One of the features of the new offset strut fairing was the integration/collocation of the fairing with a flap hinge fairing. In order to wrap such a significant structural member with an aerodynamic fairing, an airfoil of high thickness/chord ratio must be installed. Ideally, the size of

the fairing is minimized. However, the location of the fairing makes the integration with the wing particularly challenging. It was shown in Phase III (5) that a secondary aerodynamic fairing (referred to in the previous design as a 'typhoon' fairing) was required to be installed on the back of the offset fairing in order to eliminate a region of flow separation behind the pylon, as shown in Figure 106.

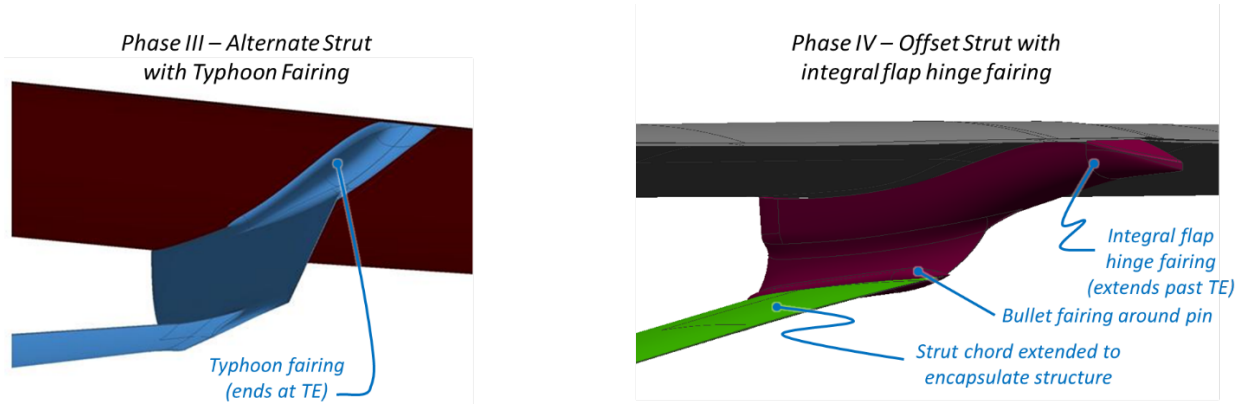


Figure 106 – Alternate and Offset Strut Fairings from Phase III and Phase IV.

Once the initial aerodynamic fairing was created, it was analyzed in OVERFLOW. The initial design of the pylon (shown in Figure 107) had some shock-induced separation on the outboard side, a large region of flow separation on the inboard side, and a strong shock on the upper side of the strut. Similar to the approach used for 1104-001-RC, manual design adjustments were made to the fairing and local strut geometry to reduce the severity of these flow features – changes to theleading edge radius, local airfoil droop, toe-out of the strut attachment, and a large localized wing bump were all required to address these areas.

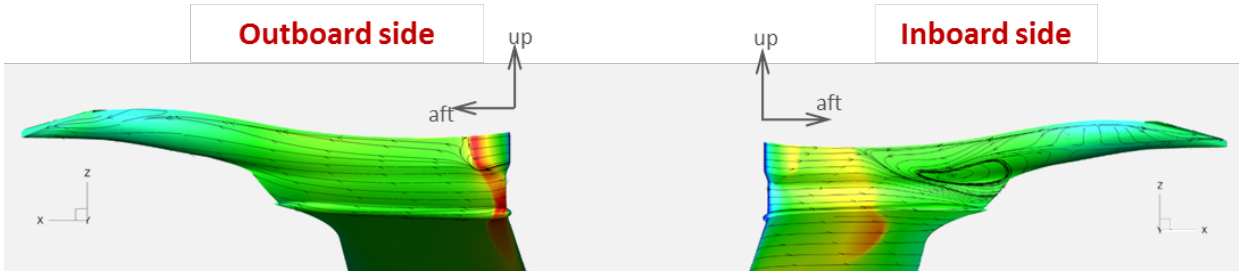


Figure 107 – OVERFLOW analysis of starting offset strut fairing geometry showed significant flow separation on the inboard and outboard sides at Mach = 0.8, C_L = 0.695, Re_{mac} = 14M.

The end result of the changes to the design are shown in Figure 108. Although this design has not undergone significant design optimization, the regions of flow separation and the strut upper surface shock have been eliminated.

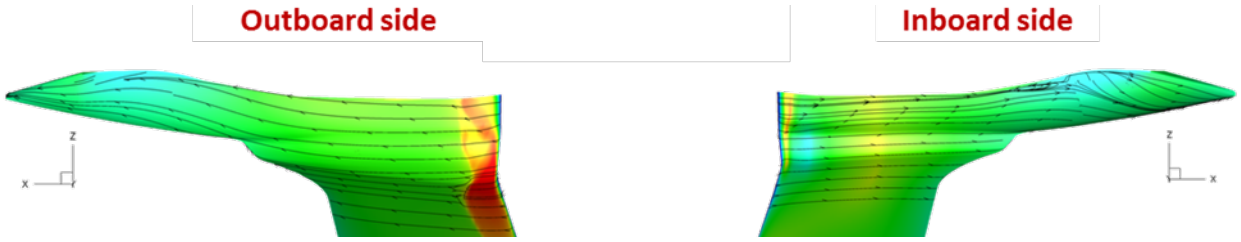


Figure 108 – OVERFLOW analysis of final offset strut fairing geometry at Mach = 0.8, C_L = 0.695, Re_{mac} = 14M.

When tracking these design changes at the configuration level, it is evident that the aerodynamic performance of the –RE offset strut configuration is essentially equivalent to the performance of the -RC baseline strut configuration. This performance comparison includes a flap hinge fairing that is not included in the baseline strut solution. Since the offset strut has a relatively thick airfoil section wrapped around it as a fairing, there is a high degree of synergy to include the flap hinge fairing in the offset strut to minimize drag of the vehicle as a whole.

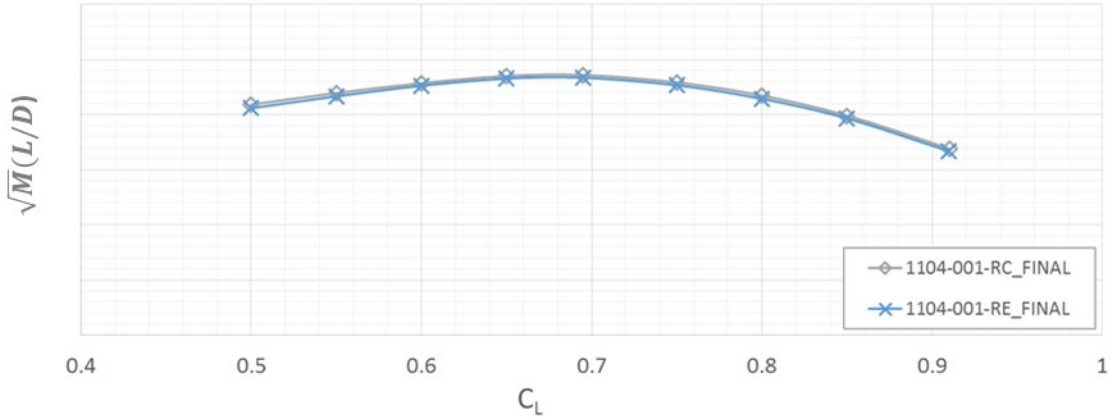


Figure 109 – Comparison of baseline and offset strut performance at Mach = 0.80 Re_{mac} = 14M.

One of the primary objectives of the offset strut design was a targeted reduction in the severity of the required wing shaping near the wing-strut juncture. While the baseline strut requires significant shaping (local thinning of the wing section), it was the hope that the offset strut could reduce this severity, restoring the structural depth of the section. The wing airfoil for the baseline strut configuration has been significantly thinned (as shown in Appendix Figure A.25) in order to prevent the formation of a strong shock in the wing-strut channel. Therefore, the basic premise that the offset strut can be at least aerodynamically similar to the baseline strut without significant thinning of the local wing section appears viable. That being said, performance at the vehicle level would have to trade the added weight of the offset strut attachment as compared to the increase in wing weight required to locally thin the wing with the baseline strut attachment concept.

Throughout this phase of work the offset strut concept has been in continual development. The latest revision to this concept is shown in Figure 110.

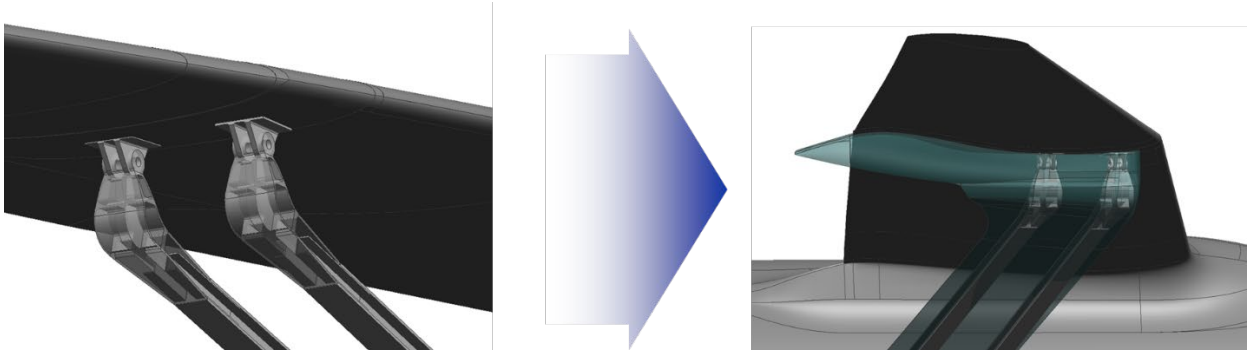


Figure 110 – Updated Curved Beam Strut Attachment.

While the aerodynamic and structural performance of the offset strut configuration remains of interest, challenges in adapting the optimization process to this geometry along with the parity in performance relative to the baseline strut configuration suggested that it was sufficient to continue with the baseline strut when moving into the optimization phase of design. For this reason, the 1104-001-RF configuration was not investigated in detail.

4.1.3 Regions of Special Consideration

The TTBW configuration has several regions where special attention is needed in regard to design. Many of these regions are not typical areas of design focus for low-wing cantilevered aircraft, but can have a large effect on the performance of the aircraft.

4.1.3.1 *Wing-body fairing Design*

For conventional cantilevered low-wing designs, the shape of the wing-body fairing, which nominally encapsulates the landing gear and additional equipment, does not have a first-order effect on the aerodynamic performance of the vehicle. For a high-wing aircraft in which significantly more lift can be carried over top of the body, this region takes on a higher importance. And, in the case of a TTBW configuration, that importance increases further still since the thin, high aspect ratio wing has considerably less volume to host systems, fuel, and equipment than a cantilevered wing design with a Yehudi on the inboard wing. The proper design of a wing-body fairing for a TTBW aircraft therefore provides a significant opportunity to increase aircraft performance, and provide volume for fuel and systems.

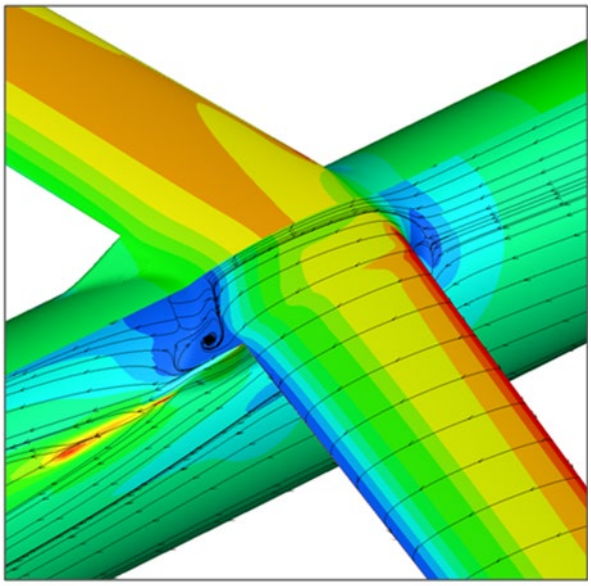


Figure 111 – OVERFLOW solutions of the original wing-body fairing design at the start of Phase III. Contours on the left of the symmetry plane are C_p, contours on the right are C_f at Mach = 0.745, C_L = 0.73, Re_{mac} = 12.3M (5).

The original loft of the wing-body fairing at the beginning of Phase III used a fairly minimalistic approach to closing the wing-body intersection. While this approach minimizes the wetted area of the vehicle, it has an obvious negative effect on the drag of the vehicle resulting from several regions of flow separation and pressure drag as illustrated in Figure 111 and Appendix Figure A.26. In addition, at cruise, the vehicle lift does not appear to carry over the body to the extent possible. The performance of the wing-body region at low speed was also examined to ensure compatibility of the design with high-lift systems integration.

The wing-body fairing was first examined for its performance at high-speed. As stated, the design objectives were to: a) remove any areas of flow separation, b) increase body carry-over lift without the formation of a strong shock across the vehicle symmetry plane, and c) provide additional volume for systems, fuel, etc. Fortunately, many of these objectives drive the design in a similar direction, producing a fairing of increased volume relative to the starting geometry. If this volume is allocated properly, the fairing can also have a net positive effect on the vehicle's area ruling, providing additional benefit at high speed.

The first design of an updated fairing (shown in Figure 112 and Appendix Figure A.27) reduced the drag of the vehicle significantly. However, the shock on the top of the body remained locally strong, thus indicating room for improvement in the design. In addition to examining the design at cruise speeds, the vehicle was also analyzed at low speed (M=0.2) to ensure that the high-lift system would not be adversely impacted by the design. When analyzing the clean wing-strut geometry (no wing leading or trailing edge devices), a significant vortex was discovered emanating from the wing-body juncture. The flow had the characteristics of a strong junction vortex. Since this vortex had the potential to interact with the strut or tail surfaces downstream

or could cause substantial unsteadiness of the vehicle in the wind tunnel, a new series of designs sought to weaken or eliminate this vortex.

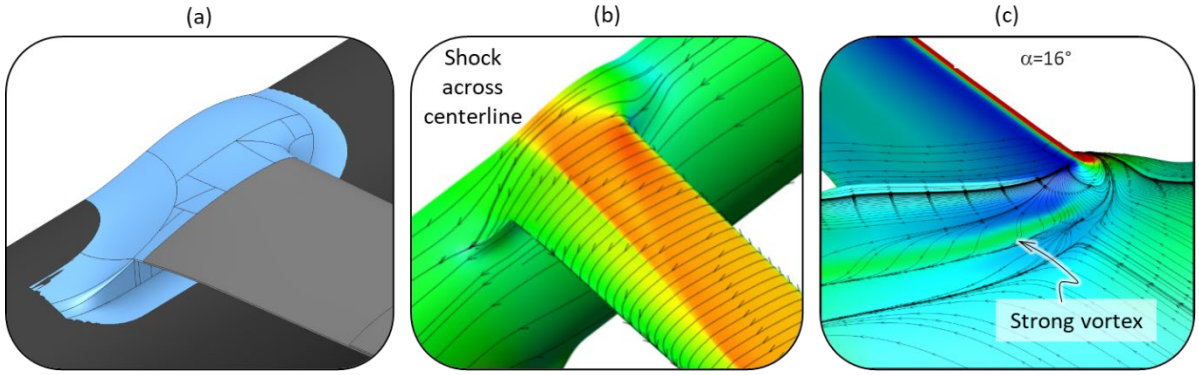


Figure 112 – First Attempt at a re-lofted wing-body fairing (a) CAD geometry (b) Mach = 0.80, C_L = 0.695, Re_{mac} = 14M (c) Mach = 0.20, α = 16°, Re_{mac} = 13M.

The first set of designs analyzed employed a leading edge horn (or strake) to break up the formation of the vortex. One of those designs (shown in Figure 113 and Appendix Figure A.28) met many of the design criteria desired for the fairing (particularly low drag at cruise), but were unsuccessful in breaking up the vortex at low speed. The final design (Figure 114) employed a strake with a reversed curvature (when observed in a planform view). This geometry successfully reduced the drag of the vehicle at cruise, significantly weakened the junction vortex, had a larger internal volume (for fuel and aircraft systems), and also provided wiping/sealing surfaces for the wing's leading and trailing edge high-lift devices.

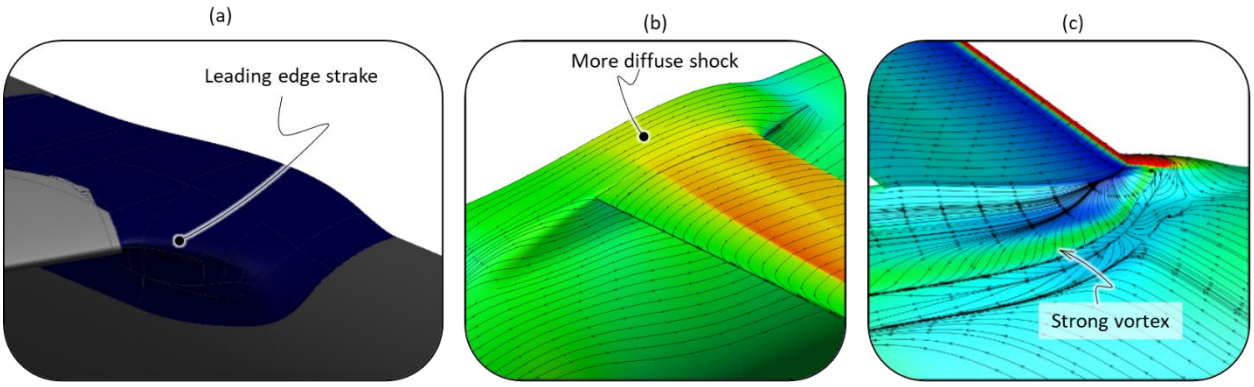


Figure 113 – Revised fairing increases volume, reduces shock strength, but strengthens the low-speed vortex (a) CAD geometry (b) Mach = 0.80, C_L = 0.695, Re_{mac} = 14M (c) Mach = 0.20, α = 16°, Re_{mac} = 13M.

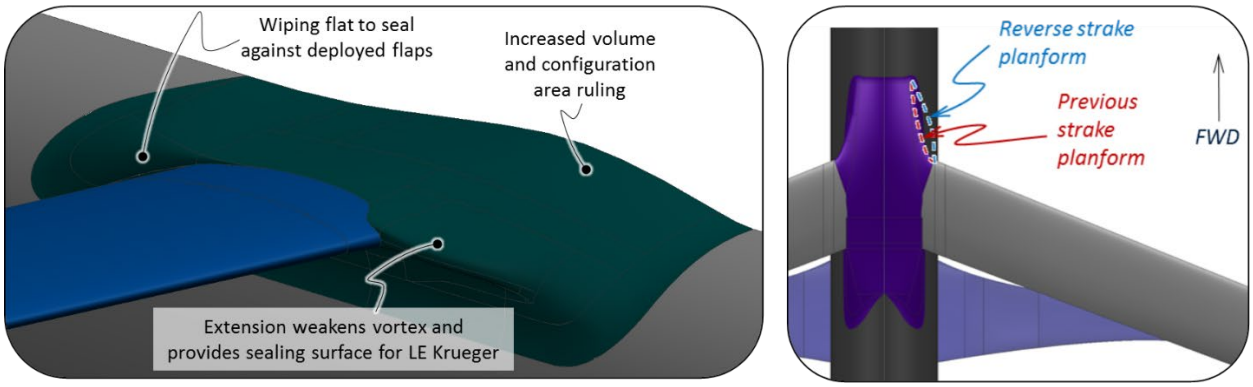


Figure 114 – Reverse planform wing-body strake.

4.1.3.2 *Baseline Strut Wing-Strut Juncture Design*

In order to keep interference drag to a low level when operating at transonic conditions, the wing-strut juncture requires special attention in design. The wing and strut surfaces must be designed in such a way that at cruise conditions, the flow into the juncture does not culminate in a strong shock. The flow interactions between the surfaces results in a highly three dimensional design space. Previous design studies (Phase III) showed that a local downloading of the strut aerodynamic load near the wing-strut juncture – the result of localized wing and strut shape tailoring – is the most critical component to wing-strut juncture design. However, in the course of this contract, additional investigations have focused on the compatibility of this juncture off-design, with special emphasis on low-speed operations and high-C_L operation (near buffet).

Low-Speed Compatibility

Preliminary high-lift analysis of the configuration (with high-lift surfaces deployed) showed that the original wing-strut fairing design had a significant negative effect on aircraft stall at low speed. The primary issue with fairing compatibility at low-speed was due to the forward extent of the fairing. In order to sufficiently blend the wing and strut together, the fairing extended forward on the underside of the wing, approaching the wing leading edge. While this design represented a low-drag solution at cruise, it resulted in a cutout (or spanwise gap) in the wing's leading edge protection during high-lift operations. At low speed and high angle of attack, this cutout created a large region of separated flow, which dictated the maximum lift coefficient of the entire aircraft. For this reason, the design of the wing-strut fairing was revisited with special attention on high-lift system compatibility.

While there are potential mechanical solutions that could 'open' up the forward extent of the fairing in order to deploy a leading edge device, it was believed that such a concept represented a degree of mechanical complexity that was not desirable. Therefore, the forward extent of the fairing was trimmed back to a chordwise extent that would allow for a conventional Krueger mechanism to deploy from the wing lower surface. (refer to Figure 115).

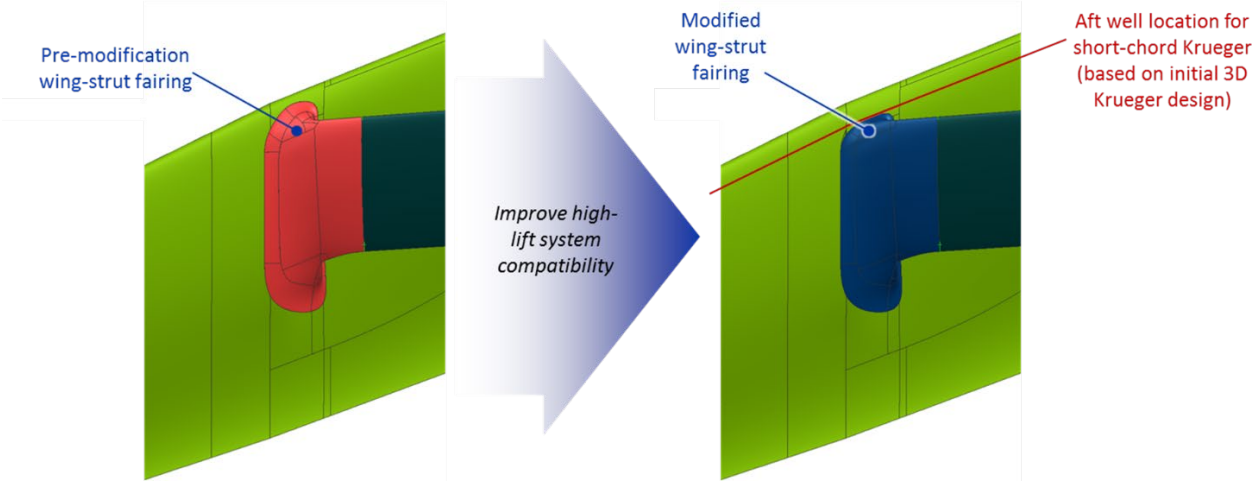


Figure 115 – The wing-strut fairing was trimmed back to enable compatibility with a leading edge Krueger.

The cutback fairing geometry was then analyzed throughout the aircraft's operational envelope to determine its associated drag penalty as compared to a more blended solution. OVERFLOW analysis (results shown in Figure 116 and Appendix Figure A.29) determined that the drag penalty was ~0.1 cts at the design condition. Given the potential mechanical complexity (and associated cost), it was decided that this represented an acceptable compromise to aircraft performance.

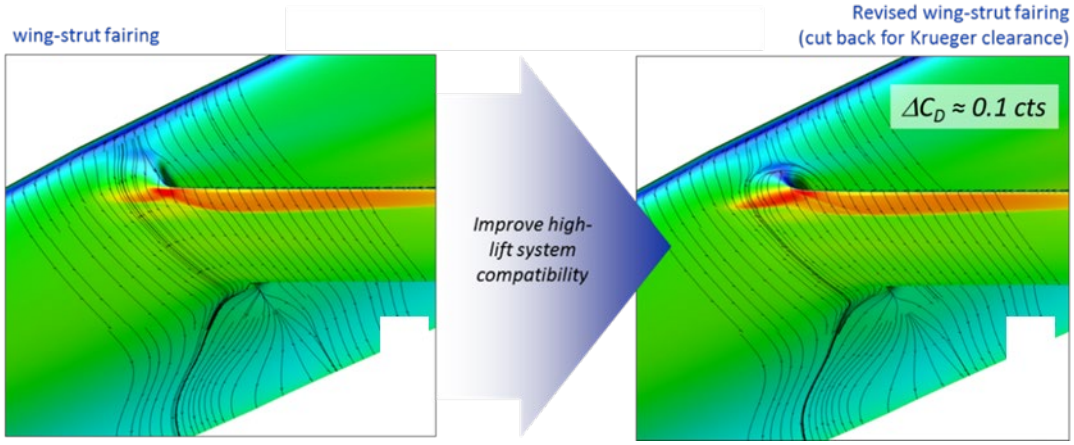


Figure 116 – Revisions to the wing-strut fairing to ensure high-lift system compatibility.

High-Speed Compatibility

In addition to high-lift compatibility requirements, the design of the wing-strut juncture at off-design high-speed conditions was also considered. A study was undertaken to determine the effects of a plain flap deflection in the wing-strut juncture region (extent shown in Figure 117) to determine if such a device could alleviate any potential undesirable flow conditions within the channel (such as the formation of strong shocks) when operating across the flight envelope. The flap would achieve this end by providing the ability to alter the mass flow into the wing-strut channel, thereby affecting local flow conditions. If the internal channel flow was critical, the flap could deflect up to spill flow out of the channel. If the underside of the strut becomes critical

(such as at very low lift coefficients), the flap could deflect down to mitigate shock strength on the underside of the strut.

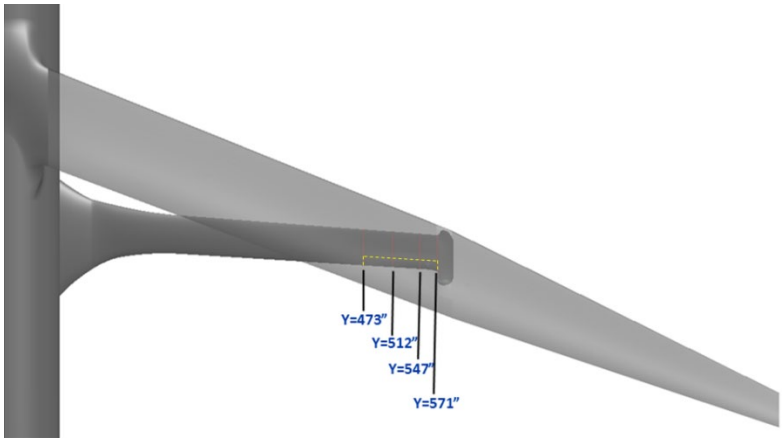


Figure 117 - Strut Flap Definition

This study compared the effects of three different spanwise flap extents across a range of deflection angles (-2°, -4°, -10°): a 'large' flap (extending from Y=473" to 571"), a 'medium' flap (extending from Y=512" to 571"), and a 'small' flap (extending from Y=547" to 571"). The study assumed a 20% chord simple-hinge device of similar construction to an aileron. This device would be considered a fast-moving device that is a part of the aircraft control system, rather than part of the aircraft's high-lift system. Appendix Figure A.30 illustrates the strut flap geometry and the three different span extents.

The various flap deflection angles and extents were analyzed in OVERFLOW across a range of lift coefficients and Mach numbers to determine aircraft performance sensitivities to device configuration. In general, the results showed that system performance could be improved off-design, and that channel shock strength could be controlled via deflection of a strut flap. While the study did not seek to determine the 'optimum' size and deflection of a strut flap for this configuration, the flap was shown to provide a benefit across a wide range of flow conditions. The effects of the strut flap deflection at a high lift coefficient off-design condition are shown in Appendix Figure A.31 and the effects at a high Mach number off-design condition are shown in Appendix Figure A.32.

Analysis of the strut flap across a range of lift coefficients showed successful mitigation of channel shock strength via deflection of the strut flap. In the case of the -4° deflection, the channel shock was virtually eliminated. Varying lift coefficient produced trends showing a more localized benefit to system performance via flap deflection in that the smaller flaps were more effective at improving system performance than the large flap.

In contrast, when increasing vehicle Mach number the greatest performance benefit came from the large flap span. This suggests the configuration benefits from a more global effect, in which the channel Mach number is decreased across a larger region of wing-strut interaction.

The range of benefits shown by strut deflections of various span extents shows that a strut flap would be a valuable tool for inclusion in typical aircraft spanload control systems, providing improved flexibility in aircraft operations across a range of conditions. In addition, the deflection of a strut flap has been shown to mitigate shock strength in the wing-strut region, and may provide additional control for the mitigation or alleviation of buffet-causing flow features at the farthest extents of the flight envelope. It is therefore possible that given these findings the basic strut design could benefit from a relaxed set of design requirements in which more aggressive strut geometries could be examined.

4.1.3.3 *Flap Hinge Fairing Design*

As the design of the TTBW vehicle has increased in maturity, additional details of a complete aircraft configuration have been included in the design. This phase of the TTBW design effort has sought to include low-speed (high-lift) design requirements into the final high-speed geometry. Flap Hinge Fairings (FHFs) provide an aerodynamic covering for the mechanisms that deploy the flaps during high-lift operations (Figure 117).

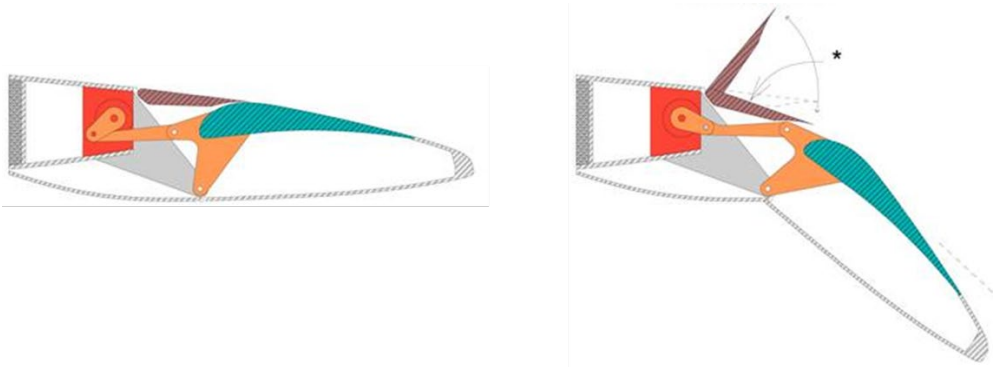


Figure 118 – Flap articulation mechanism schematic (14).

While at this time the final TTBW high-lift architecture has not yet been determined, a representative set of fairings has been analyzed in order to determine if any unique considerations need to be made in order to accommodate wing-strut interactions. In particular, the outboard-most fairings may have a significant interaction with the strut as it approaches the wing-strut join region. The fairings size (volume) and shape being utilized for the study are approximately representative of a simple-hinge with drooped spoiler trailing edge high-lift architecture. Given the uncertainty surrounding the final high-lift architecture, a detailed analysis of the flap high-lift structure has not been completed at this time. Therefore, the FHFs examined represent a ‘typical’ set of fairings for the control system planform detailed in Section 5.3.

However, while the strut poses some unusual possibilities for fairing-strut aerodynamic interaction, it also provides a unique opportunity at a system level. The short-chord high aspect ratio wing of the TTBW has less chordwise extent available for the closeout of the engine pylon. In SUGAR Phase III (5), it was shown that some substantial aerodynamic filleting was required to mitigate the adverse pressure gradients created by the superposition of the wing and engine pylon closeouts. This problem was also present in the Phase III alternate strut pylon design, which required the use of a 'typhoon fairing' in order to mitigate the closeout. However, in the case of the Phase IV design, it is possible to take advantage of design synergies coming from integration of the wing and engine pylon attachments with the FHFs. Both the wing-strut join (Figure 118) and the engine pylon (Figure 119) provide a benefit for system-level drag reduction by collocating these fairings, thereby reduced the wetted area and frontal area of the FHFs as compared to a an unintegrated solution. This also provides the potential for a structural benefit in the form of potential load-sharing between the support structures. The configuration with all FHFs installed (shown in Figure 120) highlights the proximity of the 2nd-most-outboard FHF to the proximity of the strut.

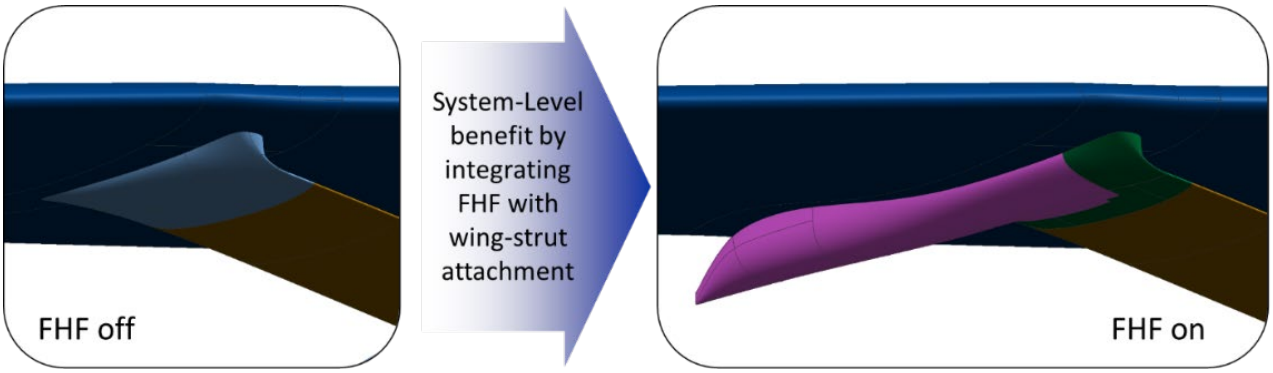


Figure 119 – Wing-strut fairing with integrated FHF.

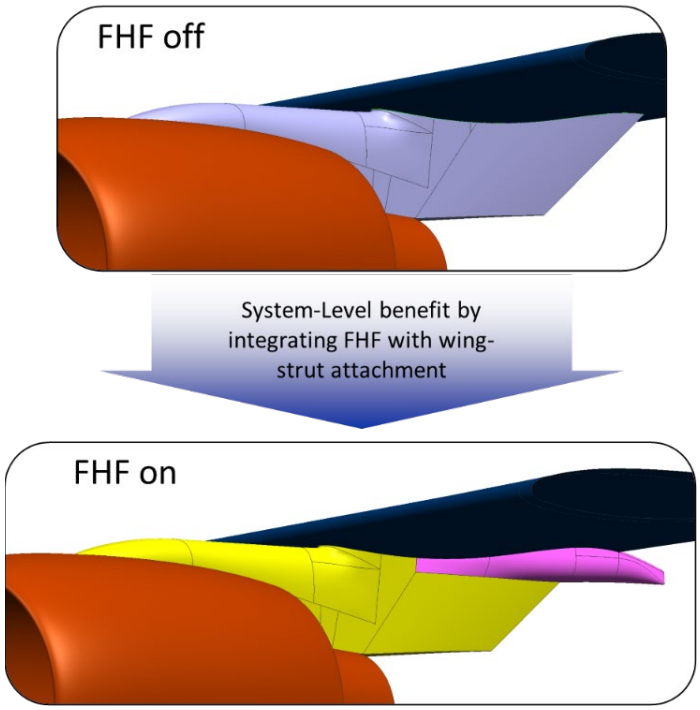


Figure 120 – Engine Pylon fairing with integrated FHF.

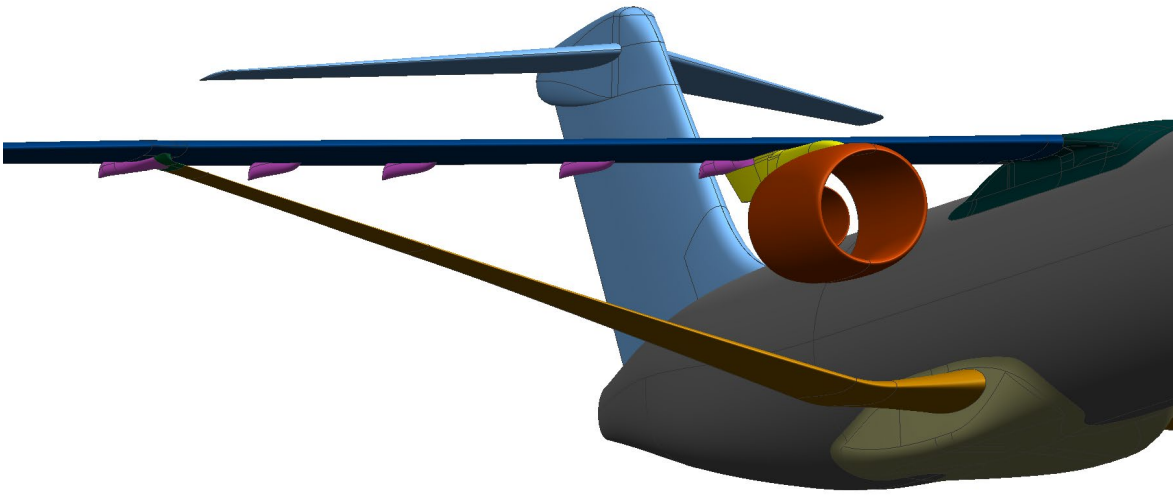


Figure 121 – Configuration with all FHFs installed.

The FHFs were analyzed in OVERFLOW to determine if the strut-FHF aerodynamic interactions resulted in any undesirable flow features, such as a significant strengthening of the channel juncture shock. The OVERFLOW skin friction coefficient results with the unintegrated FHFs added to the configuration are shown in Figure 122 and Appendix Figure A.33.

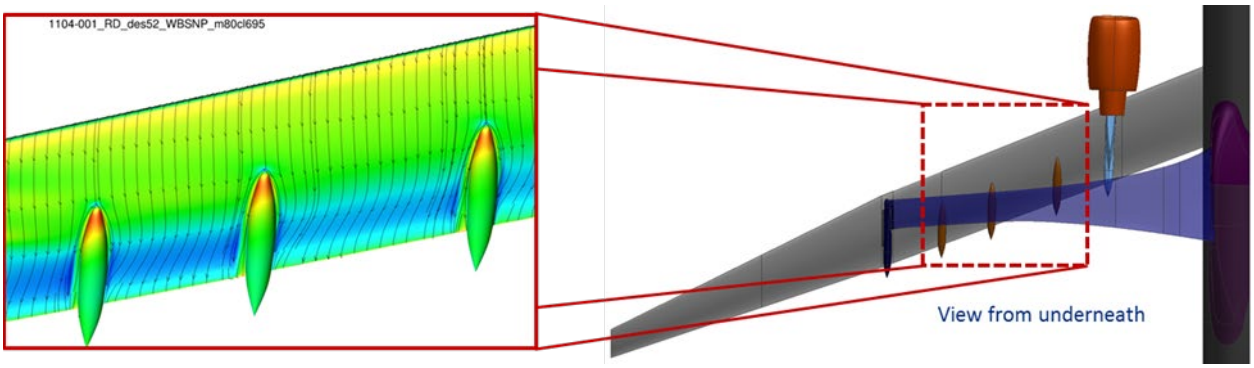


Figure 122 – OVERFLOW C_f results of the flow around the middle (unintegrated) FHFs (Mach = 0.80, C_L = 0.695, Re_{mac} = 14M).

The results of the OVERFLOW analysis showed that the net effect of the FHF installation was a general slowing of the flow into the channel, particularly near the wing-strut juncture. This effect is indicated in Figure 123 (and Appendix Figure A.34) by the reduction in severity of flow acceleration around the upper surface of the strut leading edge. The installation also had the net effect of increasing the lift of the wing (creating a corresponding decrease in the strut lift), which resulted in a decrease in vehicle angle of attack of ~0.04° at the design condition.

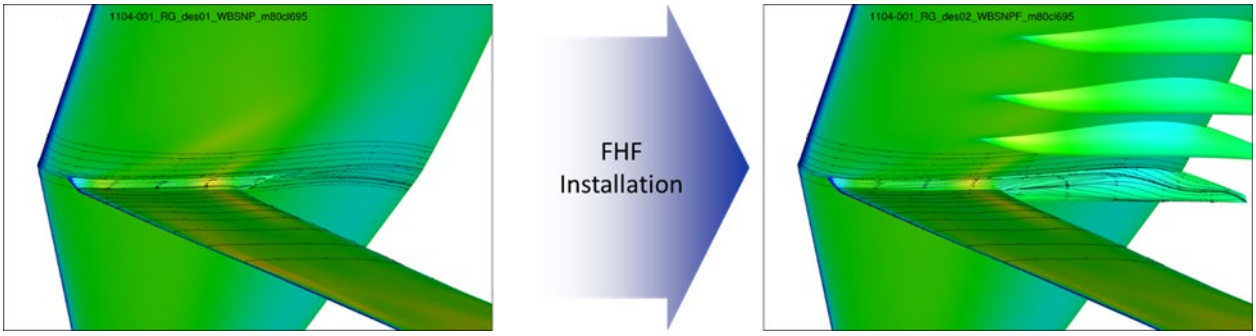


Figure 123 – Flap Hinge Fairing (FHF) installation on the wing-strut fairing surface C_p (Mach = 0.80, C_L = 0.695, Re_{mac} = 14M).

In general, the integration of the FHFs into the solution were not found to have any significant negative effect of the cruise performance of the vehicle, with no special areas of concern related to FHF-strut interaction. The net change in drag for FHF installation was roughly consistent with drag increments of other aircraft operating at these conditions.

4.1.3.4 *Jury Strut Design*

Over the course of Phase IV, the location of the jury strut has been under consideration. The jury location (determined in Phase III; inboard jury location shown in Figure 124), was based on a structural design laid out in SUGAR Phase II (2; 4), and was coupled to EI/GJ design constraints. The location and structural constraint of the jury position was maintained as a constraint during the M=0.745 aerodynamic design task completed in SUGAR Phase III. However, when the aircraft geometry was updated for a M=0.8 planform, the location of the jury strut location and structural constraint was revisited. During the design phase of the M=0.8 1104-001-RD configuration, it became clear that a revision to the strut planform (and associated jury strut location) was

required (refer to Section 4.1.2.5 for details). This revision moved the jury strut ~40" outboard of the Phase III location (center jury location shown in Figure 123). Following the aerostructural design optimization (described in detail in Section 4.1.1.3), the jury-strut attachment was finalized at the outboard-most location shown in Figure 124 (Y=425").

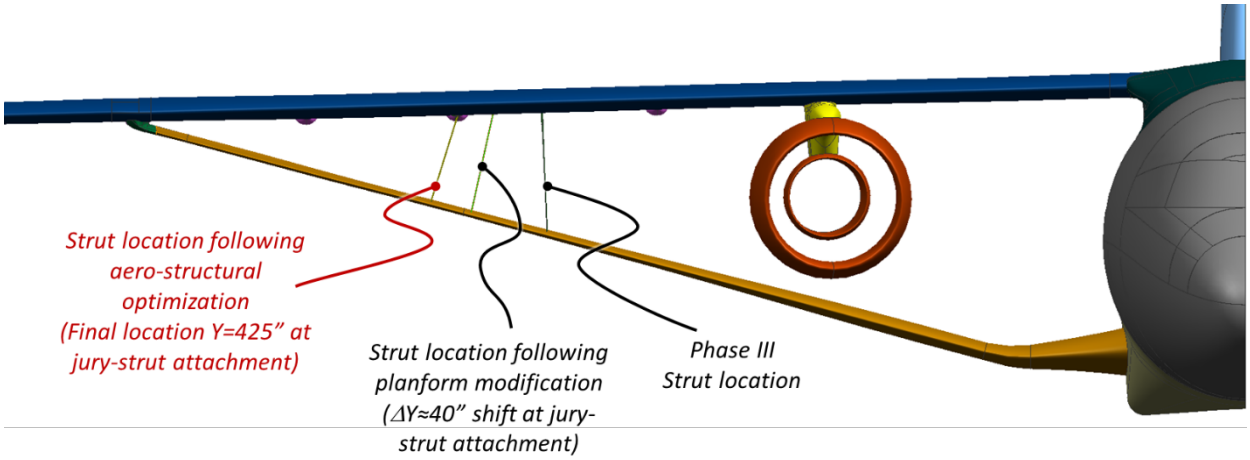


Figure 124 – Design Progression for Jury Strut Location.

When the final jury strut-to-strut spanwise location was chosen, the wing attachment point of the jury was allowed to fluctuate within a small range. Inclusion of the flap hinge fairings into the final aerodynamic design created some location constraints for the jury-wing attachment location due to the potential for aerodynamic interference between the jury strut and FHF. It was therefore decided to collocate the two structures in order to minimize the potential for interference. While this also creates the potential for load-sharing between the jury support structure and flap structural hardpoints, the design of this joint has not yet been examined in detail.

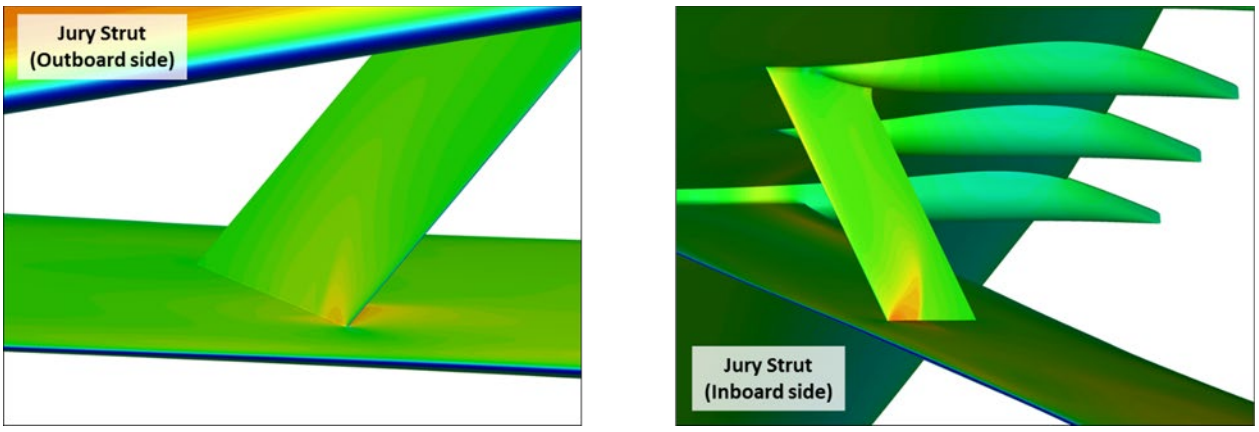


Figure 125 – OVERFLOW results of the final jury strut installation surface C_p (Mach = 0.80, C_L = 0.695, Re_{mac} = 14M).

The final jury strut location (collocated with the FHFs) was analyzed in OVERFLOW to determine the net change in aircraft performance, and to determine if any negative aerodynamic interference results from the intersection of the two structures. The results (highlighted in Figure

125 and Appendix Figure A.35) show a small high-velocity region at the root of the jury-to-strut intersection, with a more pronounced zone of flow acceleration on the inboard side of the jury. While some potential for a reduction in drag may still exist for the jury strut installation, the potential benefit was considered to be too small to warrant additional design effort.

4.1.3.5 *Nacelle-Pylon Design*

The nacelle-pylon installation for Phase IV was initially derived from the nacelle and pylon geometry used during Phase III. However, the nacelle geometry and aft pylon closeout were modified to account for operation at higher freestream Mach number. The nacelle outer mold line was optimized using the Boeing optimization tool MDOPT. The nacelle orientation was then adjusted using MDOPT to reduce total system drag by determining the optimum toe and pitch engine alignment angles.

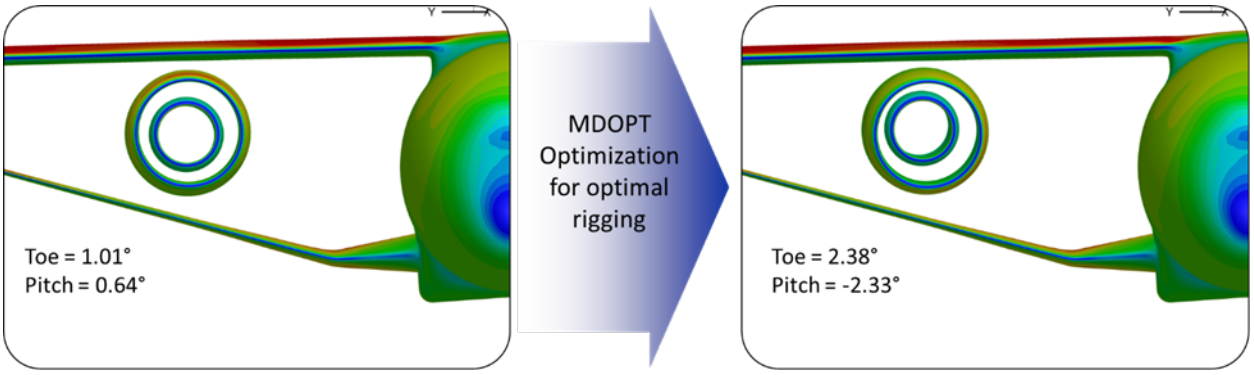


Figure 126 – Nacelle Shape and Rigging were optimized using MDOPT to reduce installed drag (Mach = 0.80, C_L = 0.695, Re_{mac} = 14M).

The MDOPT optimization process reduced the nacelle pitch angle by almost 3.0° from the original location, and toed-in the nacelle an additional 1.37° as shown in Figure 126 and Appendix Figure A.36. However, the results also showed that near the optimum drag location, the drag of the engine installation was relatively insensitive to small perturbations to the orientation of the nacelle, particularly in toe angle. Therefore, the final nacelle orientation was finalized based on a combination of the optimization results combined with design guidance from the propulsion group. The end result was a toe-in angle of ~1.92° and pitch angle of -0.76°.

4.1.4 1104-001-RG – Final Configuration Aerodynamic Performance

The final assessment of the updated M=0.80 high-speed OML was assessed in OVERFLOW for a variety of configurations, starting with the wing-body-strut (WBS), and ending with a 'full-up' trimmed configuration. Based on the confidence gained during Phase III in predicting component increments, the revalidation of the basic configuration building blocks (i.e. body only, body-sponson, etc.) of the configuration are not presented. In addition, the increment for a body-wing-alone configuration (no strut) is not presented since the proper quantification of wing-strut interference would require the development of a wing designed in isolation (i.e. no strut

influence), combined linearly in drag with a strut designed in isolation (i.e. no wing influence to provide a fair assessment of wing-strut interference for a system in which the wing and strut have been designed in tandem). This is consistent with the planned wind tunnel test entry in which wing and strut will only be tested together.

4.1.4.1 *Configuration Details*

Following completion of the high-speed design phase of the program, the configuration underwent a reloft and smoothing process to prepare the final lines. The process included airfoil smoothing, thickness and twist distribution smoothing, renormalization of wing and strut chords to the vehicle planform, and a reshearing of both the wing and strut airfoils. The wing reshear process was primarily focused on producing a geometry that was conducive to the cutout of the high-lift system. Since the leading edge device was more likely to be sensitive to variation in rigging (relative to the wing) across the span, the wing airfoils were resheared to a projection of the Krueger leading edge (in the stowed position) onto the wing reference plane. The reshearing therefore emphasized leading edge smoothness at the expense of a larger variation in trailing smoothness. The results of the reloft process resulted in new twist and thickness characteristics (new twist distributions are shown in Figure 127 and the thickness distribution is shown in Appendix Figure A.37).

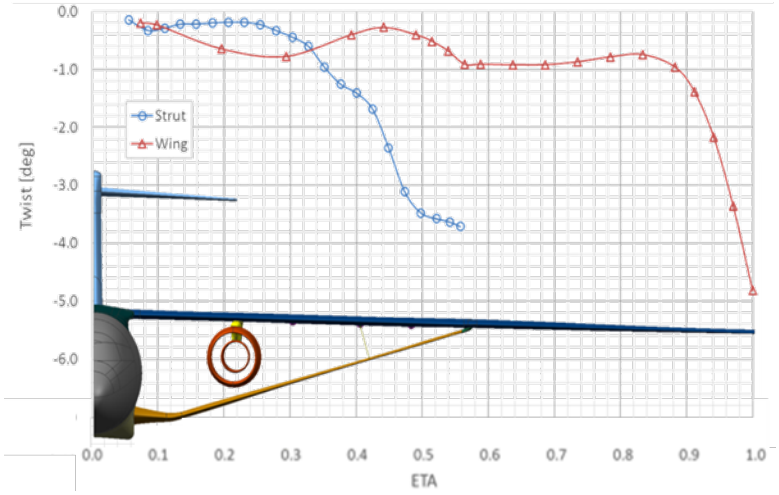


Figure 127. Configuration 1104-001-RG: Final Wing Twist Distributions.

4.1.4.2 *High-Speed Design Results*

The final configuration build-up results for the 1104-001-RG design are presented herein. Results, as acquired from OVERFLOW, are shown primarily for the midcruise design point (M=0.80, Alt=40kft, C_L=0.695), with excursions to high and low lift coefficients where stated. Results shown are for flight wind tunnel Reynolds number only – quantification of low-Re results for wind tunnel application will be presented in a subsequent report (Volume II) following the completion of the planned transonic wind tunnel test in January 2019.

Wing-Body Strut (WBS) Results

The vehicle spanload for the WBS system is shown in Figure 128. The plot shows the breakdown in vehicle lift for the wing and strut individually (red and blue curves respectively) along with the

total spanload (black curve). An elliptical spanload guideline (dashed line) based on the wing-strut contribution to vehicle lift (no body effect) is shown for reference.

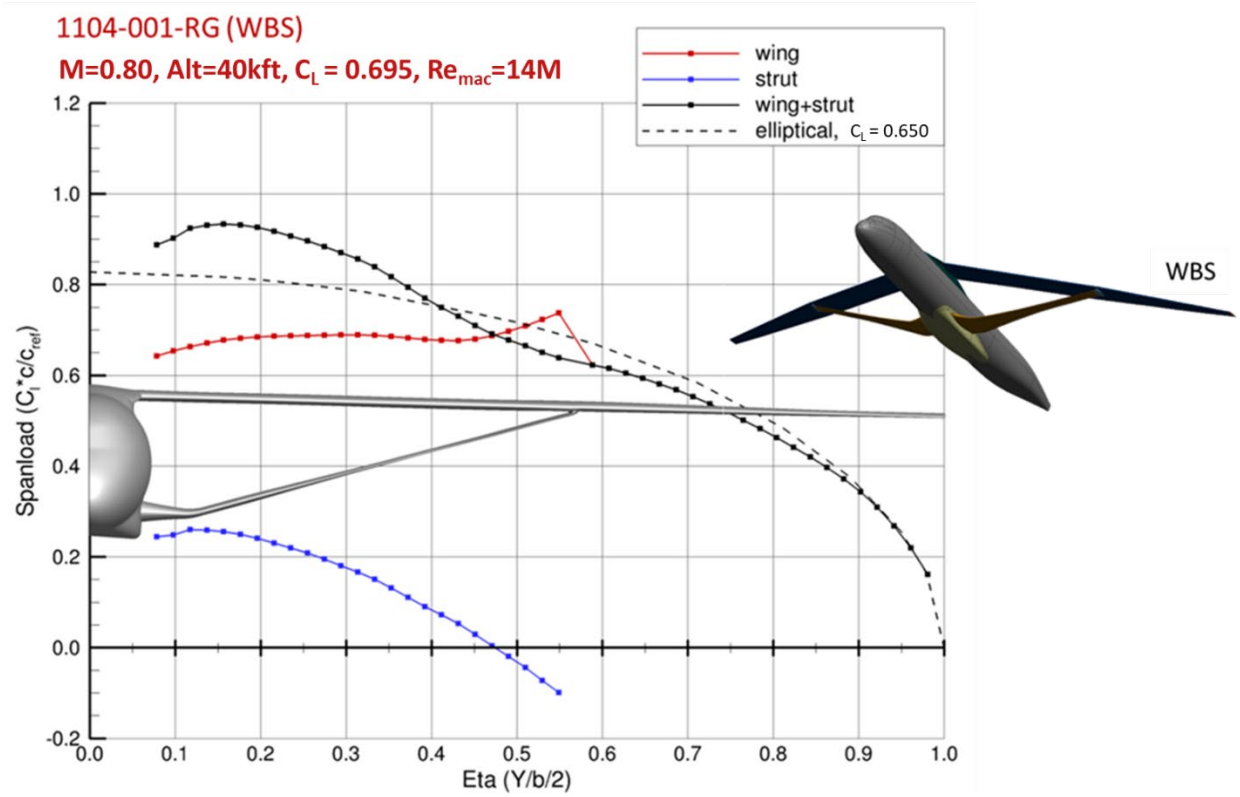


Figure 128 – Configuration 1104-001-RG (WBS) Spanload at the Cruise Design Point (α = 1.51°).

The results in Figure 128 highlight the change in design philosophy from the Phase III design approach. For the M=0.80 design, an active decision was made to increase strut loading from previous levels. This approach was aided by the configuration changes when moving to a higher-Mach design. As highlighted in Figure 129, the increase in wing sweep in Phase IV had a net beneficial effect on the overall performance of the configuration. The most critical aspect of this was an aerodynamic decoupling of the inboard wing and strut flows. While the Phase III design had a more significant 'stacking' of the wing and strut flows, the Phase IV design offset the wing and strut root chords (relative to each other) so that the inboard strut was now located significantly behind the wing root. In addition, the change in overlap also propagated outboard – the regions in which the thickest portions of the wing and strut airfoils overlap near the wing-strut juncture was also significantly reduced. These changes allowed strut loading (particularly inboard) to be increased significantly from earlier designs.

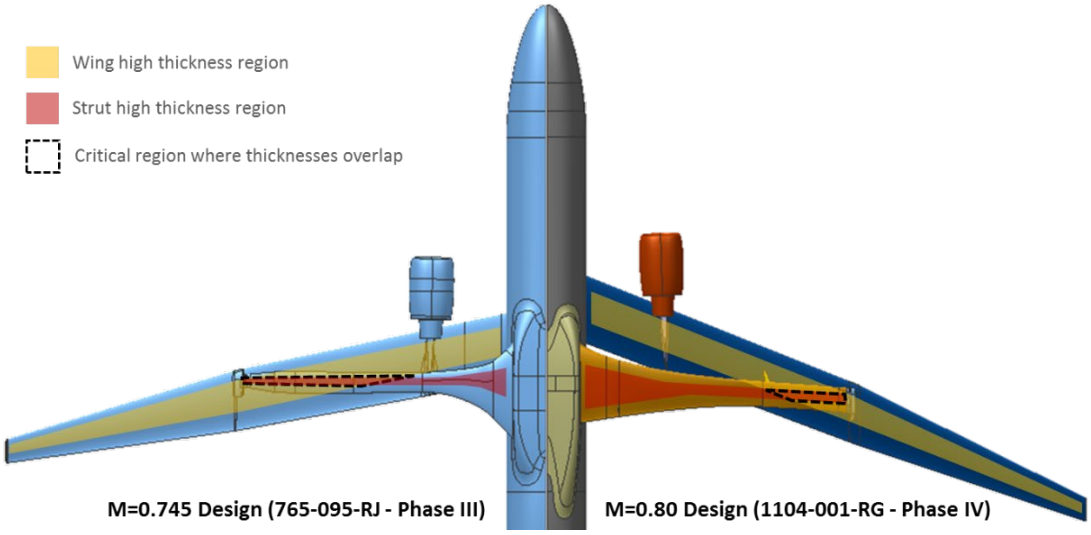


Figure 129 – Comparison of wing-strut overlap regions for M=0.745 design vs. M=0.80 design.

Figure 130 and Appendix Figure A.38 show the surface C_p contours for the WBS configuration (strut displaced for clarity). Although the final geometry was designed with the nacelle and pylon installed, the flow is well behaved over the wing. Inboard strut loading is relatively low as compared to previous designs with shorter chords. Some waviness in pressures on the inboard strut are the result of removal of the nacelle and pylon from the WBS solution.

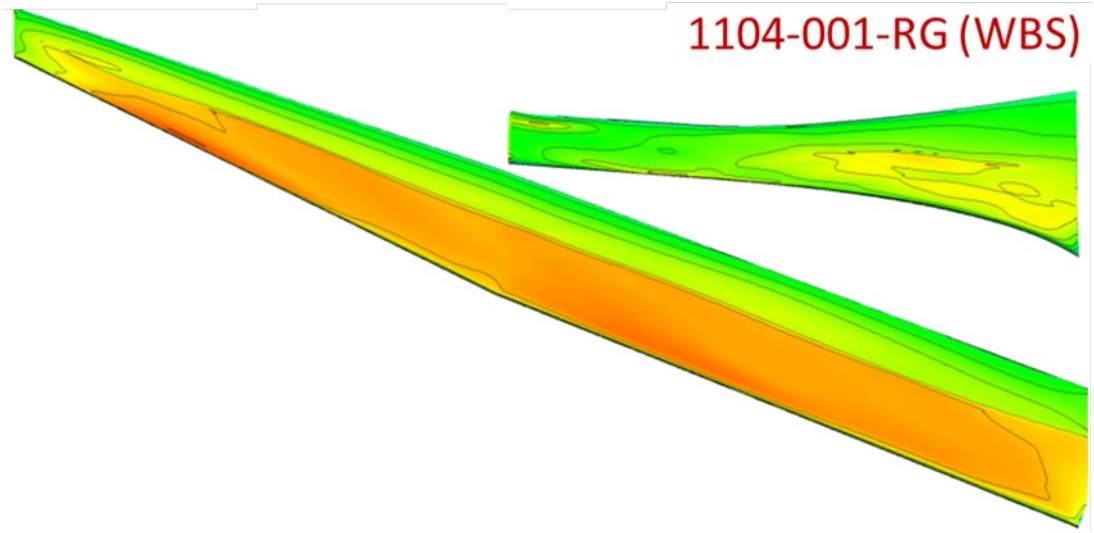


Figure 130 – Wing and Strut surface C_p results from OVERFLOW for WBS Configuration at Mach = 0.80, C_L = 0.695, Re_{mac} = 14M.

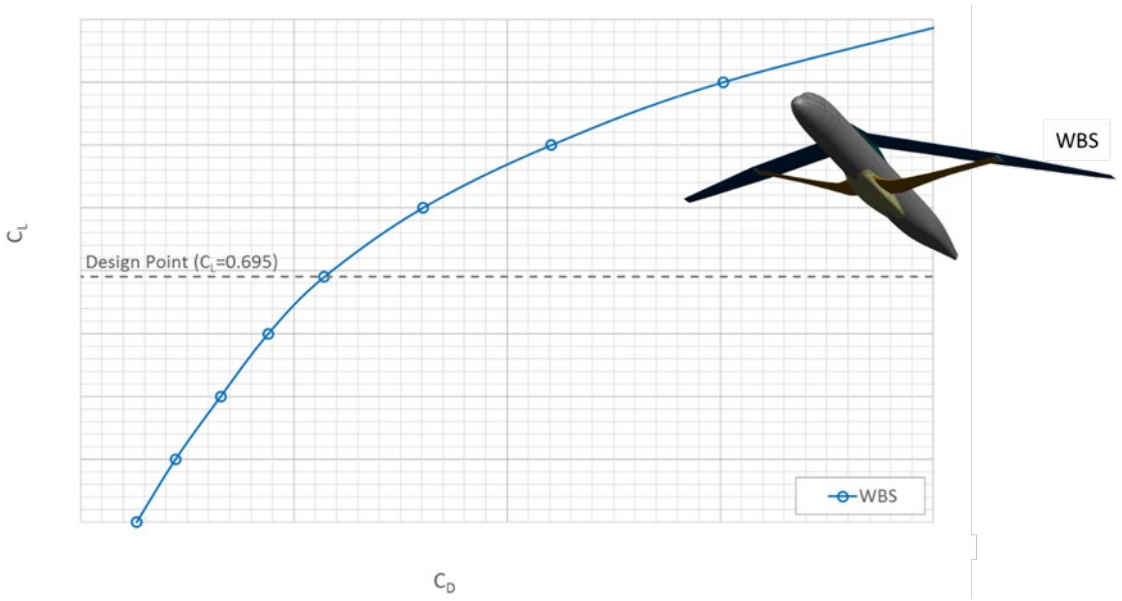


Figure 131 – Drag Polar for 1104-001-RG (WBS) at Mach = 0.80, Re_{mac} = 14M.

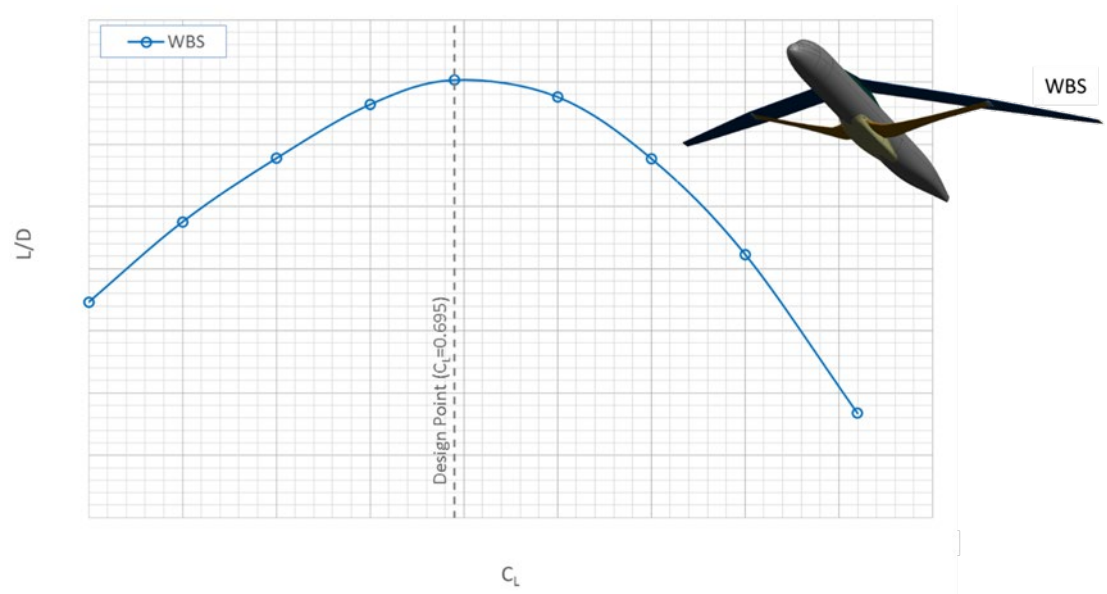


Figure 132 – L/D for 1104-001-RG (WBS) at Mach = 0.80, Re_{mac} = 14M.

Figures 131 and 132 (and Appendix Figures A.39 and A.40) document the performance of the WBS configuration. This configuration is used in the aircraft-level performance analysis to anchor the conceptual methods to the hard CFD data on the configuration. The maximum L/D of the WBS system is just over 27.0 (untrimmed). Additional items added to the configuration (nacelle and pylon, tail, etc.) will reduce the system-level L/D as described in the following paragraphs. The majority of the aerodynamic design and optimization was performance using the WBS configuration, with both manual methods and inverse design tools CDISC (8) used to refine the optimized configurations for the effects of the installed nacelle and pylon.

Wing-Body-Strut-Nacelle and Pylon (WBSN) Results

The final stage of the detail design effort focused on tailoring the WBS configuration results to minimize engine interference, and return the wing and strut pressures both on and off-design to desired targets. As shown in Figure 133, the optimized spanload distribution of the WBS configuration has been altered by the presence of the engine nacelle and pylon. While some of the 'divot' in the total configuration spanload is filled by the nacelle's contribution to lift, the net effect of the installation is a decrease in wing load and corresponding increase in strut loading, particularly on the inboard strut. The end result for the WBSN configuration (Figure 133a) has been adjusted through the use of CDISC to the presented spanload distribution.

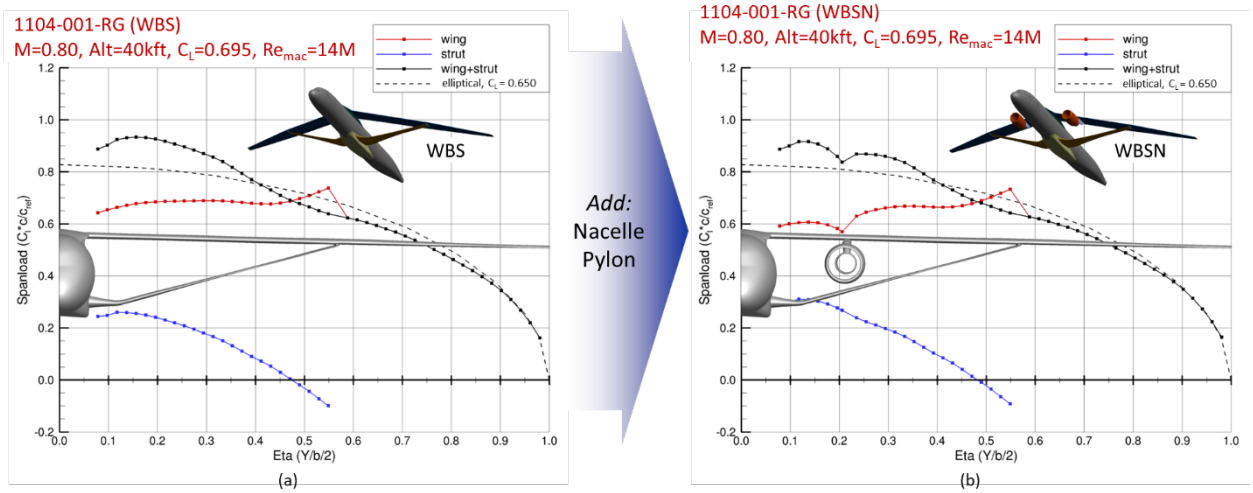


Figure 133 – Configuration 1104-001-RG Spanload - Effects of engine and pylon installation (Mach = 0.80, C_L = 0.695, Re_{mac} = 14M).

The performance of the final WBSN configuration is compared to the WBS geometry in Figure 134 and Figure 135 (and Appendix Figures A.41 and A.42). At flight Reynolds number, the drag of the configuration has increased at the cruise design point. Presented drag values (for all subsequent installations in which the nacelle is installed) have been adjusted from baseline CFD drag values to remove the skin friction from nacelle internal surfaces, core, and scrubbed areas of the pylon that are accounted for in the aerodynamic performance build-ups as part of the propulsion system. Peak L/D values of the fully turbulent results have decreased.

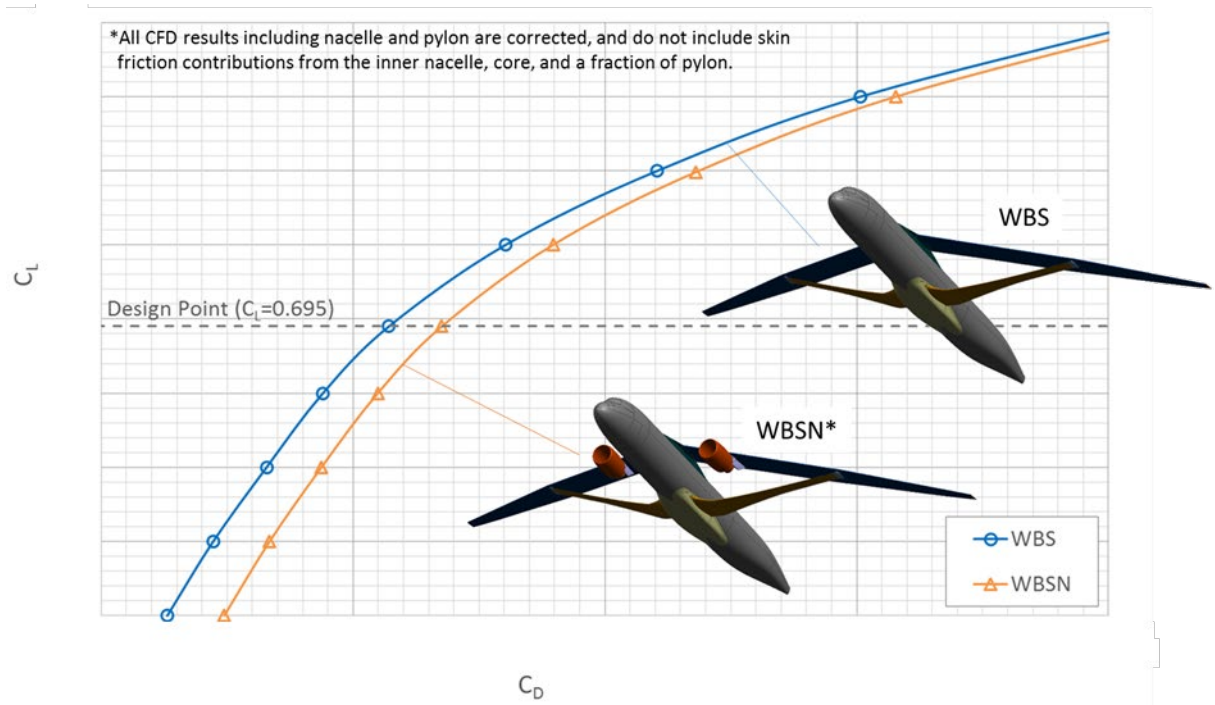


Figure 134 – Configuration 1104-001-RG – Effects of engine installation on the vehicle Drag Polar (Mach = 0.80, Re_{mac} = 14M).

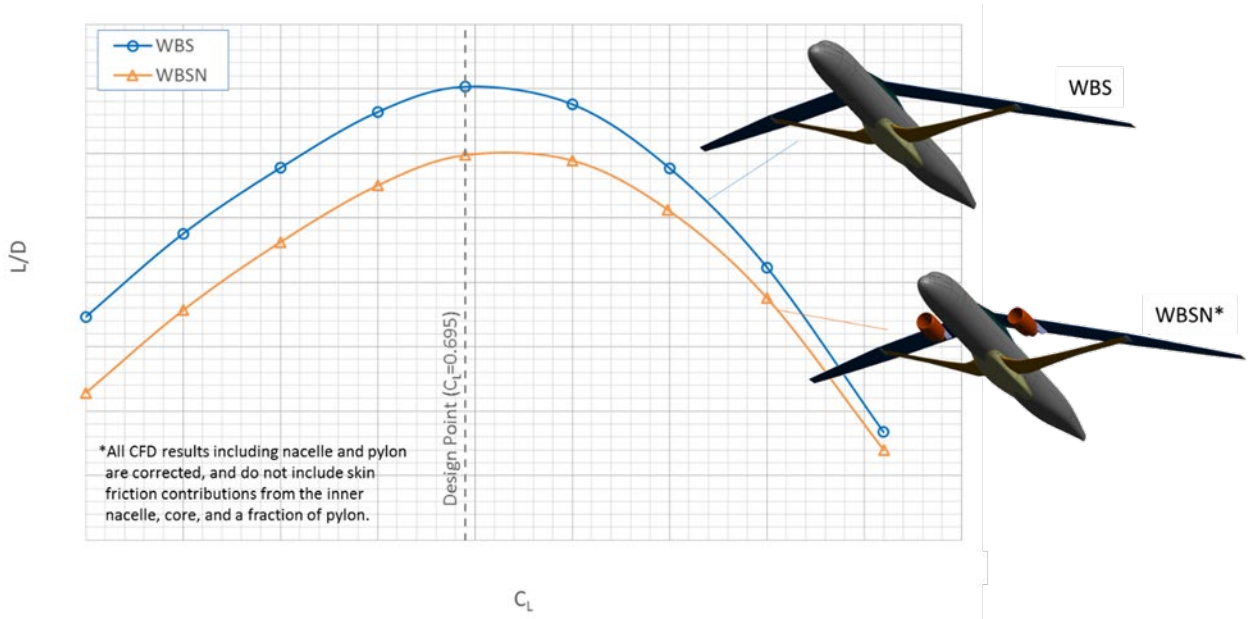


Figure 135 – Configuration 1104-001-RG – Effects of engine installation on the vehicle L/D (Mach = 0.80, Re_{mac} = 14M).

OVERFLOW analysis comparing the wing and strut pressures for the same configurations are shown in Figure 136 and Appendix Figure A.43. The configuration with the engine installed showed several changes to the WBS configuration aerodynamically optimized by the TRANAIR design process. Inboard wing loading in the proximity of the engine decreased, while inboard strut loading increased. To compensate for a small loss in lift for the configuration, angle of attack

increased from α=1.512° to α=1.578°. Outboard wing loading remained essentially constant, as did the strut and wing loading proximate to the wing-strut juncture.

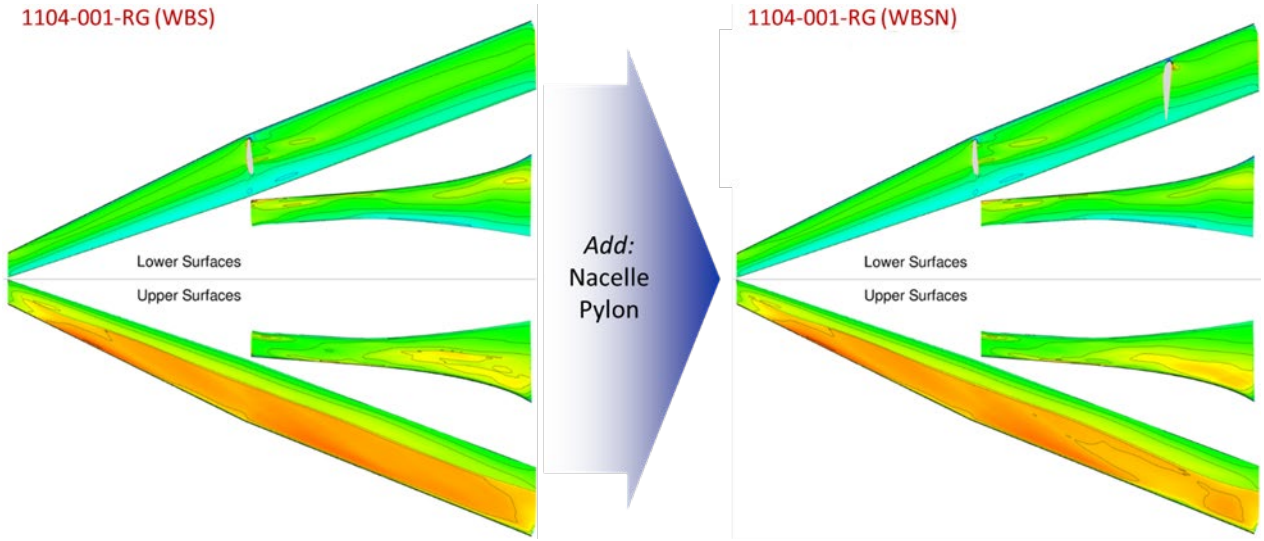


Figure 136 – Configuration 1104-001-RG - Effect of engine installation on wing and strut surface pressure contours at Mach = 0.80, Re_{mac} = 14M.

Wing-Body-Nacelle and Pylon-Flap Hinge Fairing-Jury Strut (WBSNFJ)

Prior to the investigation of tail installation and trim effects, the configuration was finalized with the addition of flap hinge fairings (FHFs) and the jury strut. While these elements would ideally have no negative net effect on the aircraft performance, in reality these structures could potentially introduce localized areas of concern or have unanticipated global effects – the proximity of the FHFs to the wing-strut juncture were of particular concern. The spanload plot shown in Figure 136 highlights the changes in spanload caused by these installations. Wing loading in the wing-strut juncture has increased slightly, with a step-change in spanload distribution slope occurring outboard of the FHF-jury-strut intersection. To compensate, local strut download in the juncture has increased, resulting in a small angle of attack decrease from α=1.578° to α=1.527°.

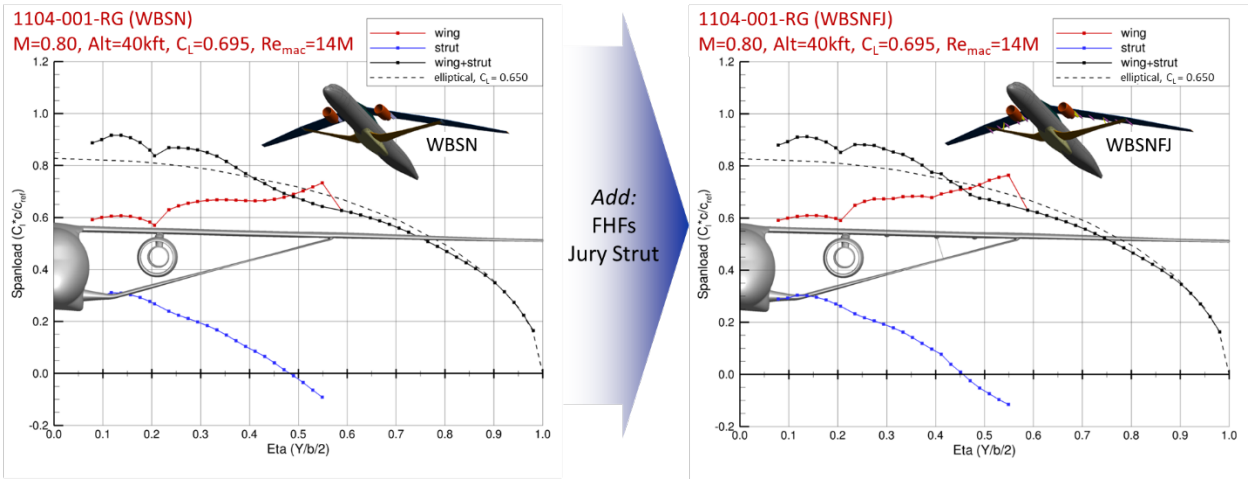


Figure 137 – Configuration 1104-001-RG Spanload - Effects of FHF and jury strut installation (Mach = 0.80, C_L = 0.695, Re_{mac} = 14M).

The performance of the WBSNFJ configuration is compared to the WBS and WBSN geometries in Figure 138 and A.44, Figure 139 and A.45, and Figure 140 and A.46. At flight Reynolds number, the drag of the configuration has increased at the cruise design point relative to the WBSN configuration. Peak L/D values of the fully turbulent results have decreased. Figure 140 also plots the aerodynamic performance of the configuration as a pseudo range factor, in which $\sqrt{M}$ is multiplied by the L/D of the vehicle. This relationship combines the typical metric for aerodynamic efficiency found in the Breguet range equation with an approximation of the slope of the SFC curve which is proportional to $\sqrt{M}$.

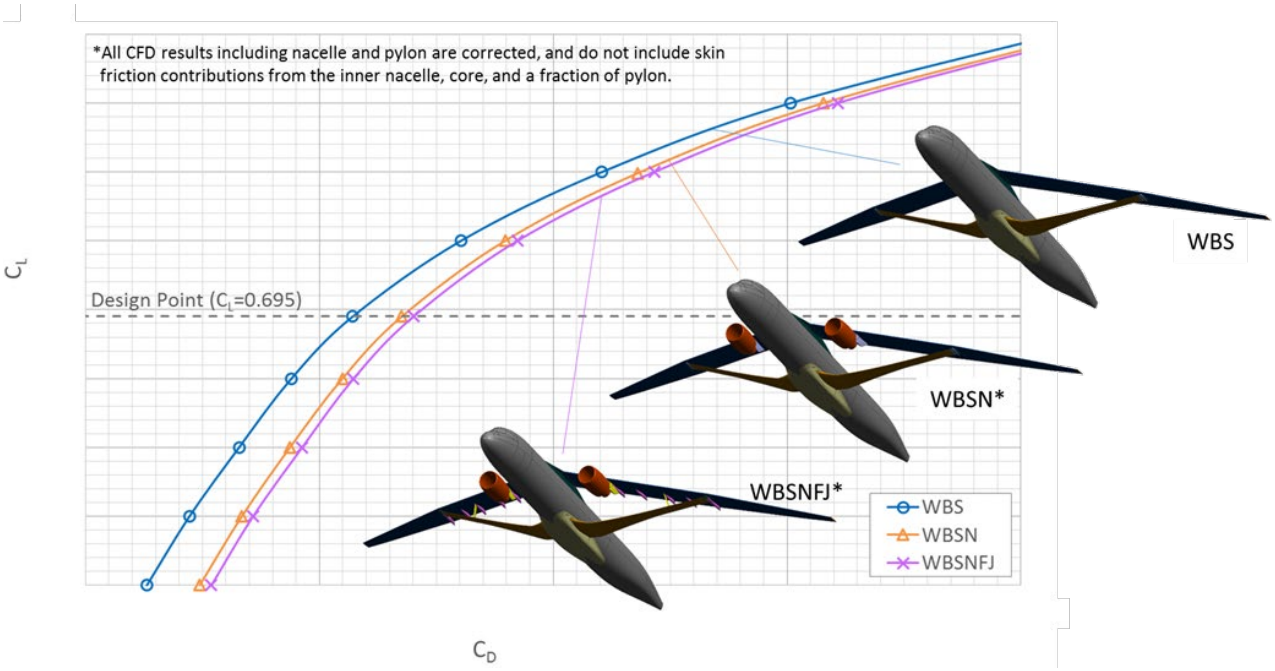


Figure 138. Configuration 1104-001-RG – Effects of FHF and jury strut installation on the vehicle Drag Polar (Mach = 0.80, Re_{mac} = 14M).

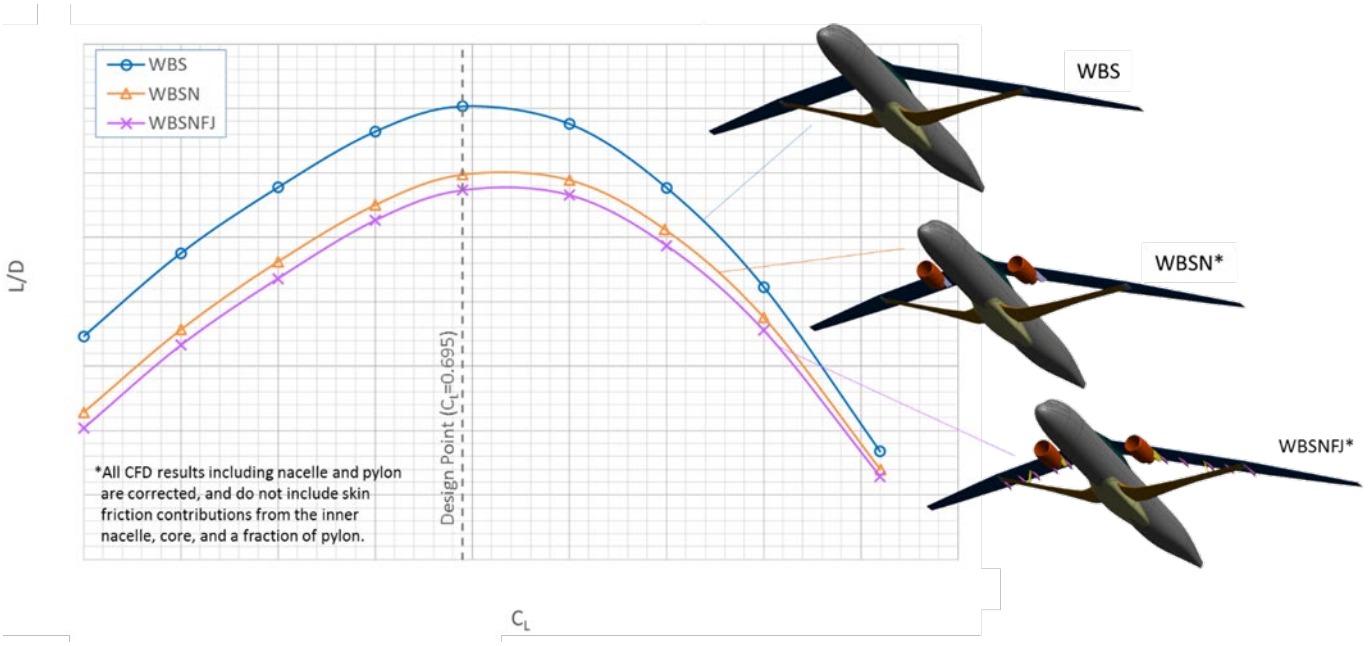


Figure 139 – Configuration 1104-001-RG – Effects of FHF and jury strut installation on vehicle L/D (Mach = 0.80, Re_{mac} = 14M).

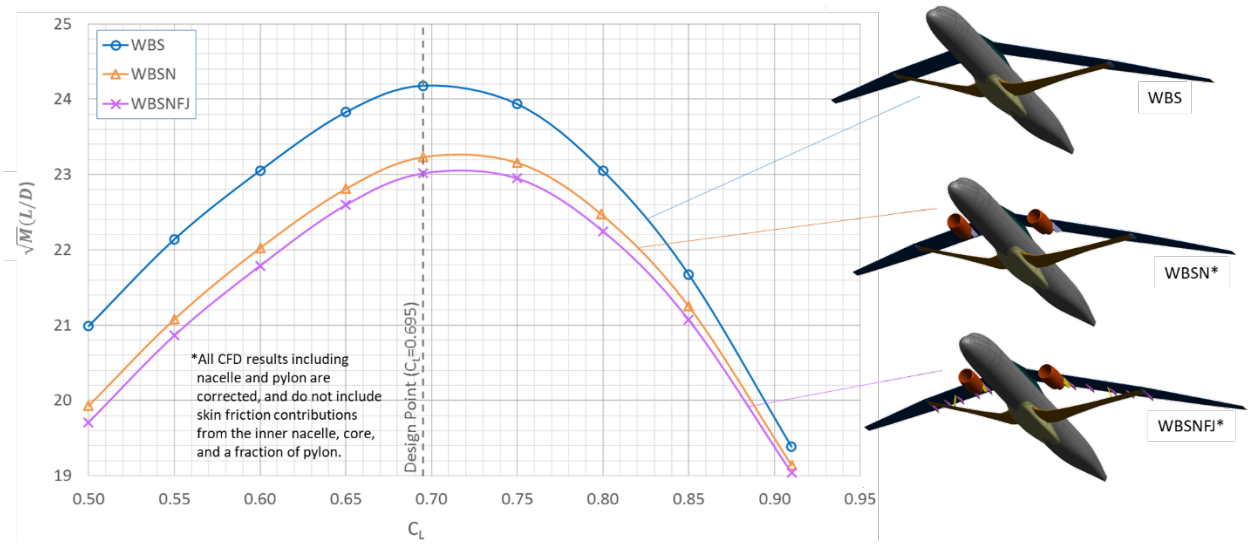


Figure 140 – Configuration 1104-001-RG – Effects of FHF and jury strut installation on vehicle Aerodynamic Performance (Mach = 0.80, Re_{mac} = 14M).

Figure 141 and Appendix Figure A.47 show the wing pressures for the final WBSNFJ configuration operating at the cruise design point. The pressures on this turbulent wing design are the end result of a combined design process in which aerodynamic optimization via the TRANAIR tool was combined with manual changes to the geometry along with inverse aerodynamic design via CDISC. Although the wing was designed and analyzed as a fully turbulent geometry, the sectional wing pressures were intended to remain 'laminar friendly', in that the distributions did not deviate far from a pressure architecture that could be made more conducive to laminar, particularly considering the relatively short-chord (high aspect ratio) wing.

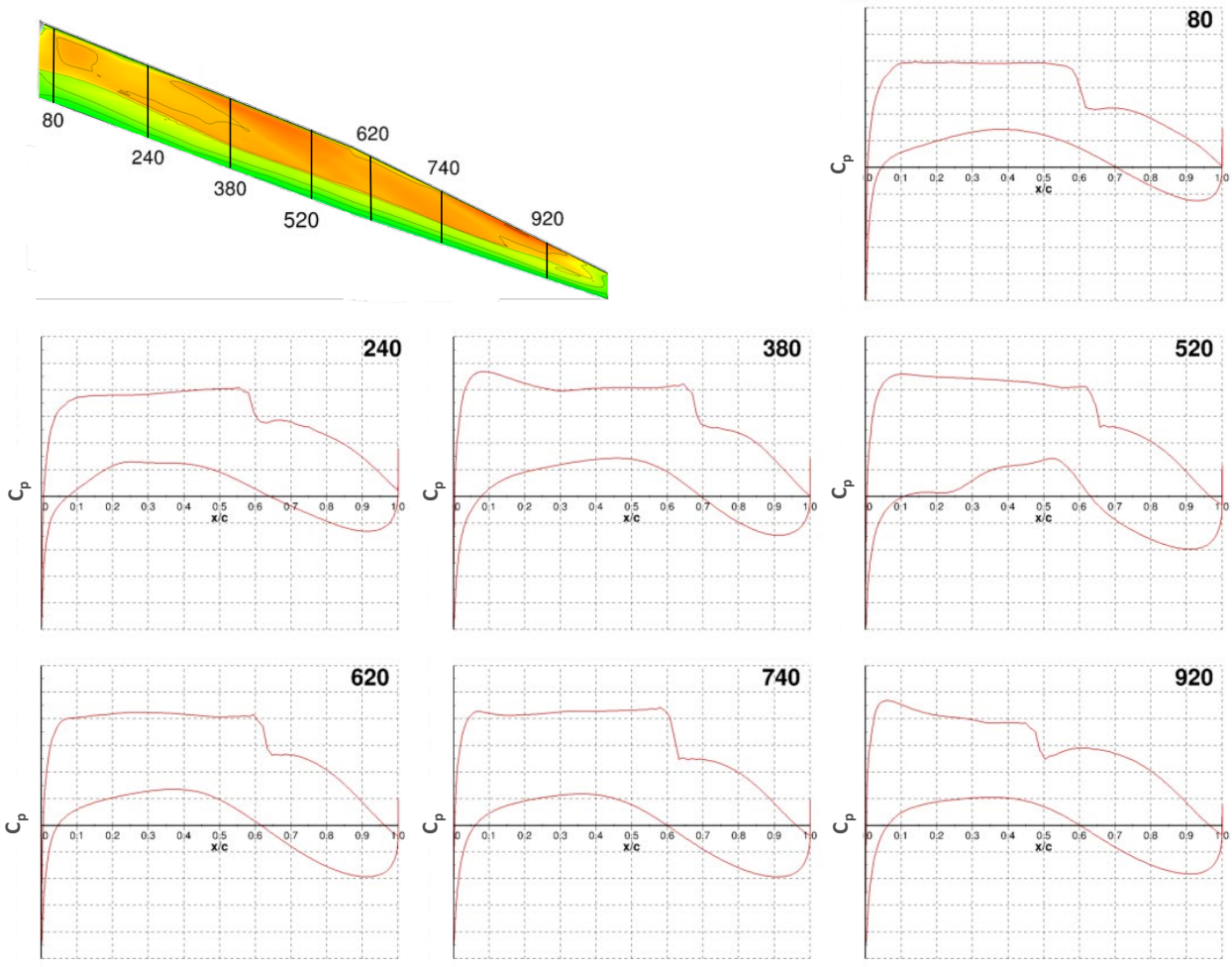


Figure 141 – Configuration 1104-001-RG - Wing Pressures (WBSNFJ) M=0.80, C_L=0.695, Alt=40kft, Re_{mac} = 14M.

Appendix Figure A.48 shows the strut pressures for the cruise design point, as well as sectional wing pressures at the same spanwise locations. The figure highlights the increased inboard strut loading that was targeted for this configuration. Shocks on the strut upper surface are very weak, allowing the strut to contribute to the lift of the vehicle with very little compressibility drag. This level of loading enables the strut to avoid being a simply parasitic contributor to aircraft drag. The strut contours have primarily been a result of aerodynamic optimization, but have also been heavily dependent on aerostructural optimization to maintain the structural viability of the strut design. (details of this design procedure are shown in Section 4.1.1.3). In addition, while an increased level of strut lift has been a strategic goal from the beginning of the Phase IV design effort, the optimal contribution of strut lift to the vehicle spanload remains an area in which further study is required.

The net changes to the lift distribution is reflected in the wing and strut surface C_p contours shown in Figure 142 and Appendix Figure A.49. With the exception of the localized flow acceleration on the upper surface of the strut at the jury strut attachment location, the differences to the surface pressure distributions are relatively small. The increased flow acceleration around the underside of the outboard strut on the WBSNFJ configuration suggest an increase in flow spillage from the channel between the jury-strut attachment and wing-strut attachment.

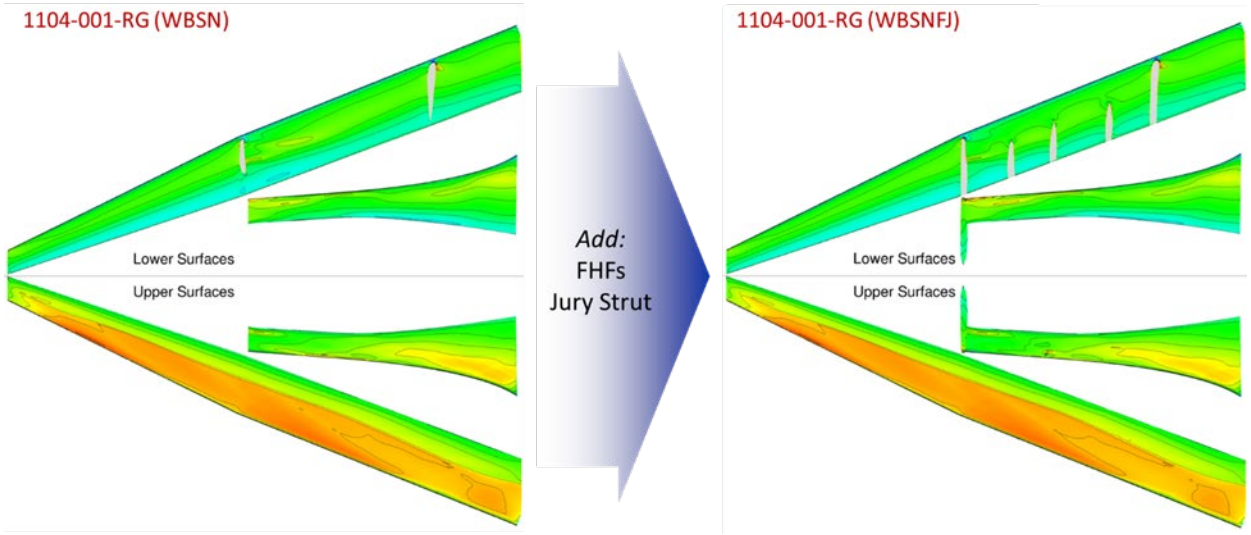


Figure 142 – Configuration 1104-001-RG - Effect of FHF and jury strut installation on wing and strut surface pressure contours (M=0.80, C_L=0.695, Re_{mac} = 14M).

Drag Divergence Mach (M_{DD}) and Long-Range Cruise (LRC)

The performance of the tail-off configurations was examined to determine an estimate for vehicle Long Range Cruise (LRC). The method assumes that LRC point is 1% down from the peak 'range factor' curve plotted as a function of operating Mach number. The results presented in Figure 143 and Appendix Figure A.50 show that the built-up configurations have essentially the same predicted LRC point – this suggests that no one component exhibits unusual interference as a function of operating Mach.

Drag rise curves of the configuration component build-up are shown in Figure 144 and Appendix Figure A.51. The calculated drag divergence Mach (M_{DD}) of the configuration is presented for each configuration. As shown, the design is operating efficiently at the design cruise Mach number. A small amount of drag creep is found in the WBS solution; since the final configuration was designed with the nacelle and pylon installed, the WBS-only design is slightly compromised in design when analyzed in isolation.

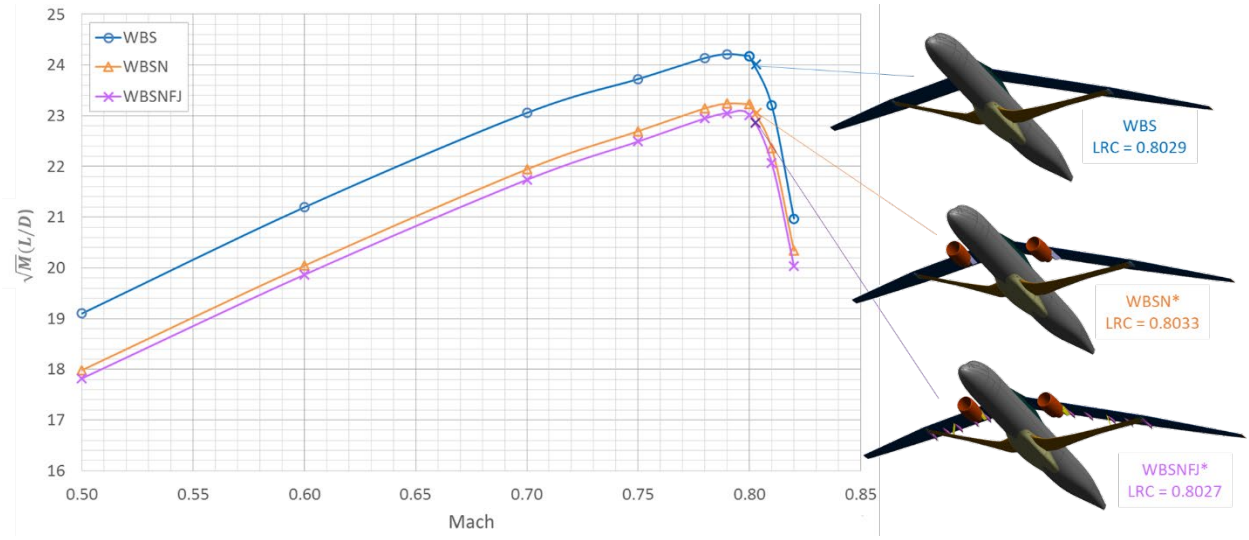


Figure 143 – Configuration 1104-001-RG Long-Range Cruise (LRC) Estimates (C_L = 0.695, Re_{mac} = 14M).

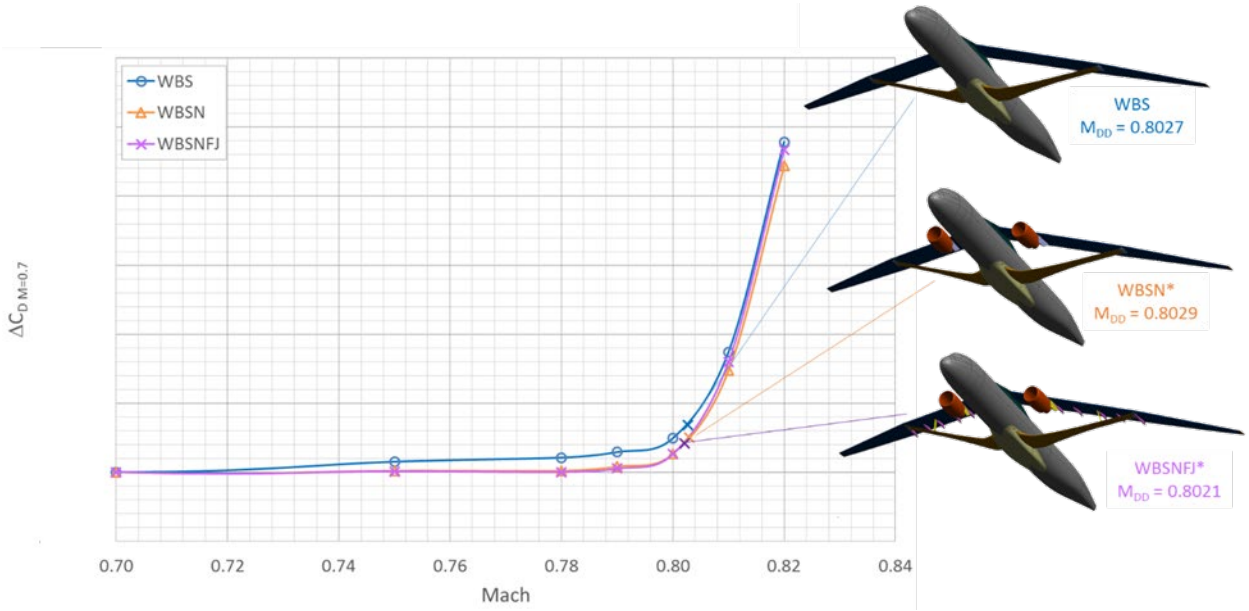


Figure 144 – Configuration 1104-001-RG Drag Rise Component Buildup (C_L = 0.695, Re_{mac} = 14M).

Buffet Analysis

The BUFFET program was used to analyze the final design performance at the upper and lower lift coefficients to determine the potential for aerodynamic buffet. As stated previously, the TTBW has the theoretical possibility for buffet to occur and both high lift coefficients (where the wing and wing-strut juncture may be critical) and at low lift coefficients (where the strut lower surface and wing-strut juncture may be critical). The code quantifies shock strength on the critical surfaces and compares it against an estimated critical level. The critical surfaces for high and low lift coefficient cases are shown in Figure 145 (Appendix Figure A.52) and Figure 146 (Appendix Figure A.53) respectively. At high lift coefficient values, the only critical surface is the wing upper

surface inboard of midspan (i.e. the strut and wing-strut junction are not critical). At low lift coefficient values, there are actually no surfaces that are predicted to be close to buffet boundary. Figure 146 shows that there is significant margin to the critical Mach number on the strut lower surface.

It should be noted that that while the FAA regulations for "buffet free" flight are based on the perception of buffet created by a structural response to flow separation, it is unclear if the BUFFET results presented herein are a true indicator of (local) buffet on the wing or strut. It is also unknown if such local buffeting would be perceived by the pilot and deemed unacceptable. Further study and dedicating testing is needed to answer these questions.

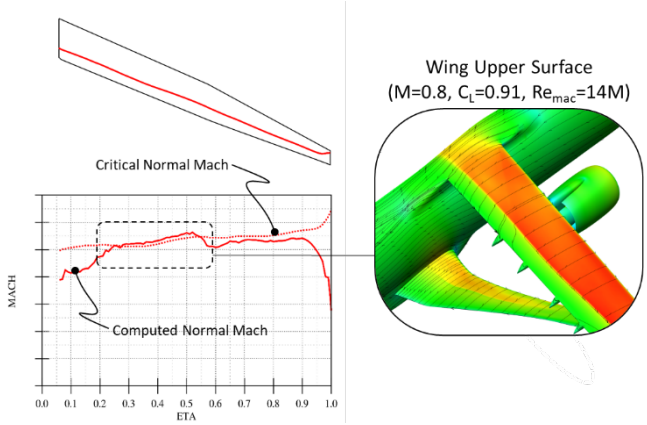


Figure 145 – Buffet analysis of wing upper surface at high lift coefficient (Mach=0.80, C_L = 0.91, Re_{mac} = 14M).

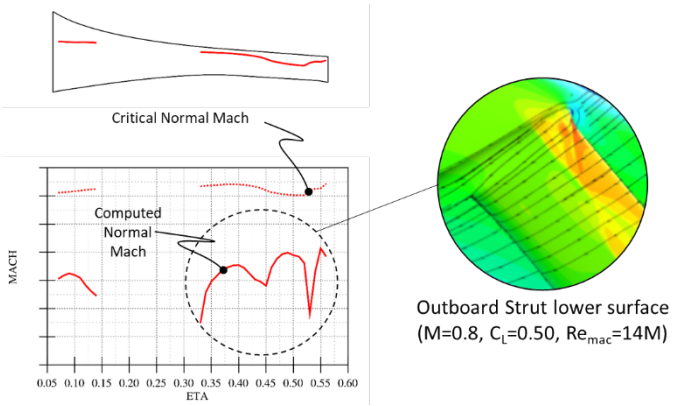


Figure 146 – Buffet analysis of strut lower surface at low lift coefficient (Mach=0.80, C_L = 0.50, Re_{mac} = 14M).

Trimmed Performance

The performance of the finalized vehicle design, including tail and trim penalty were computed. OVERFLOW analysis of the full configuration were analyzed for a range of horizontal tail settings in order to determine the tail setting where trim occurs. The results of the analysis, presented in Figure 147 (Appendix Figure A.54) and Figure 148 (Appendix Figure A.55), show that the fully trimmed design is operating with the peak performance occurring very near the intended cruise C_L of 0.695. The drag offset from the fully turbulent, untrimmed WBS solution includes the drag

offset for the nacelle and pylon, flap hinge fairings, and both horizontal and vertical tail surfaces for a fully trimmed configuration.

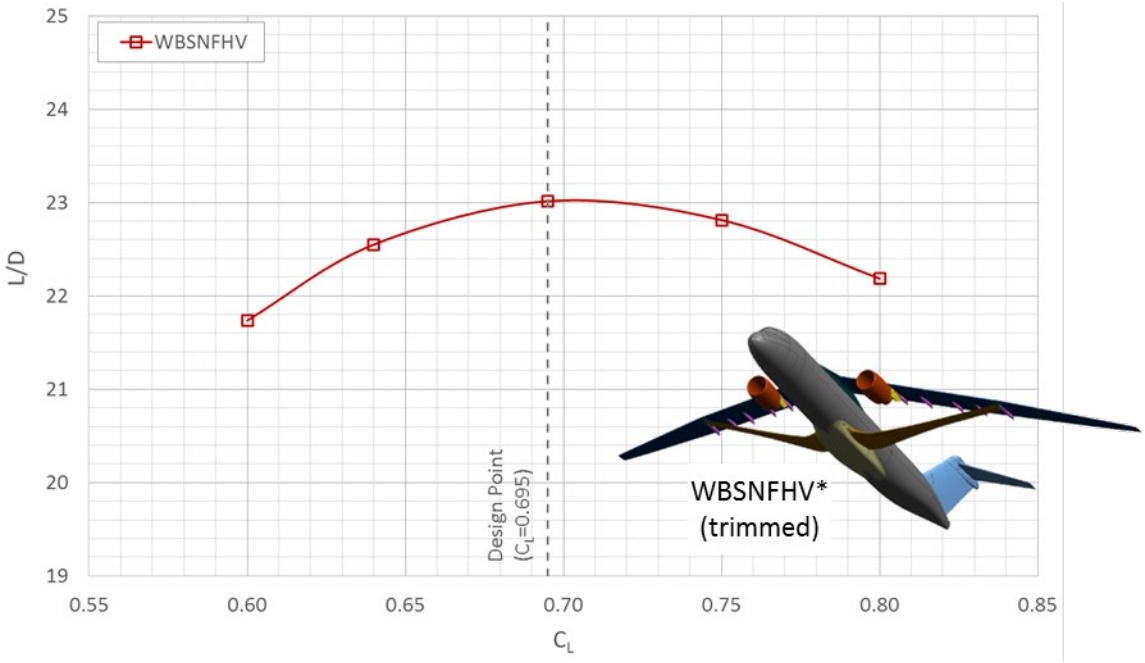


Figure 147 – Configuration 1104-001-RG – Trimmed Vehicle L/D (Mach = 0.80, Re_{mac} = 14M).

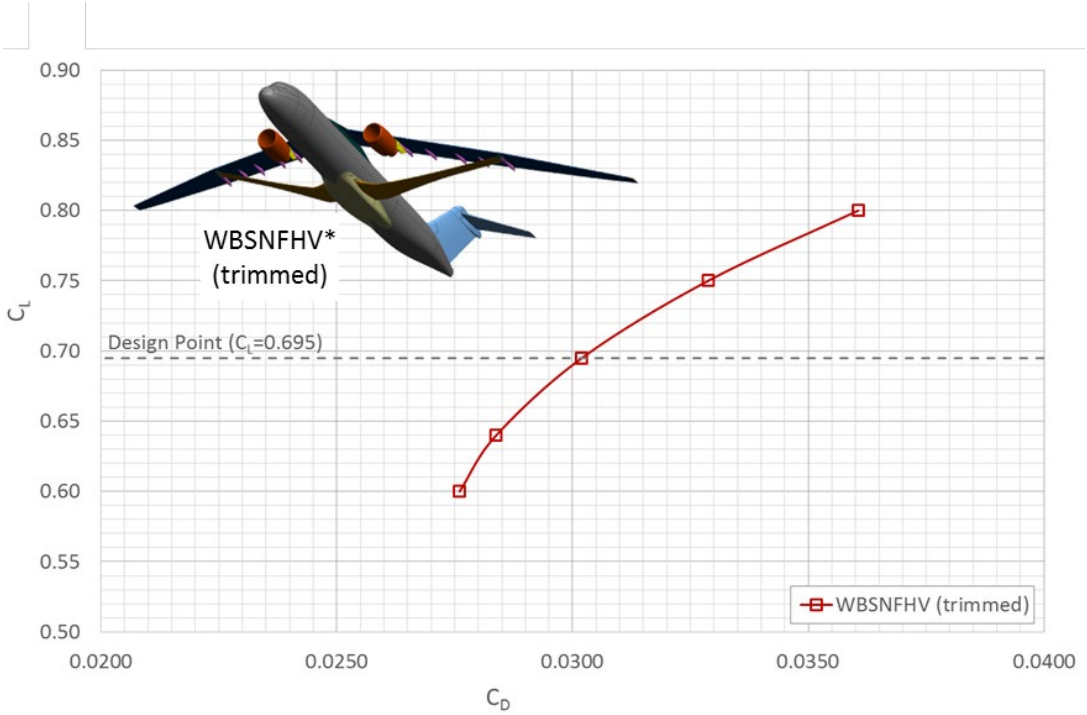


Figure 148 – Configuration 1104-001-RG – Trimmed Vehicle Drag Polar (Mach = 0.80, Re_{mac} = 14M).

Final High-Speed Performance

The aerodynamic performance results presented herein detail the high cruise efficiency of the TTBW concept operating at M=0.80. Results from OVERFLOW indicate that the TTBW is aerodynamically well suited to operation at the design M=0.80 transonic cruise Mach number. And, although significant time and effort has been invested into maximizing the performance of this configuration, the design was performed under significant design constraints (fixed planform, wing sweep, etc.). Therefore, it is reasonable to assume that this configuration can be rightly considered a 'snapshot' of the possible design potential of the TTBW concept, and is not intended to suggest the vehicle's upper limit of performance. The results obtained in this detailed study are a large component of the performance estimates outlined in Section 6.0. However, the analyzed configuration does not include potential performance increments for items such as laminar flow potential and excrescences that must be considered in order to determine aircraft-level performance.

When the CFD data is folded into the aircraft-level performance, and adjusted as per the conceptual design build-up procedure, the demonstrated performance benefit of the TTBW concept (independent of other technologies applied on the SUGAR configuration) has been calculated to be a 7.2% improvement in fuel burn (per seat) for an economic mission of 900nm, and a 9.0% improvement in fuel burn (per seat) for a 3500nm mission with full passenger payload. The benefits quoted are relative to an aspect ratio 13 conventional tube and wing configuration of equivalent technology development. For full details of the aircraft level performance benefit, please refer to Section 6.0.

5.0 Configuration Analysis

This section includes the discipline analyses of the configuration documented in Section 2.0. These analysis data are representative of the 1104-001-RG configuration.

5.1 Aerodynamics

The aerodynamics analyses are divided into high speed and low speed sections.

5.1.1 High Speed

Computer Aided Sizing and Evaluation System (CASES) cruise drag bookkeeping is shown in Figure 149.

$$C_D = C_{Do} + C_{Di} + C_{Dc} + C_{Dt} \qquad (7)$$

Parasite drag represents the incompressible zero-lift drag (C_{Do}). Induced drag (C_{Di}) accounts for the drag due to lift based on airplane efficiency factor at Mach 0.50. Compressibility drag (C_{Dc}) is a function of both Mach and lift coefficient while trim drag (C_{Dt}) accounts for pitching moment on the configuration.

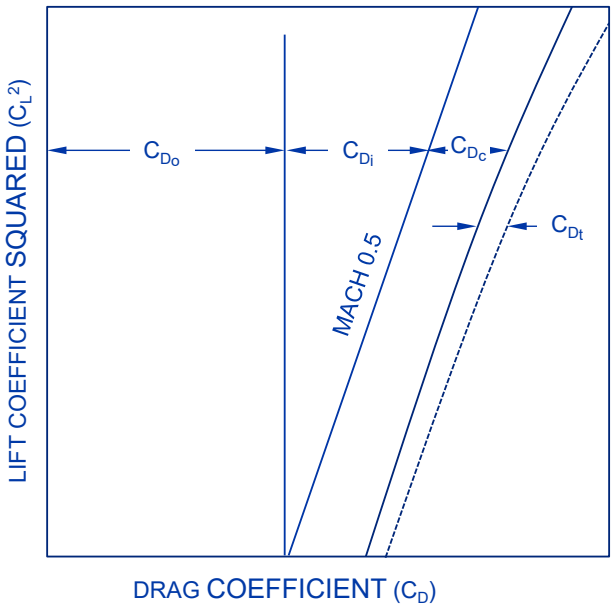


Figure 149 – CASES Standard Buildup.

Using CASES accounting and leveraging the wing-body-strut CFD solutions from 765-095 Rev-J (Mach 0.745 configuration), the high speed aerodynamic buildup for 1104-001-RG as compared to 765-095 Rev-J is shown in Table 20.

It should be noted that the aerodynamic technologies benefit (NLF/HLFC/Riblets) does not include the wing natural laminar flow (NLF) benefit. Wing upper surface NLF was book-kept under airplane compressibility drag during the Phase II study, and that convention is maintained here. CASES, like many performance routines, bookkeeps all drag due to Mach number as compressibility drag, which for this study, includes a change in drag due to natural laminar flow as illustrated in Figure 150. This explains why the compressibility drag appears as a negative number in the drag buildup.

Configuration 1104-001-RG aerodynamic characteristics reflect the design Mach number of 0.80. The resulting high speed data are shown in Figure 151. The figure illustrates the maximum aerodynamic efficiency (M*L/D) occurring at the design cruise Mach (0.80) and C_L (0.695). In the performance results, this is representative of long range cruise (LRC) speed while minimum fuel consumption occurs at lower Mach number.

Table 20 – SUGAR TTBW Speed Buildup.

765-095 Rev-D, 765-095 Rev-J, and 1104-001-RG High Speed Buildup		
CONFIGURATION	765-095 Rev-J	1104-001-RG
WING AREA	1477	1477
SWEEP (DEG)	12.58	22.46
T/C-AVE	0.120	0.104
AIRFOIL TYPE	SUPERCRIT. DTE	SUPERCRIT. DTE
F BUILD-UP (FT2)		
FUSELAGE	8.4463	8.3505
WING	10.1499	9.6340
STRUT / JURY	3.1527	3.4500
FLAP SUPPORT	0.2604	0.2604
HORIZONTAL	1.6693	1.6486
VERTICAL	1.9116	1.8724
N&P	1.8450	1.8130
CANOPY	N/A*	0.0405
GEAR PODS	1.3043	1.2920
NLF / HLFC	-2.6182	-2.6609
RIBLETS	-0.9787	-0.9993
EXCRESCENCE	2.3929	2.0739
STRUTS C_{DC}	N/A*	N/A*
UPSWEEP	N/A*	N/A*
WING TWIST	0.6298	0.7385
TURBULENT CDC INCREMENT	N/A*	N/A*
FUSELAGE BUMP	N/A*	0.2587
F-TOTAL (FT2)	28.1653	27.7722
E-VISC	**0.9068**	**0.8707**
CRUISE CD BUILD-UP		
M-CRUISE	0.745	0.80
C_L-CRUISE	0.7635	0.695
CRUISE ALTITUDE	40000	40000
C_{Do}	0.01907	0.01880
C_{Di}	0.01038	0.00903
C_{DC}	-0.00086	-0.00143
C_{DTRIM}	0.00057	0.00054
C_{DTOT}	0.02916	0.02695
L/D	26.184	25.788
M L/D	19.507	20.631

* Not applicable as this drag is booked in other areas.

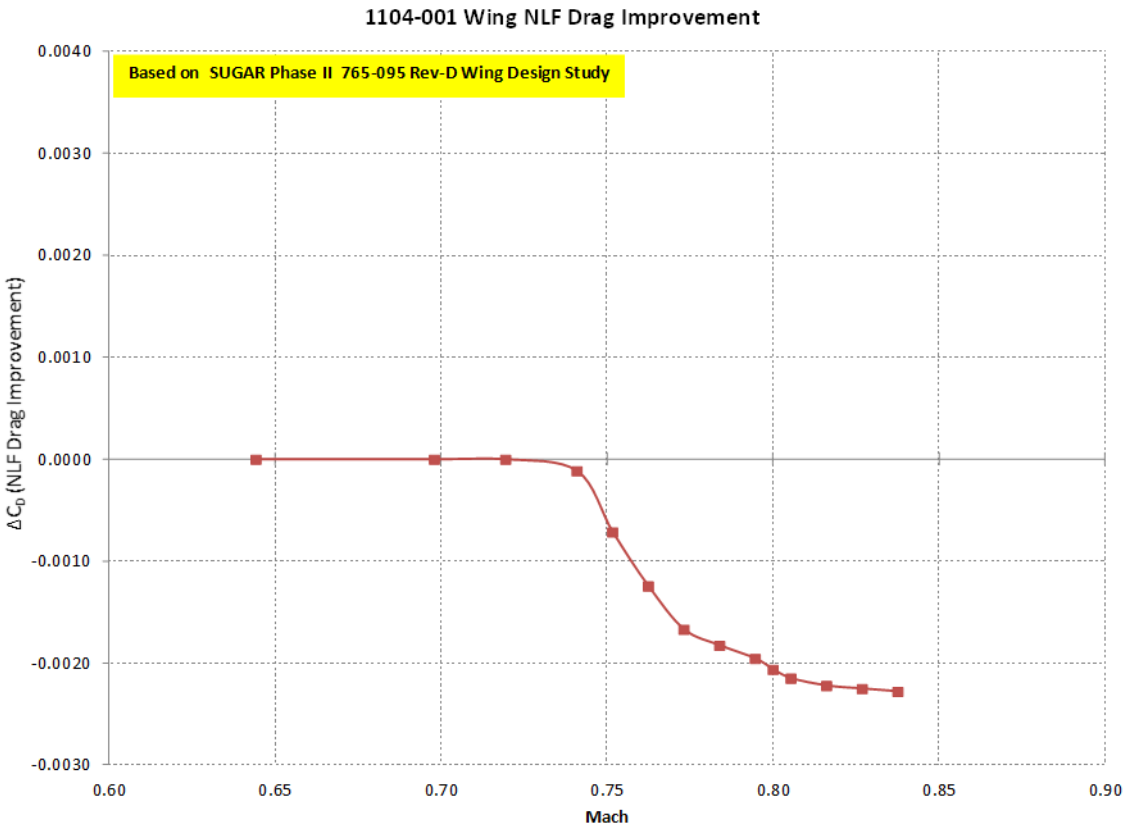


Figure 150 – 1104-001-RG – Wing NLF Drag Improvement (C_L = 0.695, Re_{mac} = 14M).

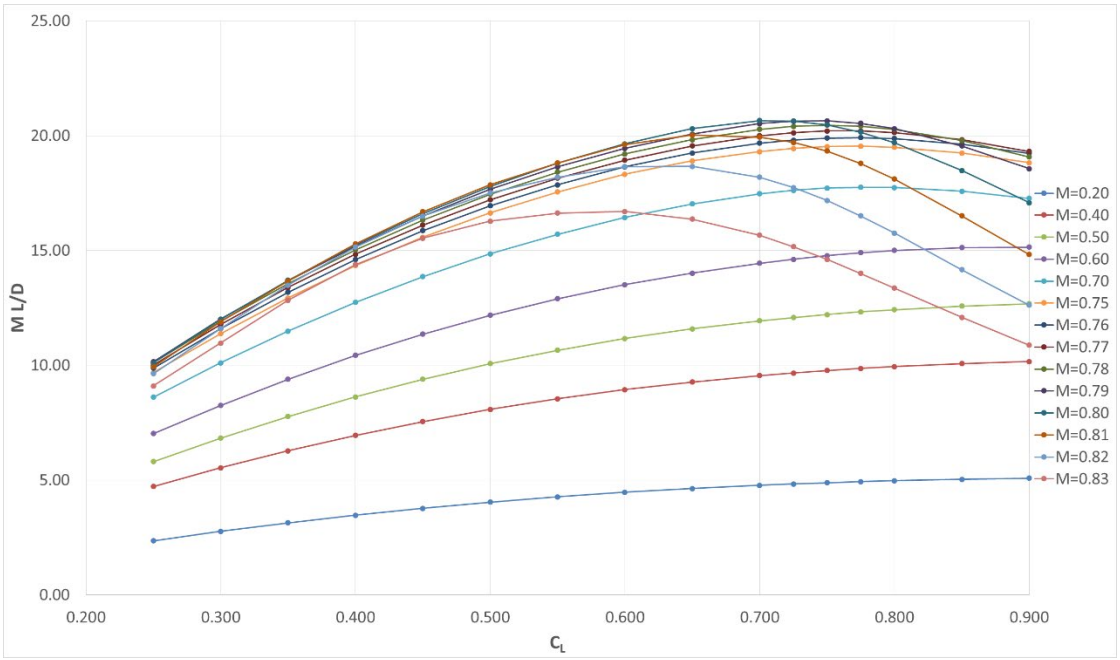


Figure 151 – 1104-001-RG – M(L/D) Total.

5.1.2 Low Speed

Figure 152 through Figure 154 show the low speed characteristics for SUGAR 1104-001-RG based on the CASES conceptual method, which has tracked closely with the Mach 0.745 configuration results. (5) Low speed data are trimmed as a function of angle of attack, lift coefficient, and drag coefficient at each flap detent. Low speed high lift devices on wing leading and trailing edges are deployed.

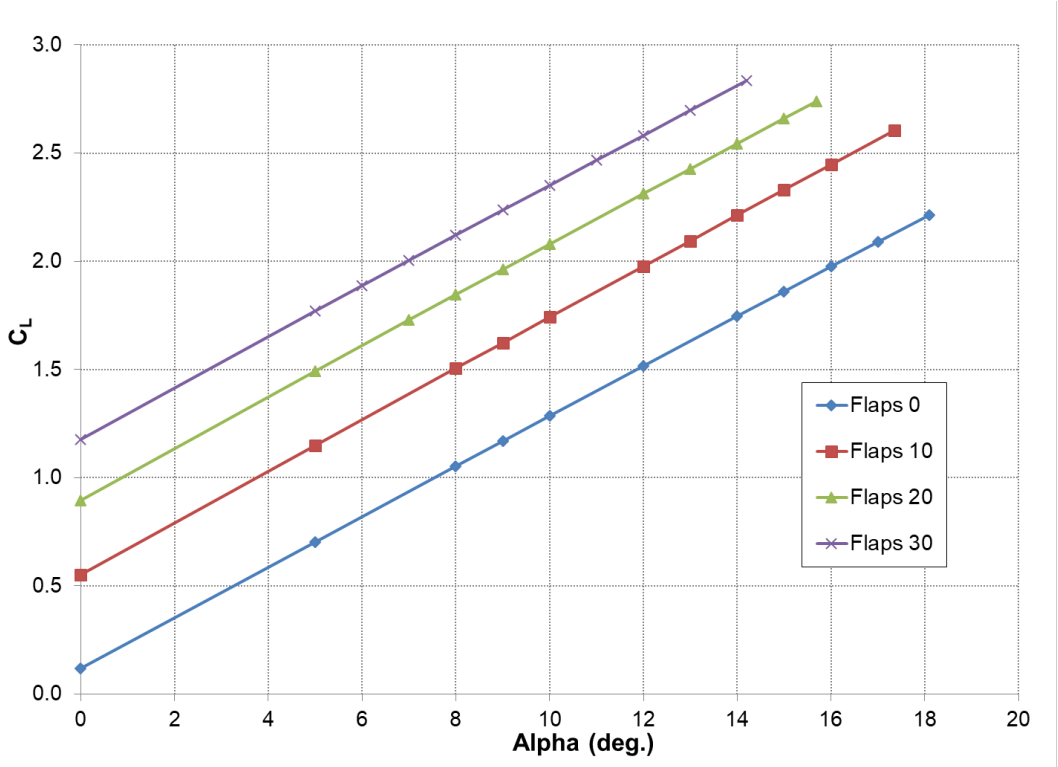


Figure 152 – 1104-001-RG – Low Speed Lift Curve, Free Air at Mach = 0.20, Re_{mac} = Flt Re.

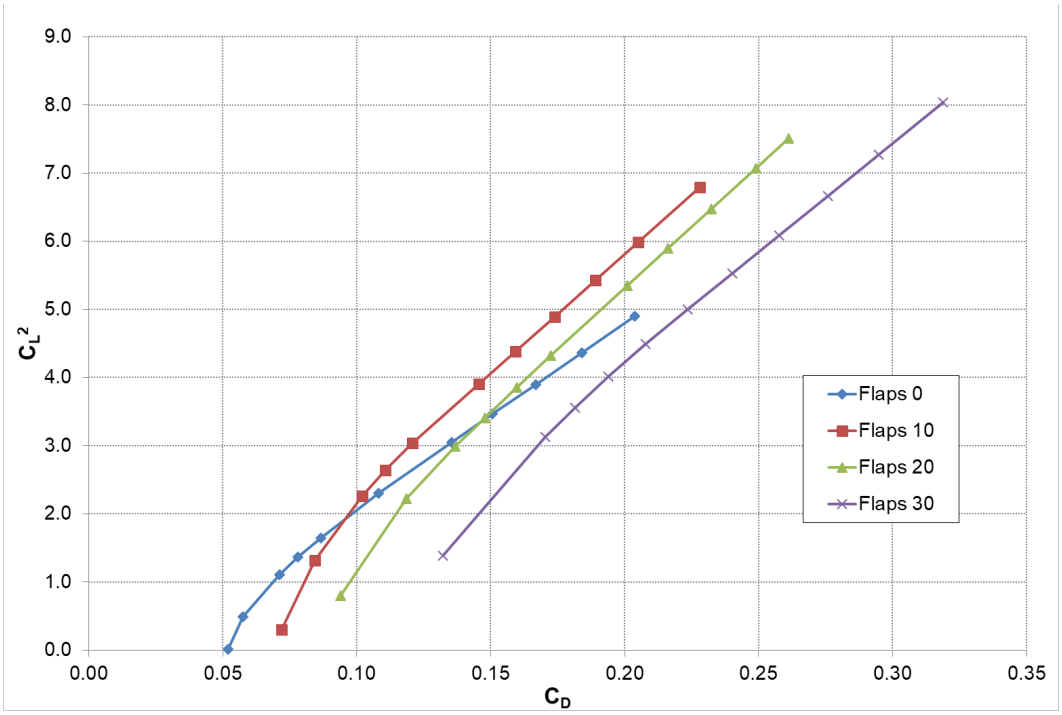


Figure 153 – 1104-001-RG – Low Speed Polar, Free Air (Mach = 0.20, Re_{mac} = 9.8M).

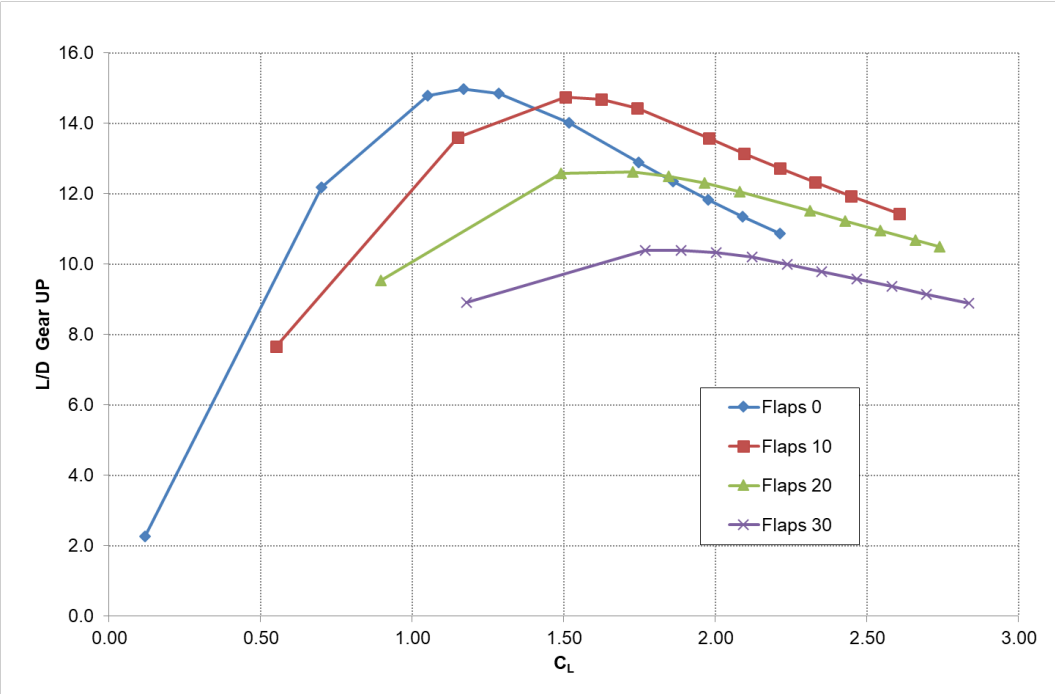


Figure 154 – 1104-001-RG – Low Speed Lift / Drag, Free Air (Mach = 0.20, Re_{mac} = 9.8M).

5.2 Mass Properties

The group weight statement for the 1104-001-RG is shown in Table 21. These weights incorporate the results of the 765-095 FEA and aeroelastic wind tunnel work from Phase II and III, and have been cycled with Aerodynamic Performance. The mass properties data are based on 765-095-Revision H, which is similar to revision J and does not necessitate an update of the analysis.

Boeing's weight estimation tools include sensitivity to wing sweep and thickness, however, on the TTBW, some additional weight must be accounted for in the fuselage. As the wing sweeps about its mean aerodynamic center (to maintain balance and loadability), the distance between the wing carry through and strut carry through lengthens. This portion of fuselage must carry the load imparted between these two structural elements in shear. Reviewing fuselage frame and stiffened panel data of existing aircraft led to adding 100 pounds to account for this increased loading.

A preliminary look at the vehicle balance diagram is shown in Figure 155. Understanding the vehicle's loading characteristics is required to provide the attendant mass distributions for structural loads cases.

A couple of items are noteworthy. First, with the amount of fuel available with the wing as drawn, the vehicle cannot meet the same 150,000 pounds MTOW used for the 765-095 series, so the MTOW was capped at 145,000 pounds; this is born out in the cycled MTOW. Second, the next vehicle iteration would address the fact that this aircraft's loading flexibility would be significantly improved by shifting the wing forward to encompass the typical forward biased passenger loading case, while also encompassing the typically loaded baseline mission case. Such a wing shift, without an envelope expansion, would likely reduce the required sizes for the tails, and, if the main landing gear remains in the same location, add weight to the fuselage shell, as described above.

Table 21 – 1104-001 Group Weight Statement.

GROUP	WEIGHT (LB)	
WING	**16,095**	
BENDING MATERIAL		7,488
SPAR WEBS		842
RIBS AND BULKHEADS		875
AERODYNAMIC SURFACES		3,030
SECONDARY STRUCTURE		3,860
HORIZONTAL AND VERTICAL TAILS	**2,759**	
FUSELAGE	**15,563**	
LANDING GEAR (MLG + NLG)	**4,891**	
NACELLE & PYLON (BOTH)	**4,902**	
WING STRUT & JURY & INSTALLATION	**3,836**	
PROPULSION	**10,161**	
ENGINES		8,436
FUEL SYSTEM		1,733
FLIGHT CONTROLS	**2,706**	
COCKPIT CONTROLS		252
SYSTEM CONTROLS		2,454
POWER SYSTEMS	**4,086**	
AUXILIARY POWER PLANT		1,014
HYDRAULICS		775
PNEUMATICS		0
ELECTRICAL		2,297
INSTRUMENTS	**774**	
AVIONICS & AUTOPILOT	**1,504**	
FURNISHINGS & EQUIPMENT	**9,114**	
AIR CONDITIONING	**1,441**	
ANTI-ICING	**126**	
MANUFACTURER'S EMPTY WEIGHT (MEW)	**77,964**	
OPERATIONAL ITEMS	7,207	
OPERATIONAL EMPTY WEIGHT (OEW)	**85,172**	
USABLE FUEL	29,028	
DESIGN PAYLOAD	30,800	
TAKEOFF GROSS WEIGHT (TOGW)	**145,000**	

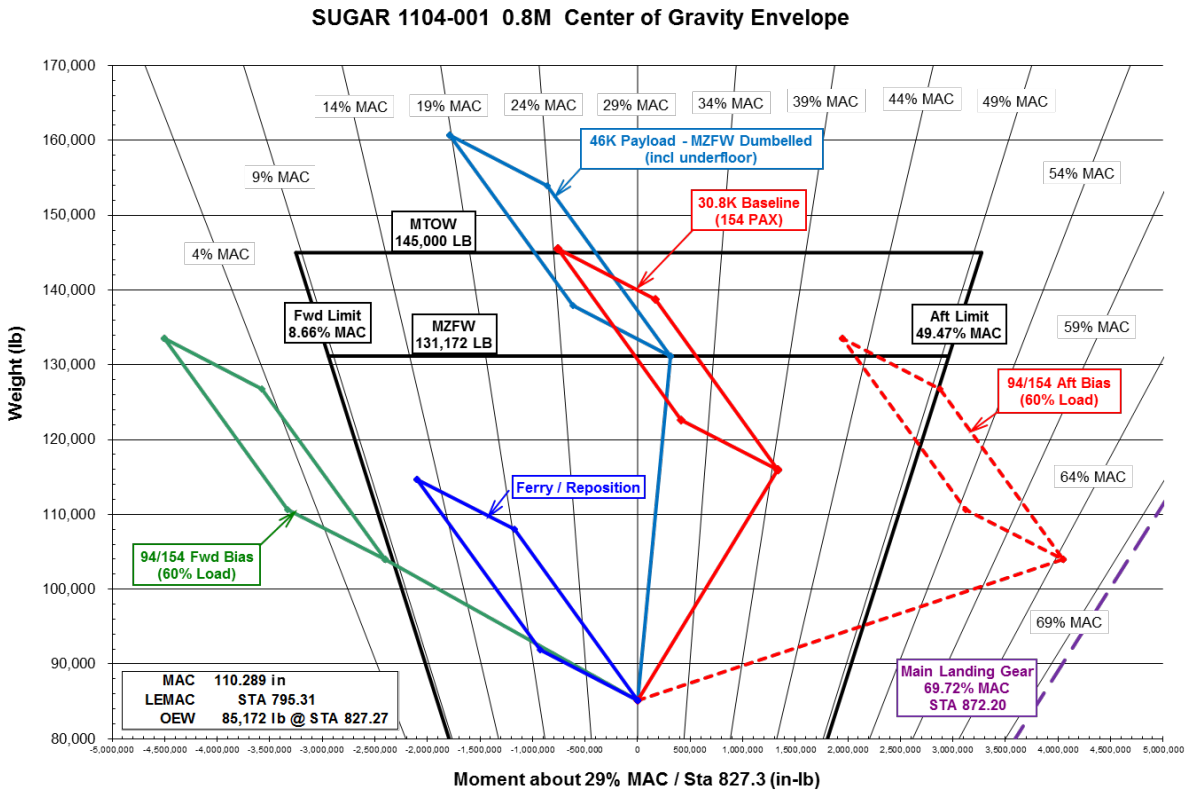


Figure 155 – 1104-001 Preliminary Vehicle Balance Diagram.

5.3 Stability & Control

This section describes the work performed to evaluate the Stability and Control of the Mach 0.80 TTBW configuration.

5.3.1 Longitudinal Stability and Control Assessment

Longitudinal Stability and Control analysis was focused on defining the center of gravity (CG) envelope for the aircraft that encompasses the desired loadability cases of the aircraft. These loadability cases were defined by weights and reported in Section 5.2. In finalizing the S&C CG limits, an iterative process between the S&C team and Mass Properties occurs to converge on CG limits that both meet all requirements and encompass all desired loadability cases. For the purposes of the Mach 0.80 TTBW, only an assessment was made on the longitudinal Stability and Control. Any design changes required to meet the longitudinal requirements were not implemented for this design in order to keep a common empennage OML to the Phase III effort. Instead, recommendations are given on solutions that would potentially satisfy all longitudinal S&C requirements while maximizing the loadability of the aircraft.

Longitudinal Stability and Control Requirements

The requirements by which to assess the longitudinal S&C properties of the aircraft are primarily derived from Boeing internal requirements. Boeing has historically shown that meeting these

internal requirements enable the aircraft to meet the requirements outlined in 14 CFR Part 25 by the FAA. It is necessary to meet these requirements for the FAA to certify the aircraft.

The forward CG limit is defined by the most critical (i.e. most aft) of the following requirements:

- Takeoff Rotation – At the most critical weight, thrust, and high lift settings, the airplane must rotate from ground attitude to the takeoff attitude with adequate pitch acceleration.
- Go-Around – At the most critical weight at glide slope of -3 degrees, the aircraft must rotate from approach attitude to the go-around climb attitude with adequate pitch acceleration.
- Nose Wheel Hold Off – After the main gear touches down on landing with the most critical weight and high lift settings, the pilot must be able to hold the nose gear off the ground up to the stall speed of the aircraft.

The aft CG limit is defined by the most critical (i.e. most forward) of the following requirements:

- Stall Recovery – This requirement is captured in 14 CFR 25.145(a) which specifies that the pilot must be able to make a "prompt" nose down recovery during a stall maneuver. This translates to a required nose-down pitch acceleration that the vehicle must meet at stall at the most critical weight and high lift settings.
- Nose Wheel Steering – For adequate steering capability, a certain percentage of the aircraft weight must be applied to the nose gear when the vehicle is on ground and static.
- Static Margin – Internal Boeing studies have determined a minimum static margin necessary that would allow the pilot to control the aircraft and land safely in the event of a failure in the pitch stability augmentation system.

Longitudinal S&C Analysis

To evaluate these requirements for this aircraft, aerodynamic data is required for the vehicle. Typically, aero data from the highest fidelity source is used in these assessments. In this case, wind tunnel data from the Phase III Mach 0.745 vehicle is used. The data is then adjusted using results from a lower order code such as Athena Vortex Lattice (AVL) (14) to be representative of the Mach 0.80 TTBW vehicle. AVL models of the Mach 0.745 vehicle and the Mach 0.80 vehicle were created and run to produce ratios and increments that are applied to the Phase III wind tunnel data to create an aero database suitable for CG limit analysis.

This analysis was performed on the 1104-001-RCdes13 version of the vehicle. Since the wing planform has not changed since that version, this analysis is still generally applicable to the final design of the vehicle.

These representative aero data along with mass properties, thrust data, and vehicle geometry data are then analyzed using Boeing's CG limit evaluation tools for conceptual design. The results of the analysis are typically presented in the form of a "scissor" plot. This plot (Figure 156) shows the CG limits of the vehicle for a given horizontal tail volume. Note that in the plot, the stall recovery and static margin lines overlap.

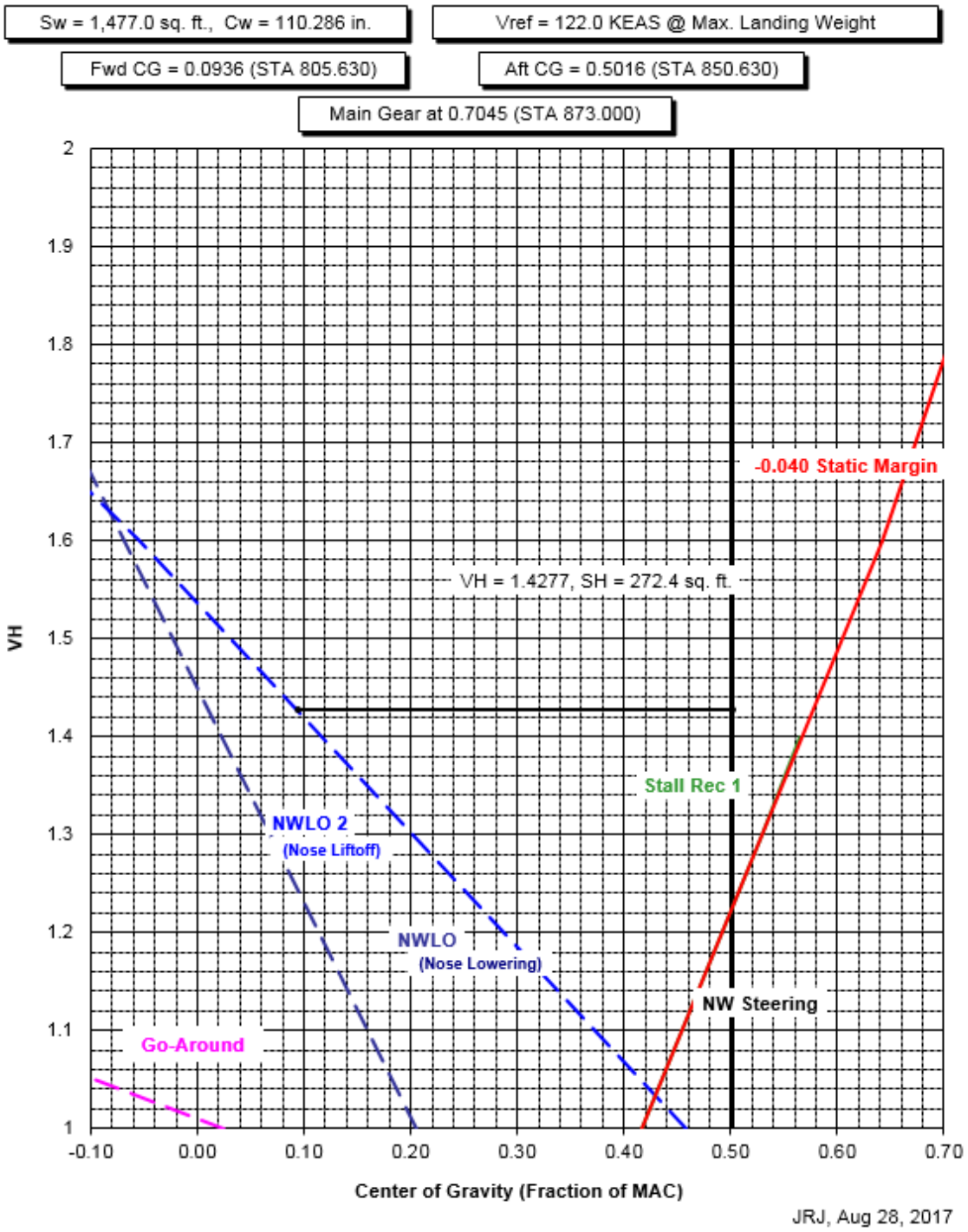


Figure 156 – 1104-001-RG Scissors Plot.

To achieve a 45 inch CG range identified in previous work, a tail volume of 1.4277 was be achieved. This translates to a tail area of 272.4 ft^2. Previously for Phase III this resulted in a tail area of 273.3 ft^2. Ideally, to maximize the CG range for a given tail, the nose wheel steering requirement line (NW Steering) should intersect the Static Margin requirement line at the point where the aft CG limit is located. For this vehicle, Nose Wheel Steering is the limiting case for the aft CG limit while the Nose Wheel Liftoff (i.e. Takeoff Rotation) requirement sets the forward CG limit. These limits were then applied to the Weight and Balance diagram for this vehicle to get a clear picture of whether this vehicle can meet all the loading missions. The Weight and Balance diagram from Mass Properties is detailed in Figure 155.

To read this diagram properly, each "balloon" is a separate scenario the aircraft may experience when loading payload and fuel. The "stick" of each balloon is the payload being loaded onto an empty airplane at Operational Empty Weight (OEW). The "balloon" part of each scenario represents the fuel loading. Any point within the balloon is an achievable loading by appropriately loading the fuel tanks. Thus, to successfully load the aircraft according to each scenario, the point at which the "stick" and "balloon" must fall within the CG limits. That point represents the aircraft in flight with zero fuel and that specific payload.

With the current CG limits of roughly 10% to 50%, the main mission, ferry mission, and Max Zero Fuel Weight scenario can be achieved. However, both the forward biased payload and aft biased payload mission are unattainable (these are not necessarily requirements). This is because the lower right point of those two scenarios (which represents that specific payload arrangement at zero fuel) does not fall within the CG limits. The forward and aft biased loadings represent two extreme scenarios that an airline may experience. However, airlines typically will ensure that the payload is loaded such that the CG of the aircraft falls within an acceptable range. Additionally, passengers typically don't all sit in the front or back of an airplane, they tend to distribute themselves evenly among the cabin.

For the purposes of this project, the current horizontal tail will remain unchanged however, with detailed wing and landing gear shift trades, more loadability or smaller tail sizes could be attained.

5.3.2 Lateral Stability and Control Assessment

One of the primary goals of the Phase IV effort is to design and analyze a high lift system for the Mach 0.80 TTBW vehicle. Toward that end, a control surface layout was designed such that the high lift system can operate while meeting all roll requirements. The initial layout proposed in Phase II consisted of a high speed inboard flaperon and an outboard aileron with flaps and spoilers.

Five different control surface layouts were proposed as options for this vehicle. Each one was evaluated for roll authority against roll requirements. The planform that performed the best was baselined for this vehicle. The candidate planforms are outlined in Figure 157.

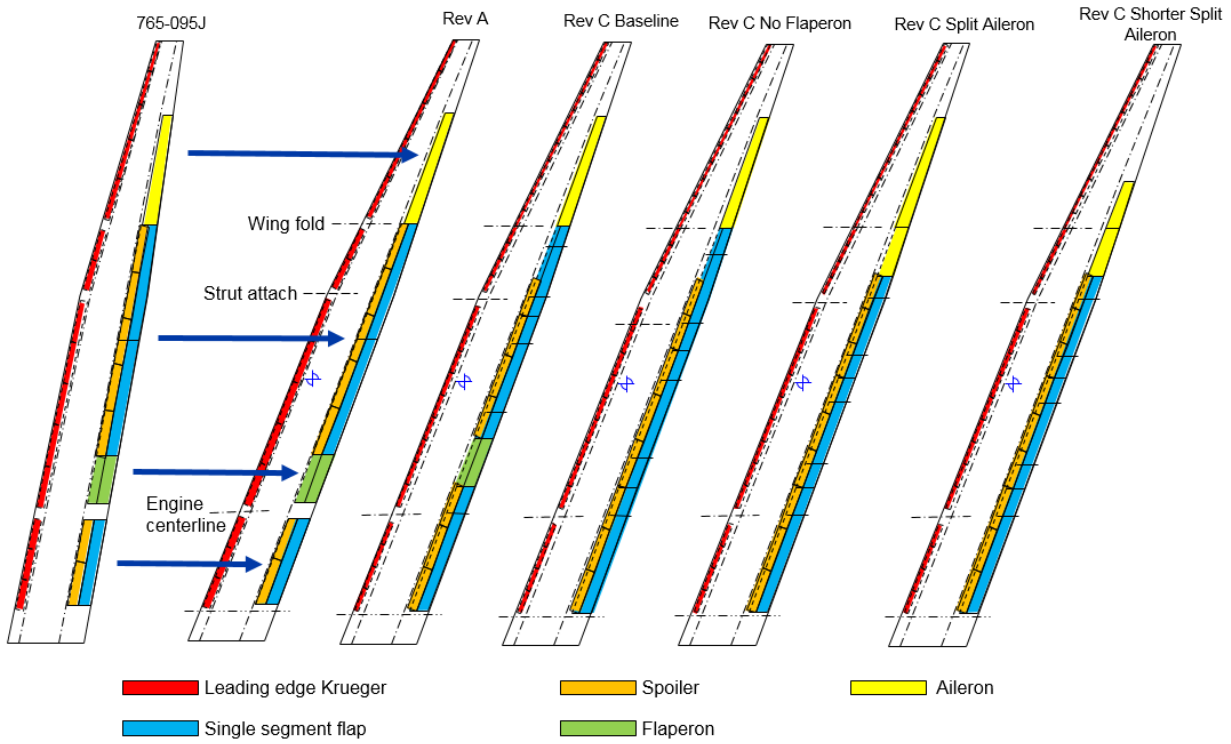


Figure 157 – Candidate Wing Control Surface Layouts.

The left wing is the layout as of the end of Phase III on the Mach 0.745 wing planform. The five layouts on the right are the candidate layouts for the Mach 0.80 TTBW aircraft.

Roll Requirements

The two primary roll authority requirements are Maximum Steady State Roll Rate and Time-To-Bank. The minimum steady state roll rate required for the vehicle depends on the flight conditions. Under normal operation, 25 degrees per second is the minimum target. Above cruise Mach (M_C) or cruise velocity (V_C), the requirement is relaxed to 15 degrees per second.

The time-to-bank requirement is set by the time it takes the aircraft to bank 30 degrees. For the terminal flight phase, the aircraft must bank in less than 2.5 seconds to meet Level 1 flying qualities. In nonterminal flight phase, the requirement is relaxed to 3 seconds for Level 1 flight and 6 seconds for Level 2 flight. Note that above the max operating Mach (M_{MO}), Level 2 flying qualities are allowed.

Other considerations for selecting the most feasible layout are that the aircraft must have the capability for lateral trim at high speed. Typically, this function is performed by inboard aileron/flaperon and is not used for roll.

Additionally, if the control surface experiences aeroelastic reversal at any point in the flight envelope, the surface is locked out in that flight regime and cannot be used for roll or trim. This is typically experienced by the outboard aileron, which can only be used for low speed roll.

Roll Authority Analysis

To analyze the roll authority of the Mach 0.80 TTBW design, wind tunnel data from the Phase IV Retest of the Mach 0.745 vehicle (Ames 11ft. NASA Test designation AT0343) was used. This data was adjusted using AVL to represent aero data for a Mach 0.80 TTBW design. However, because the proposed layouts do not directly match up with the layout on which wind tunnel data was collected, control surfaces must be mapped from the original layout. The diagram below shows how the control surfaces were mapped to each of the candidate planforms (Figure 158).

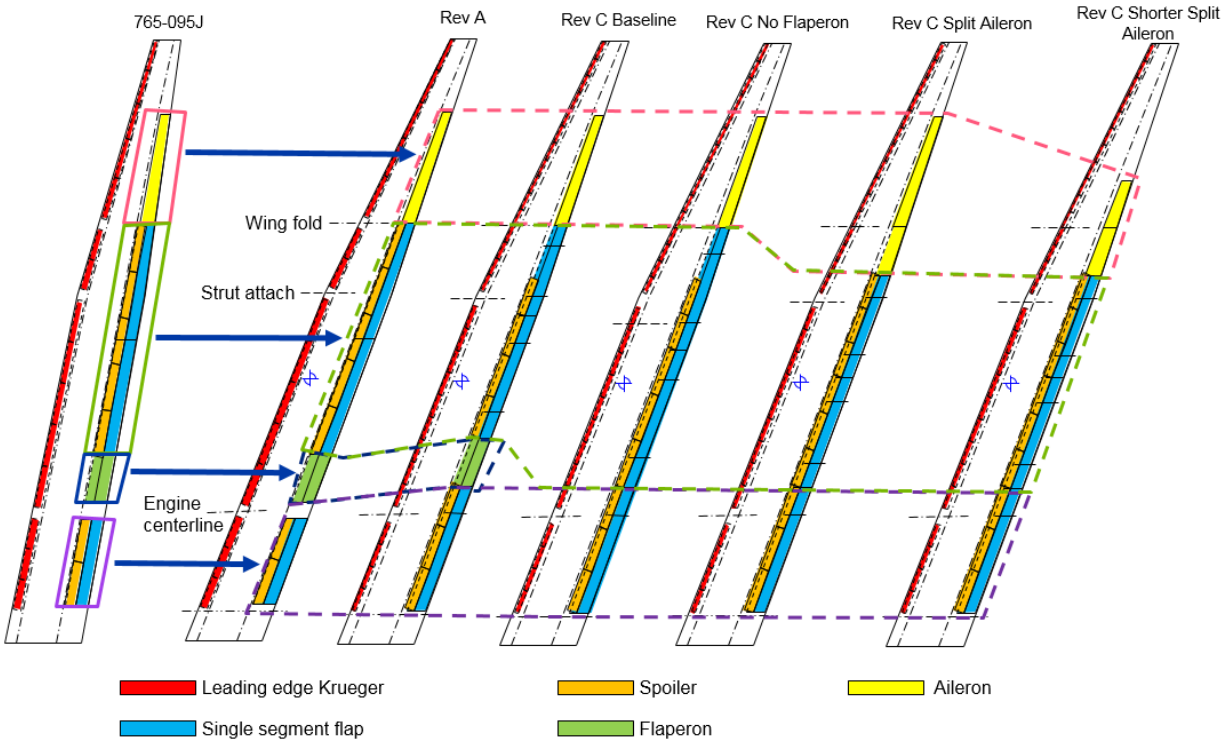


Figure 158 – Control Surface Layout Similarity.

Estimates of the aeroelastic effects of the vehicle were taken from results from the Mach 0.80 FEM produced in Phase III. Spoiler aeroelastic effect trends were taken from legacy McDonnell-Douglas aircraft data.

The max deflections of all ailerons was 40 degrees trailing edge up and 30 degrees trailing edge down. The max deflections of spoilers were 60 degrees trailing edge up. In all scenarios, the max deflection of all surfaces were used. Note that only spoilers were used to roll the aircraft for all starred regions of the flight envelope in the tables that follow. This is because any surface that aeroelastically reverses at any part of the flight envelope is locked out from use. Reversal has

been observed in the outboard aileron. All available surfaces were used for Approach. The results are summarized Table 22 and Table 23.

Table 22 – Maximum Steady-State Roll Rate Results Summary. Green cells exceed requirement, orange cells, meet requirement, red cells do not meet requirement.

Maximum Steady State Roll Rate (dps) Alpha = 10 deg @ M = 0.2, Slat Retracted Alpha = 3 deg @ M > 0.2								
Envelope	Mach	Dynamic Pressure (psf)	Required Roll Rate (dps)	Planform 1	Planform 2	Planform 3	Planform 4	Planform 5
Approach	0.2	Internal Boeing Requirement						
	0.2							
	0.2							
	0.2							
	0.2							
	0.2							
	0.2							
	0.2							
Cruise*	0.8							
	0.8							
	0.8							
	0.8							
	0.8							
	0.8							
	0.8							
Max Operating*	0.83							
	0.83							
	0.83							
	0.83							
	0.83							
	0.83							
	0.83							
Dive*	0.9							
	0.9							
	0.9							
	0.9							
	0.9							
	0.9							
	0.9							

Table 23 – Time-to-bank results summary. Green cells exceed requirement, orange cells meet requirement, red cells do not meet requirement.

Time-to-Bank

Alpha = 10 deg @ M = 0.2, Slat Retracted
Alpha = 3 deg @ M > 0.2

Envelope	Mach	Dynamic Pressure (psf)	Required Time-to-Bank (s)	Required Bank Angle (deg)	Planform 1	Planform 2	Planform 3	Planform 4	Planform 5
Approach	0.2	55	Internal Boeing Requirement						
	0.2	100							
	0.2	200							
	0.2	300							
	0.2	400							
	0.2	500							
	0.2	550							
Cruise*	0.8	100							
	0.8	200							
	0.8	300							
	0.8	400							
	0.8	500							
	0.8	550							
Max Operating*	0.83	100							
	0.83	200							
	0.83	300							
	0.83	400							
	0.83	500							
	0.83	550							
Dive*	0.9	100							
	0.9	200							
	0.9	300							
	0.9	400							
	0.9	500							
	0.9	550							

Before discussing the results summarized above, some planform layouts can be eliminated immediately. Because the outboard aileron is locked out from use at high speed, there are no other devices with which to laterally trim the vehicle for Layout 3. Thus, Layout 3 can be eliminated as a viable option. All other planforms have some method of laterally trimming the vehicle at high speed provided that the inboard aileron does not reverse.

While all layouts do not meet both roll requirements at Approach, Layout 4 shows the best performance, particularly at low dynamic pressures where aircraft will be realistically flying (typical approach dynamic pressure is around 55 psf). This area of the envelope is the driving case for sizing surface areas and setting max deflections of control surfaces. This is due to the more stringent requirement at low speed combined with the low dynamic pressure. Depending on the flexibility of the wing, some small aeroelastics effects may also be present which might limit roll performance.

Even though Layout 4 is not predicted to meet all requirements, the design is feasible and may close with higher fidelity analysis and/or continued trade studies. Since this situation is a commonly encountered trade-space in aircraft design, there are a range of available potential solutions, such as: increasing the low speed surface deflections of the outboard ailerons, increasing the aileron area, increasing the stiffness of the wing, or utilizing more advanced technology to increase the effectiveness of the control surfaces. While the high AR makes the problem more challenging by shortening the chord lengths of roll control surfaces, shortfall in roll power at this point in the design cycle is not normally considered a showstopper especially when estimated with a low order analysis.

6.0 Performance

Boeing's Computer Aided Sizing and Evaluation System (CASES) tool has been used here to calculate mission performance including payload, range and fuel consumption. The CASES tool consists of separate programs for analyzing mission, takeoff, and landing performance, respectively, all of which have been validated over time against empirical airplane performance data. These analyses may be conducted for various atmospheric conditions, and low-speed field length analyses include both all-engine and one engine inoperative (OEI) calculations.

Performance and sizing for SUGAR is performed within a ModelCenter environment, which serves as a wrapper for the various CASES performance analysis components. Aerodynamic, propulsive and mission data are specified, as are the basic empty weight and sizing derivatives. The ModelCenter environment provides a platform for running the parametric trade studies and optimizations necessary for performance and sizing in addition to providing some data visualization tools. Engine thrust and wing area were varied to minimize block fuel per seat while enforcing Takeoff Field Length (TOFL), Initial Cruise Altitude Capability (ICAC), climb, approach speed, and fuel margin constraints to size the latest SUGAR 1104-001 configuration. The sizing process is illustrated in Figure 159.

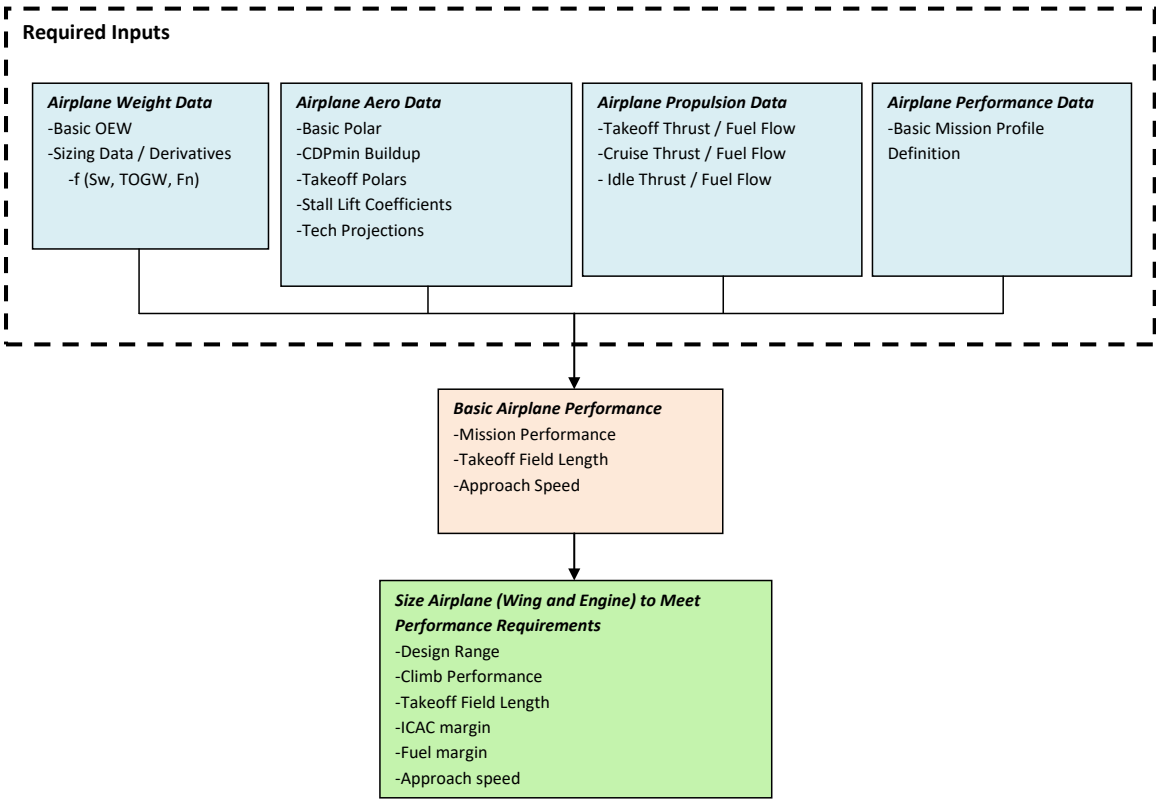


Figure 159 – Airplane Sizing Using CASES / ModelCenter.

6.1.1 Sizing Requirements

A set of top level requirements for the SUGAR vehicles was generated from the future scenario previously reported in SUGAR Phase I (12). These top level requirements were turned into specific payload-range requirements, which are illustrated in Figure 160. The figure has several points of interest indicated and described below.

1. The airplane is required to fly the average range (900 nm) at the maximum payload condition (which is the same as the maximum zero fuel weight condition). The maximum payload is required to be 15,200 pounds heavier than the payload corresponding to Point 2.
2. The airplane is required to fly the maximum range (3,500 nm) at the average number of filled seats using 200 pounds per passenger and no revenue payload. This point must be achieved using less than 90% of the useable fuel.
3. Point 3 is used to calculate vehicle fuel consumption and take-off field length (TOFL) performance for the SUGAR program. This is the point that represents the most common operating condition for this vehicle class, and corresponds to a range of 900nm.

Both Points 1 and 2 are required for sizing because airplane characteristics may alter which of the two is critical. The mission profile for SUGAR 2035 concepts is shown in Figure 161. Advanced concepts studied under this program are evaluated using the illustrated mission while the reference vehicle SUGAR Free (2005 best-in-class) is flown with a non-advanced air traffic management system. These missions are further documented in the Phase I report (1).

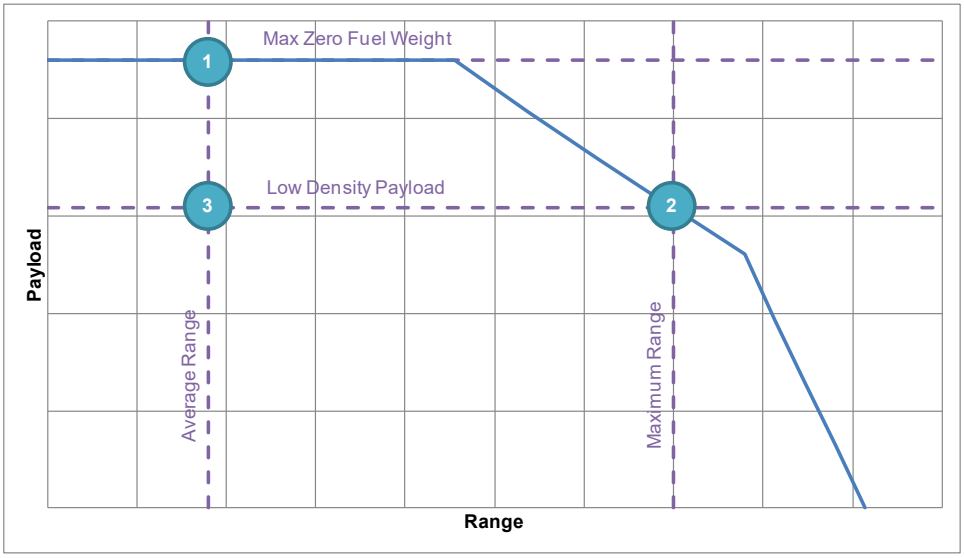


Figure 160 – Payload-Range Requirements.

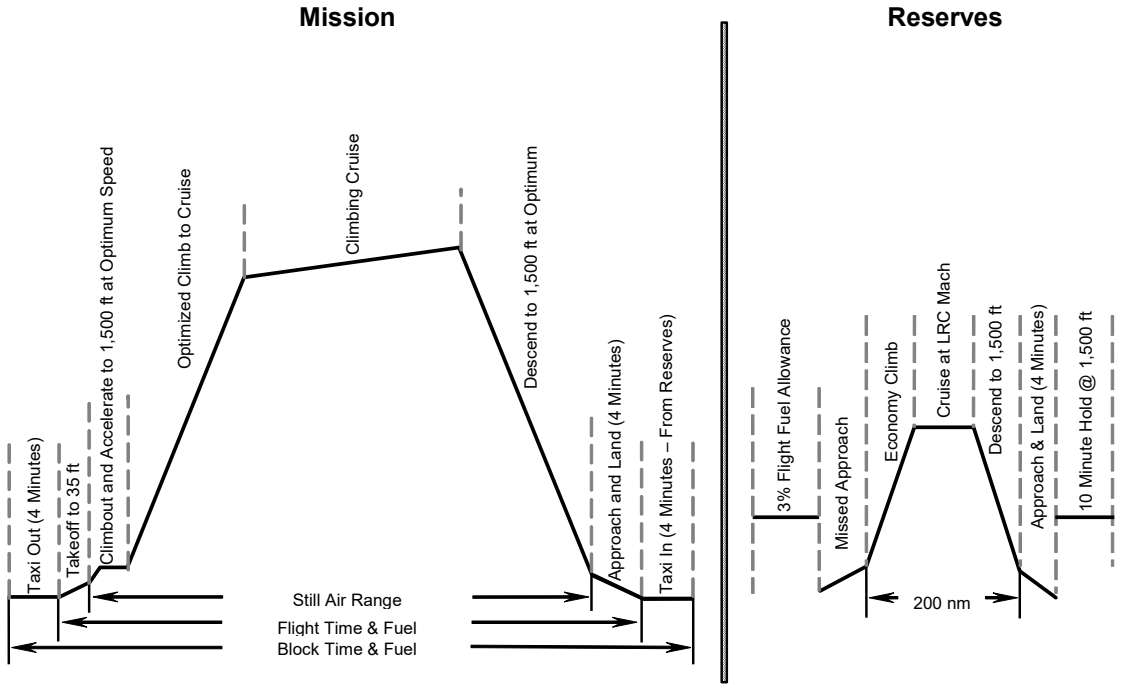


Figure 161 – 2035 Mission Profile with NextGen Air Traffic Management.

6.1.2 Sizing Results

The performance of the SUGAR 1104-001-RG is shown in Table 24, compared against SUGAR 765-095-RJ, which is the Mach 0.745 variant.

There are several different sizing cases shown; from left to right, the first two columns are referred to as 'As-Drawn' meaning the performance was run at the reference wing area, thrust, and MTOW used to generate the baseline vehicle data. The next set of columns represent sized data for minimum fuel consumption constrained by initial cruise altitude capability (ICAC) and fuel margins. The ICAC constraint requires that the aircraft be able to climb to the altitude yielding best specific range (its optimum altitude). It should be noted that the takeoff field length, climb performance, and approach speed constraints were inactive. These configurations were sized at maximum range cruise (MRC) Mach. The remaining two columns illustrate the corresponding fallout performance data for the MRC-sized configurations run at long-range cruise (LRC) Mach, which seeks to fly at 99% of the maximum specific range. Operation at LRC allows an increase in aircraft productivity with only a modest impact to fuel consumption.

The performance of the airplane is shown relative to the SUGAR Free baseline (configuration 765-093 with mission performance run in BMAP, an alternative sizing and performance tool) in Table 25. This shows a 57.0 and 55.9 percent reduction in fuel consumption for the 765-095-RJ and 1104-001-RG respectively.

Table 24 – 765-095-RJ and 1104-001 Mission Performance.

Model Sizing level		765-095-RJ As-Drawn	1104-001-RG As-Drawn	765-095-RJ Sized, MRC, Min Fuel	1104-001-RG Sized, MRC, Min Fuel	765-095-RJ LRC fallout performance	1104-001-RG LRC fallout performance
PASSENGERS / CLASS		154 / DUAL	154 / DUAL	154 / DUAL	154 / DUAL	154 / DUAL	154 / DUAL
MAX TAKEOFF WEIGHT	LB	150,000	145,000	131,557	137,775	131,557	137,775
MAX LANDING WEIGHT	LB	138,987	139,172	131,208	135,157	131,208	137,157
MAX ZERO FUEL WEIGHT	LB	130,987	131,172	123,208	129,157	123,208	129,157
OPERATING EMPTY WEIGHT	LB	84,987	85,172	77,208	83,157	77,208	83,157
FUEL CAPACITY REQ / AVIL	USG	5,684 / 5,417	4,351 / 3,594	3,533 / 3,533	3,573 / 3,573	3,533 / 3,533	3,573 / 3,573
ENGINE MODEL		gFan+	gFan+	gFan+	gFan+	gFan+	gFan+
FAN DIAMETER	IN	71	71	66	72	66	72
BOEING EQUIVALENT THRUST (BET)	LB	23,000	23,000	20,158	23,383	19,866	23,383
WING AREA / SPAN	FT^2 / FT	1,478 / 170	1477 / 170	1142 / 149	1270 / 158	1142 / 149	1,270 / 158
ASPECT RATIO (EFFECTIVE)		19.56	19.56	19.56	19.56	19.56	19.56
OPTIMUM C_L		0.7463	0.6314	0.8177	0.7439	0.7516	0.6983
CRUISE L/D @ OPT C_L		26.202	24.768	25.01	24.642	24.359	24.259
MID-CRUISE C_L - L/D		0.742 - 25.964	0.6261 - 24.493	0.8122 - 24.785	0.725 - 24.565	0.745 - 24.045	0.6935 - 24.030
DESIGN MISSION RANGE	NMI	4,944	4,482	3,500	3,500	3,466	3,497
PERFORMANCE CRUISE MACH*		0.720 (MRC)	0.775 (MRC)	0.718 (MRC)	0.775 (MRC)	0.744 (LRC)	0.800 (LRC)
LONG RANGE CRUISE MACH (LRC)		0.747	0.80	0.745	0.800	0.745	0.800
INITIAL CRUISE THROTTLE SETTING	%	0.951	0.969	0.956	0.970	0.964	0.976
CLIMB CL (INITIAL - END)		0.4699 - 0.7463	0.4191 - 0.6314	0.4986 - 0.8177	0.4621 - 0.7439	0.5024 - 0.7516	0.4621 - 0.6983
ROC (INITIAL - END)	FT / MIN	3,645 - 299	3,748 - 300	3,675 - 301	4,143 - 300	3,673 - 304	4,143 - 300
THRUST ICAC (MTOW, ISA)	FT	41,363	41,640	40,469	42,957	40,211	42,973
TIME / DIST (MTOW, 35k FT, ISA + 15C)	MIN / NMI	21 / 121	21 / 132	20 / 124	18 /112	21 / 131	18 / 112
OPTIMUM ALTITUDE (MTOW, ISA)	FT	42,626	44,437	40,469	42,957	40,410	43,055
BUFFET ICAC (MTOW, ISA)	FT	43,546	47,365	40,869	45,270	41,400	46,004
TOFL (MTOW, SEA LEVEL, 86 DEG F)	FT	3,846	5,742	6,731	5,910	6,731	5,910
APPROACH SPEED (MLW)	KT	116.5	122.0	128.8	130.6	128.8	130.6
BLOCK FUEL / SEAT (900 NMI)	**LB**	**42.50**	**41.42**	**39.31**	**40.39**	**39.58**	**40.52**

* Cruise Mach is set as MRC or LRC which is then calculated and reported by the performance routine

Table 25 – 765-095-RJ and 1104-001 Mission Performance Comparison.

Model Sizing level		765-093 SUGAR Free (2005 Best in Class)	765-095-RJ Sized, MRC Min Fuel	1104-001-G Sized, MRC Min Fuel
PASSENGERS / CLASS		154 / DUAL	154 / DUAL	154 / DUAL
MAX TAKEOFF WEIGHT	LB	182,600	131,557	137,775
MAX LANDING WEIGHT	LB	149,400	131,208	135,157
MAX ZERO FUEL WEIGHT	LB	140,400	123,208	129,157
OPERATING EMPTY WEIGHT	LB	94,400	77,208	83,157
FUEL CAPACITY REQ / AVIL	USG	9,633 / 9,633	3,533 / 3,533	3,573 / 3,573
ENGINE MODEL		CFM56-7B27	gFan+2	gFan+2
FAN DIAMETER	IN	62	66	72
BOEING EQUIVALENT THRUST (BET)	LB	27,900	20,158	23,383
WING AREA / SPAN	FT^2 / FT	1,406 / 121	1142 /149	1,381 / 164
ASPECT RATIO (EFFECTIVE)		10.41	19.56	19.56
OPTIMUM C_L		0.584	0.8174	0.7283
CRUISE L/D @ OPT C_L		17.997	24.958	24.708
DESIGN MISSION RANGE	NMI	3,680	3,500	3,500
PERFORMANCE CRUISE MACH*		0.79 (LRC)	0.718 (MRC)	0.775 (MRC)
LONG RANGE CRUISE MACH (LRC)		0.79 (LRC)	0.745	0.80
THRUST ICAC (MTOW, ISA)	FT	36,200	40,469	42,957
TIME / DIST (MTOW, 35k FT, ISA + 15C)	MIN / NMI	23 / 148	21 / 126	18 /112
OPTIMUM ALTITUDE (MTOW, ISA)	FT	34,900	40,469	42,957
BUFFET ICAC (MTOW, ISA)	FT	36,200	40,869	45,270
TOFL (MTOW, SEA LEVEL, 86 DEG F)	FT	8,190	6,731	5,910
APPROACH SPEED (MLW)	KT	126	128.8	130.6
BLOCK FUEL / SEAT (900 NMI)	LB	91.51 (Base)	39.31 (-57.0%)	40.39 (-55.9%)

* Cruise Mach is set as MRC or LRC which is then calculated and reported by the performance routine

Performance was evaluated at various combinations of fuel and payload weights to generate the payload-range curve shown in Figure 162. This curve shows that the 1104-001 variant, like the 765-095-RJ, does not meet the stated range requirements at the maximum payload condition with only 798 nautical miles of range. The airplane was not sized to accommodate this maximum payload condition in an effort to maintain consistency with the 765-095-RD UDF (9) and clearly illustrate the improvements made during the Phase III study. The flat upper portion of the curve (at 46,000 lb. payload) represents the maximum zero fuel weight constraint of the airplane. The shallow sloped portion of the curve is set by Maximum Takeoff Weight (MTOW). The final far right region of the chart is set by the fuel volume limit.

Block Fuel for each configuration is compared to the SUGAR Free in Figure 163. The NASA goal is a 60% reduction. The fuel consumption per segment in comparison to SUGAR Free is shown in Figure 164 for the 900 nautical mile economic mission. Fuel consumption as a function of range is illustrated by Figure 165.

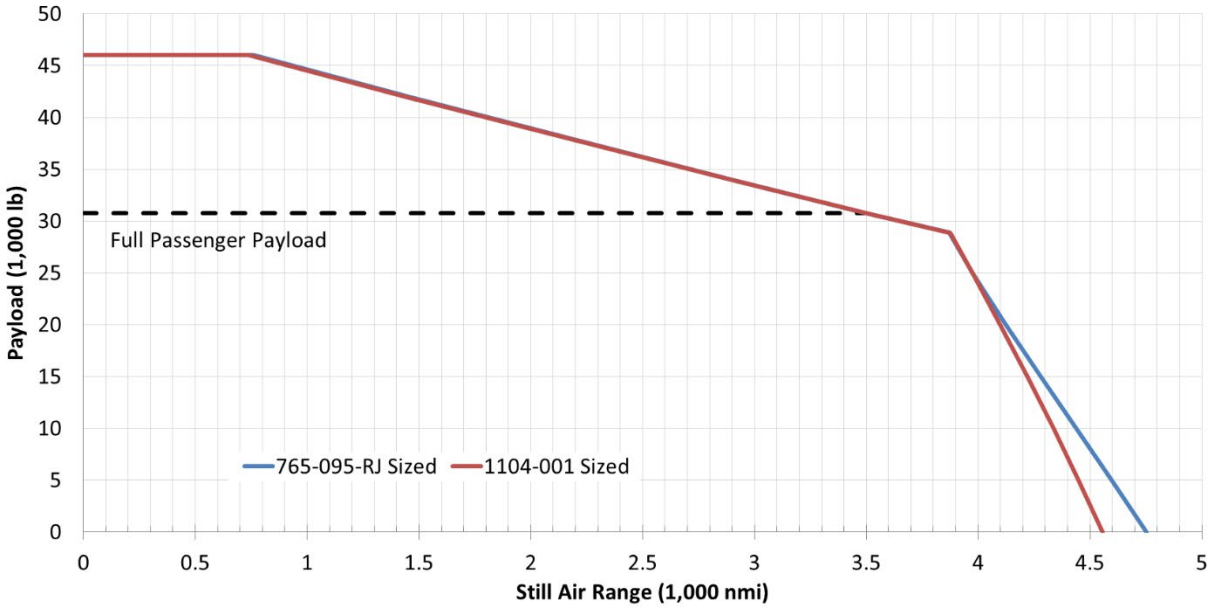


Figure 162 – 765-095-RJ and 1104-001-RG Sized Payload-Range Curves.

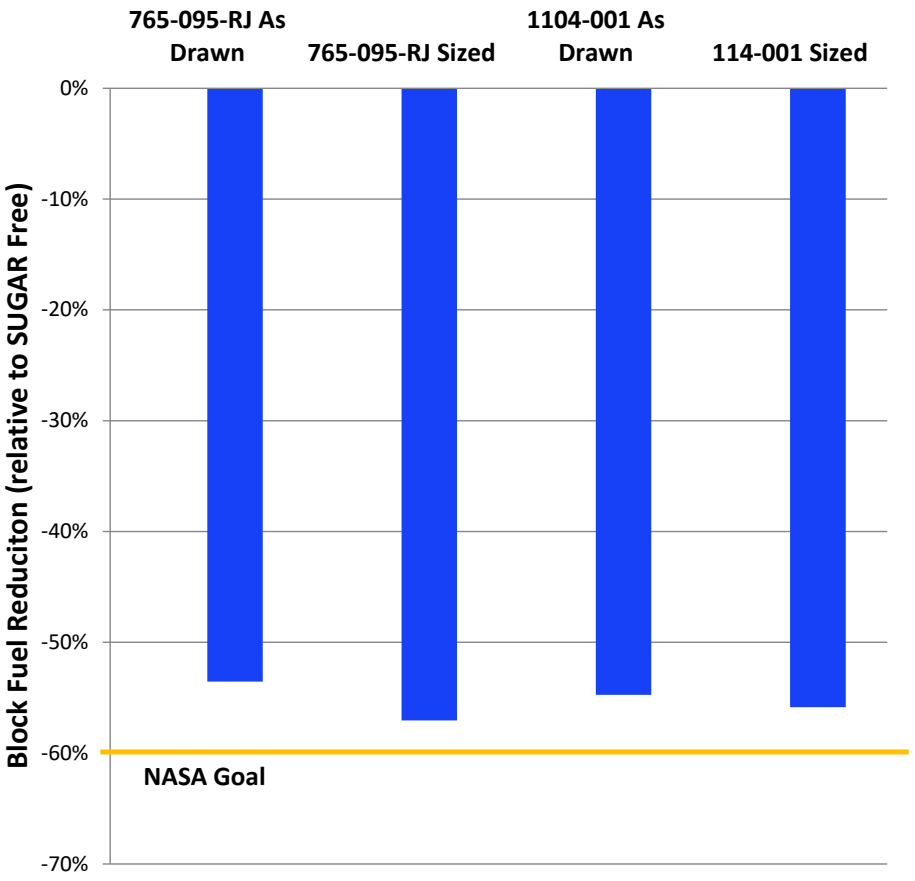


Figure 163 – Block Fuel Reduction Compared to NASA Goal.

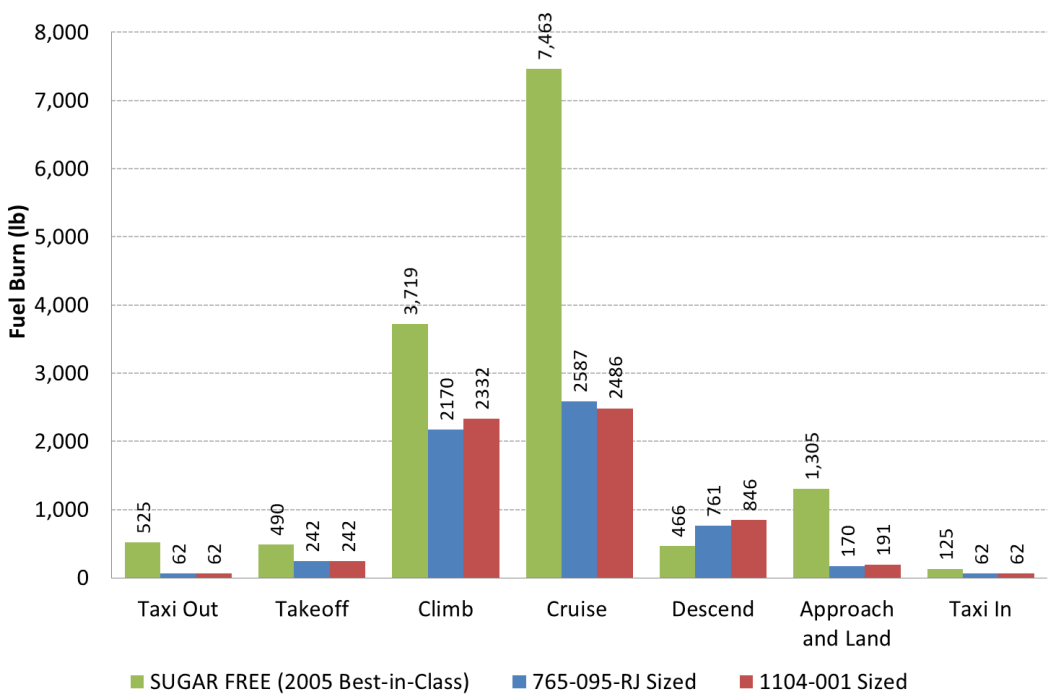


Figure 164 – Fuel Consumption per Segment.

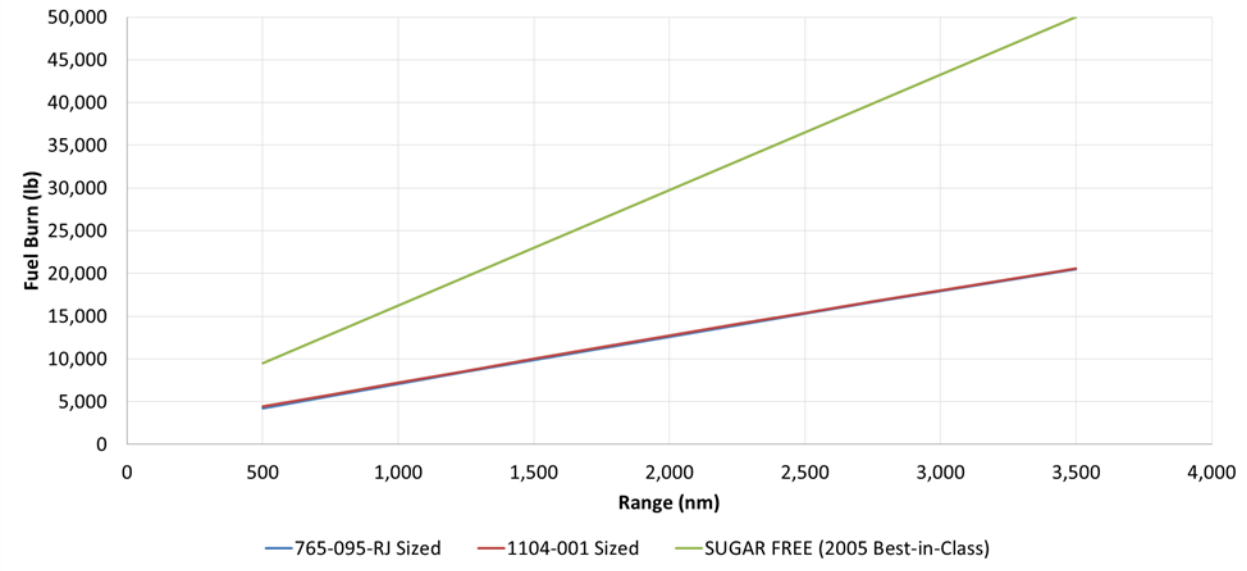


Figure 165 – Block Fuel vs. Range between SUGAR FREE (2005 Best-in-Class), 765-095-RJ Sized, and 1104-001 Sized.

It should be noted that in the sizing results presented thus far, both the 765-095-RJ and the 1104-001-RG configurations contained 1,000 gallons of fixed body fuel tank volume. This decision slightly reduced fuel consumption as fuel volume constraints were relaxed on the wing planform. Because the body tank size was held constant between the two variants and the Mach 0.745 aircraft has lower total fuel consumption, this means a greater percentage of the fuel was stored in the body for the slower aircraft. As both wings are sized to accommodate the additional fuel required, this led to a slightly larger wing on Mach 0.80 aircraft (a slight discrepancy in sizing). To allow a more direct comparison, both vehicles were also sized without a body fuel tank. These variants are denoted 795-095-RJ-01 and 1104-001-01. The results are shown in Table 26 below, where they are referenced to the SUGAR Free aircraft. It can be seen that removing the body tank causes both variants to size up and increases fuel consumption. The fuel use difference between the Mach 0.745 and 0.80 aircraft is reduced from 1.08 lbs/pax to 0.93 lbs/pax when the aircraft are compared without body fuel, and it is believed that this is a more accurate depiction of the fuel consumption delta associated with higher Mach number cruise.

Table 26 – 765-095-RJ and 1104-001 Sized With and Without Body Fuel Tank.

Model Sizing level		765-093, SUGAR FREE (2005 Best in Class)	765-095-RJ, Sized, MRC Min Fuel, With Body Fuel Tank	765-095-RJ-01, Sized, MRC Min Fuel, No Body Fuel Tank	1104-001-RG, Sized, MRC Min Fuel, With Body Fuel Tank	1104-001-RG-01, Sized, MRC Min Fuel, No Body Fuel Tank
PASSENGERS / CLASS		154 / DUAL	154 / DUAL	154 / DUAL	154 / DUAL	154 / DUAL
MAX TAKEOFF WEIGHT	LB	182,600	131,557	138,307	137,775	144,035
MAX LANDING WEIGHT	LB	149,400	131,208	136,439	135,157	141,943
MAX ZERO FUEL WEIGHT	LB	140,400	123,208	123,439	129,157	133,943
OPERATING EMPTY WEIGHT	LB	94,400	77,208	82,439	83,157	87,943
FUEL CAPACITY REQ / AVIL	USG	9,633 / 9,633	3,533 / 3,533	3,764 / 3,764	3,573 / 3,573	3,803 / 3,803
ENGINE MODEL		CFM56-7B27	gFan+	gFan+	gFan+	gFan+
FAN DIAMETER	IN	62	66	74	72	77
BOEING EQUIVALENT THRUST (BET)	LB	27,900	20,158	25,243	23,383	26,727
WING AREA / SPAN	FT^2 / FT	1,406 / 121	1142 /149	1,587 / 176	1,381 / 164	1,645 / 179
ASPECT RATIO (EFFECTIVE)		10.41	19.56	19.56	19.56	19.56
OPTIMUM C_L		0.584	0.8174	0.8149	0.7283	0.6619*
CRUISE L/D @ OPT C_L		17.997	24.958	26.18	24.708	25.41
DESIGN MISSION RANGE	NMI	3,680	3,500	3,500	3,500	3,500
PERFORMANCE CRUISE MACH*		0.79 (LRC)	0.718 (MRC)	0.719 (MRC)	0.775 (MRC)	0.775 (MRC)
LONG RANGE CRUISE MACH (LRC)		0.79 (LRC)	0.745	0.745	0.8	0.8
THRUST ICAC (MTOW, ISA)	FT	36,200	40,469	45,008	42957	45,520
TIME / DIST (MTOW, 35k FT, ISA + 15C)	MIN / NMI	23 / 148	21 / 126	14 / 91	18 /112	16 / 101
OPTIMUM ALTITUDE (MTOW, ISA)	FT	34,900	40,469	44,903	42,957	47,107
BUFFET ICAC (MTOW, ISA)	FT	36,200	40,869	46,290	45,270	49,744
TOFL (MTOW, SEA LEVEL, 86 DEG F)	FT	8,190	6,731	4,214	5,910	4,187
APPROACH SPEED (MLW)	KT	126	128.8	115.1	130.6	116.8
BLOCK FUEL / SEAT (900 NMI)	LB	91.51 (Base)	39.31 (-57.0%)	42.92 (-53.1%)	40.39 (-55.9%)	43.85 (-52.1%)

* Cruise Mach is set as MRC or LRC which is then calculated and reported by the performance routine

7.0 Summary

In Phase I of the SUGAR project, a truss-braced wing configuration was identified as having the potential to reduce fuel consumption and emissions for a domestic passenger transport mission. Two primary areas of risk were identified: novel aeroelastic effects and uncertainty in the assumed level of aerodynamic interference between the wing and strut at transonic conditions.

During Phase II, the first of these risk areas was addressed through the development of a detailed analytical model and an aeroelastic wind tunnel test in the NASA Langley Research Center Transonic Dynamics Tunnel. Both flutter speed and mechanism were found to be analytically predictable, and the weight increment associated with flutter margin was found to be small enough to maintain the aerodynamic advantage of increased span. Further work remains in introducing unsteady aerodynamic effects to better capture the aeroelastic boundary shapes with the theoretical model, but the results indicate that aeroelastic phenomena should not pose a major barrier to the development of transonic truss-braced wing aircraft.

During Phase III the second primary risk area was addressed through detailed aerodynamic design of a truss-braced wing aircraft with a nominal cruise Mach number of 0.745. A variety of modern computational fluid dynamics and optimization tools were used, including Navier-Stokes-based methods, and a series of transonic wind tunnel tests was performed to validate the predicted aerodynamic performance. Based on computational results, interference effects between the wing and strut were reduced to approximately 1% of total airplane drag at this Mach number and uncertainty in predicted aircraft performance was significantly reduced. Wind tunnel tests of the configuration were performed at the NASA Ames 11-ft TWT. Preliminary results are presented in the Appendix of this report. Detailed analysis of the results will be presented in a subsequent volume.

An additional task during Phase III was the preliminary conceptual design of a higher speed airplane, with a cruise Mach approaching 0.80. The higher cruise Mach number enables increased aircraft productivity, and is believed to more closely align to market demand in the single-aisle domestic passenger transport class. This activity became the basis for this Phase IV activity documented herein.

The results of the Phase IV design effort focused on the development of TTBW technology for a Mach 0.80 aircraft. Detailed high-speed design optimization, vehicle high-lift system design and performance, and structural concept development sizing tasks were completed. Validation tests were conducted both for transonic cruise performance as well as high-lift performance, with the results of these tests presented in a separate series of reports (13) (14) (15).

The performance of the updated Mach 0.80 TTBW design was quantified at the aircraft level, with the TTBW vehicle showing a significant improvement in performance relative to a conventional tube and wing aircraft. Based on detailed Reynolds-averaged Navier Stokes analysis obtained using the NASA code OVERFLOW, in combination with the conceptual design build-up procedure, the predicted performance benefit of the TTBW concept was calculated to show a 7.2% improvement in fuel burn (per seat) for an economic mission of 900nm, and a 9.0% improvement in fuel burn (per seat) for a 3500nm mission with full passenger payload. This benefit is relative to an aspect ratio 13 conventional tube and wing configuration of equivalent technology. When considering the TTBW as part of the suite of technologies that make up the SUGAR concept (as described in the Phase I report (12)), the Mach 0.80 TTBW aircraft was found to enable a 55.9% reduction in fuel use (for a 900nm economic mission) relative to a best-in-class single-aisle transport typical of the 2008 fleet. Although operating at Mach 0.80 has reduced the fuel burn benefit by 1.1% as compared to the Mach 0.745 TTBW SUGAR aircraft, the increase in cruise speed has significantly improved the aircraft's productivity.

Structural concept development work completed in Phase IV has identified several strut attachment concepts that are worth additional development activity – the inboard strut attachment swivel joint concept enables the strut to carry axial loads while avoiding strut bending induced from wing twist as the wing lifts during flight, significantly simplifying the construction of the main strut. The outboard strut attachment offset (curved beam) strut concept holds potential for further reducing the aerodynamic interference in the wing-strut channel and further mitigating buffet concerns.

Based on work performed to date on Phase IV and the previous phases of the SUGAR program, the TTBW concept continues to remain a viable concept for significantly improving the performance of future aircraft. High-fidelity aerodynamic analysis of the Mach 0.80 TTBW aircraft has shown fuel burn improvement that has exceeded initial expectations despite the increase in cruise Mach number. Structural concept maturation has continued to refine the TTBW structure, and stability and control assessments of the vehicle have been made, with neither effort finding any immediate 'show-stoppers' to date. Therefore, the potential benefit of improved performance through the use of a very high aspect ratio strut-braced wing continues to warrant additional study.

7.1 Further Considerations

The aerodynamic performance of the Mach 0.80 TTBW at cruise currently exceeds previous expectations and maintains significant performance advantage over comparative cantilever aircraft of equivalent technology. As a part of the Phase IV effort, wind tunnel testing of both high- and low-speed performance took place starting in 2019. These tests helped to validate vehicle performance predictions, particularly near the cruise design point. While the high-speed

test largely achieved the planned objectives, challenges in the low-speed test delayed some desired objectives, particularly surrounding ice-effects testing and in-ground-effect performance. These objectives have been deferred to a later test entry.

There are therefore several additional areas post-Phase IV remaining in TTBW aerodynamic development which require attention in order to further reduce configuration risk. The most immediate risks regarding the TTBW vehicle aerodynamics are:

1) Uncertainty surrounding the prediction of buffet boundary.
2) High-lift system performance and stall behavior under icing conditions and in-ground-effect.
3) Low-speed performance at higher Reynolds Numbers

The ability to accurately predict aerodynamic buffet (item 1) as well as the structural response of TTBW structure to aerodynamic forcing functions remains uncertain. Current prediction methods for determining buffet boundary are empirically-derived from flight and wind tunnel tests of conventional cantilever wing aircraft. Applicability of the established boundaries to this species of aircraft is yet to be validated, and requires a focused study. Given the existence of a final set of Mach 0.80 high-speed TTBW loft, this could be initially addressed via a dedicated buffet-focused wind tunnel test. This model would have significant instrumentation requirements in excess of previous TTBW wind tunnel models, and would likely be achieved through the use of a transonic semi-span model.

Additional low-speed test data focused on icing effects and performance in-ground-effect continues to be an area of interest. These items both address potentially unique sensitivities of the TTBW configuration due to its high aspect-ratio design. In particular, the increased leading edge length and small leading edge radius of both the wing and struts could substantially increase anti-ice system energy requirements, while significantly decreasing the amount of space available for the integration of anti-ice systems. Also, the high wing aspect ratio is likely to have significantly different sensitivities to performance in ground effect as compared to a conventional configuration.

In addition, the data collected in the low-speed wind tunnel to date has been at very low Reynolds Numbers. Since vehicle stall behavior and C_{Lmax} levels are a function of Re, it will be important to quantify the vehicle low-speed performance in the tunnel at higher Re. This data is critically important for establishing the low-speed performance data needed for sizing the vision vehicle.

The Phase IV study was undertaken using a fixed planform defined by a multidisciplinary optimization carried out by Virginia Tech during Phase I. The significant performance advantage of the Mach 0.80 configuration studied in Phase IV again has illustrated that additional multidisciplinary planform optimization is required including variables such as strut and jury tie-

in location, cruise Mach number and strut tie-in strategy. This analysis needs to include detailed aeroelastic investigations, structural modeling of the vehicle's non-linear structural reponse, as well as high-fidelity aerodynamic modeling in order to determine reliable system-level trades.

Perhaps the most significant remaining uncertainty in the TTBW concept is the maturity of structural concepts and associated vehicle weight. Investigations to date have focused primarily on either the development of conceptual concepts or global-level analyses. While many of these structures have been investigated in detail, true maturation of the TTBW structure will require a detailed, integrated structural design in which the various concepts are combined into a working model. These integrated structural concepts must be investigated, developed, and demonstrated to address requirements regarding damage tolerance, fail-safe design, and failure modes.

7.2 Recommendations

Based on lessons learned to date and the remaining configuration unknowns, the following recommendations are made:

- Perform a dedicated buffet-focused wind tunnel test. Use data to improve and/or validate buffet boundary prediction methods for TTBW configurations.
- Perform a second high-lift wind tunnel test using the existing low-speed model to investigate icing effects and performance in-ground-effect.
- Perform a high-Re Number low-speed wind tunnel test to determine performance sensitivitiest to Re. Establish vehicle maximum lift levels to be used for updated vision vehicle sizing analysis.
- Launch a detailed structural integration and design effort to mature TTBW structural concepts. This activity should include design requirements documentation, preliminary structural design, and detailed design and integration of critical structure. The activity should also plan (and execute) structural tests focusing on damage tolerance (bird strike) of the wing, strut, and jury strut and consider other options such as a fuselage drop test for high wing aircraft.
- Perform equivalent conceptual-level design, sizing and optimization studies of cantilever and truss-braced wing aircraft of the same technology level to allow a more fair and transparent comparison of the two configurations. Anchor studies using newly collected aerodynamic and aeroelastic data obtained during Phase II through IV, as well as data that will become available after the test of a Mach 0.80 TTBW aircraft.
- Conduct the preliminary design phase of a possible transonic truss-braced wing demonstrator aircraft.

References

1. **Bradley, M. and Droney, C.** *Subsonic Ultra Green Aircraft Research: Phase I Final Report.* s.l. : NASA, 2011. CR-2011-216847.

2. **Bradley, M., Droney, C. and Allen, T.** *Subsonic Ultra Green Aircraft Research Phase II: Volume I - Truss Braced Wing Design Exploration.* s.l. : NASA, 2014. CR-2015-218704/VOL1.

3. **Bradley, K. and Droney, C.** *Subsonic Ultra Green Aircaft Research Phase II: Volume II - Hybrid Electric Design Exploration.* s.l. : NASA, 2014. CR-2015-218704/VOL2.

4. **Allen, T., Bradley, M. and Droney, C.** *Subsonic Ultra Green Aircraft Research Phase II: Volume III - Truss Braced Wing Aeroelastic Test Report.* s.l. : NASA, 2014. CR-2015-218704.

5. **Droney, C., Sclafani, A. and Grasch, A.** *Subsonic Ultra-Green Aircraft Research Phase III: Mach 0.745 Aerodynamic Design.* s.l. : NASA, 2015.

6. **Jameson, A. and Caughey, D.** *A Numerical Calculation of the Transonic Flow Past a Swept Wing.* s.l. : NASA, 1977. CR-153297.

7. **NASA.** TRANAIR. [Online] https://ntrs.nasa.gov/archive/nasa/casi.ntrs.nasa.gov/19950021809.pdf.

8. **Campbell, R.** *Efficient Viscous Design of Realistic Aircraft Configurations.* s.l. : AIAA Journal, 1998. Paper 98-2539.

9. **Nichols, R. and Buning, P.** *User's Manual for OVERFLOW Version 2.2l.* 2008.

10. **NASA.** Chimera Grid Tools (CGT). [Online] https://www.nas.nasa.gov/publications/software/docs/chimera/index.html.

11. —. HYPGEN. [Online] http://people.nas.nasa.gov/~wchan/cgt/doc/hypgen.html.

12. **Suhs, N., Rogers, S. and Dietz, W.** *PEGASUS 5: An Automated Pre-processor for Overset-Grid CFD.* s.l. : AIAA Journal, 2002. 2002-3186.

13. **Harrison, Neal A., Sclafani, Anthony J., Hoffman, Krishna., Lazzara, David S., Reichenbach, Eric Y.** *Subsonic Ultra-Green Aircraft Research: Phase IV Final Report - Volume I: Mach 0.80 Transonic Truss-Braced WIng High-Speed Design Report.* April 2020.

14. **Commons, Wikimedia.** Flaps Mechanism B787 A320. [Online] 06 2018. https://commons.wikimedia.org/wiki/File:Flaps_Mechanism_B787_A320.png.

15. **Drela, M. and Youngren, H.** AVL. [Online] https://web.mit.edu/drela/Public/web/avl/.

16. **Harrison, Neal A., Sclafani, Anthony J., Beyar, Michael D., Dickey, Eric D., Intravartolo, Niko M.** *Subsonic Ultra-Green Aircraft Research: Phase IV Final Report - Volume II: Transonic Truss-Braced Wing High-Speed Test Report.* March 2020.

17. **Dickey, Eric D. and Beyar, Michael D.** *Subsonic Ultra-Green Aircraft Research: Phase IV Final Report - Volume III: Transonic Truss-Braced Wing High-Lift System Design Report.* 2020.

18. **Dickey, Eric D and Beyar, Michael D.** *Subsonic Ultra-Green Aircraft Research: Phase IV Final Report - Volume IV: Transonic Truss-Braced Wing High-Lift Test Report.* 2020.

19. **Droney, C., Sclafani, A., and Grasch, A.** *SUGAR Phase III: Mach 0.745 Aerodynamic Design Report.* s.l. : NASA CR-2018-xxxx, 2015.